INTERNATIONAL DOCTORAL
SCHOOL OF THE USC

Bastián
Carnero Groba

PhD Thesis

Fabrication of microfluidic devices with optical technologies that can contribute to the development of personalized therapies

Santiago de Compostela, 2024

Doctoral Programme in Laser, Photonics and Vision

USC UNIVERSIDADE DE SANTIAGO DE COMPOSTELA
ESCOLA DE DOUTORAMENTO INTERNACIONAL DA USC

DOCTORAL THESIS

FABRICATION OF MICROFLUIDIC DEVICES WITH OPTICAL TECHNOLOGIES THAT CAN CONTRIBUTE TO THE DEVELOPMENT OF PERSONALIZED THERAPIES

Bastián Carnero Groba

Director: María Teresa Flores Arias

PHD PROGRAMME IN LASER, PHOTONICS AND VISION
SANTIAGO DE COMPOSTELA
2024

Para Áurea

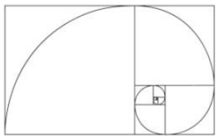

This work has been partially funded by various sources.

The author thanks Axencia Galega de Innovación / Xunta de Galicia for Industrial PhD contract 11-IN606D-2021-2604925.

We thank European Regional Development Fund / Consellería de Educación / Xunta de Galicia for grant ED431B 2023/07.

We thank Grant PID2022-138322OB-100 funded by Ministerio de Ciencia, Innovación y Universidades / Agencia Estatal de Investigación / 10.13039/501100011033 and by European Regional Development Fund "A way of making Europe".

AGRADECEMENTOS / ACKNOWLEDGEMENTS

"La ciencia es mentira sin ti."

Baila Sumeria - Triángulo de Amor Bizarro (Salve Discordia, 2016)

Esta tese é produto de case cinco anos de traballo nos que estiven acompañado de xente marabillosa á que lle debo agradecer tanto que precisaría outras 200 páxinas. Tentarei ser breve.

En primeiro lugar, quero agradecer á miña directora de tese Maite Flores pola súa infinita sabedoría e paciencia, polas horas de terapia no seu despacho e, sobre todo, pola súa inspiradora capacidade de apagar lumes sen despeinarse.

A Bruno K. Rodiño, polos seus consellos e por ensinarme o divertido que pode ser pasar os días, as tardes (e se fora por el, as noites) no laboratorio. Tamén aos compañeiros de BFlow.

Como non, á miña familia. Comezando pola miña nai, a cal me ensinou matemáticas e me motivou a matricularme en física. Ao meu pai, o primeiro investigador que coñecín. Á miña irmá, por sempre abrir camiño. Ás miñas sobriñas Elia e Clara, por animarnos a todos ata nos momentos máis escuros. Ao meu cuñado Javi, pola súa amabilidade con todos nós. E sobre todo á miña avoa Áurea, por criarme. Sei que me verá converterme en doutor dende alá arriba.

Aos meus amigos e amigas de Ponteareas, que sempre estiveron e estarán aí, salvándome a vida (e finxindo entender o que facía). Grazas por preguntarme se xa rematara a tese unhas vinte e sete veces ao día durante os dous últimos anos... aquí a tedes! Moitas grazas Anxos, Uxía, Mateo, Carli, Isaac, Adrián, Jacobo, Iván, Pablo, Jorge, Laura, Iria, Arón, Javi, Desi, Mar, Paula, Gero e á súa señoría Alba Fernández. Moitas grazas a Aloia, sen a cal esta tese non existiría. Grazas a Joaquín, sen o cal quen non existiría sería eu.

A toda a xente que coñecín nos 10 anos que levo no meu querido Santiago. Grazas Carba, Boulli, Bala, Vicky, Cabaleiro, Amparo, Mar, Cósima, Sara e Aldara. Aínda que cada un esteamos nunha punta lévovos sempre no corazón. Grazas a toda a xente que chegou despois: Doval, Martina, Cris e Carmen, grazas por acollerme na vosa casa (e alimentarme) tantas noites. Grazas Yago por axudarme a manterme positivo durante os

momentos difíciles. Grazas a toda a xente de Luzada: aos Damiáns, Irene, Marta, Alicia, Jose, Verónica, Dani, Sabela, Javier, Mónica, Xoel e Adrián. Grazas a Ana, María, Ferrán, Ángel, Carmen, Justo, Eva e aos demais membros de Photonics4Life. Grazas a todos os compañeiros que pasaron polo despacho de Bolseiros de Óptica durante todos estes anos. Grazas aos estudantes de GFNL por acompañarme en tantas comidas en matemáticas, especialmente a Mateo, Vanesa e Marcos. Grazas a Tarasca, ao Avante e ao Maycar. Grazas aos fantabulosos membros de Termotalina, sen dúbida un dos proxectos máis tolos nos que me vin involucrado durante a tese, á par que bonito. Rockanrollear convosco tres edicións do Quantum e deixalo tan en alto foi un auténtico privilexio. Así que grazas Raquel, Balsa, Aisha, Antonio, Marta, Adri, Jose, Javi, Guti, Caetano, Kim e Laupe pola música. Grazas tamén aos meus queridísimos qUANTUM sTRAITS e a Manuéh, o noso fan number one convertido en membro. Grazas en especial a Adela, por aparecer, por darme folgos no sprint final e por prestarme a súa camiseta de Oasis.

Grazas a toda a xente que coñecín polo mundo adiante, na manchea de aventuras nas que a tese me meteu. En particular aos compañeiros de OSAL, cos cales sempre é un pracer coincidir en eventos, organizar MYROs ou directamente irnos de casa rural a Arbo. Grazas por axudarme e apoiarme cando o precisei. Tamén á miña familia galego-belga, por sempre facerme sentir na terriña: Sara, Andrea, Alberto, Nerea, Alejandro, Laura, Irene e María, vémonos no vindeiro EmigraSon! Por suposto a Heidi Ottevaere, a Sara Abassi e ao resto de compañeiros do grupo B-PHOT de Bruxelas. Tamén a Lorena Diéguez, Miguel Xavier e Alar Ainla do INL de Braga, cos cales foi un absoluto pracer poder colaborar.

Por último, e non menos importante, grazas a Nicolas Pokemon, querido anónimo belga que atopou o meu Mac perdido nun tren e tivo a ben abrilo, buscarme en Google e escribirme un correo para avisarme. Grazas polo detalle de non extorsionarme.

Antes de soltarvos o rollo, unhas poucas palabras para quen queira que remate lendo esta tese: querido lector, aquí tes as miñas respostas. Espero deixarte con moitas preguntas.

A ciencia sería mentira sen todos vós.

Grazas pola luz ✨

RESUMO

A investigación presentada nesta tese céntrase na fabricación e desenvolvemento de plataformas microfluídicas mediante tecnoloxías láser para a realización de estudos *in vitro* que contribúan ao desenvolvemento de terapias personalizadas.

A motivación desta investigación xorde da significativa diferenza que existe entre os datos obtidos no desenvolvemento de novos fármacos e os resultados experimentais, obtidos durante a aplicación de ditos medicamentos. Esta diferenza ten a súa orixe nas discrepancias que existen entre as condicións dos experimentos *in vitro,* que involucran moléculas ou células, e as que se dan durante a validación preclínica, en órganos illados e ensaios *in vivo*, o que leva a erros terapéuticos. Para abordar isto, resulta crucial levar a cabo melloras nas estratexias e nas plataformas de descuberta e testado de fármacos, permitindo aumentar a eficiencia, reducindo custos e acurtando os procesos. Unha das propostas con máis potencial á hora de reducir esta diferenza é realizar probas *in vitro* en ambientes ca maior semellanza posible aos fisiolóxicos, de xeito que as células poidan recrear as súas respostas naturais. Esta idea, situada no campo da microfluídica, campo científico que se centra na manipulación e estudo de fluídos a microescala, levou ao desenvolvemento de plataformas coñecidas como Órgano-nun-chip (*Organ-on-a-Chip* en inglés, abreviado no texto como OOC).

É ben sabido que o comportamento das células humanas e, en xeral, dos mamíferos está significativamente influenciado pola súa matriz extracelular e o ambiente circundante. Este principio fisiolóxico indica que ambientes con máis semellanza fisiolóxica producen respostas celulares máis precisas e naturais. A pesar disto, a industria farmacéutica aínda foi quen de adoptar completamente as tecnoloxías OOC debido á insuficiente estandarización e validación, xerando importantes perdas económicas. Polo tanto, resulta necesario avanzar na investigación e no desenvolvementos destas plataformas, co obxectivo de estandarizalas e integralas correctamente nos fluxos de traballo de desenvolvemento de fármacos, ca fin de aproveitar os seus potenciais beneficios en termos de eficiencia, fiabilidade, custo e redución do tempo de desenvolvemento.

Historicamente, a principal técnica de fabricación de dispositivos de microfluídica foi a fotolitografía de materiais coma o vidro ou o silicio, orixinaria da industria dos semiconductores. Esta técnica, a través da irradiación selectiva dunha fotoresina, permite alta resolución, aínda que a súa complexidade (require de salas limpas e involucra numerosos e complexos pasos), a súa limitación en xerar estruturas en 3D (só permite a estruturación de superficies en 2D) e a alta toxicidade dos residuos xerados fan que sexa unha técnica a superar.

Durante o auxe do desenvolvemento dos procesos de microfabricación producido a partir da metade do século pasado, xurdiron novas técnicas que permiten a microestruturación dunha ampla gama de materiais (metais, polímeros, vidros…), mellorando en aspectos como a facilidade de fabricación, a versatilidade ou mesmo a biocompatibilidade, reducindo os custos e complexidade global. Entre estas técnicas de fabricación destacamos a litografía branda, relacionada co uso de moldes para obter réplicas de polímeros, como é o caso do polidimetilsiloxano (PDMS), un polímero con innumerables aplicacións no eido da bioloxía; a estereolitografía, un tipo de impresión 3D baseada na irradiación selectiva dun polímero líquido cunha fonte de luz (xeralmente un láser); e a ablación con láser pulsado, que ten como principais vantaxes a súa velocidade e versatilidade, permitindo a estruturación dunha gran variedade de superficies de vidros ou metais. Este proxecto profundará nelas, co obxectivo de desenvolver unha serie de protocolos e técnicas de fácil implantación, chegando incluso a propoñer técnicas híbridas na que as tres tecnoloxías se empreguen simultaneamente para obter OOC de gran versatilidade e fiabilidade.

Os contidos desta tese resúmense do seguinte xeito:

RESUMO

Este capítulo describe a motivación e a estrutura da tese, centrada na fabricación de plataformas microfluídicas mediante tecnoloxías láser para a realización de estudos *in vitro* que contribúan ao desenvolvemento de terapias personalizadas.

INTRODUCIÓN

Este capítulo proporciona unha visión xeral dos temas clave tratados na tese. En primeiro lugar, realízase unha introdución detallada á tecnoloxía láser, comezando polo seu desenvolvemento histórico e fundamentos teóricos. O láser, acrónimo de *Light amplification by stimulated emission of radiation*, é un dos avances tecnolóxicos máis destacados do século XX, revolucionando campos como a óptica, as telecomunicacións, a fabricación e mesmo a ensinanza. A súa orixe está ligada ao concepto de emisión estimulada, proposto por Albert Einstein no 1917. Einstein suxeriu que, en determinadas condicións, os fotóns podían inducir a emisión de fotóns adicionais en átomos, resultando nunha amplificación da luz. Os compoñentes básicos dun láser inclúen un medio activo, unha fonte de enerxía e unha cavidade

óptica. O medio activo contén átomos ou moléculas que, ao seren excitados, emiten fotóns mediante emisión estimulada. A cavidade óptica, composta por dous espellos, reflicte os fotóns emitidos a través do medio activo, amplificando o proceso de emisión estimulada ata que parte da luz escapa como un feixe coherente.

As propiedades únicas da luz láser, como a súa monocromaticidade, colimación e coherencia, permiten innumerables aplicacións. En medicina, os láseres permitiron cirurxías minimamente invasivas e intervencións moi precisas. Ademais son fundamentais nas redes de telecomunicación modernas, permitindo a transmisión de datos a gran velocidade. No eido da fabricación, no que se centra esta tese, a elevadísima precisión que ofrecen permite cortar, soldar e gravar con eficiencia unha manchea de materiais. Finalmente, en campos como a espectroscopía e a mecánica cuántica, os láseres son ferramentas esenciais para explorar a natureza fundamental da materia e a enerxía.

Como vemos, o papel do láser é crucial no avance do coñecemento e no desenvolvemento científico. En particular, o campo da microfluídica non é excepción e así se discute neste capítulo. A microfluídica é un eido interdisciplinar que combina principios da física, da enxeñería, da química e da bioloxía, permitindo o control preciso de pequenos volumes de líquidos, da orde de mililitros, nanolitros ou mesmo picolitros. A microfluídica destaca principalmente na análise química e biolóxica debido á súa capacidade para utilizar cantidades mínimas de mostras e reactivos, así como á súa alta resolución e sensibilidade.

A historia da microfluídica deriva de tres áreas principais: a análise molecular, a microelectrónica e a bioloxía molecular. Os métodos de microanálise, como a cromatografía, revolucionaron a química, mentres que a microelectrónica contribuíu á miniaturización de dispositivos fluídicos grazas á fotolitografía. A explosión da xenómica nos anos 80 requiriu métodos de alta sensibilidade, facendo da microfluídica unha solución moi cotizada. Nos anos 90, a microfluídica emerxe como un campo propio, grazas ao desenvolvemento de sistemas microelectromecánicos que permitiron a creación de microcanles e válvulas. O seu máximo expoñente son os dispositivos coñecidos como Laboratorio-nun-chip (*Lab-on-a-chip* en inglés, abreviado como LOC), que son quen de integrar múltiples funcións de laboratorio nun único dispositivo, reducindo os volumes das mostras e os custos. A elevada portabilidade deste tipo de dispositivos fan deles unha opción destacada para realizar investigación en países sen recursos. Actualmente a microfluídica ten un gran impacto no eido da medicina, especialmente no diagnóstico e na medicina personalizada, permitindo a detección rápida de enfermidades. Esta tecnoloxía tamén facilita o descubrimento de fármacos ao permitir o testado simultáneo de miles de compostos, debido á pouca cantidade de mostra necesaria.

Analízanse os principios teóricos detrás das técnicas de fabricación típicas da microfluídica, poñendo especial énfase naquelas que involucran o emprego de láseres, como a ablación por láser pulsado (*Pulsed laser ablation* en inglés, abreviado como PLA), a ablación indirecta

asistida por plasma inducido por láser (*Laser-induced plasma-assisted ablation* en inglés, abreviado como LIPAA) e a impresión 3D baseada na estereolitografía (*Stereolithography* en inglés, abreviado como SLA).

O capítulo conclúe detallando a liña que seguirá a tese, centrada en propoñer e desenvolver tecnoloxías ópticas para a fabricación en microfluídica, debido ao gran potencial que ofrece no desenvolvemento de dispositivos máis precisos e fiables, centrando o seu uso en terapias personalizadas.

OBXECTIVOS

Os sete obxectivos principais da investigación realizada nesta tese enuméranse neste capítulo. Estes obxectivos inclúen o deseño de plataformas microfluídicas biocompatibles para o cultivo celular de células endoteliais, a fabricación de estruturas de microcanles en 3D que mimeticen capilares e vasos sanguíneos e o uso de técnicas de impresión 3D estereolitográfica para obter estruturas biocompatibles. Ademais, proponse o estudo de sinerxias entre a ablación láser e a estereolitografía co obxectivo de desenvolver tecnoloxías de fabricación híbridas. O proxecto tamén se centra na creación de plataformas microfluídicas amplamente empregadas e sistemas analíticos como a cámara de Ussing, así como no seguimento en tempo real da morfoloxía das células endoteliais.

MATERIAIS E MÉTODOS

Este capítulo proporciona unha visión xeral dos materiais e a instrumentación utilizada para o desenvolvemento, fabricación e caracterización de plataformas microfluídicas, xunto coas súas respectivas características. Ao longo da tese, empréganse resinas de impresión 3D e vidro de sílice como materiais substrato para obter dispositivos microfluídicos e moldes. Realízase unha análise química e óptica destes substratos para caracterizar as súas propiedades. Ademais, introdúcense materiais como o PDMS para a replicación de canles.

Os procesos de fabricación desenvoltos ao longo da tese involucran a utilización de dous sistemas diferentes baseados en láseres: dous sistemas de láser pulsado e un de láser continuo (en particular, unha impresora 3D estereolitográfica). En concreto, no primeiro caso, empréganse láseres de duración de pulso en nanosegundos (ns) e femtosegundos (fs) para realizar a ablación directa e indirecta de diferentes substratos de vidro, metal e polímero. Este capítulo tamén aborda outra instrumentación utilizada no estudo, como un limpador de plasma para o selado, un forno para tratamentos térmicos, o software utilizado para deseño e simulación dos dispositivos, e ferramentas de caracterización como microscopios ópticos ou confocais.

En canto aos métodos, introdúcese unha nova técnica que implica ablación subacuática, supoñendo un avance respecto á LIPAA. Pola súa parte, a impresora 3D tamén se usa para obter moldes para a litografía branda de PDMS. Ademais, introdúcese un método híbrido, que

combina tanto a ablación con láser como a estereolitografía, ofrecendo resultados prometedores.

TÉCNICA DE ABLACIÓN INDIRECTA SUBACUÁTICA PARA O PROCESAMENTO DE VIDRO E MICROFLUÍDICA

Este capítulo propón un enfoque novidoso, a Ablación indirecta subacuática asistida por plasma inducido por láser (*Subaquatic LIPAA* en inglés, abreviado como SLIPAA), desenvolvida para superar as limitacións dos métodos habituais baseados en láser na obtención de estruturas profundas con alta precisión e paredes verticais rectas. A SLIPAA fundaméntase na introdución dunha capa de auga entre o obxectivo metálico e o substrato de vidro. Deste xeito, a combinación dos mecanismos de ablación, as ondas de choque e as burbullas de cavitación melloran o procesamento e acabado. Os resultados experimentais demostran a efectividade de SLIPAA na fabricación de estruturas de alta profundidade con perfís de sección rectangular en vidro. Investígase de forma detallada a influencia dos parámetros de ablación na forma e calidade da estrutura final, utilizando microscopía óptica e confocal, tomografía microcomputada e microscopía electrónica de varrido. Ademais, a análise composicional utilizando EDX confirma a transferencia de material do obxectivo metálico ás canles fabricadas.

Empregando a técnica proposta, producíronse canais de 1000 µm de anchura, cunha profundidade máxima media que se achega ás 1400 µm despois de 30 pasadas do feixe láser. Unha análise comparativa entre o procesamento con e sen a capa de auga destaca a mellora significativa conseguida coa técnica proposta.

Os achados remarcan o potencial da SLIPAA como un método transformador para o procesamento de vidro, permitindo a fabricación de estruturas máis profundas e complexas. Ao refinar as técnicas de enfoque do láser e integrar películas de auga en condicións de fluxo, esta técnica resulta moi prometedora á hora de ofrecer novas posibilidades en diversos campos onde se require unha microfabricación precisa de vidro.

ESTEREOLITOGRAFÍA COMO TECNOLOXÍA CLAVE PARA A FABRICACIÓN DE DISPOSITIVOS MICROFLUÍDICOS

As impresoras estereolitográficas revolucionaron moitos procesos de fabricación pola súa capacidade para producir facilmente estruturas moi detalladas. No campo da microfluídica, esta técnica reduce moitos pasos dos procesos de fabricación sen necesidade de equipos moi complexos, tal e como ocorre nas tecnoloxías convencionais. Neste capítulo analízanse as capacidades que ofrece esta tecnoloxía empregando unha impresora Form 3B, mediante a fabricación de microcanles e piares.

Estúdase a eficacia á hora de fabricar estruturas internas e superficiais para sete resinas de impresión en diferentes configuracións. Realízase unha caracterización completa das estruturas impresas mediante microscopía óptica, confocal e SEM, ademais dunha análise EDX. Obtéñense canles internas desobstruídas para diámetros e ángulos maiores de 500 μm e 60º, respectivamente. Pódense fabricar canles superficiais externas e internas no rango de centos de micrómetros cun perfil preciso, imprimíndoas cunha orientación perpendicular respecto á base, permitindo unha adecuada evacuación da resina non curada. As canles externas son replicadas por litografía branda utilizando PDMS. As resinas Clear, Model e Tough amosan un bo comportamento para seren utilizadas como moldes, pero as resinas Amber e Dental presentan unha baixa transferencia da topoloxía do molde á réplica. Por último, avalíase a transparencia segundo as necesidades dos dispositivos utilizados para a investigación biolóxica e biomédica.

TÉCNICA HÍBRIDA PARA O MICROESTRUTURADO SUPERFICIAL COMBINANDO ABLACIÓN POR LÁSER PULSADO E IMPRESIÓN 3D ESTEREOLITOGRÁFICA PARA APLICACIÓNS MICROFLUÍDICAS

As estruturas a microescala, incluíndo microcanles e conxuntos de microlentes, xogan un papel vital en varios campos como a enxeñaría, a óptica e a microfluídica, permitindo o manexo de fluídos e un enfoque preciso da luz, respectivamente. Non obstante, os procesos de microfabricación convencionais, caracterizados pola súa complexidade, atopan habitualmente problemas como irregularidades na forma, rugosidade superficial elevada e dificultades no replicado. Estas limitacións reducen o rendemento e a fiabilidade dos dispositivos a microescala, dificultando a súa adopción xeneralizada na investigación e na industria.

Este capítulo propón unha nova técnica híbrida que combina a Estereolitografía (SLA) e a Ablación por Laser Pulsado (PLA) para abordar os desafíos asociados coa fabricación de microlentes e microcanles. Utilizando cada tecnoloxía no seu rango dimensional máis adecuado, o obxectivo é conseguir microestruturas precisas e uniformes con propiedades fluídicas e ópticas incrementadas.

O capítulo presenta un estudo profundo dos parámetros óptimos de ablación para superficies de resina tanto pulidas como sen pulir. A topoloxía das estruturas revela como os láseres desempeñan un papel crucial tanto na fabricación a escala milimétrica (SLA) como na fabricación a escala micrométrica (PLA). O estudo identifica parámetros axeitados para producir microcanles optimizadas para unha mestura de fluídos mellorada e conxuntos de microlentes con diámetros e profundidades adaptables.

APLICACIÓNS BIOLÓXICAS

Despois de establecer as bases coa exploración de varias técnicas de fabricación nos capítulos anteriores, o foco desprazase agora cara a un campo prometedor: a aplicación de diferentes plataformas microfluídicas no eido da biomedicina.

Este capítulo comeza cun profundo estudo de biocompatibilidade dos principais materiais empregados nesta tese para a fabricación de dispositivos microfluídicos. As probas deben ser específicas para a liña celular empregada, xa que a biocompatibilidade pode variar moito entre diferentes tipos de células. Este capítulo avalía a biocompatibilidade de materiais como resinas de impresión 3D e dous tipos de PDMS para asegurar o seu uso seguro en aplicacións biolóxicas e médicas, enfocándose no uso de células endoteliais de vea umbilical humana (*Human umbilical vein endothelial cells* en inglés, abreviado como HUVEC), de gran interese na microfluídica biolóxica dada a súa sensibilidade ás condicións de fluxo.

A continuación, fabricarase unha plataforma microfluídica e utilizarase para estudar a deposición de células tumorais circulantes (CTC), un evento crítico na propagación da metástase. Ademais do atrapamento físico, responsable da maioría dos eventos de deposición, o sistema vascular aporta factores xeométricos que gobernan a biomecánica do fluxo e afectan ao percorrido das CTC. Para isto, fabricáronse microcanles en forma de Y bifurcados, mediante estereolitografía e litografía branda de PDMS. Realizouse cultivo celular dentro das canles aplicando condicións de fluxo biolóxico. Estes resultados tamén foron validados matematicamente e empregados en modelos de rato *in vivo*. Os nosos resultados tamén demostran que a viscosidade, un dos parámetros máis relevantes para o número de Reynolds, que define a biomecánica do fluxo, pode ser modulada para limitar ou impedir a acumulación de CTC na bifurcación dos vasos sanguíneos. Este resultado atópase en concordancia co aparente efecto positivo observado no ámbito clínico producido polos fármacos anticoagulantes en enfermidades oncolóxicas avanzadas.

A segunda plataforma consiste nunha cámara de Ussing microfluídica sensorizada, un sistema amplamente utilizado no estudo de barreiras biolóxicas como a barreira epitelial do intestino. Esta sección aborda desafíos tradicionais da cámara como a súa complexidade, os altos volumes de mostras que require e a limitada compatibilidade que ofrece con sistemas de obtención de imaxe. Combinando técnicas estereolitográficas e de litografía branda, fabricarase unha cámara Ussing microfluídica, superando estas limitacións e incorporando compatibilidade con microscopía. A validación mediante medicións de resistencia eléctrica trans-epitelial (*Trans-Epithelial Electrical Resistance* en inglés, abreviado como TEER) confirma a súa eficacia na avaliación da dinámica de permeabilidade iónica, utilizando monocapas de células Caco-2, mostrando a capacidade da cámara fabricada para detectar o impacto do calcio nas unións estreitas das células.

CONCLUSIÓNS

Esta sección resume os principais achados obtidos na investigación realizada durante esta tese.

Desenvolveuse unha nova técnica chamada SLIPAA, que supera as limitacións na fabricación de canles máis profundas con paredes rectas, utilizando un láser de nanosegundos en substratos de vidro. A SLIPAA logra canles de alta calidade con profundidades superiores a un milímetro, superando as técnicas anteriores (como a LIPAA) en termos de profundidade e calidade superficial.

A investigación sobre impresión 3D, en particular a fundamentada en SLA, centrouse no estudo de sete resinas comerciais, e nos diferentes resultados que estas ofrecen para aplicacións microfluídicas. A resina Dental destacou pola súa rapidez de impresión, mentres que as resinas Clear e Model ofreceron a maior resolución. A orientación das pezas durante a impresión resultou crucial para evitar acumulacións de resina, causantes de obstrucións.

Desenvolveuse unha técnica híbrida que combina PLA e SLA para fabricar estruturas microfluídicas, como micromesturadores e microlentes. Os experimentos demostraron que estes dispositivos melloran a eficiencia de mestura en comparación cas canles planas. Ademais, a fabricación dunha cámara de Ussing sensorizada ofreceu un avance significativo para esta plataforma, permitindo a avaliación en tempo real da integridade de monocapas epiteliais.

Os dispositivos microfluídicos bifurcados fabricados permitiron estudar os mecanismos que levan á deposición das células tumorais circulantes (CTC) nas bifurcacións dos vasos sanguíneos, revelando que a xeometría dos vasos e a viscosidade do fluído influencian a acumulación de CTC. Estes achados suxiren que modificar a viscosidade do sangue podería ser unha estratexia terapéutica para reducir a metástase.

No que respecta ao traballo futuro, propóñense avances na cámara Ussing e na fabricación de estruturas fisioloxicamente miméticas para o estudo de enfermidades. Ademais, proponse abrir unha nova liña de investigación, centrada no potencial que ofrece a microfluídica na refrixeración de compoñentes electrónicas (tal e como sucede en moitos organismos), ofrecendo así solucións innovadoras a problemas de disipación de calor.

LISTA DE PUBLICACIÓNS

Este capítulo compila todas as publicacións académicas derivadas desta tese, incluíndo artigos publicados en prestixiosas revistas internacionais.

REFERENCIAS

As referencias bibliográficas da tese recóllense nesta sección.

1. SUMMARY

This thesis focuses on the manufacturing and development of microfluidic platforms employing laser technologies for conducting *in vitro* studies that can contribute to the development of personalized therapies.

The motivation for this research stems from the significant gap between data obtained from new drugs and their actual results during drug discovery and application. This gap arises from discrepancies between *in vitro* experiments with molecules or cells and preclinical validation in isolated organs and *in vivo* assays, that leads to therapeutic failures. To address this, improvements in drug discovery strategies and platforms are crucial, as they will enhance efficiency, reduce costs, and shortening processes. One approach to bridge this gap is conducting *in vitro* tests in more physiological environments where cells can mimic their natural responses. This idea, situated within the field of microfluidics, scientific field that focuses on the manipulation and study of fluids at a microscale, has led to the development of platforms known as Organ-on-a-Chip (OOC).

It is well-established that the behaviour of human and mammalian cells is significantly influenced by their extracellular matrix and surrounding environment. This physiological principle indicates that more physiologically relevant environments produce more accurate and natural cellular responses. Despite this, the pharmaceutical industry has not yet fully adopted OOC technologies due to insufficient standardization and validation. Advanced research and development are required to standardize these systems and integrate them effectively into drug development workflows, to harness their potential benefits in terms of efficiency, reliability, resource use, and reduced development time.

Historically, the main technique for fabricating microfluidic devices has been photolithography of glass or silicon materials, originating from the semiconductor industry. This technique, through selective irradiation of a photoresist, allows for high resolution, although its complexity (requiring clean rooms and numerous steps), its limitation in generating 3D structures (only allowing 2D surface structuring), and the high toxicity of the waste generated make it a technique to be surpassed.

With the development of microfabrication processes, new techniques have emerged allowing the microstructuring of a wide range of materials (metals, polymers, glasses...), leveraging for each the ease of fabrication, low cost, great versatility, or biocompatibility that characterize them. Among these fabrication techniques, we highlight the soft lithography related to the use of masters to obtain polymer replicas like polydimethylsiloxane (PDMS), with many applications in biology; stereolithography, a type of 3D printing based on the selective irradiation of a liquid polymer with a laser; and pulsed laser ablation, which has as its main advantages its speed and versatility, allowing the structuring of a wide variety of materials, as glasses or metals. This project will focus on them.

The contents of this thesis are organized into the following chapters:

SUMMARY

This chapter outlines the motivation and structure of the thesis.

INTRODUCTION

This chapter provides an overview of the key topics addressed in the thesis. It begins with an extensive exploration of laser technology, covering its historical development and theoretical foundations. The structural aspects and properties of laser light are examined, highlighting its crucial role in advancing scientific knowledge.

Transitioning to microfluidics, the chapter explores its origins and evolution into modern applications. Various manufacturing techniques in microfluidics are discussed in detail, including lithography, soft lithography, and advanced methods like pulsed laser ablation. The theoretical principles behind these techniques are analysed, followed by innovative approaches such as Laser-Induced Plasma-Assisted Ablation and Stereolithographic 3D Printing. The theoretical framework of both techniques is specifically elaborated upon.

The chapter concludes with a comprehensive outline of the thesis, focused in proposing and developing optical technologies for microfluidic manufacturing, given their great potential in the development of more precise and reliable devices for personalized therapies.

OBJECTIVES

The main objectives of the research conducted in this thesis are listed in this chapter.

MATERIALS AND METHODS

This chapter provides an overview of the materials and instrumentation utilized for the developing, manufacturing and characterization of microfluidic platforms, along with their respective characteristics. Throughout the thesis, 3D printing resins and soda-lime glass are

used as substrate materials for obtain microfluidics devices and masters. Chemical and optical analysis of this substrates is performed in order to characterize their properties. Additionally, materials such as polydimethylsiloxane for channel replication are introduced.

The manufacturing processes developed throughout the thesis involve the utilization of two different systems based on lasers: pulsed laser systems and a stereolithographic 3D printer. Nanosecond and femtosecond pulse duration lasers are employed to perform direct and indirect ablation of different substrates. This chapter also delves into other instrumentation used in the study, such as a plasma cleaner for bonding, furnace for thermal treatments, software used for design and simulation, and characterization tools like optical or confocal microscopes.

Regarding methods, a new technique that involves subaquatic ablation is presented. For its part, 3D printer is also used to obtain masters for further soft lithography of PDMS. Furthermore, a hybrid method, that combines both laser ablation and stereolithography is introduced, offering promising results.

SUBAQUATIC INDIRECT LASER ABLATION TECHNIQUE FOR GLASS PROCESSING AND MICROFLUIDICS

This chapter proposes a novel approach, Subaquatic Indirect Laser-Induced Plasma-Assisted Ablation (SLIPAA), developed to overcome the limitations of standard laser-based methods in achieving deep structures with high precision and vertical straight walls. SLIPAA introduces a water layer between a metallic target and a soda-lime glass substrate, leveraging a combination of ablation mechanisms, shock waves, and cavitation bubbles for enhanced processing. Experimental results demonstrate the effectiveness of SLIPAA in fabricating high-depth structures with rectangular cross-sectional profiles in glass. The influence of processing parameters on structure shape and quality is comprehensively investigated using optical and confocal microscopy, microcomputed tomography, and scanning electron microscopy. Additionally, compositional analysis using energy dispersive X-ray technique confirms the transference of material from the metallic target to the fabricated channels.

Employing the proposed technique, channels of 1000 μm width are successfully produced, with an average maximal depth nearing 1400 μm after 30 passes of the laser beam. A comparative analysis between processing with and without the water layer highlights the significant improvement achieved through the proposed technique.

The findings underscore the potential of SLIPAA as a transformative method for glass processing, enabling the fabrication of deeper and more complex intricate structures. By refining laser focusing techniques and integrating pulsed flowing water films, the approach holds promise for unlocking new possibilities in various fields where precise glass microfabrication is required.

STEREOLITHOGRAPHY AS KEY TECHNOLOGY FOR MANUFACTURING MICROFLUIDIC DEVICES

Stereolithographic printers have revolutionized many manufacturing processes due to its capacity to easily produce highly detailed structures. In the field of microfluidics, this technique avoids the use of complex steps and equipment of the conventional technologies. In this chapter, the potential of low force stereolithography technology is analysed using a Form 3B printer through the fabrication of microchannels and pillars.

Manufacturing performance of internal and superficial channels and pillars is studied for seven printing resins in different configurations. A complete characterization of printed structures is carried out by optical, confocal and SEM microscopy, and EDX analysis. Internal channels with unobstructed lumen are obtained for diameters and angles greater than 500 μm and 60º, respectively. Outward and inward superficial channels in the range of hundreds of microns can be fabricated with an accurate profile, printing them with a perpendicular orientation respect to the base, allowing a proper uncured resin evacuation. Outward channels are replicated by soft lithography using polydimethylsiloxane. Clear, Model and Tough resins show a good behaviour to be used as master, but Amber and Dental resins present a poor topology transference from the master to the replica. According to the needs of devices used for biological and biomedical research, transparency is evaluated.

HYBRID TECHNIQUE FOR SUPERFICIAL MICROPATTERNING BY COMBINING PULSED LASER ABLATION AND STEREOLITHOGRAPHIC 3D PRINTING FOR MICROFLUIDICS APPLICATIONS

Microscale structures, including microchannels and microlens arrays, play vital roles in various fields such as engineering, optics, imaging, and microfluidics, offering capabilities for fluid handling and precise light focusing. However, conventional micro manufacturing processes, characterized by their complexity, frequently encounter issues such as irregularities in shape, surface roughness, and difficulties in replication. These limitations reduce the performance and reliability of microscale devices, hindering their widespread adoption in research and industry.

This chapter proposes new hybrid technique that combine Stereolithography (SLA) and Pulsed Laser Ablation (PLA) to address the challenges associated with microlens and microchannel manufacturing. By using each technology on its most suitable dimensional range, the aim is to achieve precise and uniform microstructures with improved fluidic and optical properties.

The chapter presents a comprehensive study to determine optimal ablation parameters for both unpolished and polished resin surfaces The topology of structures reveals how lasers play

a crucial role both in millimetre-scale (SLA) and micrometre-scale (PLA) manufacturing. The study identifies suitable parameters for producing optimized microchannels for enhanced fluid mixing and microlens arrays with tailored diameters and depths.

BIOLOGICAL APPLICATIONS

After laying the groundwork with an exploration of various manufacturing techniques in the preceding chapters, the focus now shifts towards a promising field: the practical application of different microfluidic platforms within the field of biomedical science.

This chapter begins with a deep biocompatibility study of the main materials employed in this thesis for manufacturing microfluidic devices. Testing must be specific to the cell line in use, as biocompatibility can vary greatly between different cell types. This chapter evaluates the biocompatibility of materials such as 3D printing resins, PDMS, and UV-PDMS to ensure their safe use in biological and medical applications, focusing in the use of Human Umbilical Vein Endothelial Cells (HUVEC), of great interest in biological microfluidics given their sensitivity to flow conditions.

Next, a microfluidic platform will be manufactured and used to study the homing of Circulating Tumour Cells (CTC), which represent a critical event in metastasis dissemination. In addition to physical entrapment, probably responsible for the majority of the homing events, the vascular system provides geometrical factors that govern the flow biomechanics and impact the fate of the CTC. For this, bifurcated Y-shaped microchannels were manufactured, by stereolithography and soft lithography of PDMS. Cell culture was performed inside the channels and biological flow conditions were applied. These results were also validated mathematically and employed *in vivo* mice models. Our results also demonstrate that viscosity, as a main determinant of the Reynolds number that defines flow biomechanics, may be modulated to limit or impair CTC accumulation at the bifurcation of blood vessels, in agreement with the apparent positive effect observed in the clinical setting by anticoagulants in advanced oncology disease.

The second platform consists in a sensorised, microfluidic Ussing chamber, a system widely used in studying biological barriers like the epithelial barrier of the gut. This section addresses traditional Ussing challenges like complexity, high sample volumes, and limited compatibility. By combining stereolithography and soft lithography techniques, a microfluidic Ussing chamber will be manufactured, overcoming these limitations, and incorporating compatibility with microscopy. Validation through Trans-Epithelial Electrical Resistance (TEER) measurements confirm its efficacy in assessing ion permeability dynamics, utilizing Caco-2 cell monolayers, showcasing the capability of the manufactured chamber for sensing impact of calcium on tight junctions.

CONCLUSIONS

Finally, this chapter summarizing the key findings of the research, reflecting on their implications, and discussing directions for future work.

LIST OF PUBLICATIONS

This chapter compiles all the academic publications derived from this thesis, including articles published in prestigious international journals.

2. INTRODUCTION

This chapter is a partial reprint of:

Bastián Carnero[a,b], Carmen Bao-Varela[a], Ana Isabel Gómez-Varela[a] and M. Teresa Flores-Arias[a], *Internal Microchannel Manufacturing Using Stereolithographic 3D Printing*, Trends and Opportunities of Rapid Prototyping Technologies (2022), DOI: 10.5772/intechopen.102751, ISBN: 978-1-80355-727-4

[a]Photonics4Life research group, Departamento de Física Aplicada, Facultade de Física, iMATUS, Universidade de Santiago de Compostela, Campus Vida, Santiago de Compostela, 15782, Spain

[b]BFlow SL, Edificio Emprendia, Santiago de Compostela, 15706, Spain

---

"If I have seen further, it is by standing on the shoulders of giants."
Sir Isaac Newton, 1675

2.1 THE HISTORY OF LASER

The laser, an acronym for Light Amplification by Stimulated Emission of Radiation, is one of the most significant technological advancements of the 20th century. Its development not only revolutionized fields such as optics, telecommunications, and manufacturing but also captured the imagination of popular culture, inspiring countless works of science fiction. From its theoretical foundations laid down by Albert Einstein to its practical realization by Theodore H. Maiman, the history of the laser is a tale of collaborative work, scientific innovation and imagination.

The history of laser begins with the understanding of stimulated emission, a concept introduced by Einstein in 1917 (Einstein, 1917). He proposed that under certain conditions, photons could stimulate atoms to emit additional photons of the same energy and phase, leading to an amplification of light. However, it wasn't until the mid-20th century that this theory was put into practice. The maser (Microwave Amplification by Stimulated Emission of Radiation), developed by Charles Townes and Arthur Schawlow (Gross & Herrmann, 2007), was the precursor to the laser, operating on the same principle but in the microwave spectrum.

The leap from maser to laser was a natural progression, yet it required overcoming significant technical challenges. On May 16th (declared International Day of Light years later) of 1960, Theodore Maiman successfully operated the first laser using a ruby crystal (Maiman, 1960). This marked a pivotal moment in scientific history, demonstrating the feasibility of light amplification in the visible spectrum. Maiman ruby laser emitted a coherent beam of red light (λ=694.3 nm), a stark contrast to the chaotic nature of most natural light sources to date.

2.1.1 Theoretical fundaments of laser

To understand in more detail how a laser works, we must grasp the fundamentals of radiation-matter interaction. First, we assume the fact that atomic systems exist in discrete energy levels. Next, we consider an atom or molecule with two energy levels: a higher energy state (E_2) and a lower energy state (E_1). The transition between these energy levels can be fostered by the spontaneous absorption (Figure 2.1a) or emission (Figure 2.1b) of a photon with an energy corresponding to the difference of energy levels ($\Delta E = E_2 - E_1$). Furthermore, a third scenario can occur when an atom in the higher energy state E_2 encounters a photon with energy matching the difference between these states (ΔE), inducing the atom to transition to the lower energy state E_1. During this process, the atom releases a photon identical to the incident one, a phenomenon named stimulated emission (Figure 2.1c) (Siegman, 1986).

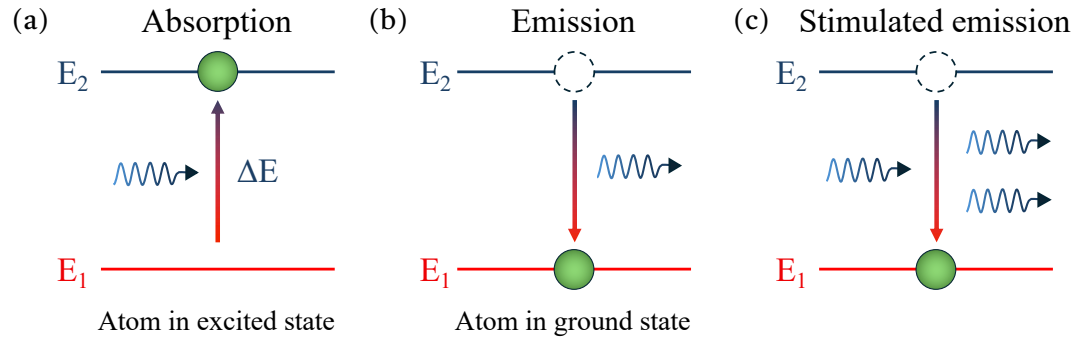

Figure 2.1: Diagram of the main processes of radiation-matter interaction: a) absorption, b) spontaneous emission and c) stimulated emission.

As we mentioned, to transition between two levels, atoms need to absorb or emit the corresponding amount of energy in the form of a photon. The frequency (ν) of that absorbed or emitted photon is related to ΔE according to Bohr's equation (Bohr, 1913):

$$\Delta E = E_2 - E_1 = h\nu$$

where h is Planck's constant.

An incident beam propagating through a material with an atomic density (N_1, N_2) in two energy levels (E_1, E_2, respectively) that satisfy Bohr's equation will experience a decrease in intensity due to absorption. It can be deduced that if $N_1 > N_2$, the beam intensity will decrease due to the predominance of absorption, and only in the case where $N_2 > N_1$ amplification will occur. For this, it is necessary to modify the energy balance of a material so that the higher energy levels are also the most populated, with the atoms acting as energy stores. This situation is sustainable only if the material receives energy from an external source, called pumping, which allows constant energy absorption, overpopulating the higher levels (Svelto, 2010). This state is known as population inversion and is essential to obtain laser light.

2.1.1 Structure of laser

Considering this, the basic components of a laser include an active medium, an energy source, and an optical cavity (Figure 2.2) (Koechner, 1976). The active medium contains atoms or molecules capable of being excited to higher energy states by the pump. The optical cavity, typically consisting of two mirrors facing each other, provides feedback by reflecting the emitted photons back and forth through the active medium, thereby amplifying the stimulated emission process.

As the pump energizes the active medium, more atoms or molecules are excited to the higher energy state. When these excited atoms or molecules encounter photons of the right energy, they undergo stimulated emission, emitting additional coherent photons. These photons stimulate further emissions, creating a cascade of identical photons. The mirrors in the optical

cavity ensure that this process continues, amplifying the light with each pass through the active medium. One of the mirrors is partially transparent (R=99%), allowing some of the amplified light to escape as a coherent laser beam.

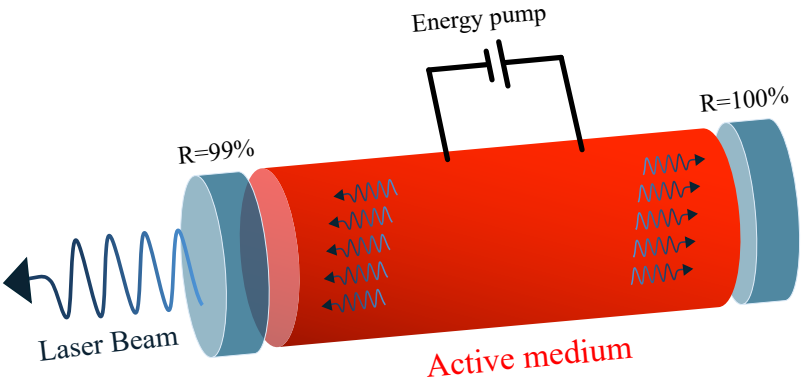

Figure 2.2: Laser oscillator diagram.

2.1.2 Properties of laser light

The applications of lasers depend on the unusual characteristics of this type of light, which are significantly different from conventional light sources. Their main characteristics are (Träger, 2007):

1. Monochromaticity: The ability of lasers to emit light with a defined spectrum around a single frequency is due to two circumstances. The first stems from Bohr's frequency condition, which states that only the frequency corresponding to the energy difference of the transition between levels is amplified. The second is related to the cavity where the light is generated, where only frequencies corresponding to the resonance are allowed. This results in a much narrower spectrum (with a value of $\Delta\nu$ of just a few hertz) than the width corresponding to the energy transition itself.

2. Collimation: One of the most important features of laser radiation is its ability to be collimated, directed, and even focused with great ease. For conventional light sources, whose light spreads in all directions in a solid angle of 4π steradians (sr), it is almost impossible to efficiently collect all that energy. However, for a laser, due to its small divergence angle, energy can be easily collected and redirected even at great distances from the emission source. It is important to note that while the divergence of a laser is very small, it is never zero. The existence of a minimum value for this parameter arises not from engineering limitations but from the physical limitations of the process due to diffraction.

3. Spatial Profile: There are certain distinctive profiles for the intensity of a laser beam across the cross-section. These spatial profiles, known as transverse electromagnetic modes (TEM), originate from the resonance of light amplifying within the oscillator and are related to the geometry of the cavity. TEM modes are designated with two subscripts (TEM_{mn}) that

represent the nodes of the oscillation modes perpendicular to the direction of propagation. Regardless of the shape of the cavity, the TEM_{00} mode always corresponds to a Gaussian beam profile, while higher-order modes exhibit patterns that depend on the cavity's geometry (Kogelnik & Li, 1966).

4. Temporal Behavior: While most conventional light sources exhibit continuous emission, lasers can operate in a wide range of pulses of different temporal durations. Even when operating in continuous mode, lasers exhibit intensity fluctuations due to various factors such as thermal effects in the active medium or different longitudinal modes within the cavity. Solid-state lasers mostly operate in pulsed mode, with pulse durations ranging from milliseconds, as in the case of ruby lasers, to tens of picoseconds for some neodymium-doped crystals and to femtoseconds for Ti:Sapphire lasers. The intervals between pulses vary in frequencies from one pulse per second to several tens of kilohertz .

5. Coherence: Spatial coherence is simply defined as a property of an electromagnetic wave when it can maintain a constant phase difference between two points separated in space. The high degree of spatial coherence of laser radiation is due to the fact that the spatial distribution of the field of the beam generated by stimulated emission is a mode of the optical oscillator. Temporal coherence, on the other hand, exists if, for the same point at two different times (t and t+τ), the phase difference between both times for a specific delay τ remains constant regardless of the value of t. If this occurs for any delay τ, the wave is said to have perfect spatial coherence, while if it only occurs for times less than τ0, this is defined as the coherence time of a wave. The concept of temporal coherence is closely related to monochromaticity since it can be shown that the coherence time of a wave is related to the width of its spectrum by the simple relation $\tau_0 \approx 1/\Delta\nu L$. The high degree of temporal coherence of a laser is thus due to its high degree of monochromaticity (Born et al., 1999).

6. Radiance: Radiance is defined as the power emitted per unit area and per solid angle. The extremely high radiance of lasers comes from their ability to emit high power peaks in very small solid angles, on the order of 10^{-6} sr. The importance of this quantity lies in its ability to provide high irradiance (power emitted per unit area) on a surface, which is crucial for material processing applications. In this field, the development of laser systems specifically designed to maximize radiance has led to neodymium crystal lasers capable of reaching radiances of $2 \cdot 10^{17}$ W/cm² sr. For He-Ne lasers, the values are around 10^6 W/cm² sr.

7. Power: One of the most decisive aspects of differentiating lasers from other light sources is their ability to generate extremely high powers. This is due to their ability to concentrate energy both spatially and temporally in regions just a few microns in diameter and intervals as short as femtoseconds. Solid-state lasers presently achieve the highest power peaks. Commercial neodymium lasers with nanosecond pulses can reach powers of up to 10^{11} W. Currently, the highest peak powers in femtosecond lasers are achieved at the Extreme Light

Infrastructure – Nuclear Physics (ELI-NP) facility. Their High Power Laser System (HPLS) has generated 10 PW (10^{16} W) laser pulses at a repetition rate of one shot per minute (Radier et al., 2022), employing a 6 fs Ti:Sa oscillator.

2.1.3 The role of laser in science

When the laser was first invented, it was famously described as "a solution seeking a problem", a phrase attributed to Irnee D'Haenens, a colleague of Maiman. Despite this initial scepticism, and thanks to the imagination of researchers, the laser has revolutionized numerous fields of physics and beyond.

In medicine, lasers revolutionized surgical procedures, enabling minimally invasive surgeries with unprecedented precision (Azadgoli & Baker, 2016; Donaldson et al., 2013). Ophthalmology, in particular, benefited immensely, with techniques like LASIK (Laser-Assisted In Situ Keratomileusis) transforming corrective eye surgery (Reinstein et al., 2012). The precision and control offered by lasers have made them indispensable tools in medical diagnostics and treatments.

In the realm of telecommunications, lasers have become the backbone of modern communication networks. Fiber-optic technology, which relies on lasers to transmit data over long distances at the speed of light (Culshaw & Kersey, 2008), has facilitated the exponential growth of the internet and global connectivity. The ability to send vast amounts of data quickly and reliably has had profound implications for industries ranging from finance to entertainment.

Manufacturing has also been revolutionized by laser technology. The precision cutting, welding, and engraving (Aymerich López, 2019) capabilities of lasers have enabled the production of intricate components with minimal waste (Beloso Aragón, 2019). Industries such as automotive (Hong & Shin, 2017), aerospace (O'Briant et al., 2016), and electronics rely heavily on laser processes for manufacturing high-quality products efficiently (Kim et al., 2021).

In fields such as spectroscopy (Bloembergen, 1982) and quantum mechanics, lasers provide the tools necessary to probe the fundamental nature of matter and energy. The development of laser cooling techniques (Wineland & Itano, 1987), which allow atoms to be cooled to near absolute zero, has opened new frontiers in quantum computing and ultra-precise measurement.

In education and outreach, lasers serve as a powerful tool for inspiring and training the next generation of scientists and engineers. The author of these lines has utilized lasers in schools, high schools, and science fairs to effectively demonstrate phenomena such as fluorescence, phosphorescence, visual optics, and microscopy, captivating both children and adults (Carnero, De Las Heras, et al., 2022). Educational programs that emphasize photonics and laser technology prepare students for careers in a rapidly evolving technological landscape.

Moreover, the economic impact of laser technology cannot be overstated. The global laser market, encompassing industries as diverse as healthcare, telecommunications, and manufacturing, is worth billions of dollars. Continued investment in laser research and development is essential for maintaining and expanding this economic influence. Governments and private enterprises alike recognize the strategic importance of laser technology and continue to support its advancement (National Research Council (U.S.) et al., 2013).

The history of the laser is marked by interdisciplinary collaboration, involving significant contributions from physicists, engineers, and chemists. This collaborative effort is highlighted by the thirteen Nobel Prizes awarded in this field (Table 2.1) (Nobel Prize organisation, n.d.) demonstrating the diverse range of expertise and innovation that progress in laser technology

	Year	Winner	Research field
1	1964	N. C. Townes, A. P. Basov	Fundamental research for the development of the laser and maser
2	1971	D. Gabbor	Holography realized with laser
3	1981	N. Bloembergen, A. Schawlow	Development of laser spectroscopy
4	1997	S. Chu, W. Phillips, C. Cohen-Tannoudji	Atomic cooling and creation of atomic traps using laser
5	1999	A. Zewail	Study of chemical reactions on femtosecond timescales
6	2000	Z. Alferov, H. Kroemer	Invention of heterostructures essential for high-speed optoelectronics
7	2001	E. Cornell, C. Wieman, W. Ketterle	Production of Bose-Einstein condensates
8	2005	R. Glauber	Quantum theory of optical coherence
9	2005	J. Hall, T. Hänsch	Development of precision spectroscopy based on laser
10	2009	C. Kao	Transmission of light in optical fibers
11	2017	R. Weiss, B. Barish, K. Thorne	Contributions to the LIGO laser detector for gravitational waves
12	2018	D. Strickland, G. Mourou, A. Ashkin	Development of revolutionary techniques in the field of laser physics
13	2023	P. Agostini, F. Krausz, Anne L'Huilleier	Generation of attosecond pulses of light to study electron dynamics

Table 2.1: List of Nobel Prizes awarded in the laser field.

has driven. It is the responsibility of today's scientists to keep expanding the horizons of laser applications. For this reason, this thesis will focus on the applications of laser manufacturing in the novel and rapidly growing field of microfluidics.

2.2 MICROFLUIDICS

The field of microfluidics, which involves the manipulation and study of fluids at the microscale, has emerged as a revolutionary technology with profound implications for science, medicine, and industry. This interdisciplinary domain, integrating principles from physics, engineering, chemistry, and biology, allows for the precise control of small volumes of fluids, typically ranging from nanoliters to picoliters (Whitesides, 2006). The historical evolution of microfluidics, from its conceptual origins to its current state, is always pushing the boundaries of what is possible at the microscale.

As far as this thesis is concerned, microfluidics has great potential in chemical and biological analysis due to its extraordinarily useful characteristics: the ability to use very small amounts of samples and reagents, high resolution and sensitivity for separations and detections, short analysis times, small footprints for the analytical devices (Manz et al., 1992) and low cost. This technology often exploits both its most obvious feature (very small dimensions) and some less evident fluid behaviours in microchannels. For instance, effects of gravity on fluids at this scale are much smaller compared to the macro scale, while surface tension and capillarity become dominant and can be used for various tasks: passive fluid pumping through microchannels (Walker & Beebe, 2002), precise surface modelling with user-defined substrates (S. H. Lee et al., 2010), or filtering multiple analytes (Berry et al., 2012), and forming monodisperse droplets (Anna et al., 2003) in multiphase fluid streams for a variety of applications.

The examples listed represent only a small fraction of the countless problems this technology aims to address and solve. Essentially, microfluidics offers precise control of molecule concentrations in space and time, difficult to achieve by other means, evolving towards creating devices capable of integrating laboratory functions into a single, very small device, just a few millimeters or centimeters in size.

2.2.1 The origins of Microfluidics

The field of microfluidics originates from three branches: molecular analysis, microelectronics and molecular biology (Sackmann et al., 2014). Historically, the first was analysis, specifically microanalytical methods such as gas-phase chromatography, high-pressure liquid chromatography, or capillary electrophoresis. The latter revolutionized chemical analysis in its capillary format (Manz et al., 1992). These methods (combined with improvements in optical detection) simultaneously achieved high sensitivity and resolution, using very small sample quantities. With these achievements, it became necessary to develop

more modern, compact, and versatile formats for new applications in chemistry and biochemistry.

The second contribution to microfluidics came from microelectronics. The development of photolithography and etching methods in the 1960s, originally to produce integrated circuits, laid the groundwork for the miniaturization of fluidic devices. Some early work on fluidic microsystems indeed used silicon and glass, though soon plastics were also explored. For the analysis of biological samples in water, devices made from glass and silicon are usually not the most suitable. Silicon is expensive and opaque to visible and ultraviolet light, thus unsuitable for conventional optical detection methods. Elastomers are more suitable for making microanalytical systems, especially pumps and valves, due to their flexibility. During this period, Richard Feynman, in his famous 1959 lecture "There's Plenty of Room at the Bottom" (Feynman, 1959), envisioned the manipulation of materials at the atomic level, a concept that indirectly influenced the future trajectory of microfabrication technologies, including microfluidics .

A third motivation for microfluidics came from molecular biology. The genomics explosion in the 1980s, followed by other areas of microanalysis related to molecular biology, such as DNA sequencing, required analytical methods with much higher performance, sensitivity, and resolution than biology had anticipated. Microfluidics offered very useful approaches to overcome these problems.

By the late 1980s and early 1990s, microfluidics began to distinguish itself as a separate field. The invention of the microelectromechanical systems (MEMS) technology provided the tools necessary for creating micro-scale channels and valves (Verpoorte & De Rooij, 2003). Notable early developments include the inkjet printer heads, which utilized MEMS-based nozzles to eject tiny droplets of ink with high precision. This innovation not only demonstrated the potential of microfluidic systems but also highlighted their commercial viability.

A pivotal moment in the history of microfluidics was the introduction of the concept of lab-on-a-chip (LOC) devices (Ramsey, 1999). These devices integrate multiple laboratory functions onto a single chip, significantly reducing the required sample volumes, reaction times and costs. The seminal work by Andreas Manz (Manz et al., 1992) and his colleagues in the early 1990s demonstrated the feasibility of miniaturizing chemical analysis systems. Their pioneering efforts led to the development of micro-total analysis systems (μTAS), which paved the way for a myriad of applications in chemical and biological analysis.

2.2.2 Modern microfluidics

Currently, in the realm of medicine, microfluidics has revolutionized diagnostics and personalized medicine. Point-of-care (POC) testing devices, which often incorporate microfluidic components, enable rapid and accurate detection of diseases at the patient's bedside

or in remote locations. These devices have been crucial in managing infectious diseases, as demonstrated during the COVID-19 pandemic (Li et al., 2023), where rapid diagnostic tests played a vital role in controlling the spread of the virus. Microfluidic chips, integrated with biosensors, have the potential to detect pathogens, biomarkers, and even perform complex assays with minimal user intervention (Estevez et al., 2012).

Furthermore, the field of microfluidics has significantly impacted drug discovery and development. Microfluidic platforms facilitate high-throughput screening of potential drug candidates by allowing simultaneous testing of thousands of compounds on cellular models. This accelerates the identification of potential drugs and reduces the time, and costs associated with traditional drug development processes. Organ-on-a-chip devices, which replicate the microenvironment of human organs on microfluidic devices (Huh et al., 2011; Leung et al., 2022), are revolutionizing toxicology studies and providing more accurate models for studying disease mechanisms and therapeutic responses, with promising results. These platforms, much closer to reality than the studies carried out by traditional methods, involving testing in wells (static regime), could decreases the animal experimentation needed for testing drugs before the patient dispensation.

The thriving state of microfluidics is evident in the increasing presence that terms like “Lab on a chip”, “Microfluidics” and “Organ on a chip” have had in scientific publications since the 90s (source: SCOPUS).

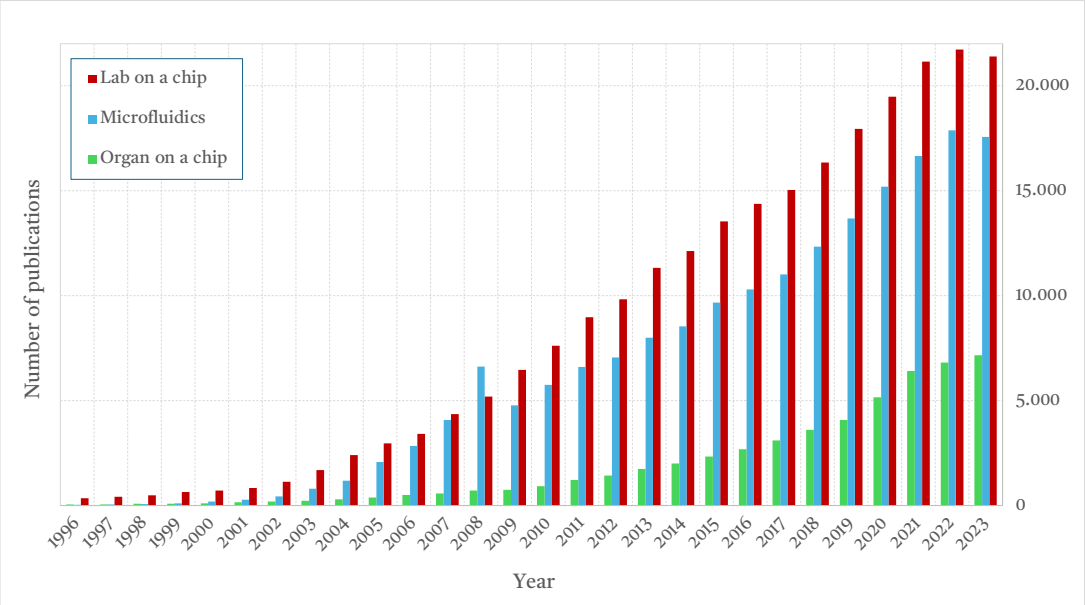

Figure 2.3: Histogram of the evolution of the number of publications in “Lab on a chip”, “Microfluidics” and “Organ on a chip” from 1996 to 2023. Source: SCOPUS.

Furthermore, the intersection of microfluidics and material science has led to the development of innovative materials and fabrication techniques. Polydimethylsiloxane

(PDMS), a silicon-based organic polymer, has become a popular material for constructing microfluidic devices (Fujii, 2002) due to its biocompatibility, optical transparency, and ease of fabrication. Soft lithography, a technique involving the molding of PDMS, allows for the rapid and cost-effective production of microfluidic structures. This has democratized access to microfluidic technologies, enabling researchers worldwide to design and fabricate custom devices tailored to their specific needs.

Despite the remarkable progress, the field of microfluidics continues to face challenges that drive ongoing research and innovation (Battat et al., 2022). One such challenge is the integration of microfluidic systems with existing laboratory and clinical infrastructure. Standardization and scalability are critical for the widespread adoption of microfluidic technologies in practical applications. Additionally, the development of user-friendly interfaces and automation systems is essential to make these technologies accessible to non-specialist users in clinical and industrial settings.

In the future, advancements in manufacturing techniques are set to define the trajectory of microfluidics. These new methods are expected to significantly enhance speed, precision, simplicity, and versatility, qualities where laser technologies have demonstrated transformative potential.

2.2.3 Manufacturing techniques in microfluidics

2.2.3.1 Lithography

Lithography is one of the earliest techniques used for fabricating fluidic chips, originating from the MEMS field. Essentially, it involves exposing a sensitive resist to electromagnetic or particle radiation to transfer a pattern onto a substrate, which can be made of glass, silicon, or polymer (Brambley et al., 1994). The resist, a polymer, undergoes a chemical reaction when exposed to radiation. Electromagnetic exposure, known as photolithography (Figure 2.4) (Becker & Gärtner, 2000) can occur in the ultraviolet (UV) spectral range or even X-ray range, typically requiring a mask to transfer the pattern to the surface. This method remains predominant in microfluidics manufacturing. Alternatively, particle beam lithography uses electron or ion beams to expose the resist without needing a mask.

First, the substrate is prepared to ensure proper adhesion of the resist to its surface, often by baking it in a vacuum or dry nitrogen environment. Then, the resist is deposited over the substrate through spin coating, forming a uniform film. If a mask is required, it is carefully aligned over the substrate, and the resist is exposed to radiation. The mask, resistant to radiation, selectively exposes certain areas of the polymer to transfer the pattern. The resist changes chemically when exposed: in positive lithography, the polymer degrades and becomes more soluble, while in negative lithography, it crosslinks and hardens. The mask can be placed in contact with the resist or slightly separated. Contact minimizes diffraction effects but damages

the mask over time; separation extends mask life but increases diffraction-induced failures, which are reduced when working in UV or X-ray regimes. During development, the irradiated region (positive lithography) or the non-irradiated one (negative lithography) of the polymer is removed.

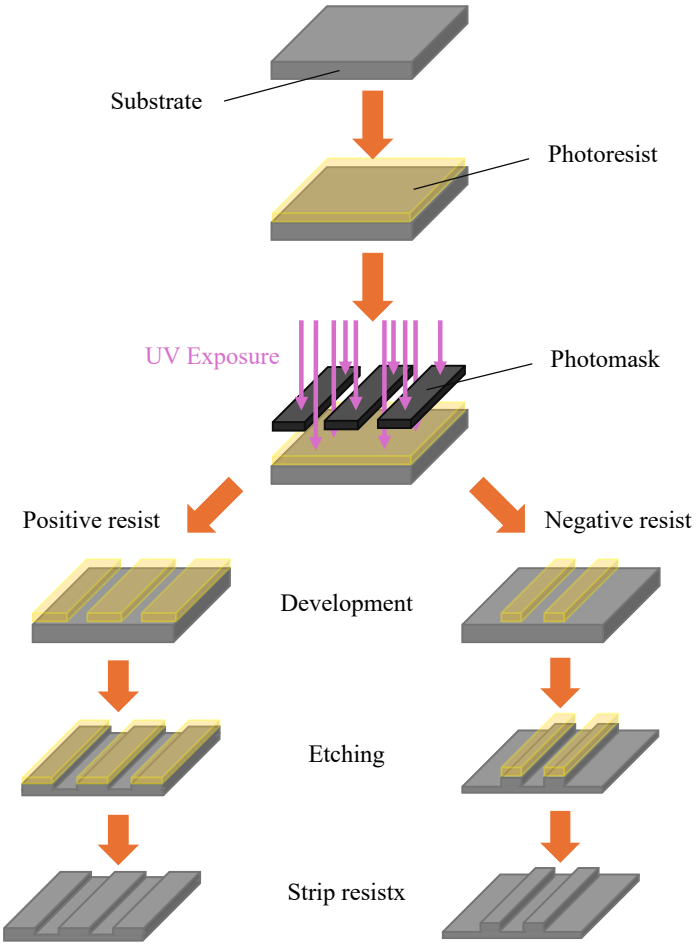

Figure 2.4: Schematic representation of the photolithography process and its steps.

Next, the substrate is etched to transfer the structure from the resist to the final material. The resist withstands the etching process, which only attacks the unprotected substrate. There are two types of etching: wet and dry. Wet etching, an inexpensive and straightforward technique, uses an etchant solution like acid to chemically attack the substrate isotropically. However, this can lead to undercutting, where the substrate is etched beneath the resist. Dry etching, or reactive ion etching (RIE) (Schwartz & Schaible, 1979), is an anisotropic process that solves the problems of wet etching. It uses a chemically reactive plasma formed by applying an electric field, which accelerates ions toward the sample, resulting in directional etching. Finally, after the pattern is transferred to the substrate, the resist is stripped from the chip.

Not all lithography methods require a mask. Particle beam lithography with ions and electrons, and photolithography with laser beams, can directly write patterns on the polymer

resist. These techniques, collectively known as scanning beam lithography, take more time than conventional photolithography but offer higher resolution and precision. Scanning beam lithography is often used to fabricate photomasks for further lithographic processes rather than for making final devices.

While lithography is a well-established technique, it has drawbacks, such as the need for cleanroom facilities, high costs, and the use of toxic chemicals.

2.2.3.2 Soft lithography

Soft lithography stands as the second most widely adopted technique in the field of microfluidics manufacturing. It is based in the principle of replication, employing an elastic polymer, generally polydimethylsiloxane (PDMS), to accurately reproduce the surface topology of a master, down to nanoscale features. This technique, developed as an alternative to photolithography was initially pioneered at Harvard in the 1990s by G. M. Whitesides (Xia & Whitesides, 1998; Whitesides et al., 2001), soft lithography has since become widely adopted in academia and industry for manufacturing a wide range of microfluidic devices.

Soft lithography process includes mixing PDMS components (curing agent and base), pouring the elastomer onto the master substrate to transfer patterns, curing it by heating, and peeling off to obtain replicas. Advantages of soft lithography include lower costs, reduced cleanroom requirements, and the ability to pattern non-planar and flexible substrates. Challenges include lower resolution compared to advanced photolithography and potential issues with stamp deformation and fidelity. Ongoing research focuses on enhancing materials and improving pattern transfer accuracy, further integrating soft lithography with other fabrication methods.

2.2.3.3 Laser ablation

This thesis will focus on laser technologies, including advanced and versatile processes such as laser ablation, that involves the removal of material by directing an intense laser beam onto a surface (Miller, 1994). This technique is notable for its ability to its precision, versatility, and speed, among other attributes, enabling the creation of micrometer-scale features on various material surfaces. The laser was first used for fabricating a microfluidic device in 1997, with the production of a polymer device and the characterization of its flow reported that year (Roberts et al., 1997). Currently, many fluidic chips are manufactured using this technology (B.-B. Xu et al., 2013) due to the numerous benefits it offers. Laser ablation is a non-contact process that, when used correctly, avoids thermal or mechanical deformation of the sample. It is highly suitable for in mass production processes because of the speed of the ablation process and its low operational costs once the equipment is installed. Furthermore, it is a non-toxic process that does not require special environments or clean rooms. This precise and versatile

manufacturing technique enables the creation of highly complex geometries at the micrometric scale.

2.2.3.3.1 Light-matter interaction during laser ablation

The physical processes of laser ablation depend on the characteristics of both the substrate and the laser beam, particularly its wavelength and pulse duration. Fundamentally, when a material is subjected to laser irradiation, it absorbs the energy, initiating a transformation of its state. The initial step in this process is the absorption of light energy by the material. These absorption mechanisms vary between absorbent materials like metals and transparent dielectric substrates such as glass or plastics. The type of absorption also varies with the pulse duration of the laser.

One of the most critical parameters to understand laser ablation is the electron-lattice relaxation time (τ_r), which typically ranges in picoseconds. This magnitude influences how materials behave relative to the pulse duration (τ_p) of the incident laser. Long pulses ($\tau_p >> \tau_r$), are characteristic of nanosecond (ns) pulses. In contrast, pulses are considered ultrashort when the time of energy transfer to the lattice exceeds the pulse duration. That occurs for femtosecond (fs) pulses.

First, for the case of long pulse durations ($\tau_p >> \tau_r$), linear absorption predominates in absorbent materials. Here, a high density of free electrons absorbs energy through inverse Bremsstrahlung. Valence electrons, with ionization potentials lower than photon energies, can promote to the conduction band via single photon absorption (Miller, 1994). This absorption process generates heat through the Joule effect, where electron kinetic energy converts into thermal energy upon collision with the lattice. As the material heats up, it reaches its melting or vaporization temperature, resulting in irreversible damage. This process is accompanied by acoustic waves and optical radiation. Under moderate laser intensities, vaporization typically dominates the ablation process, although higher intensities can lead to phase explosion or explosive boiling (Bulgakova & Bulgakov, 2001).

In dielectric materials, the absorption mechanisms are significantly different. In this case, the ionization energy exceeds the photon energy, preventing direct promotion of electrons from the valence to the conduction band. Instead, the transparent surface must first be transformed into an absorbent plasma by laser irradiation. This plasma then absorbs laser energy, leading to heating and irreversible damage of the material. The absorption mechanism depends on a small number of conduction or free electrons within the material, which act as seed electrons to initiate the process. These electrons can originate from metallic impurities, inclusions, or thermal ionization processes. By inverse Bremsstrahlung, these electrons absorb energy and are accelerated into the conduction band. When the kinetic energy of a free electron exceeds the ionization potential and it collides with a bound electron, the free electron transfers most of its energy to the bound electron in the valence band, resulting in two free electrons with low kinetic

energy in the conduction band. This process, known as impact ionization, can lead to avalanche ionization, where the number of free electrons in the conduction band increases exponentially and is responsible of dielectric light absorption (Lenzner, 1999). Once the electron density reaches a critical value, the transparent material undergoes laser-induced breakdown, transforming from a fully transparent substance to a state resembling metal. Electrons transfer energy to the lattice, heating the material and causing material ejection. In transparent materials with a damage threshold, where seed electrons are essential, the ablation process exhibits statistical variability. This variability arises because the laser-induced optical breakdown threshold depends on the probability of seed electrons being present in the material (Manenkov, 2014).

Second, in the ultrashort pulse regime ($\tau_p << \tau_r$), the processes of laser-matter interaction are more complex than those with long pulses, especially for wide bandgap dielectrics, as more absorption mechanisms are involved. In this case, the interaction with both opaque and transparent materials occurs in a similarly nonlinear manner, unlike long pulses where metal ablation occurs at relatively low intensities through a linear process, whereas transparent materials exhibit low absorbance.

In the ultrashort temporal regime, opaque materials are almost ionized at the beginning of the laser pulse. Conduction band electrons are already present, and the laser energy is absorbed by these free electrons via inverse Bremsstrahlung (Nolte et al., 1997). Due to the extreme intensities of ultrashort laser pulses, absorption is enhanced by nonlinear processes (Ropers et al., 2007), leading to a nonlinear dependency of laser ablation on the laser pulse, unlike in the nanosecond regime (Itina, 2005). As the pulse width decreases, ablation enters a regime where the threshold energy does not depend on pulse duration. The "two-temperature" model is commonly used in the literature to describe the ablation behaviour of ultrashort pulses over metals (J. K. Chen et al., 2006).

For transparent materials, the primary difference from metals lies in the initial absence of free carriers, necessitating energy for their creation. Electrons in the valence band must be promoted to the conduction band, as the bandgap is larger than the photon energy. Several absorption mechanisms facilitate this transition. One such mechanism is multiphoton absorption, where bound electrons simultaneously absorb multiple photons during the laser pulse interaction, with their combined energy exceeding the bandgap. This multiphoton absorption serves two roles: it acts as the primary ablation mechanism under strong laser fields and high frequencies, and it generates free electrons for subsequent free carrier absorption and avalanche ionization processes.

At high laser intensities and low frequencies, tunnel ionization becomes the predominant absorption effect, rather than multiphoton absorption. In tunnel ionization, the potential barrier between valence and conduction bands is significantly reduced by the electric field, allowing

electrons to tunnel through the barrier into the conduction band. The Keldysh parameter, introduced by Keldysh in 1965, determines the probabilities of tunnel ionization and multiphoton processes based on laser intensity and frequency. Additionally, already excited electrons from tunneling or photoionization can sequentially absorb several photons from the same laser pulse, reaching higher energy states. This free carrier absorption, known as electron heating, results in non-thermal bond breaking. When an electron's energy in an excited state surpasses the conduction band minimum by more than the bandgap energy, it can ionize another valence band electron, resulting in two excited electrons in the conduction band through impact ionization. This process can continue as long as the intense laser field is present, leading to avalanche ionization (Lenzner et al., 1998).

The way energy is transferred through the material after absorption depends on the pulse width, which typically differs from the electron-phonon relaxation time. After several picoseconds, laser-excited electrons transfer their energy to the lattice. In the case of nanosecond pulses (Figure 2.5a), where $\tau_p >> \tau_r$, the energy is transferred to the lattice as heat, allowing sufficient time for the thermal wave to propagate through the substrate. Initially, the laser energy heats the target to its melting point and subsequently to its vaporization temperature. As evaporation occurs from liquid to vapor, the resulting structure is characterized by irregular edges, thermal ablation debris, collateral damage, and a significant heat-affected zone (Chichkov et al., 1996).

In contrast, for ultrashort pulses (Figure 2.5b) where $\tau_p << \tau_r$, the electron-lattice coupling can be neglected. After laser irradiation, electrons rapidly cool down, and the material transition is considered a direct solid-vapor step. This process is driven purely by electrons, resulting in a negligible heat-affected zone and highly precise material structuring, with no debris or thermal effects.

For picosecond pulses, where $\tau p \approx \tau r$, an intermediate scenario occurs. Ablation is accompanied by the formation of a melted zone in the material and electronic heat conduction. Although a direct solid-vapor transition may occur at the surface, the presence of a liquid phase within the material can reduce the quality of the ablation (Hamad, 2016).

Despite the various applications of lasers, the fundamental mechanisms of laser-matter interaction remain a topic of discussion, with differing opinions among researchers and discrepancies between theoretical predictions and experimental results. Further studies are needed to achieve a better understanding of the physical phenomena involved.

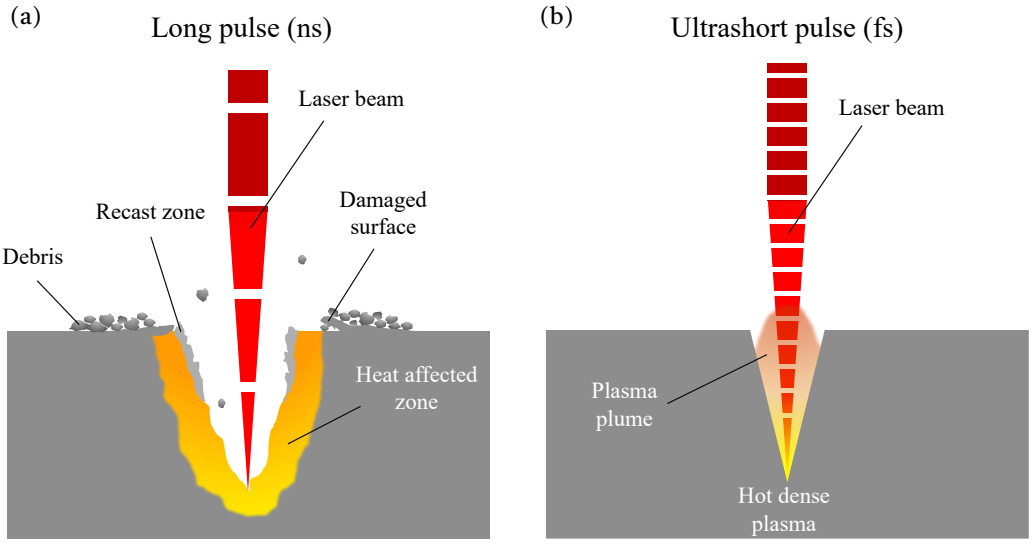

Figure 2.5: Scheme of laser ablation with a) long and b) ultrashort pulses.

2.2.3.4 Laser-Induced Plasma-Assisted Ablation

In addition to direct laser ablation, materials can also be structured using indirect ablation, known as laser-induced plasma-assisted ablation (LIPAA). Unlike direct laser writing techniques, LIPAA is suitable for fabricating large dimensional structures, especially when dimensions exceed a few micrometers. This technique was first introduced in 1998 by the Mirodikawa group in Japan (Zhang et al., 1999). LIPAA involves using a laser wavelength that is transparent to the substrate, such as infrared for glass. A metal foil, opaque to the laser energy, is placed beneath the substrate. The laser fluence should be below the threshold for the glass but above the threshold for the metal. This setup allows the laser beam to pass through the substrate and be absorbed by the metal, generating laser-induced plasma over the metal (Figure 2.6). The interaction between the plasma and the laser beam results in ablation at the backside side of the glass (Nikumb et al., 2005). Without the metal foil, or if the laser irradiation is not perpendicular to the sample, ablation does not occur. LIPAA has typically been demonstrated with nanosecond lasers since laser-induced plasma forms a hundred picoseconds after irradiation.

The plasma, composed of ions, clusters, and large particles, alters the target surface upon impact, creating absorbing sites for the laser beam and resulting in ablation (Zhang et al., 1998a). However, the mechanisms of plasma-beam interaction are not yet fully understood. The distance between the metal and the substrate significantly affects the quality of the ablation. If the materials are too far apart, the plasma's influence is weak, leading to minimal ablation, though some metal species might deposit on the substrate. Conversely, when the metal is in contact with the substrate, the ablation rate increases. For finer ablation marks, a separation of a few microns between the materials is ideal. The ablation process on the back face of the glass

is accomplished through the combination of mechanical shock waves, the ablation plume and the cavitation bubbles produced during the process (Gómez-Varela et al., 2022).

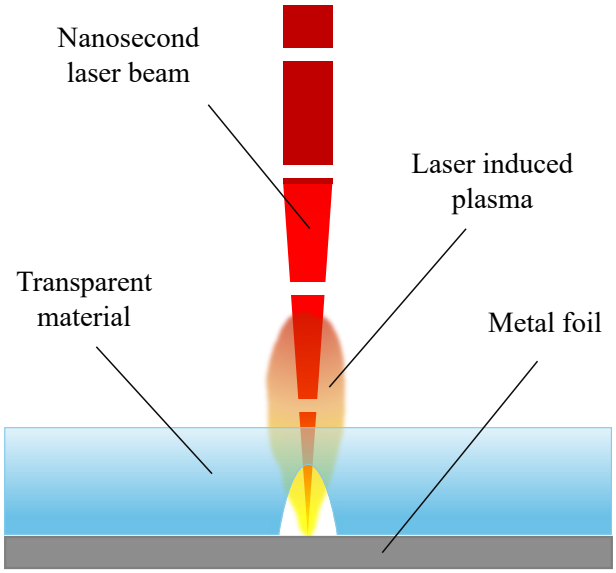

Figure 2.6: Schematic representation of laser-induced plasma-assisted ablation.

2.2.3.5 Stereolithography

The second technology in which this thesis will focus is the 3-dimensional (3D) printing. 3D printing has recently become one of the most promising and ground-breaking manufacturing techniques (Bozkurt & Karayel, 2021; Jones, 2012; Palmara et al., 2021), allowing to produce highly detailed structures following simple and systematic steps without the need of the very expensive equipment of traditional technologies that normally require the use of cleaning rooms in large facilities (as photolithography or RIE). This has facilitated the access to complex processes of manufacturing to a lot of researchers and many and varied industries (Sandeep et al., 2021). Among others, the microfluidics field is a clear beneficiary from the role that 3D printing plays in the microfabrication processes (Bhattacharjee et al., 2016). The 3D technology emerges as a promising one since allows to achieve in an easy and fast way, microchannels with very high resolutions with simple procedures; to select different geometries for the microchannel profile (circular, rectangular, triangular...) and to create channels on complex surfaces in 3D or even internally.

Currently, two 3D printing technologies outstand above the rest (Rupal et al., 2019a; Zhu et al., 2013): Fused Deposition Modelling (FDM) (Cailleaux et al., 2021; Romanov et al., 2018) and Stereolithography (SLA) (Heidt, Rogosic, Bonni, Passariello-Jansen, Dimech, Lowdon, Arreguin-Campos, Steen Redeker, Eersels, Diliën, Van Grinsven, et al., 2020; Moreno-Rivas et al., 2019a). FDM printers are based on the extrusion of a heated polymeric filament fused that forms consecutive layers of a piece (Figure 2.7a) while SLA printers use photopolymerization by laser to selectively cure a liquid resin contained in a tank (Figure 2.7b)

manufacturing the model in a layer by layer process. Both technologies are widely used given their versatility and efficiency, but SLA offers the highest accuracies (Gong et al., 2017; Knowlton et al., 2016; Moreno-Rivas et al., 2019a). Given the high quality of the surfaces fabricated by SLA printers, a variety of biocompatible materials suitable for its use with this equipment have emerged, increasing the potential biological applications to be used for (Hart et al., 2020a; Kreß et al., 2020a; X. Xu et al., 2021). There are many examples that show the prospective of SLA printers for complex microfluidic devices fabrication, making them a viable option for researchers focused on 3D printing of reliable, accurate, and biologically compatible microfluidic devices. However, some technical aspects must be considered to optimize the printing results. Considering all these aspects and their relationship with laser technology, this thesis will focus on SLA technology.

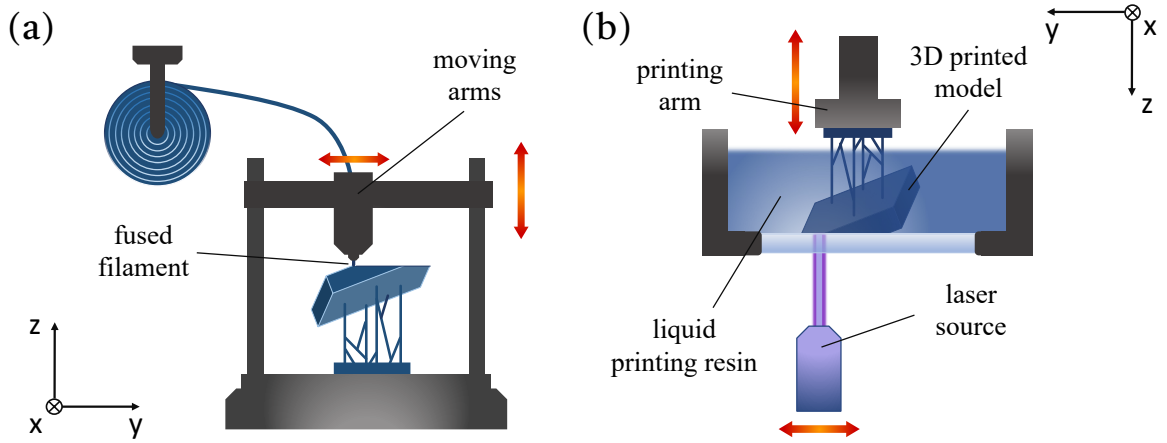

Figure 2.7: Most common 3D printing technologies: a) fused deposition modelling (FDM) and b) stereolithography (SLA).

2.2.3.5.1 Theoretical fundaments of stereolithography

The polymerization of photosensitive resins is mainly governed by two parameters (Jacobs, Paul Francis, 1992): penetration depth of the curing light and the minimum energy required for polymerization. The penetration of light follows the well-known Beer-Lambert law of exponential light absorption given by

$$P_z = P_0 e^{-z/D_P}$$

being P_Z the light power measured at a depth z from the surface; P_0, the power at the surface; and D_P, the depth reached when light intensity decreases by a factor 1/e of the surface intensity. Note that D_P is a factor that depends on the resin composition, that determines its absorbance characteristics (dispersion and absorption) (J. H. Lee et al., 2001). Power terms can be rewritten in terms of energy (so z will become the cure depth when the appropriate amount on light is provided) to obtain the working curve equation for SLA 3D printers:

$$C_D = D_P ln\left[\frac{E_0}{E_c}\right]$$

where C_D is the depth/thickness at which the light energy is sufficient to convert the liquid resin in a gel; E_0 is the energy of light at the surface; and E_C is the critical energy necessary to initiate photopolymerization. According to the Beer-Lambert law, the exposed light intensity reaches its maximum value (E_{max}) at the surface of the resin and decreases exponentially as light penetrates through the resin due to the attenuation of the absorbing medium.

In the resin, the photopolymerized volume increases with the ultraviolet (UV) irradiation until the resin reaches to gel point, where it transforms from liquid to solid state. D_P and E_C are parameters that depend on the chemical characteristics of the resins and can be determined drawing a semi log plot of C_D vs. E_0 obtaining a straight-line curve with slope D_P and a x-intercept of E_C (Bennett, 2017). Once D_P and E_C are known, it is possible to optimize printing process choosing properly the exposure parameters and achieve the designed piece properties. This is the key for obtaining good results with a high resolution SLA printing, where minimizing the thickness of the deposited and light cured layer to achieve the maximum detail is critical.

In most SLA printers, the light source used to perform photopolymerization is a laser, so the XY resolution is given by the size of the laser spot on the surface. Knowing the aforementioned parameters, the user or printer manufacturer can choose the proper parameters of light exposure (scan speed, power) to optimize the curing conditions and achieve the best resolution for the final device. Another determining factor is the minimum Z-step allowed by the printing arm, which gradually raises the piece from the bottom of the tank, that determines the corresponding layer thickness for each resin.

2.3 THESIS OUTLINE

In the process of drug discovery and application, there is a significant gap between the data and results obtained for new drugs. This gap is largely due to discrepancies between *in vitro* experiments with molecules or cells and the preclinical validation of function in isolated organs and *in vivo* assays. Consequently, there is a high rate of efficacy loss, which leads of failures in therapeutic validation. This scenario has been prevalent until now. For this reason, any improvement in the design of drug discovery strategies that reduces this gap will have a significant impact on the efficiency of the process. One hypothesis to reduce this gap, which generally exists between cellular experimentation and *in vivo* models, is that *in vitro* tests should be conducted in more physiological environments where cells can exhibit their functions, mimicking their normal responses to any stimulus. In the field of microfluidics, this is known as "Organ-on-a-Chip" technology.

The research presented in this thesis focuses on the manufacturing and development of Organ-on-a-chip and microfluidic platforms employing laser technologies for conducting *in vitro* experiments under controlled laboratory conditions that can contribute to the development of personalized therapies. The goal is to bridge the gap between laser technology and microfluidics, offering a new fabrication approach in a field traditionally dominated by complex methods like photolithography. Additionally, the development of these platforms may help reduce the need for animal testing.

The thesis is structured as follows: *Chapter 1. Summary* acts as abstract of the thesis. *Chapter 2. Introduction* provides an overview of the current landscape of laser technology and its importance in the manufacturing of microfluidic devices, detailing prevalent materials and fabrication technologies. *Chapter 3. Objectives* defines the objectives of this work. *Chapter 4. Materials and Methods* details the materials and methodologies utilized in this study.

Chapter. 5 Subaquatic indirect laser ablation technique for glass processing and microfluidics introduces a new subaquatic laser-induced plasma-assisted technique, proposed to achieve millimetric structures with high reliability and enhanced quality. In *Chapter 6. Stereolithography as key technology for manufacturing microfluidic devices,* an in-depth study of a stereolithography (SLA) 3D printer is conducted to analyse its potential for microfluidic device manufacturing. *Chapter 7. Hybrid technique for superficial micropatterning by combining pulsed laser ablation and stereolithographic 3D printing for microfluidics applications* introduces a novel hybrid laser technique to manufacture a challenging microfluidic devices, a straight micromixer, and a demanded feature in microfluidic devices, a microlens array. Finally, in *Chapter 8. Biological applications*, results obtained employing the platforms fabricated during the development of this thesis are presented. These platforms, created through the combination of laser ablation, 3D printing, and soft lithography, have enabled studies on circulating tumour cells and the replication of a widely used device in biotechnology laboratories, the Ussing chamber.

Chapter 9. Conclusions wraps up the thesis by emphasizing the key learnings and insights acquired throughout the research and *Chapter 10. List of publications* provides a comprehensive list of all the published works resulting from this thesis.

3. OBJECTIVES

The main objective of this thesis is to manufacture microfluidic platforms using laser technologies for *in vitro* studies aimed at advancing personalized therapies. This overarching goal will be achieved through the following specific objectives:

Objective 1: Design and fabricate microfluidic platforms using biocompatible materials that support the culture of endothelial cells on the inner walls of the channels, mimicking physiological structures, as human blood vessels. These platforms should be capable of withstanding the continuous flow of physiological solutions and be compatible with standard imaging systems.

Objective 2: Design, fabricate, and characterize 3D microchannel structures using direct and indirect laser irradiation of biocompatible materials to replicate capillaries where tumour cell colonization is more prevalent. Regarding indirect ablation, explore and develop methods to achieve deeper structures without thermal damage employing nanosecond laser, predominant in the industry.

Objective 3: Design, fabricate, and characterize 3D microfluidic platforms using stereolithographic 3D printing techniques. This includes a detailed analysis of the resolution, finish, transparency and biocompatibility of the various 3D printing resins used.

Objective 4: Explore the synergies between the laser ablation and stereolithography with the aim of developing and validating a hybrid manufacturing technology. Determine the dimensional range in which each technology yields its best results and combine them accordingly.

Objective 5: Manufacture highly demanded microfluidic features (such as microlens, micropillars, serpentines, and reservoirs) using the developed manufacturing techniques. Additionally, reproduce standard analytical systems utilized in biomedical laboratories, such as the Ussing chamber, leveraging the capabilities of microfluidics to enhance their features. Recreate specific physiological structures to simulate relevant vascular scenarios, including stenosis, bifurcations, and thrombosis.

Objective 6: Monitor in real-time the morphology of endothelial cells under different stimuli, and assess endothelial functions such as barrier function, inflammatory response, and adhesion of circulating cells.

Objective 7: Validate the technology through a pilot screening test using a small chemical library of drugs with endothelial activity.

4. MATERIALS AND METHODS

4.1 MATERIALS

4.1.1 Soda-lime glass

This thesis utilizes soda-lime glass as a substrate for manufacturing structures through both direct and indirect pulsed laser ablation. Glass offers valuable properties such as robustness, chemical resistance, and optical transparency (Nieto, Delgado, et al., 2014a). Furthermore, the soda-lime glass selected for these experiments is inexpensive and sourced from local suppliers. The transmission spectrum of this material is examined using a PerkinElmer Lambda 25 spectrometer (see Section 4.1.6.6), and the resulting graph is depicted in Figure 4.1.

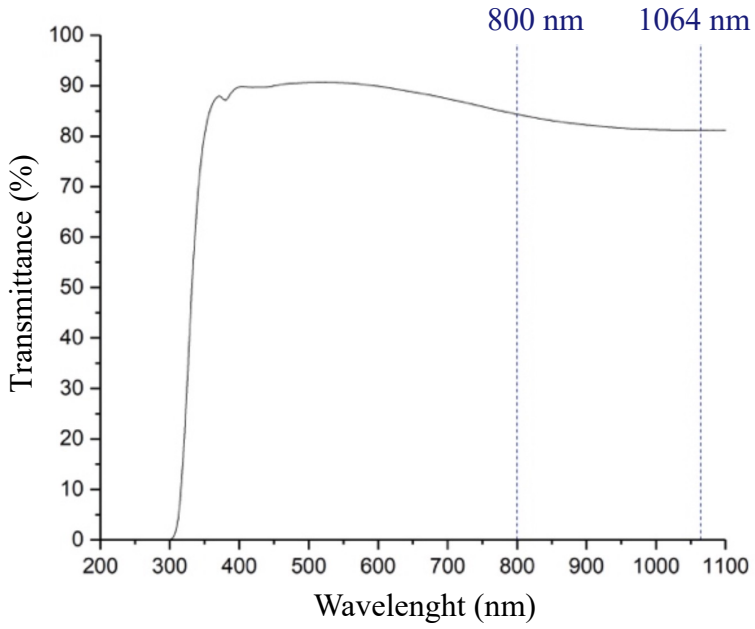

Figure 4.1: Optical transmission of commercial soda-lime glass from 190 to 1100 nm wavelength.

As depicted in Figure 4.1, soda-lime glass exhibits high absorbance in the ultraviolet (UV) region (under 380 nm) and transparency in the visible spectrum (around 380-750 nm), making

it suitable for microscope inspections. In the infrared regime (over 750 nm), it demonstrates low absorbance, with a transmittance value of approximately 80% at 1064 nm and 85% at 800 nm, i.e. the spectral range in which the lasers employed in this thesis for glass machining operate. Chemical analysis of soda-lime glass was conducted using Energy Dispersive X-ray Spectroscopy in a Zeiss FESEM-Ultra Plus scanning electron microscope (see Section 4.18.5). Evaluation of both sides of the material is presented in Table 4.1.

Undoped side elements	Weight %
O	50.25
Si	33.08
Na	9.08
Ca	4.87
Mg	2.19
Al	0.53

Doped side elements	Weight %
O	48.97
Si	32.34
Na	9.14
Ca	4.91
Mg	2.24
Al	0.49
Sn	1.91

Table 4.1: Chemical composition of areas of soda-lime glass in both sides of the substrate.

As indicated in Table 4.1, silicon dioxide (SiO_2) constitutes the primary component on both surfaces of soda-lime glass. To enhance its properties, a “soda” component, sodium oxide (Na_2O) derived from soda ash, is incorporated, reducing the glass transition temperature. The “lime” component takes the form of calcium oxide (CaO), sourced from limestone or dolomite, contributes to the material overall durability. Additionally, magnesium oxide (MgO) from dolomite and aluminium oxide (Al_2O_3) from feldspar are introduced.

The analysis unveils a noteworthy distinction between the two sides of the material: one side is doped with tin, while the other remains undoped. This doping disparity arises from the glass fabrication process known as floating glass. In this method, molten glass is floated over molten tin for cooling, transferring tin to the side in contact with the metal. These dopants play a pivotal role in the subsequent ablation process, as elaborated in previous work (Delgado et al., 2016). Despite its suitability for laser microstructuring, it is crucial to note that the impermeability of soda-lime glass poses a limitation for long-term cell cultures.

4.1.2 Polydimetilsyloxane

Polydimethylsiloxane (PDMS) is the polymer employed for the replication of glass and 3D printed resin masters in order to create microfluidic devices with the desired geometry, given its optical transparency, permeability to gases, elasticity, and biocompatibility. For these reasons, is one of the most used polymers to fabricate microfluidic devices (McDonald et al., 2000a; Raj M & Chakraborty, 2020a), allowing the cells to have a suitable environment for

experimentation. Two different types of PDMS were used during this thesis. This elastomer is typically provided in a dual-component liquid form consisting of a prepolymer base and a cross-linking agent (see Figure 4.2a), which should be mixed in a determined ratio. Structural formula of PDMS is presented in Figure 4.2b.

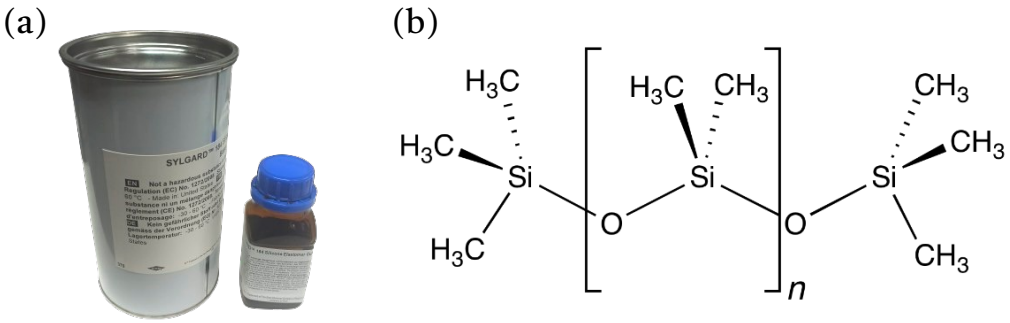

Figure 4.2: a) PDMS Sylgard 184 from Down Corning. b) Structural formula of Polydimethylsiloxane (C_2H_6Osi).

4.1.2.1 Thermally curable PDMS

In the first instance, thermally curable PDMS was obtained from commercial Sylgar 184 elastomer (Dow Chemical Company, Midland, Michigan), which recommends a weight ratio of 10:1. The mixture is then deposited on the printed master or plate, forming a small silicone sheet and introduced in a vacuum chamber 40 min at 400 mbar to remove bubbles produced during the mixing process. Finally, the master with the degassed PDMS is introduced in an oven for 12 h at 60 ºC (Nieto et al., 2015a; Otero-Cacho et al., 2018). This process hardens the material through the cross-linking of polymer chains, and will be referred to as curing from now on. Some properties of PDMS are presented in Table 4.2.

Property	**Value**
Viscosity (base)	5.2 Pa·s
Viscosity (uncured mix 10:1)	3.5 Pa·s
Specific gravity (uncured)	1.03
Specific gravity (cured)	1.04
Work life at 25 ºC	1.4 h
Cure time at 25 ºC	48 h
Cure time at 100 ºC	35´
Shelf life at 25 ºC	24 months
Tensile strenght	7.1 MPa

Elongation	120%
Shore hardness (type A)	44
Refractive index at 589 nm	1.4118
Refractive index at 632.8 nm	1.4225
Refractive index at 1321 nm	1.4028

Table 4.2: Manufacturer properties of 184 Sylgard PDMS.

4.1.2.2 Ultra violet curable PDMS

Ultraviolet curable PDMS (UV-PDMS) was prepared from KER-4690 A/B (Shin-Etsu Europe BV). It consists of two components, KER-4690-A and KER-4690-B, that the manufacturer recommends mixing in a 50:50 weight ratio. The mixture was degassed under the same conditions as stated above and totally cured by irradiation to a 405 nm LED flood at 5.34 mW/cm^2 for 10 min in a chamber heated at 50 °C (FormCure, Formlabs Somerville, Massachusetts, USA). This specific combination of curing conditions for PDMS yielded homogeneous curing of the material with efficient processing time, although alternative combinations of temperature and UV exposure can also be utilized.

Transmission spectra of both polymers is examined using a PerkinElmer Lambda 25 spectrometer (see Section 4.1.6.6). Both PDMS materials are highly transparent from 300 to 850 nm spectral region with a very flat behaviour in the visual region. UV-PDMS shows 5% higher visible and NIR light transmittance compared to thermally cured PDMS.

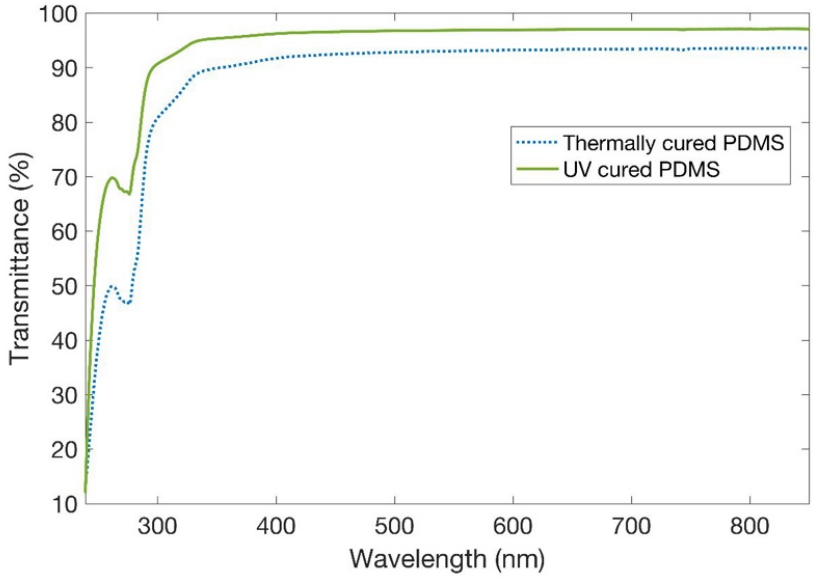

Figure 4.3: Optical transmission spectra of thermally treated PDMS (blue dashed line) and UV-PDMS (green solid line) sheets.

4.1.3 3D printing resins

Seven commercial resins from Formlabs were analysed: Clear V4, Dental LT V1, Tough 2000 V1, BioMed Amber V1, Flexible 80A V1, Elastic 50A V1 and Model V2. Resins are compatible with the 3D printer we will introduce in (Section 4.1.5.2), and the operating principle involves selective curing layer by layer through UV light irradiation, as mentioned in the Introduction. One of the most critical parameters when studying the surface finishing of the prints is the layer height (z-step) that every resin offers, commonly referred as resolution. In order to achieve the optimal performance in each case, the pieces were always printed with the maximum resolution (minimum z-step) available for each of the resins. Thereby, the theorical Minimum Thickness of the Layer (MTL) provided by the supplier and other characteristics of interest are presented in Table 4.3.

Priting Resin	**Clear**	**Model**	**Tough**	**Amber**	**Flexible**	**Elastic**	**Dental**
MTL (μm)	25	25	50	50	50	100	100
Washing time (min.)	5+5	10	10+10	20	10+10	10+10	20
Curing temperatures (°C)	60	60	70	70	60	60	80
Curing time (min.)	30	60	60	30	60	20	20
Transparency	✓	×	×	✓	✓	✓	✓

Table 4.3: Manufacturer characteristics of the 3D printing resins used in this work.

4.1.4 Instruments

4.1.4.1 Nannetti LKN 86 furnace

The Nannetti LKN 86 furnace (Figure 4.4) is utilized to conduct thermal treatments on both soda-lime glass and resin samples. With external dimensions of 500×750×750 mm³ and a weight of 86 kg, the furnace features an interior composed of insulating low-density refractory brick, measuring 200×300×150 mm^3. It can achieve a maximum temperature of 1340 °C. The furnace is equipped with a temperature ramp, enabling control over the initial, process, and final temperatures of the samples, along with the duration of heat exposure. It operates at a power of 4 kW and a voltage of 230 V.

Figure 4.4: Nannetti LKN 68 furnace.

4.1.4.2 Diener Zepto plasma cleaner

The Diener Zepto plasma cleaner (Figure 4.5) is utilized for the sealing of PDMS devices, enabling bonding between PDMS-PDMS or PDMS-glass. This method involves the chemical modification of material surfaces through exposure to a plasma generated from gases. In our specific application, the plasma process is conducted in an oxygen atmosphere. Apart from bonding, plasma cleaning serves other purposes such as the removal of organic layers, surface activation before gluing or lacquering, as well as etching or coating through plasma polymerization (Jo et al., 2000). With dimensions of 425×450×185 mm^3, the plasma cleaner chamber has a diameter of 105 mm and a length of 300 mm. Equipped with a 13.56 MHz generator, its power is adjustable up to 200 W, and the exposure time to plasma is also adjustable. The machine is connected to a high purity oxygen bottle and a Pfeiffer DUO 5.0 rotatory pump with a maximum capacity of 5 m^3/h.

The device features a rotatory control guiding users through the various process steps. Initially, a vacuum is created in the chamber. Once the desired pressure is reached, oxygen gas is introduced into the chamber, with two gas entries allowing for gas mixture. Subsequently, the generators are activated, initiating the plasma exposure. Finally, atmospheric pressure is restored, concluding the entire process.

Figure 4.5: Diener Zepto plasma cleaner.

4.1.4.3 Minipuls 3 Peristaltic Pump

For testing the real performance of the micromixers, a peristaltic pump was used. Four channel Minipuls 3 Peristaltic Pump (Figure 4.6a) was employed, allowing us to precisely control the flow rate and ensure consistent flow conditions for accurate measurements and observations. To assess the mixing capabilities and confirm the absence of any leakage (Figure 4.6b) of the micromixers, different colour dyes (red, blue or yellow) were introduced simultaneously into the system. The selection of multiple dyes offers the advantage of visualizing and quantifying the mixing process, as a distinct colour pattern emerges as a result of efficient or inefficient mixing. Regarding tubing, the flow was stablished through a 3-stop

Pump Platinum-cured silicone tube (Inner Diameter (ID) 1 mm and Outer Diameter (OD) 3 mm), connected with stopper connectors and silicon tubing (ID 1mm and OD 3 mm).

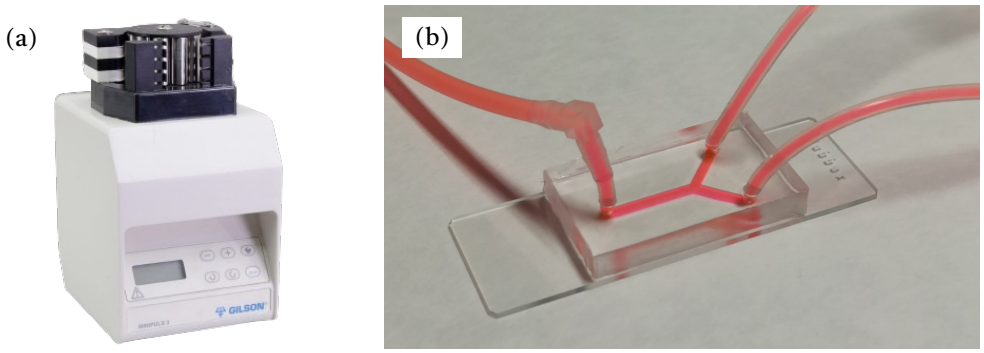

Figure 4.6: a) The Minipuls 3 Peristaltic Pump employed inflow experiments. b) A red sample flow is introduced into the bifurcation device to inspect for any potential leaks.

4.1.5 Laser systems

4.1.5.1 Pulsed laser systems

In this thesis, two pulsed lasers were used for manufacturing microfluidic devices and masters. Two temporal regime were used: nanosecond and femtosecond. The choice of each laser depens on the material used and the desired outcomes.

4.1.5.1.1 Nanosecond regime: Rofin PowerLine 20E

Selected laser for the ablation of glass surfaces is a Rofin Power Line 20E (Figure 4.7). This diode end-pumped Nd:YVO_4 laser emits pulses of 20 ns at a wavelength of 1064 nm, which corresponds to the infrared spectral range. The experimental setup for the micropatterning of substrates (metal, glass, 3D printing resin) consists of a system of galvanometric mirrors coupled to a flat flied lens of 100 mm focal length, that provides a uniform irradiance distribution on an 80×80 mm^2 surface with a spot size at the focus of 15 µm. Laser average power is up to 20 W, adjustable by controlling the amperage applied to the diodes, which is up to 45 A. The number of pulses per second can also be selected from single shot to 200 kHz repetition rate. The laser operates with integrated CAD software, allowing design creation or importation. The software controls mirrors and enables individual adjustment of laser parameters, such as: average power, repetition rate, and beam scanning velocity among others. Precise Z axis positioning is achieved using a support with micrometre rings, ensuring accurate control over ablation depth. It also features a suction system to extract the vaporized material.

Figure 4.7: Rofin PowerLine 20E laser system.

4.1.5.1.2 Femtosecond regime: Santiago Terawatt Laser

The femtosecond laser processing of 3D printing resin was performed using the Santiago TErawatt Laser (STELA) of the Laser Laboratory for Acceleration and Applications (L2A2) facility at Santiago de Compostela. This laser offers 1 mJ of energy per pulse, 35 fs of pulse duration, 1kHz of repetition rate and 800 nm of wavelength with a bandwidth of 75 nm. This output is coupled to a micropattering station (Figure 4.8) where the beam is focused through a microscope objective M Plan APO NIR20× (Mitutoyo, Sakado, Japan) on the 3D printed target. This target is hold by a high precision microprocessing system made of two ILS200LM-S stages (Newport, Irvine, California, USA) with an accuracy of 1.5 μm in X and Y axis and 100 nm in Z axis. The design of the patterns was made using Fusion 360 CAD software (see Section 4.1.7.1). The target is maintained always at the focal length of the microscope thanks to a co-lineal laser feedback with a resolution of 0.4 μm. During irradiation of the target the focal position can be automatically readjusted.

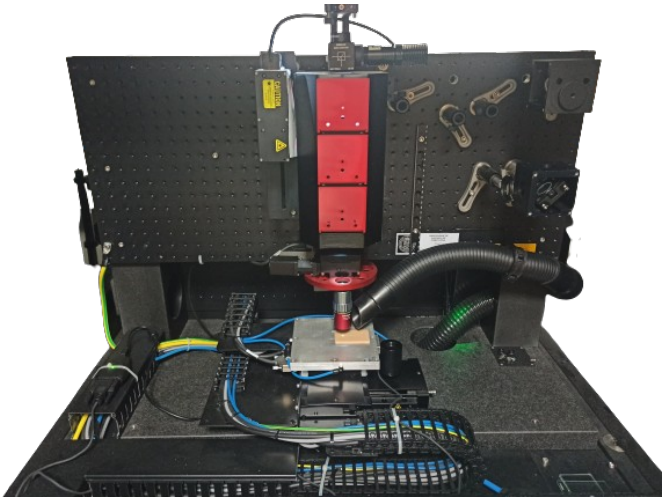

Figure 4.8: Micropatterning station of the STELA laser.

4.1.5.2 Continuous laser systems: Form 3B stereolithographic 3D printer

Furthermore, a stereolithographic (SLA) 3D printer was employed for manufacturing microfluidic devices and masters. Specifically, a Form 3B printer (Figure 4.9a) was used to fabricate the devices designed employing Fusion 360 CAD software (see Section 4.1.7.1). This printer incorporates Low Force Stereolithography (LFS) technology, which integrates a galvanometer system for laser beam direction, along with a spatial filter, fold mirror, and parabolic mirror. This novel system ensures the laser beam is consistently delivered perpendicular to the piece, making it the first SLA printer to offer this capability. This technique improves the precision and accuracy of the structures fabricated, since a more uniformity deposition of laser energy across the built-in platform is obtained. For this, a resin tank with a flexible sheet at its base is used. This base gradually deforms when the piece is pressed against it, reducing manufacturing stresses that the pieces suffer during the printing process. For the polymerization of the resin, a continuous laser system (λ=405 nm, P=250 mW) is employed. In this way, the accuracy of the 3D printed structures is improved, as a much more uniform deposition of the laser energy is ensured.

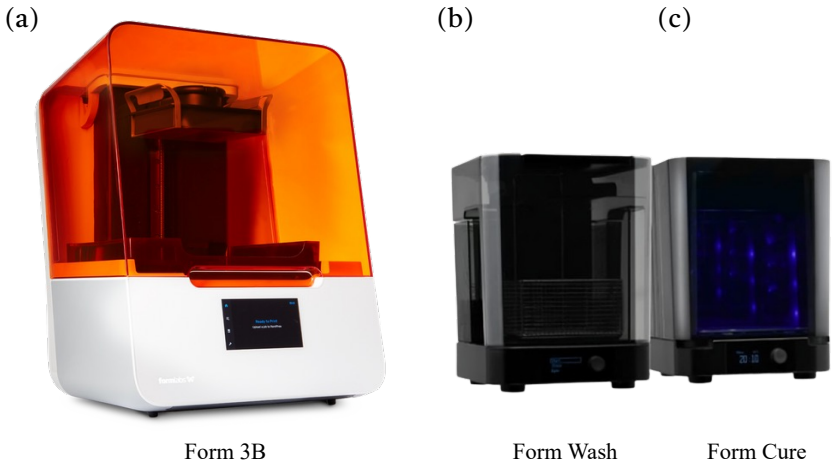

Figure 4.9: Pictures of a) Form 3B 3D SLA Printer and b) and c) Form Wash and Cure stations for postcuring the parts, respectively.

After printing the devices, it is necessary to post cure the resin pieces in a two-step process, to improve their mechanical aspects and superficial finishing. This process starts with a wash of the part in isopropanol (IPA) >90% in the Form Wash tank (Figure 4.9b), in one (Model, Amber and Dental) or two cycles (Clear, Tough, Flexible and Elastic), during specific times indicated in Table 4.3. The pieces are then left to dry and placed in the UV Form Cure chamber (Formlabs, Somerville, Massachusetts) (Figure 4.9b), that allows to control the temperature and is also provided with LEDs emitting at 405 nm.

4.1.6 Characterization tools

4.1.6.1 Nikon MM-400 microscope

A Nikon MM-400 metallurgic microscope (Figure 4.10) is employed for optical inspection of samples in transmission and reflexion mode. It has two light sources, diascopic and episcopic, composed by white LEDs. Optical head is binocular and has 300×600×638 mm^3 dimensions and 50 kg weight. Axis movement is manual and it allows non-contact measurements in the three axes. Maximum workpiece height in this instrument is 150 mm. The microscope is combined with a CCD camera and software that permits the acquisition and treatment of images. The microscope is equipped with three LU Pan Fluor series microscope objectives: 5×/0.15, 20×/0.45 and 100×/0.90.

Figure 4.10: Nikon MM-400 metallurgic microscope

4.1.6.2 Zeiss Axio Vert.A1 microscope

Zeiss Axio Vert.A1 is an inverted transmitted light and reflected light fluorescence microscope (Figure 4.11) that works under this phenomenon. Briefly, fluorescence consists in the excitation of an organic or inorganic compound with certain wavelength resulting in the subsequent emission of longer wavelength light from the sample. This emission of light is virtually simultaneous. Basically, a fluorescence microscope operates by irradiating the sample with a specific band of wavelengths and separating the excitation light from the fluorescent emitted radiation, which is much weaker than the first, by a dichroic mirror. There are plenty of materials that show autofluorescence under particular illumination. Moreover, numerous stains or fluorochromes, which attach to specific materials and allow fluorescence inspections, have been developed. Fluorescence microscopy has contributed enormously to biology and biomedical sciences, allowing identifying cells or even sub-cellular structures. Some characteristics of this microscope are showed in Table 4.4.

Figure 4.11: Zeiss Axio Vert.A1 fluorescence microscope.

Fluorescence reflected light illumination	Via exchangeable LED modules Selectable wavelengths: 365 nm, 385 nm, 420 nm, 445 nm, 455 nm, 470 nm, 505 nm,530 nm, 590 nm, 615 nm, 625 nm
Transmitted light illumination	LED illumination, wavelength from 400 nm to 700 nm, peak at 460 nm
LED illuminator (transmitted light)	Maximum power consumption 3 W Infinitely light source adjustability from <1.5 V to 12 V
Stand with objective focusing	Coarse focus 4 mm per rotation Fine focus 0.4 mm per rotation Total focusing range 13 mm
Objectives	Set of ICS objectives with M27 thread Manual change of objectives via five- position nosepiece A-Plan 10x/0.25 Dry EC Plan-Neofluar 20×/0.5 Dry LD A-Plan 20×/0.35 Dry LD A-Plan 40×/1.54 Dry Plan-APOCHROMAT 63×/1.4 Oil
Field of view	23 mm
Dimensions	235×560×560 mm
Weight	10.5 kg

Table 4.4: Zeiss Axio vert.A1 features.

4.1.6.3 Confocal microscopy

4.1.6.3.1 Sensofar S neox non-contact surface profiler

The Sensofar S neox non-contact surface profiler (Figure 4.12) combines three measurement techniques in one apparatus. These technologies are: confocal microscopy, vertical scanning interferometry and focus variation.

Confocal microscopy is an advanced imaging technique that allows to capture high-resolution three-dimensional images of materials and biological samples. For this, a pinhole is used to block out-of-focus light, preventing it from entering the optical system and allowing only information from the focal plane to be captured. This selective imaging technique significantly enhances optical resolution. By scanning the pinhole aperture and acquiring multiple two-dimensional images at varying depths, both 3D images of samples and 2D profiles can be reconstructed. This method is particularly effective for measuring highly irregular surfaces and steep slopes with precision and detail.

Interferometry microscopy is based on the different path travelled by two separated beams (reference and sample) to yield a spatial interference pattern that contains information of the topography of the sample. Great resolution is obtained but the main disadvantage of this technique is that the surface must be very smooth and it is difficult to measure step topographies.

Focus variation vertically scans the sample to obtain a continuous set of images of the surface. An algorithm determines which are the points in focus in each frame and creates an image of the sample as well as a 3D surface. It is the most resolution limited of the three techniques and has no international standard. It is also no suitable for mirror like surfaces. Nevertheless, is a technique easy to use and versatile, it is very suitable for rapid measurements and for sharp slopes.

Technical specifications of the abovementioned techniques are summarized in Table 4.5.

Figure 4.12: Sensofar S Neox profiler.

	Focus variation	Confocal	Interferometry
Z repteatibility (nm)	200	1 – 40	1
Lateral resolution (µm)	0.8	0.3	0.5
Maximum slope (º)	86	72	40
Measurement range (mm)	37	37	10

Table 4.5: Comparison among field of view, confocal and interferometry techniques for the Sensofar S neox surface profiler.

The profiler has 600×569×389 mm^3 dimension and is equipped with four light sources: red, green, blue and white red, optimizing the light source for each application. In this moment, the equipment has six different objectives: one group of TU Plan Fluor objectives with magnifications 10×, 20× and 50× for confocal and focus variation techniques and other three with the same magnification for interferometry microscopy. In Table 4.6, some properties of the brightfield objectives are presented.

Magnification	10×	20×	50×
NA	0.30	0.45	0.80
Work distance (µm)	17.5	4.5	1
Field of view (µm)	1700×1420	850×710	340×710
Spatial sampling (µm)	1.38	0.69	0.28
Optical resolution (µm)	0.46	0.31	0.17

Table 4.6: Characteristics of the brightfield objectives of the Sensofar S neox profiler.

4.1.6.3.2 Leica TSC SP8 confocal microscope

The Leica TSC SP8 microscope (Figure 4.13) combines two techniques that were previously mentioned: confocal and fluorescence microscopy. By employing a pinhole, any fluorescent signal coming from out-of-focus planes is supressed and high resolution images are obtained. As in non-fluorescent confocal microscopy, 3D images are acquired by scanning different focal planes and stacking the images. Some specifications of this equipment are listed in Table 4.7

Figure 4.13: Leica TSC SP8 confocal microscope.

Continuous wave lasers	UV diode 405 nm Solid state laser 20 mW 488 nm Solid state laser 20 mW 552 nm Solid state laser 20 mW 549 nm Solid state laser 30 mW 638 nm
Detection range	400-800 nm
Pinhole	Stable single pinhole Pinhole diameter motorized by software
Resolution	From 512 × 512 px to 8000 × 8000 px
Objectives	HC PL FLUOTAR 5×/0.15 Dry HC PL APO CS 2 10×/0.4 Dry HC HC PL APO CS 2 20×/0.75 Dry FluotarVISIR 25×/0.95 Water HC PL APO CS 2 40×/1.30 Oil HC PL APO CS 2 63×/1.4 Oil
Field of view	22 mm
Dimensions	1100×2300×1750 mm
Weight	330 kg

Table 4.7: Leica TSC SP8 confocal microscope features.

4.1.6.4 BP109-VIS beam profiler

BP109-VIS from Thorlabs beam profiler is designed for analysing cross-sectional profiles of nearly Gaussian laser beams. It allows for intensity profile measurements along user-specified X and Y axes at scan rates ranging from 2 Hz to 20 Hz, adjustable via software control. While primarily intended for continuous-wave (CW) laser beams, these profilers can also measure pulsed beams with frequencies ≥10 Hz using an averaging technique. These measurements serve various purposes, such as beam quality assessment, examination of reconstructed beam profiles, and long-term stability monitoring.

It features a Ø9 mm physical input aperture. It operates by sequentially scanning two slits, each with the same width and orthogonal orientations, across the input laser beam. The software enables users to switch between pairs of 5 µm or 25 µm width slits, select scanning-slit or knife-edge mode operation, and configure various scan options. Equipped with low-noise electronics and boasting a high dynamic range of 78 dB, this profiler can measure beams with diameters ranging from 2.5 µm to 9 mm. Beam diameter measurements conform to ISO 11146 standards and can be displayed using industry-standard clip levels like $1/e^2$ (13.5%), 50%, or a custom clip level set by the user. Technical specifications are detailed in Table 4. 8.

Wavelength Range	200 -1100 nm
Detector Material	UV-Enhanced Si
Aperture Diameter	9 mm
Scan Methods	Scanning Slits, Knife Edge
Slit Size	5 µm and 25 µm
Minimum Beam Diameter	2.5 µm
Maximum Beam Diameter	9 mm
Scan Rate	2.0 - 20.0 Hz (Continuously Variable)
Sampling Resolution	0.12 - 1.24 µm (Depending on Scan Rate)
Power Range	1 µW - 10 W
Amplifier Bandwidth	16 to 1000 kHz in 11 Steps (@ -1 dB)
Sample Frequency	0.2872 - 2.0 MHz
Dynamic Range	78 dB (Amplifier Switchable)
PD Reverse Bias Voltage	0 /-1.5 V (Switchable)
Signal Digitization	15 Bit
Dimensions	Ø79.5 mm×60.0 mm
Minimum Pulse Rate	10 Hz
Warm-Up Time for Rated Accuracy	15 in

Table 4. 8: Tecnhical specifications of BP109-VIS beam profiler.

4.1.6.5 Zeiss FESEM-Ultra Plus scanning electron microscope

Scanning electron microscopy (SEM) is a imaging technique that generates images by focusing a beam of electrons onto the sample. The electrons interact with the atoms in the sample, so that the resulting signals contain information of the sample topography and composition. As the electron beam scans over the sample, a high-resolution 2D image of the surface is produced with nanometre precision.

The Zeiss FESEM-Ultra Plus SEM (Figure 4.14) operates under high vacuum conditions with a field emission scanning electron microscope (FESEM) illumination system, distinguishing it from conventional SEM by generating highly focused electron beams, leading

to enhanced resolution. Additionally, its charge compensation system, facilitated by nitrogen injection, minimizes charging effects on non-conductive samples.

Equipped with an energy dispersive X-Ray (EDX) spectroscopy system, this SEM conducts chemical analysis on localized areas, lines, or points of the sample by detecting the X-ray radiation emitted. As X-ray scattered energy is characteristic of each element, the system can provide qualitative and semi-quantitative distribution maps of chemical elements and concentration profiles of a chemical element between two points. The system achieves a resolution of 129 eV at a working distance of 8.5 mm and a voltage of 20 kV.

Figure 4.14: Zeiss FESEM-Ultra Plus scanning electron microscope.

Some characteristics of Zeiss FESEM-Ultra Plus SEM are listed below in Table 4.9.

Detectors	Secondary electron detector In Lens
	Secondary electron detector Everhart-Thornley
	Electron selective backscattered electron ESB
	Angles selective backscattered electron ASB
	STEM
	X-ray Oxford Inca
Resolution	0.8 nm at 30 kV (STEM mode)
	1 nm at 15 kV and WD = 2 mm
	1.7 nm at 1 kV and WD = 2 mm
	3.5 nm at 0.2 kV and WD = 2 mm
	4 nm at 0.1 kV and WD = 2 mm

Acceleration voltage	0.02 V – 30 kV, adjustable with 10 V steps
Magnification	12 – 1,000000×
Working Distance (WD)	1 – 50 mm
Chamber dimensions	330 mm Ø × 270 mm length
Maximum sample weight	0.5 kg

Table 4.9: Zeiss FESEM-Ultra Plus scanning electron microscope features.

4.1.6.6 PerkinElmer Lambda 25 spectrometer

PerkinElmer Lambda 25 spectrometer (Figure 4.15) is employed for obtainig the transmittance spectrum of samples from 190 to 1100 nm wavelength. The spectrometer features a slit of 1 nm. Wavelength accuracy at D2 peak (656.1 nm) is ±0.1 nm. Wavelength reproducibility with 10 measurements at 656.1 nm is ±0.5 nm. This tool has applications in routine UV/Vis testing, in liquid analysis or pharmacopeia and regulatory test, among others.

Figure 4.15: PerkinElmer Lambda 25 spectrometer.

4.1.6.7 Microcomputed tomography scanner

Microcomputed tomography (μCT) canners are advanced imaging devices that utilize a rotating X-ray tube and an array of detectors arranged in a gantry configuration. These scanners operate by emitting X-rays through the object of interest from various angles. Then, detectors measure the amount of X-ray attenuation that occurs as the beams pass through different structures within the object, obtaining multiple X-ray projections as the tube and detectors rotate around the object. These projection data are next processed using sophisticated tomographic reconstruction algorithms to produce tomographic (cross-sectional) images, that can be conceived as virtual "slices”. This imaging technique provides high-resolution internal views of biological specimens or materials, aiding in biomedical research, clinical diagnostics, and material analysis.

In this thesis, micropatterning results were evaluated by this technique, employing a SkyScan 1272 X-ray microCT (Figure 4.16) with a resolution of 13 µm/pixel and a Cu 0.11 mm filter. The projections were reconstructed using Nrecon software and the analysis of the structures was carried out with CTAn software. The reconstructed images were volume-rendered using CTVox software (Bruker) to visualize the structures fabricated in the glass substrates. Some features and specifications of this instrument are presented in Table 4.10.

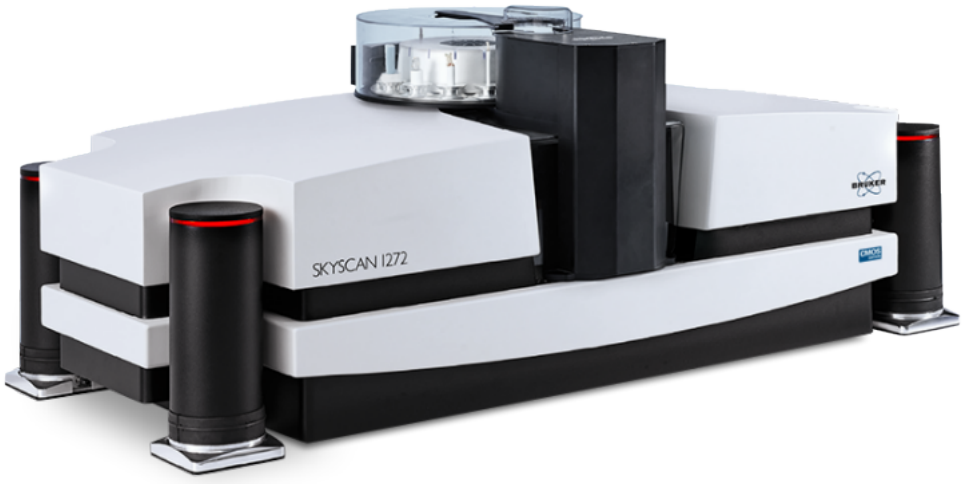

Figure 4.16: SkyScan 1272 X-ray microCT.

Feature	Specification
X-ray source	40 – 100 kV
	10 W
	< 5µ sopt size at 4 W
X-ray detector	16 MP sCMOS detector (4096 × 4096 pixels)
Object size	75 mm diameter
	80 mm height
Specific gravity (cured)	16 samples up to 25 mm diameter
	External access
Work life at 25 ºC	1160 × 520 × 330
	Weight 150 kg
Power supply	100-240V AC, 50-60Hz, 3A max.

Table 4.10: SkyScan 1272 X-ray microCT features.

4.1.7 Software

4.1.7.1 Fusion 360

Fusion 360 is a software that integrates 3D Computer-Aided Design (CAD), Computer-Aided Manufacturing (CAM), Computer-Aided Engineering (CAE), and Printed Circuit Board (PCB) design functionalities developed by Autodesk. It is compatible with Windows and macOS. In the context of this thesis, the software plays a crucial role in various aspects, including the design of 2D patters for laser ablation, the 3D design of resin of microfluidic devices and masters (Figure 4.17a), the calculus of their properties, the visualization of the PDMS replicas (Figure 4.17b), and the generation of digital twins for fluid simulations. Fusion 360 provides four licensing options to cater to different user needs. In this case we used the license for students and educators.

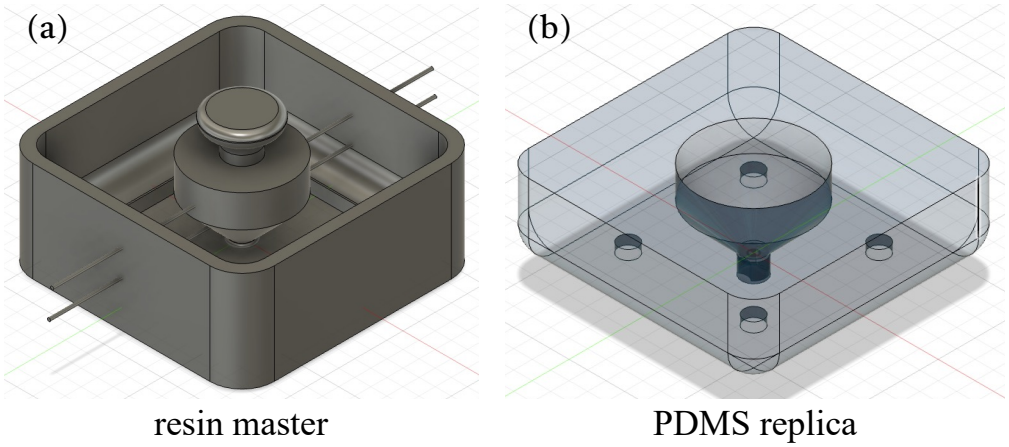

Figure 4.17: Fusion 360 CAD designs of the a) resin master and b) PDMS replica of one of the devices designed in this thesis (the Ussing Chamber).

4.1.7.2 CFD Ansys Fluent

Ansys is a multiphysics CAE simulation software for Finite Element Analysis (FEA), which includes the pre-processing, resolution and post-processing phases in a single platform. Specifically, Ansys Fluent enables to perform Computational Fluid Dynamics (CFD) simulations, predicting the properties of both liquid and gases flows obtained from the equations of mass, momentum and energy conservation. It is compatible with Windows. In the context of this thesis, various tasks were successfully solved by using the software, comprising the CFD simulation of different samples propagating along microfluidic channels (Figure 4.18), the calculation of their properties (velocity, wall shear stress, ...) and the evaluation of their mixing rate in a 2-fluid interaction scenario. Ansys provides several licensing options according to the needs of the user. In this case we employed the Free Student License.

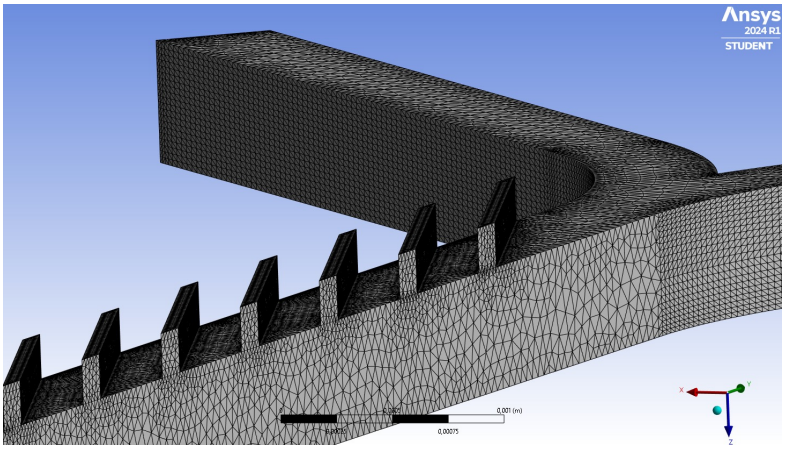

Figure 4.18: Microfluidic micromixer Ansys model used to determinate the fluid properties inside the manufactured microchannels.

4.2 METHODS

4.2.1 Soft lithography

The historical development and current relevance of soft lithography are outlined in the Introduction section of this thesis. The soft lithography process involves two main steps. First, the elastomer is prepared. As we mentioned before PDMS is presented in two parts, cure agent and base, that have to be mixed in the proper proportions for further crosslinking of the material. Secondly, the elastomer is poured over the master that transfer the pattern (Figure 4.19a,b) and it is cured either by heating or exposure to UV radiation. In our case, masters are manufactured by SLA 3D printing (Figure 4.19c). In last step, the PDMS is peeled off from the master and a replica of it is obtained (Figure 4.19d), which can be bonded to a glass slide (Figure 4.19e).

Conventionally, there has been a limitation in the ability to create fully enclosed internal cavities, as the typical practice involved structuring only one face and sealing it to a glass substrate (Figure 4.20a). In this thesis, a step further has been taken in soft lithography by developing and implementing a system of external structures adjacent to microfluidic channels, serving as autoalignment connectors (Turpin et al., 2022). These structures enable the precise coupling of two replicas through their structured faces (Figure 4.20b), enabling the formation of fully enclosed and functional internal cavities avoiding miscoupling or fluid leakage. Notably, this advancement has enabled the creation of channels with completely circular internal sections (Figure 4.20b), representing a significant stride toward mimicking the physiological structure of a blood vessel.

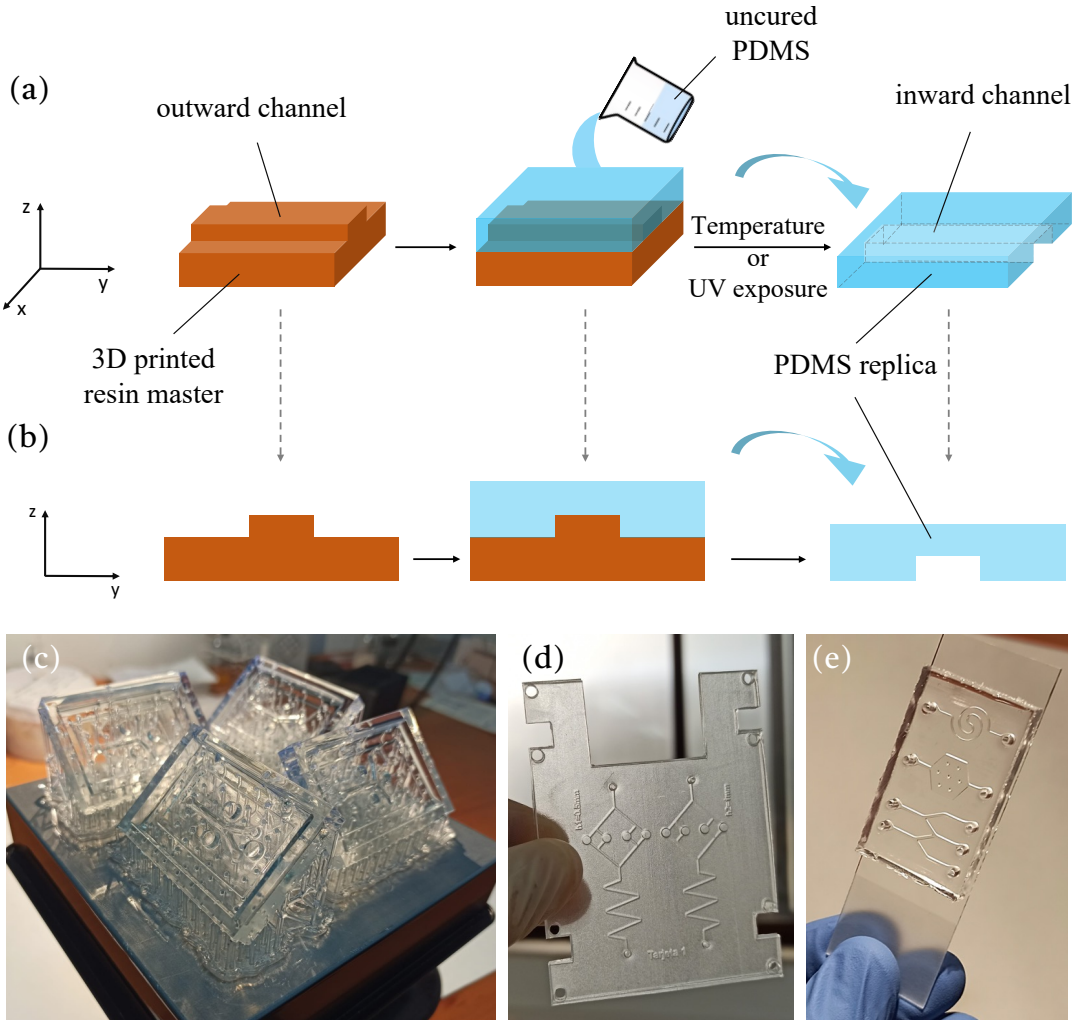

Figure 4.19: a) 3D and b) side view of the soft lithography process. Images of the manufacturing process involved in the manufacturing of different devices during this thesis: c) first, masters are 3D printed. d) Next, a replica is obtained by soft lithography of PDMS, featuring desired geometries. e) Finally, the PDMS replica is sealed to a glass slide by plasma oxygen activation.

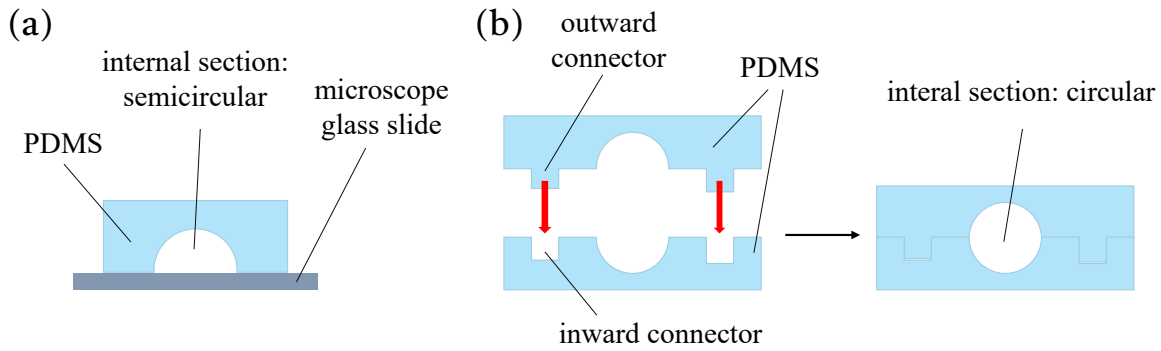

Figure 4.20: a) Conventional result of a PDMS soft lithography process, where the structured PDMS is bonded to a glass slide. Developed system in this thesis: b) devices feature extra structures that act as autoalignment connectors (outward/inward) and allow the precise coupling of the two replicas. With this approach, internal cavities can be easily formed.

4.2.2 Hybrid technique: pulsed laser ablation and stereolithography

In this thesis, a novel hybrid technique that combines PLA and SLA technologies is proposed (Carnero et al., 2024). First, the Form 3B SLA 3D printer is used to obtain the designed substrate with structures on the surface (Figure 4.21a). Next, PLA micropatterning of structures is performed using the STELA of the L2A2 facility (Figure 4.21b). Commercial Model V2 resin is employed as printing resin given the precision it offers (25 µm in Z), its performance when replicating polymers and its good response to laser ablation in the infrared (IR) regime. The printed substrates are post treated as indicated in Table 4.3.

This technique has been utilized to manufacture two different devices of significant interest in microfluidics. First, a straight channel was printed in the resin and subsequently microstructured by laser to create a micromixer (Figure 4.21c). Second, a flat resin substrate was selectively ablated to form an array of microlenses (Figure 4.21d). The final step consists in the soft lithography of the micropatterned structures employing soft lithography of PDMS, obtaining a replica that can be subsequently bonded to a glass slide or to another PDMS structure employing the autoalignment connectors introduced in previous section.

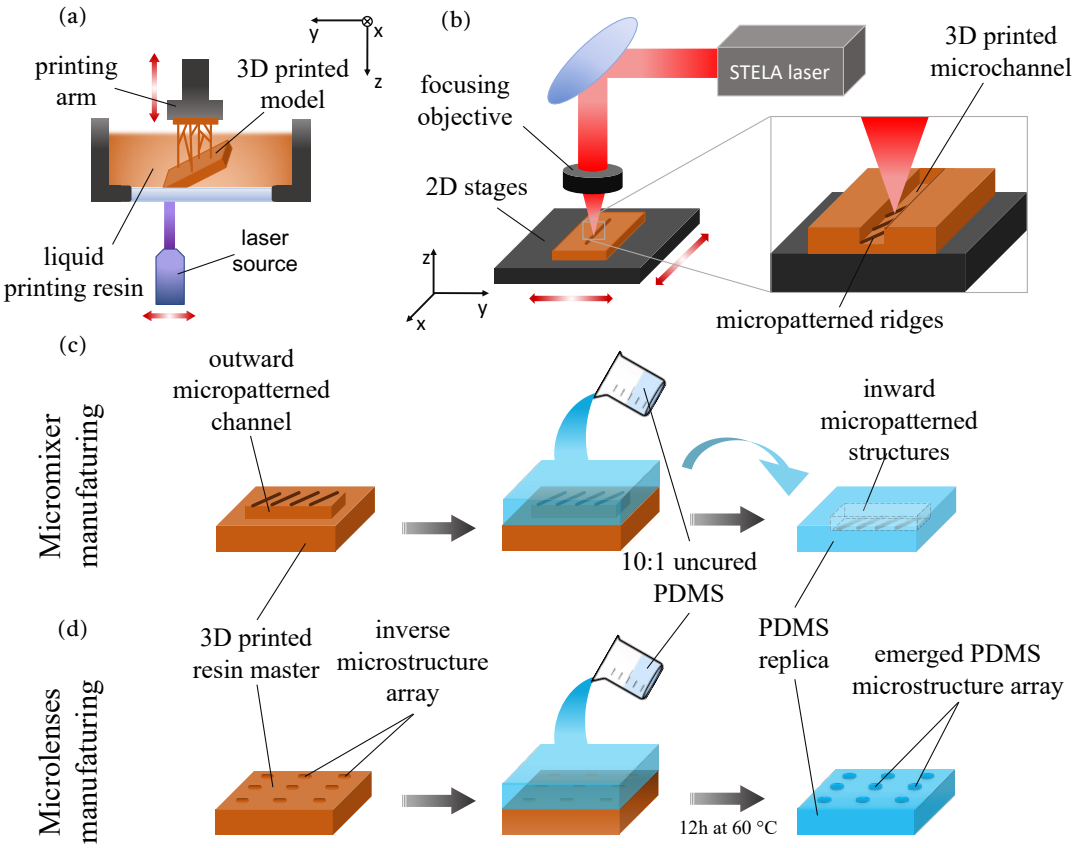

Figure 4.21: Hybrid technique steps: in the first step, a substrate with structured at the surface (for example, a microchannel) is obtained by a) SLA 3D printer. Next, the substrate is placed in the b) PLA micropatterning station to perform ablation of the structures. The second step involves c) the outward/inward micropatterned channel or the d) inward microlenses array that can be replicated by soft-lithography of PDMS to obtain an inward/outward micropatterned replica.

4.2.1 Microlenses focus characterization

To characterize the microlens arrays fabricated using the hybrid technique described in Section 4.2.2, an optical configuration was presented for focal measurement, depicted in Figure 4.22. These elements were coupled to an optical bench aligned with a He-Ne laser, that emits at $\lambda = 632,8$ nm. The spatial filter was the first element that the laser beam passed through at its output and is based on Fourier optics for coherent light beams. This filter has, in the first place, a convergent lens (analogous to a microscope objective) through which the beam is passed, so that in its focal plane the Fourier transform of the transverse energetic intensity distribution is obtained. The distribution on this plane will not be concentrated at a single point but will be concentrated at a central point surrounded by concentric rings. The next element of the filter, the pinhole (circular opening of a few microns), then comes into play, allowing only the above-mentioned central region to pass through. In this way it is possible to achieve that at the filter output, the Gaussian beam is almost perfect. Following this, a converging lens is used to collimate the Gaussian axis filtered by the previous element. This can be achieved by placing the lens at a distance from the filter equal to its focal length (5 cm). Next, the collimated beam goes through the periodic microlenses array object, put on the surface of a glass plate. Last, another microscope objective is used to amplify and project the focus of the lenses on a beam profiler placed below, thus facilitating their observation and detailed analysis.

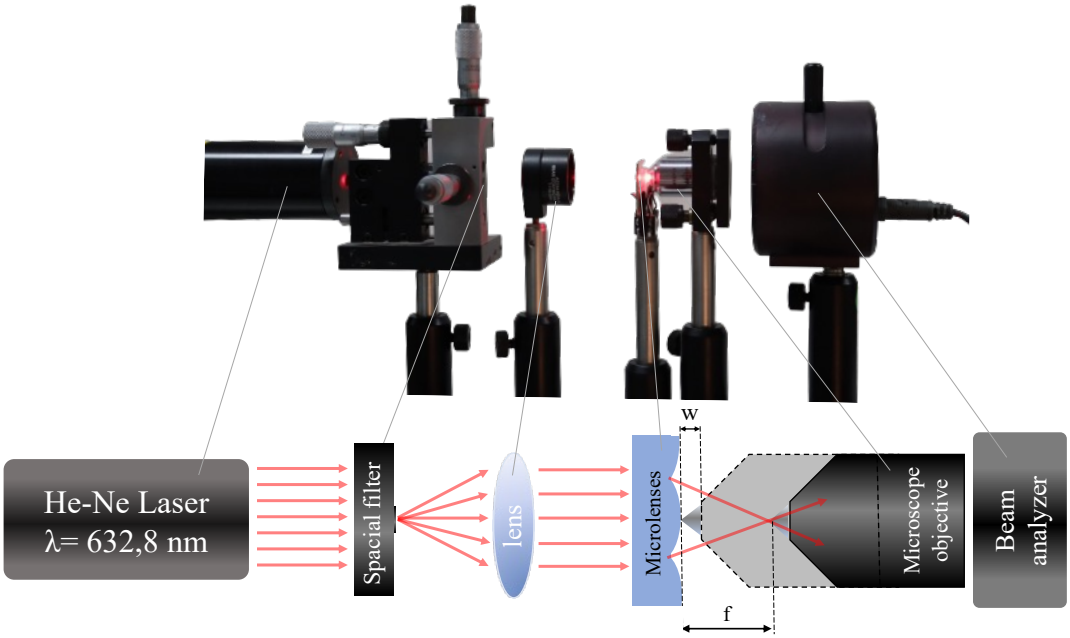

Figure 4.22: Optical setup used to analyse and measure the focus of the manufactured microlenses.

For measuring the focal length of the manufactured microlenses next protocol is followed: first, the microscope objective is focused on the surface of the microlenses and this location is recorded. Then, the microlenses array is moved along Z axis until the image of an arbitrary object is observed. The image is located at the focal plane of the microlenses. The difference

between these positions is a measure of the focal distance of the tested microlens arrays (Nieto, Delgado, et al., 2014b). The accuracy of the data acquisition for this setup is ±5 µm. For determining the quality of the focus we used the beam profiler presented in Section 4.1.6.4. The focus spot size is determined calculating the width at $1/e^2$. Additionally, the profiler can be replaced with a semi-transparent screen, allowing a camera to be positioned after it to capture images of the focal spots at desired positions.

4.2.2 Subaquatic indirect laser-induced plasma-assisted ablation

Subaquatic Indirect Laser-Induced Plasma-Assisted Ablation (SLIPAA) is proposed as a laser-based technique for glass processing (Gómez-Varela et al., 2022). SLIPAA micropatterning of soda-lime commercial glass substrates was carried out using the set-up depicted in Figure 4.23. This configuration incorporates the Q-Switched Nd:YAG laser introduced in Section 4.1.5.1.1, which operates at 1064 nm with a pulse duration of 20 ns, combined with a galvanometer system for steering the output laser beam, that provides uniform irradiance distribution on the glass substrate over a working area of 120×120 mm². The laser beam is focused onto a metallic target after passing through the glass substrate, which has low absorption in the infrared region where the laser operates. A 145 µm thick layer of deionized water is positioned between the glass substrate and the metal target. This method processes the glass by combining the ablation mechanism, shock waves, and cavitation bubbles, allowing for the production of deeper structures than those achieved with standard laser ablation techniques, resulting in glass structures with rectangular cross-sectional profiles and reduced thermal damage.

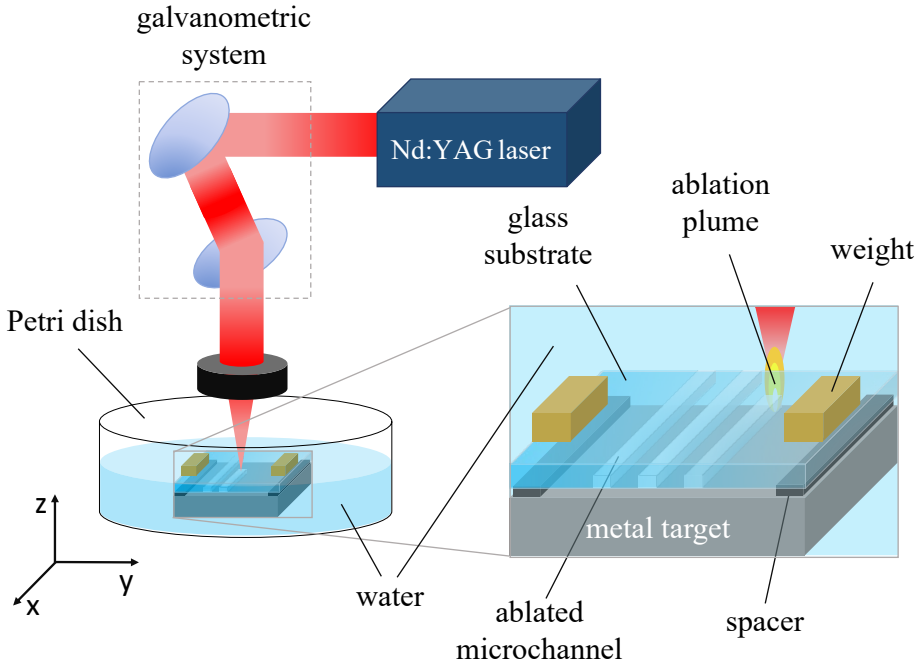

Figure 4.23: Subaquatic indirect Laser-Induced Plasma-Assisted Ablation working principle.

4.2.3 Ag/AgCl electrode manufacturing

This thesis outlines a comprehensive procedure for fabricating Ag/AgCl electrodes tailored for integration into a Ussing Chamber, one of the microfluidic platforms manufactured in this work, of high relevance for studying epithelial transport phenomena (Bzik & Brayden, 2016). The electrodes are fabricated using Ag wire (327026-4G from Merck, diameter 0.5 mm). The preparation process includes several stages aimed at optimizing their performance:

1. Ag wire is taken and polished using fine grit sandpaper, ensuring that the wire diameter matches the 23G needles used in the replication process (See Section 8.2.3.1).
2. Wire length for the Ag/AgCl electrode is determined, and the exposed surface area is calculated based on the diameter.
3. The wire is inserted into the chamber, and the end is bent to secure its position (Figure 4.24a).
4. Solder is fused to join the coated Ag wire and electrodes using a pin header for enhanced connectivity.
5. A sourcemeter or a constant current source is used to apply the appropriate current, considering the wire length.
6. In the oxidation process, the corresponding wire is connected to the anode. The chamber is filled with 0.1M HCl solution.
7. Pt counter electrode (cathode) is placed, and a current of 10mA/cm^2 is applied for 1 minute. The wire changes color and becomes matte (Figure 4.24b).
8. The counter electrode and chambers are cleaned with water.

The electrodes are now ready for use in Ussing Chamber experiments. An image shows the Ussing Chamber coupled to a commercial epithelial volt ohm meter (EVOM2) (Figure 4.24c).

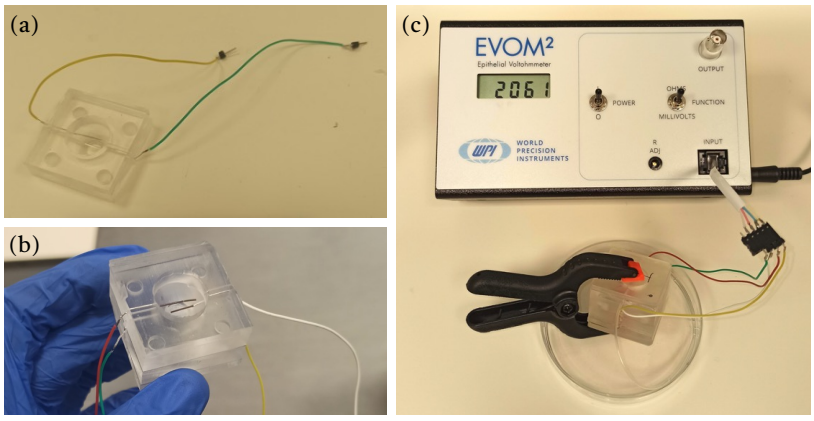

Figure 4.24: Different steps of the Ag/AgCl electrode manufacturing protocol. a) Wires are inserted in the microfluidic chamber. b) Image of the device and electrodes after the current application, when wires turn matte. c) Image of the electrodes of the Ussing Chamber coupled to a volt ohm meter for measuring.

5. SUBAQUATIC INDIRECT LASER ABLATION TECHNIQUE FOR GLASS PROCESSING AND MICROFLUIDICS

This chapter is a partial reprint of:

Ana I. Gómez-Varela[a], Raúl Sanchez[a], Bastián Carnero[a,b], Luis Diaz-Gomez[c], M. Teresa Flores-Arias[a], and Carmen Bao-Varela[a], *Subaquatic indirect laser ablation technique for glass processing*, Optics Experess (2022), DOI: https://doi.org/10.1364/OE.463803

[a]Photonics4Life Research Group, Departamento de Física Aplicada, Facultade de Física and Facultade de Óptica e Optometría, Instituto de Materiais (iMATUS), Universidade de Santiago de Compostela, Campus Vida, E15782 Santiago de Compostela, Spain

[b]BFlow S.L., Edificio Emprendia, Santiago de Compostela, Spain

[c]Departamento de Farmacología, Farmacia y Tecnología Farmacéutica, I+D Farma (GI-1645), Facultad de Farmacia, Instituto de Materiais (iMATUS) and Health Research Institute of Santiago de Compostela (IDIS), Universidade de Santiago de Compostela, E15782 Santiago de Compostela, Spain

---

5.1 INTRODUCTION

Glass substrates play a vital role in numerous research and industrial domains due to their exceptional mechanical, thermal, electrical, chemical, and optical properties. Glass as a material is of vital importance across various sectors, including aerospace, automotive, healthcare, architecture, and fundamental research in fields like biology, physics, and chemistry. From crafting optical waveguides for photonics circuits (Broquin & Honkanen, 2021; Tan et al., 2021) to producing high-efficiency diffraction gratings for telecommunication systems (Takeshima et al., 2005) and Lab-On-a-Chip systems for biological and biomedical applications (Sima et al., 2018; Wlodarczyk et al., 2019), glass is indispensable.

The global market offers a wide array of glasses with diverse characteristics tailored for specific applications. Correspondingly, various glass processing and machining technologies have been developed to align with these characteristics and desired outcomes. Over the past few decades, numerous micromachining glass technologies have emerged, enabling the creation of intricate structures comprising channels, holes, pillars, and wells (Hof & Abou Ziki, 2017; Schwarz et al., 2021). Among these techniques, laser processing stands out as one of the most promising methods due to its non-contact nature, flexibility, low environmental impact, and compatibility with mass production.

Whether employing long-pulse or short-pulse lasers depends on factors like process quality requirements, material removal volume, and cost considerations. However, directing a laser onto glass faces challenges due to its limited absorption visible (VIS) and infrared (IR) light. This makes necessary to increase the energy to start the mechanizing process, which may result in surface damage such as fractures and cracks. IR lasers are one the most implemented at the industry. Consequently, there is a need to advance techniques that enhance IR absorption, thereby refining machining outcomes. Our group has directed its focus towards this objective, investigating how impurities influence the absorption of laser energy to kickstart the ablative process (Nieto, Arines, et al., 2014). Additional methods in this realm include laser etching via self-regulating absorbing layer (LESAL) (Böhme & Zimmer, 2004), laser-induced back side dry etching (LIBDE) (Hopp et al., 2006), and laser-induced back side wet etching (LIBWE) (J. Wang et al., 1999). Nevertheless, implementing these methods can be complex, often requiring reactive gases or thin film deposition followed by chemical etching. Recent studies have also investigated laser cutting methods assisted by water to enhance efficiency and reduce side effects (Dudutis et al., 2022).

Recent studies by Dudutis et al. have delved into laser cutting techniques for soda-lime glass, both in ambient air and with water assistance, employing both picosecond and nanosecond (ns) lasers. These findings underscore the significance of advancing in the development of emerging glass processing methods (Dudutis et al., 2022). Additionally, in 1998, Zhang et al. (Zhang et al., 1998b) introduced a pioneering approach named laser-induced plasma-assisted ablation

(LIPAA) for swift glass machining. This technique enabled the utilization of nanosecond UV and VIS lasers for micromachining materials that are transparent at these wavelengths, expanding possibilities for surface microstructuring, colour marking (Hanada et al., 2007), painting, selective metallization of glass (Sugioka et al., 2004), and surface fabrication of microchannels crucial for microfluidic and biological research (Hof & Abou Ziki, 2017).

In recent years, milli and microfluidics have emerged as highly promising fields, finding applications across chemistry, engineering, medicine, and more. These devices, with their intricate structures, often feature channels as their fundamental components. Laser ablation offers versatility in crafting channels and microchannels of various dimensions and geometries on glass substrates. Glass, boasting a prolonged casting lifespan, also serves as a viable material for producing masters that can be replicated using biocompatible polymers like Polydimethylsiloxane (PDMS) for biological purposes (Aymerich et al., 2017a). Leveraging the impurities within glass allows manufacturing structures through laser ablation, even on substrates transparent to the laser wavelength, as we mentioned before (Nieto, Arines, et al., 2014). However, the scale of such structures typically falls within the tens of micrometres.

For larger-scale structures, such as millimetre-sized channels, Laser-Induced Plasma-Assisted Ablation (LIPAA) proves to be the preferred technique. This technique consists on focusing a laser onto a metallic target located under a glass or a material transparent to the wavelength of the laser used (Pan et al., 2017; Zhang et al., 1998c, 1998a). The plasma generated by the laser interaction with the metallic target initiates ablation on the glass back face. With LIPAA, millimetre-sized structures resembling large blood vessels, including coronary artery bifurcations have been produced (Aymerich et al., 2017a).

Under Liquid Laser Beam Machining (UL-LBM) involves ejecting processed material in the presence of a liquid medium. This process reduces thermal loading and material debris redeposition in the work area due to the liquid's higher specific heat capacity and thermal conductivity compared to air. Moreover, preventing the extracted material from solidifying on the substrate is an added benefit (Behera & Sankar, 2015). Liquid immersion enhances plasma-induced recoil pressure and facilitates the collapse of cavitation bubbles, further improving the machining process (Mak et al., 2011). The plasma produced during the ablation process absorbs a portion of the incoming laser energy, diminishing the coupling of laser energy with the material surface, a phenomenon known as the shielding effect. Introducing a liquid medium reduces both the size and duration of the plasma. This delay in plasma formation onset reduces the overlap with the laser pulse, weakening the plasma shielding effect and enhancing process efficiency (Lu et al., 2004). Song et al. (Song et al., 2020) recently captured images of shock wave and cavitation bubble generation during laser processing of metallic targets underwater, revealing a temporal alignment of these processes, fundamental for understanding underwater laser ablation. In a similar vein, Markauskas et al. (Markauskas & Gečys, 2018) demonstrated direct laser ablation of soda-lime glass sheets in both ambient air and water-assisted conditions

using a picosecond laser operating at 532 nm. Results indicated a 12-fold improvement in glass ablation efficiency with the application of a thin flowing water film on the surface of the sample. An et al. (An et al., 2005) proposed water immersion to mitigate redeposition and blocking effects when drilling micrometre-sized holes in soda-lime glass using femtosecond (fs) laser pulses.

A decade later, Xu et al. introduced the fabrication of glass microfluidic structures through water-assisted femtosecond laser ablation followed by electroless plating (J. Xu et al., 2015). Incorporating water during the laser ablation process enhances debris removal within the glass, thereby enhancing the quality of the ablated micropatterns. However, femtosecond systems are less prevalent in industry compared to nanosecond lasers, which have several advantages over the former, such as: low cost, compact size, robustness, minimal maintenance, lower exigences in the environment conditions and lower safety requirements. For example, Gečys et al. (Gečys, 2015) utilized a nanosecond laser operating in air at 532 nm, focused on the backside of the glass to achieve high aspect ratio micro holes.

Nevertheless, to the best of our knowledge, achieving precise manufacturing of glass with a rectangular cross-section, steep vertical edges, and considerable depth remains a challenge for nanosecond laser-based ablation techniques. The depth of channels produced by these methods is inherently limited. To address this limitation and mitigate the thermal effects induced by the laser, as well as facilitate material ejection from the laser-plasma interaction zone, we have developed and patented a novel technique termed Subaquatic LIPAA (SLIPAA), that is the core of this chapter.

SLIPAA employs a straightforward setup wherein a laser beam passes through a glass substrate and a layer of deionized water before being focused onto a metal target piece. As the laser focuses on the metal target, a plasma is generated between the glass substrate and the target and is confined by the water layer. This arrangement weakens the thermal effects of the nanosecond laser beam and facilitates material expulsion from the laser-plasma interaction zone. The ablation process on the back face of the glass is accomplished through a combination of mechanical shock waves (Charee & Tangwarodomnukun, 2018; Krstulović et al., 2013) generated by the focused laser, along with the ablation plume and cavitation bubbles produced during the process.

SLIPAA could be seen as a fusion of LIPAA and LIBWE. Both ablative techniques are thoroughly explained in (Hanada et al., 2005, 2006) and (Niino et al., 2008; Zimmer et al., 2010), respectively. However, recent investigations into underwater target ablation, such as (Song et al., 2020), must also be taken into account to fully comprehend the SLIPAA process. In their study, Song et al. illustrate how supersonic shock waves propagate from the target to the water, opposite to the direction of the laser beam. Initially, they observe the shock wave overlapping with the plasma in the water, moving into it with a planar front at supersonic

speeds. Over time, this planar wave transforms into an ideal spherical wave after a few hundred nanoseconds. Subsequently, new planar shock waves emerge microseconds later. These secondary waves are attributed to the elastic (or sound) wave propagated into the target induced by plasma. However, the mechanism for describing SLIPAA and how ablation occurs on the rear side of the glass remains unclear, necessitating further studies on laser-plasma interaction, shock wave propagation and interference, hydrodynamic behaviour of cavitation bubbles, and heat exchange processes.

In comparison to previous glass machining techniques, SLIPAA offers several advantages such as simplicity and design flexibility, capable of fabricating intricate elements with greater depth than other glass structuring methods (Sugioka et al., 2004). With a straightforward experimental setup, SLIPAA enables the processing of various structures with vertical sidewalls in both millimetre and micrometre ranges. This capability is demonstrated by manufacturing channels on glass substrates, serving as the initial step to fabricate more complex devices or circuits. Given that the performance of a fluidic device significantly relies on channel surface characteristics, the ability to modify the surface becomes crucial for optimizing overall device operation. As surface roughness can be precisely controlled through post-thermal treatments (Nieto, Delgado, et al., 2014c), certain samples have undergone heat treatment to evaluate its influence on roughness. Additionally, a comparison between channels fabricated by LIPAA and SLIPAA is presented and analysed. Samples are characterized using optical and confocal microscopy, SEM microscopy, EDX, and microcomputed tomography to evaluate surface quality, depth, roughness, and material transfer from the metallic target to fabricated structures.

5.2 MATERIALS AND METHODS

5.2.1 Materials

The glass substrate employed is a low-cost float soda-lime glass (Materials and Methods 4.1.1) of 5 mm width acquired from a local supplier. It presents low absorbance at 1064 nm, the centre wavelength of the laser system, so it is suitable for the fabrication of the elements shown in this research.

The metallic sheets used as targets to generate the ablation plume are known as “Hardened Spring Steel W.-Nr. 1.1274” (H+S Präzisionsfolien GmbH, Pirk, Germany), with a carbon content of over 1%. Glass substrates were cleaned with detergent, washed in running water and then cleaned with isopropyl alcohol (IPA) in an ultrasonic cleaner for 30 min. Metallic targets were thoroughly rinsed with IPA.

5.2.2 Fabrication method and set-up.

SLIPAA experiments on soda-lime commercial glass substrates were carried out using the set-up depicted in Materials and Methods 4.2.2. A Q-Switched Nd:YVO_4 laser (Materials and Methods 4.1.5.1.1) operating at 1064 nm and pulse duration of 20 ns is combined with a galvanometer system for steering the output laser beam. The beam is focused onto a metallic target after it passes through the glass substrate, which presents low absorption in the infrared region where the laser operates.

5.2.3 Thermal treatment.

After the SLIPAA processing of the samples, a thermal treatment is applied using a LKN 86 furnace (Materials and Methods 4.1.4.1), with the aim of modifying, in a controlled manner, the surface roughness produced by the ablation on the bottom of the samples. The furnace has a temperature ramp function that allows to control the initial, process and final temperature of the samples, as well as the time of temperature exposure.

5.2.4 Sample analysis.

The topography and surface roughness of the fabricated samples were characterized by confocal microscopy technique using a 3D optical profilometer S neox (Materials and Methods 4.1.6.3.1). The superficial quality at the edges of the structures were also inspected by optical microcopy using a Nikon MM-400 metallurgic microscope (Materials and Methods 4.1.6.1). The samples were studied using an EVO LS 15 scanning electron microscope (Zeiss; Oberkochen, Germany). Compositional analysis was performed by Energy Dispersive X- Ray system (Materials and Methods 4.1.6.5) to determine the possible transference of material from the metallic target to the fabricated channels. Data was acquired at 20 kV.

Furthermore, samples were also evaluated by microcomputed tomography using a SkyScan 1272 X-ray microCT (Materials and Methods 4.1.6.7) with a resolution of 13 μm/pixel and a Cu 0.11 mm filter. The obtained projections were reconstructed using Nrecon software and the analysis of the structures was carried out with CTAn software (Bruker; Kontich, Belgium). The reconstructed images were volume-rendered using CTVox software (Bruker) to visualize the structures fabricated in the glass substrates.

Pictures of the actual experimental set-up are displayed in Figure 5.1. The geometry of the structure to be engraved on the glass substrate is first designed using a CAD-like (computer-aided design) software. The laser beam is focused on the steel sheet and the ablation plume generated directs towards the backside of the glass substrate. It can be appreciated how part of the debris generated from the ablation of the glass has been swept along towards the edges of the substrate, an effect promoted by the addition of the water layer. In a common LIPAA process, glass debris typically accumulates and suffer a solidification below the substrate, preventing further removal of the material.

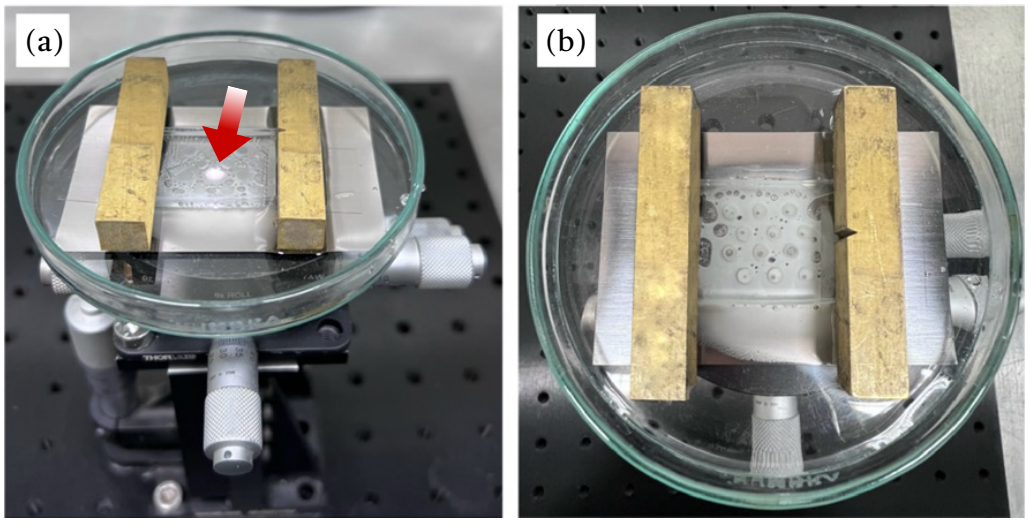

Figure 5.1: Image of the set-up for glass processing using SLIPAA. a) General view of the set-up during the laser operation. Red arrow indicates the laser plasma generated on the metallic target. b) Top view of the glass substrate once the process is finalized. The white debris corresponds to the material removed from the substrate. Some of the bubbles generated during the process can also be observed in the picture.

5.3 RESULTS AND DISCUSSION

5.3.1 Selection of the processing parameters

The laser system utilized in this setup allows different processing parameters to be varied, including average power, repetition rate, and beam scanning velocity, among others. Therefore, as an initial step in the fabrication process, an analysis for achieving the optimal laser parameters is essential. Consequently, different combinations of these processing parameters have been examined to showcase the capabilities of SLIPAA in glass structuring.

Initially, the impact of laser repetition rate on the depth of rectangular cross-sectional channels was assessed. Throughout the experiments, the intensity supplied to the laser diode pumps, corresponding to 4.92 W average power at a repetition rate of 10 kHz, remained fixed at 32 A. Multiple laser passes were conducted to achieve well-defined rectangular channel geometries. The scanning speed was set at 200 mm/s to minimize defects in channel edges, such as cracks and irregularities.

The results depicted in Figure 5.2, that illustrates the influence of laser scanning speed on superficial damage around channel edges. Optical microscope images reveal significant crack formation along the scribed channels at laser beam velocities below and above 200 mm/s. Conversely, smoother edges were observed at a scanning speed of 200 mm/s, indicating minimal surface damage. The formation of cracks at higher scanning velocities is attributed to shock wave propagation, while thermal effects combined with shock waves contribute to glass cracking at velocities below 200 mm/s. At 200 mm/s, with the processing parameters optimized

in our experiments, a balance between these effects appears to result in minimal damage to the glass surface. However, further investigation into the interplay of these effects is warranted.

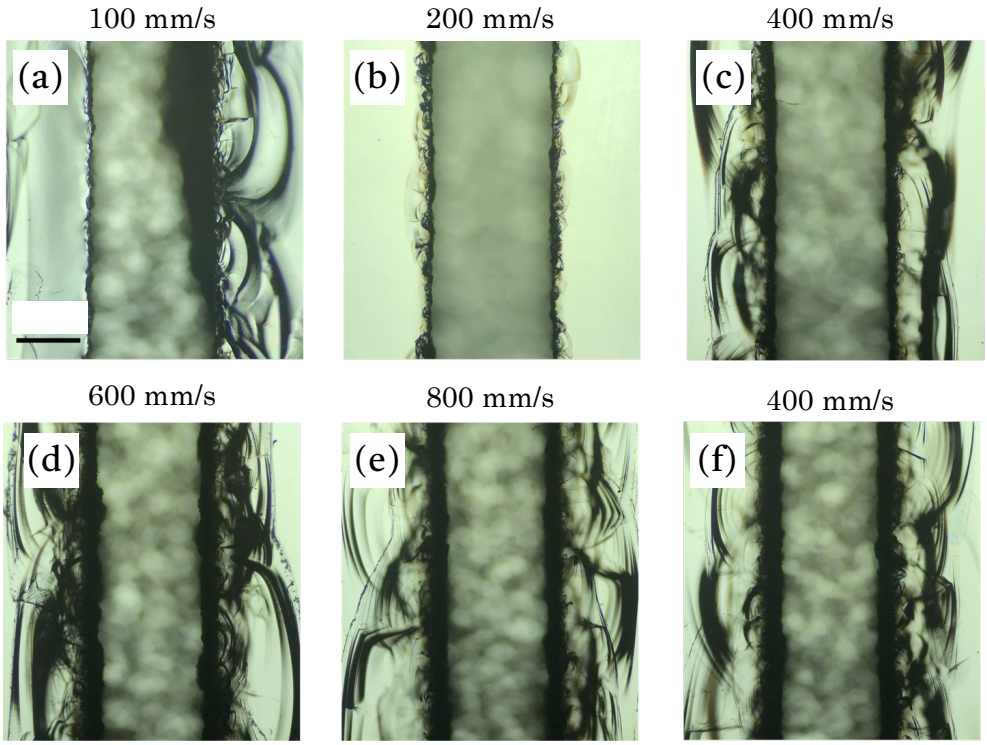

Figure 5.2: Optical microscope images of channels of 1 mm width fabricated using the following scan speeds: a) 100 mm/s, b) 200 mm/s, c) 400 mm/s, d) 600 mm/s, e) 800 mm/s, and f) 1000 mm/s. Processing parameters: wavelength 1064 nm, 10 kHz repetition rate, fluence 78.3 J/cm^2, 30 laser passes. The scale is the same in all pictures.

Figure 5.3a demonstrates that the depth of channels decreases with increasing laser repetition rate. Notably, the quality of channel edges was found to be closely linked to this parameter, with a notable increase in the number of cracks and irregularities observed at repetition rates exceeding 10 kHz. Furthermore, the reproducibility of channel depth significantly diminishes at higher repetition rates.

The study also investigates how varying the number of laser scans impacts the shape and depth of channels. Creating deep channels in glass substrates requires multiple laser passes, which also affects the channel profiles. For the upcoming experiments, a repetition rate of 10 kHz is maintained. It is noted that there is a critical threshold for the number of laser passes needed to produce channels with rectangular shapes, while the laser focal distance remains constant. Figure 5.3b illustrates the profiles of three typical channels produced using identical laser processing parameters but differing in the number of passes: 2 (black line), 5 (purple line), and 10 (yellow line). Below 10 laser scans, channels with inclined walls are observed, while 10 or more passes result in channels with vertical sidewalls. Furthermore, the depth of the channels increases proportionally with the number of laser passes.

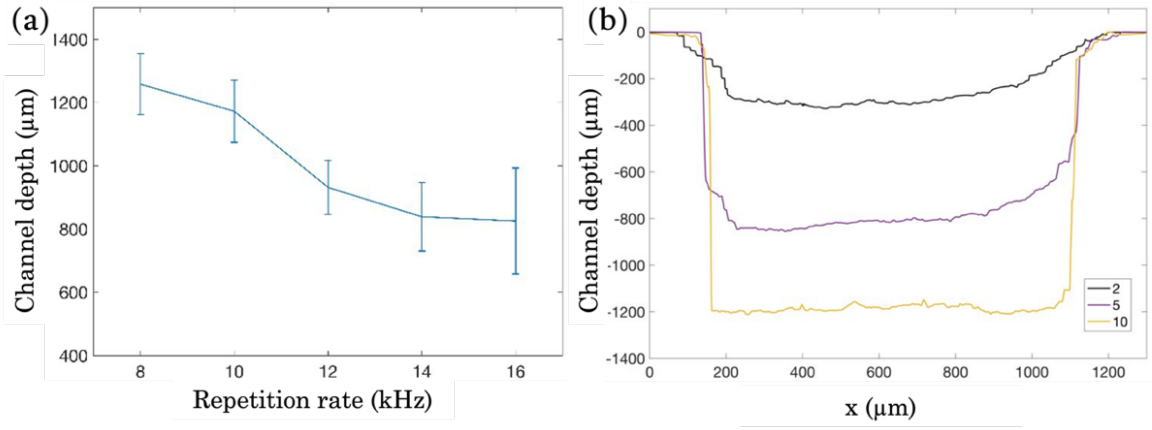

Figure 5.3: a) Evolution of the mean depth value of the channels with the laser repetition rate, using 30 laser passes. Error bars represent the standard deviation (N=10). b) Cross-sectional profiles of the channels with 2 (black line), 5 (purple line), and 10 (yellow line) laser passes, using 10 kHz of repetition rate. Well-formed channels with vertical sidewalls are obtained from 10 laser passes. Laser processing parameters: wavelength 1064 nm, fluence 78.3 J/cm^2 and beam scanning speed 200 mm/s.

Channels were created by incrementally increasing the number of laser passes from 10 to 50, in increments of 10. The maximum depth was achieved at 30 laser passes, obtaining an average depth of 1385.56 µm. Beyond 30 passes, the depth of the channels decreased, likely due to the accumulation of the ablated material that cannot be evacuated. In this case, it would seem that water movement and cavitation bubbles are not able to remove the debris produced in the ablative process out of the channel due to its deep, so solidification of some of the material at the bottom of the channel may occur. A confocal 3D reconstructed image and the extracted profile of the channel obtained after 30 laser passes showing the vertical walls attained with SLIPAA are shown in Figure 5.4a,b, respectively.

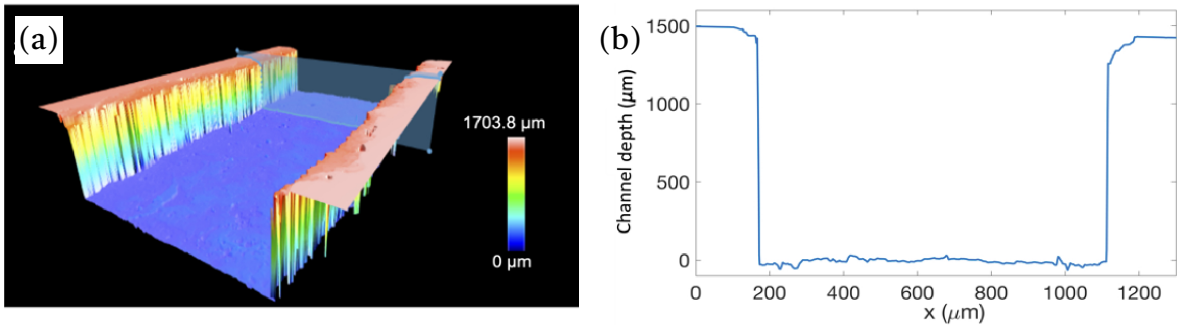

Figure 5.4: a) Confocal 3D reconstructed micrograph for surface topography analysis of one representative rectangular channel, and b) corresponding cross-sectional profile. Processing parameters: wavelength 1064 nm, 10 kHz repetition rate, fluence 78.3 J/cm^2 , beam scanning speed 200 mm/s and 30 laser passes.

The dependence of the depth of the channels on the number of passes of the laser is shown further on in Section 5.3.2, where a comparison between SLIPAA and LIPAA is presented

(Figure 5.5). Regarding the minimum achievable width, clear and unobstructed channels with a width of 300 µm and a depth of approximately 1.36 mm (aspect ratio of 4.53) were attained. Laser parameters remained consistent with those depicted in Figure 5.3b, utilizing 30 laser passes and a fixed focal position.

Roughness is another critical parameter to decide the quality of the structured surface in different applications. It affects surface wettability, which tends to improve with decreasing roughness. This is particularly relevant in fluidic experiments where flow patterns are sensitive to surface properties (Pravinraj & Patrikar, 2018). Additionally, surface modification affects cellular attachment in bioassays (Bourkoula et al., 2016; Ross et al., 2012) and the interaction of fluids with embedded optical waveguides in optofluidic devices, necessitating optimized fabrication parameters to minimize microchannel roughness.

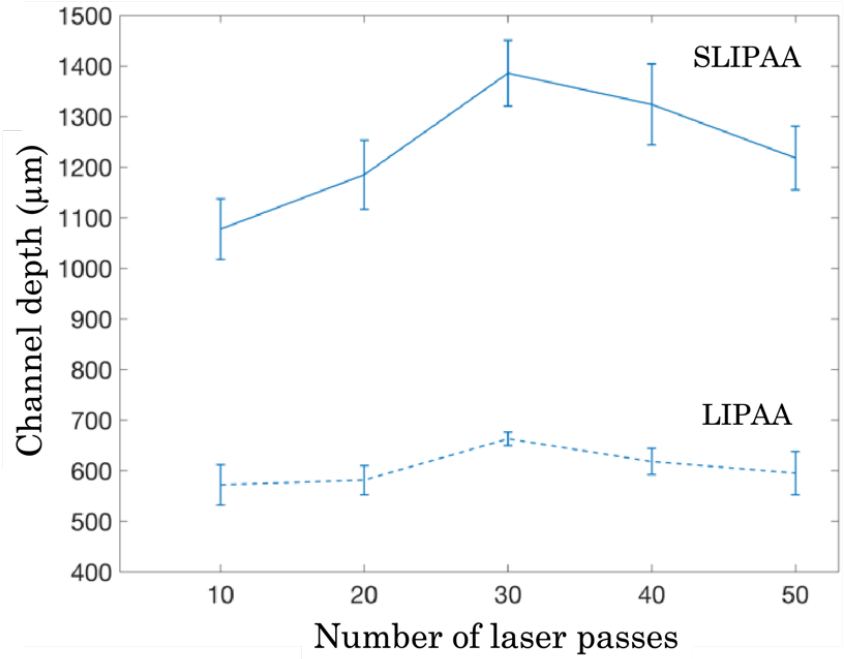

Figure 5.5: Comparison of the evolution of the depth of the channels with the number of laser passes with SLIPAA (solid line) and LIPAA (dashed line). Laser processing parameters: wavelength 1064 nm, 10 kHz repetition rate, fluence 78.3 J/cm^2, beam scanning speed 200 mm/s. Error bars represent the standard deviation (N=10).

Surface roughness at the channel bottoms shown in Figure 5.3a was assessed concerning the laser repetition rate. Using confocal microscopy, roughness was quantified by the arithmetical mean height (S_a) across a defined area of 250×250 µm². Table 5.1 displays corresponding values, ranging between 12.18 µm and 19.10 µm.

Table 5.2 presents surface roughness as a function of the number of laser passes. S_a achieves the maximum value at 30 passes of the laser and decreases at 50 passes. This effect can be attributed to the fact that after 30 laser passes the ablation efficiency of the process decreases

with more accumulation of the debris under the channels and the subsequent solidification of part of this material on the surface of the channels.

Rep. rate (kHz)	**8**	**10**	**12**	**14**	**16**
S_a (µm)	12.18 ± 3.34	13.75 ± 4.28	15.29 ± 3.81	15.01 ± 4.51	19.10 ± 5.24

Table 5.1: Arithmetical mean height values corresponding to the roughness of the bottom of the channels presented in Figure 5.3a. Measurements were performed according to the ISO 25178 standard. Number of samples for statistical analysis is N=10.

Laser passes	**10**	**20**	**30**	**40**	**50**
S_a (µm)	13.75 ± 4.28	12.91 ± 2.58	14.77 ± 3.11	11.72 ± 2.42	11.05 ± 1.19

Table 5.2: Roughness of the channels as function of the number of laser passes. Arithmetical mean height values correspond to the structures presented in Figure 5.5. fabricated by SLIPAA. Measurements were performed according to the ISO 25178 standard. Number of samples for statistical analysis is N=10.

Combining the SLIPAA technique with a post-thermal treatment enhances the optical quality of glass structures and reduces initial roughness at the channel bottoms. Following the SLIPAA fabrication process, channels underwent heating above the glass transition temperature for a specified duration. Since the glass transition temperature for soda-lime glass is 570°C, the effect on channel bottom roughness was assessed for post-thermal treatments ranging from 590 °C to 630 °C in increments of 10 °C. Each sample was pre-heated for 30 minutes from room temperature until the desired treatment temperature was achieved. The treatment temperature was maintained for 2 hours, facilitating material melting and redistribution within the channels. Table 5.3 presents the impact of post-thermal treatment on channel surface roughness reduction. It is observed that for treatment temperatures between 590 °C and 620 °C, roughness decreases without significantly altering feature dimensions, maintaining an almost rectangular cross-sectional profile. However, at 630 °C, the channel profile transitions to a concave-like shape.

Temperature (°C)	**Roughness reduction (%)**
590	26.21 ± 0.56
600	30.14 ± 0.79
610	32.15 ± 0.99
620	39.47 ± 0.43
630	63.19 ± 0.44

Table 5.3: Roughness reduction in the bottom of channels manufactured at 30 laser passes with the laser processing parameters of Figure 5.4a. Measurements were performed according to the ISO 25178 standard.

5.3.2 Comparison between channel fabrication with SLIPAA and LIPAA processes

To demonstrate the potential of SLIPAA in glass processing, we conducted a comparative analysis with channels fabricated using LIPAA. Figure 5.5 illustrates the depth evolution of channels fabricated via laser-induced plasma-assisted ablation in air (represented by the dashed line) and subaquatic laser-induced plasma-assisted ablation (represented by the solid line). The experimental setup described in Section 2 was used, with the exception that no water layer was present between the metallic target and the glass substrate; instead, they were separated by air. Therefore, 1 mm width channels were fabricated on glass for varying numbers of laser scans ranging from 10 to 50. A similar trend was observed in both cases, with a maximum channel depth reached at 30 laser scans. However, there was a significant disparity in the depth achieved between SLIPAA and LIPAA. While SLIPAA achieved a maximum average depth of 1385.56 μm, LIPAA only reached 662.92 μm.

To further illustrate the differences between the two techniques, Figure 5.6a-d show microCT images of rectangular channels fabricated with a) 30 and b) 50 laser passes in air (LIPAA) and c) 30 and d) 50 laser passes in water (SLIPAA) from Figure 5.5. Figure 5.6a,b reveal that when LIPAA is carried out, smaller aspect-ratio structures are obtained. Furthermore, a higher number of laser passes entails that the material expelled during the ablation is not able to evacuate the channel, which results in an inclined area at the bottom of the channel. On the contrary, with SLIPAA one can achieve channels with higher aspect-ratio for the same number of laser passes. Moreover, the bottom of the channel continues to be flat when the number of laser passes rises from 30 to 50.

The cross-sections of rectangular channels fabricated with SLIPAA using 30 and 50 laser scans are depicted in Figure 5.6e,f. As previously discussed, deeper structures are achieved with 30 laser passes (Figure 5.6e). However, with a higher number of passes, channel depth diminishes, as illustrated in Figure 5.6f. Notably, the bottom of the channels appears more uniform with 50 laser passes due to the redeposition of ablated material.

SEM analysis of the bottom surface of the channels produced by SLIPAA and LIPAA after 30 and 50 laser passes is presented in Figure 5.7. In both cases, SLIPAA results in a more homogeneous surface along the channel. Moreover, laser ablation under a water film generates fewer redeposited debris, evident in the images. Debris accumulation is more pronounced after 50 laser passes in air (Figure 5.7h), while minimal residue is detected when ablation occurs in water (Figure 5.7f). Furthermore, there is less evidence of debris along the substrate edges of the channel when using SLIPAA compared to channels manufactured with LIPAA, as depicted in Figure 5.7c and Figure Figure 5.7g.

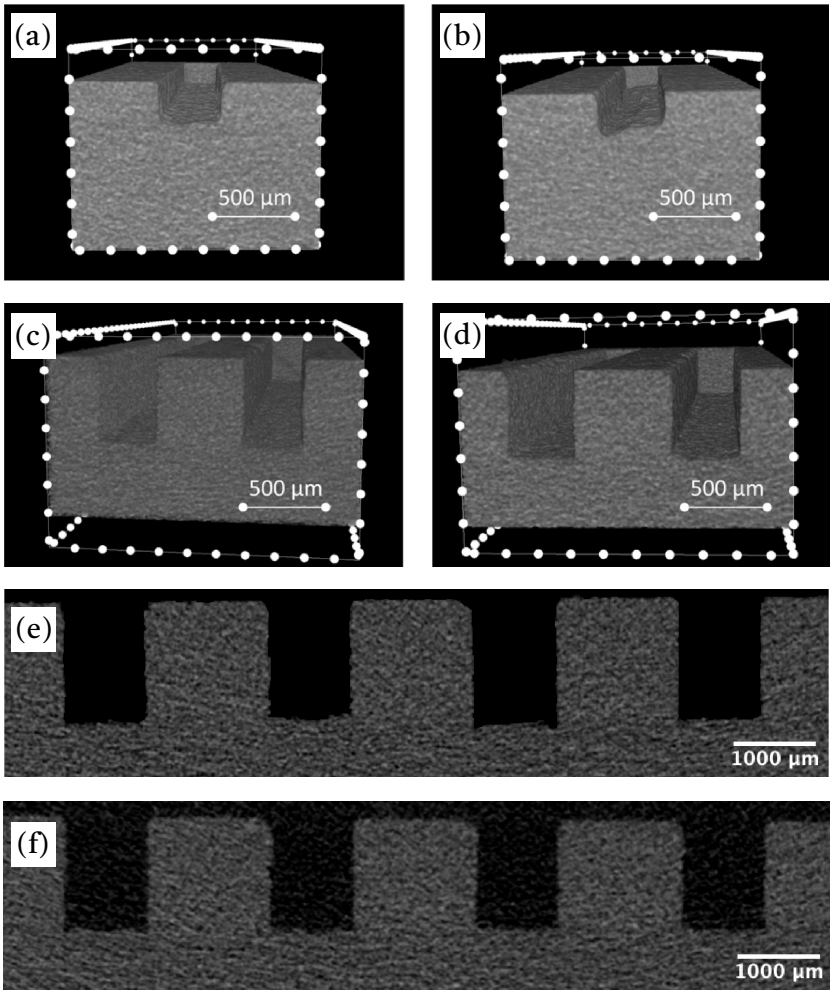

Figure 5.6: MicroCT images of representative rectangular shaped channels fabricated with a) 30 and b) 50 laser passes in air (LIPAA) and c) 30 and d) 50 laser passes in water (SLIPAA). Scale denotes the distance between two consecutive points in the 3D image. Cross section of representative channels engraved on the glass substrates using SLIPAA after 30 and 50 laser passes are shown in e) and f), respectively.

An analysis of structures fabricated using SLIPAA and LIPAA methods was performed, providing insights into their chemical composition. This evaluation encompasses various areas, including the bottom surface of the fabricated channels and the adjacent glass surfaces before and after the fabrication processes. Figure 5.8 shows the EDX results obtained for a channel fabricated after 30 laser passes by SLIPAA and LIPAA. In both cases, the chemical composition on the bottom surface of the channel has been analysed as well as on the glass surface out of the channel. The differences found in the chemical composition of the four analysed zones in comparison with the untreated glass are highlighted in red. In the channel fabricated by SLIPAA (Figure 5.8a) traces of carbon (C) are detected at the bottom of the channel and on the surface of the glass as consequence of the laser ablation of the metal layer. However, nitrogen (N) is only observed at the bottom of the channel. Note that in Figure 5.8b, corresponding to the channel fabricated by LIPAA, the untreated glass surface composition is not the same as that

given in Fig. 12 (Figure 5.8a). This is because the structures have been fabricated on different sides of the glass. During the fabrication process of the soda-lime glass, the molten glass is floated over a film of molten tin for obtaining a plane sheet glass with uniform thickness. During the fabrication of soda-lime glass, tin (Sn) is transferred to the side in contact with the metal bath, as confirmed by the EDX analysis. While tin impurities are known to influence direct laser glass micromachining, their effects are considered negligible in indirect methods like SLIPAA or LIPAA.

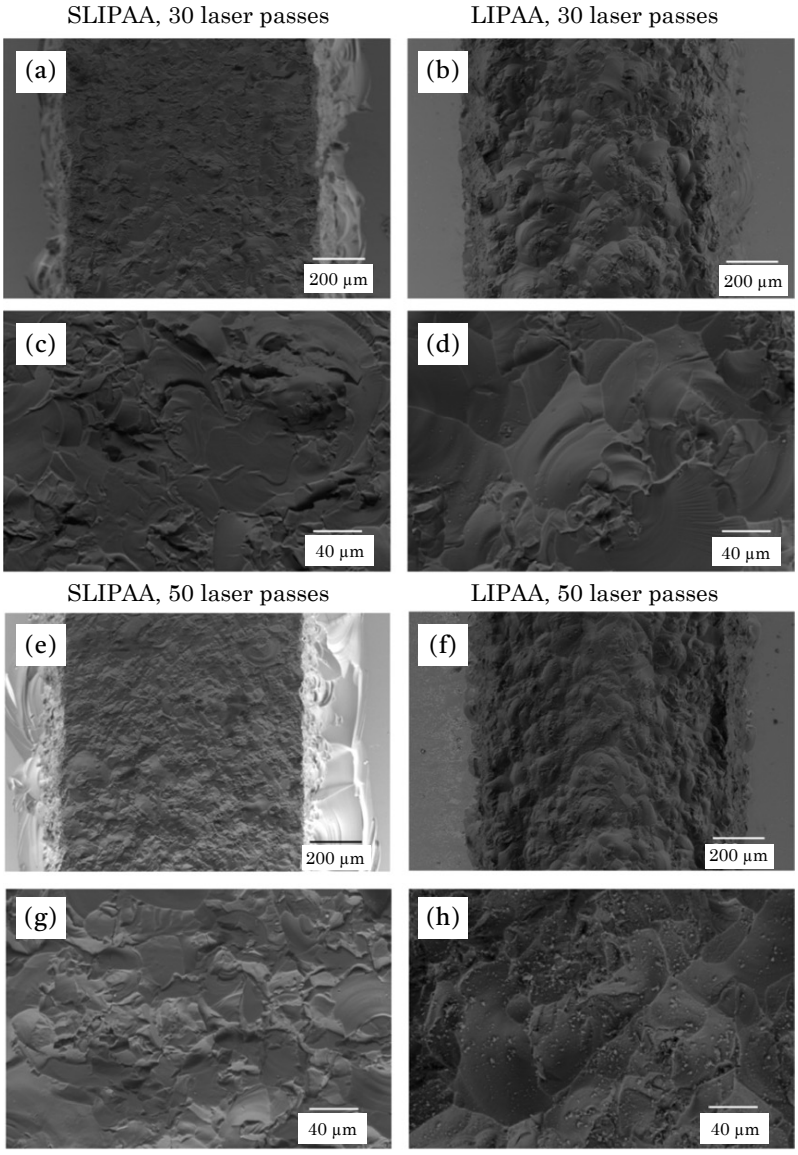

Figure 5.7: SEM images of representative channel surfaces after 30 laser passes with SLIPAA a),c) and LIPAA b),d) and after 50 laser passes with SLIPAA e),g) and LIPAA f),h).

In the case of channels fabricated by LIPAA, the EDX analysis detects traces of C, sulfur (S), potassium (K), chromium (Cr), and iron (Fe) from the metal target, as well as the glass surface near the channel where C, K and Fe are also detected as consequence of ablation debris

deposition. As a summary, for the channels fabricated by both methods, SLIPAA and LIPAA, transference from the metallic target to the channels surface is obtained, however this transfer is much less significant in the case of SLIPAA. The same trend was observed for the samples fabricated with 50 laser passes.

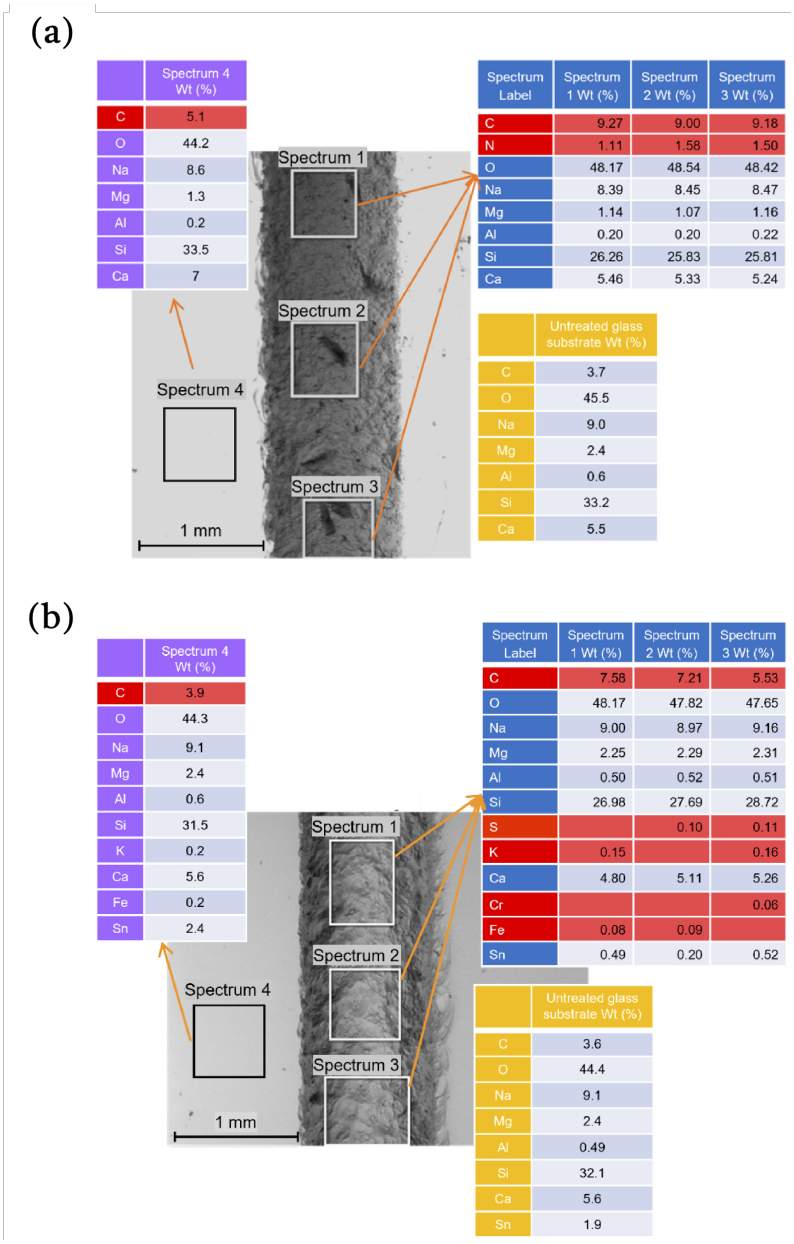

Figure 5.8: EDX spectra of the channel surface fabricated by (a) SLIPAA and (b) LIPAA after 30 laser passes. The chemical analysis was determined in the bottom of the channel and on the glass substrate. The differences on the chemical composition between the processed area and the glass without treatment are highlighted in red.

5.3.3 Versatility of the SLIPAA technique

The structures fabricated thus far were produced without the need for laser refocusing throughout the entire process, with the objective of evaluating the capabilities of the SLIPAA

technique in its most fundamental form. The results, though straightforward, were remarkable, achieving channels with a cross-sectional area of 1000 x 1400 μm² after 30 passes.

However, a notable challenge encountered in SLIPAA stems from the obstruction of the laser beam due to debris generated during ablation and the redistribution of material caused by bubbles. Nevertheless, optimization of the underwater laser ablation process can be achieved by controlling both the water flow rate and its direction (Charee et al., 2015; Kruusing, 2004). Additionally, by incorporating adjustments to the focus on the metallic target, the overall performance of the SLIPAA process can be enhanced, leading to the fabrication of deeper channels with reduced material redeposition.

Hence, apart from adjusting the number of laser passes and the laser parameters, controlling the depth of the structures can be achieved by repositioning the focal spot on the target and introducing flowing water during fabrication, to dissipate the debris. Moreover, this method is not restricted to channel production but extends to crafting structures with diverse geometries. To illustrate the versatility of this technique, Figure 5.9 displays a set of wells and structures made on soda-lime glass substrates, to be used as microreactors. Figure 5.9a showcases a top view of a 3×5 matrix of 3 mm diameter wells, while Figure 5.9b presents wells ranging from 4.14 mm to 4.02 mm in depth. Additionally, Figure 5.9c exhibits a microCT image of an array of 1 mm depth wells.

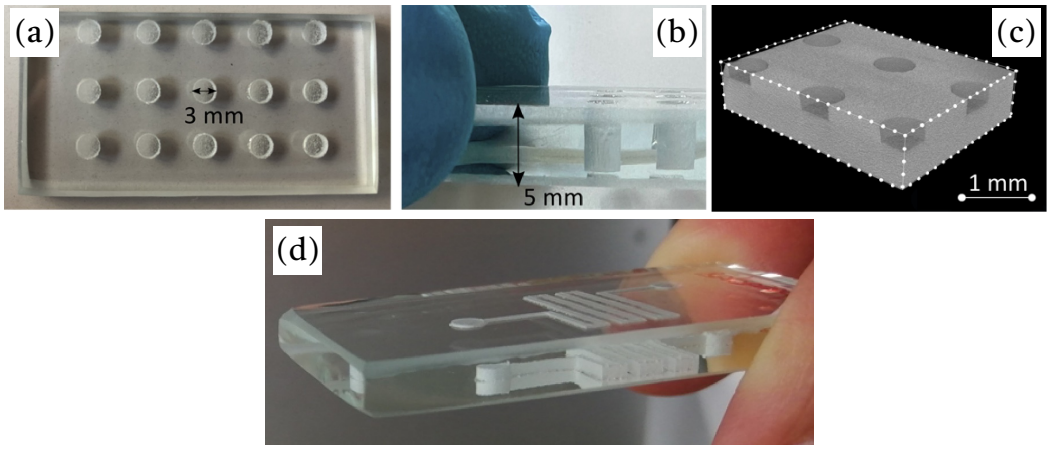

Figure 5.9: Fabrication of wells with SLIPAA. a) Top view of the 3×5 matrix of wells engraved inside a commercial soda-lime glass. b) Image showing the depth of the wells where the maximal value achieved is over 4 mm. c) MicroCT image of 1 mm deep wells with a diameter of 3 mm. A good agreement between the designed diameters in CAD and the fabricated wells is achieved. Processing parameters: wavelength 1064 nm, repetition rate 10 kHz, beam scanning speed 200 mm/s. In a) and b) the laser beam was refocused on the channel bottom surface to continue the ablation. The wells shown were obtained after 50 laser passes, where flowing water was used every 5 laser passes to carry away the debris generated during the process. In c) the focal position was fixed during the manufacturing process. The scalebar denotes the distance between any two points in the 3D image. d) Fluidic chip manufactured by SLIPAA. On the upper side of the glass one can see the reflected image of the chip. Processing parameters: wavelength 1064 nm, fluence 78.3 J/cm², repetition rate 10 kHz, beam scanning speed 200 mm/s, 10 laser passes.

For the fabrication of the wells depicted in Figure 5.9a,b, a carefully controlled water jet was intermittently applied between the metallic target and the substrate every 5 laser passes. This jet effectively removes debris generated during SLIPAA processing, which might otherwise persist due to water movement caused by shock waves. During this process, meticulous attention is required to prevent unintended substrate displacement and the entrapment of air bubbles within the structures. The pulsed water flow was administered manually. Furthermore, the laser beam is refocused by 40 μm on the metal foil every 10 laser passes to ensure consistent ablation efficiency. The processing time for each of the wells depicted in the figure is approximately 4 minutes. Wells serve various purposes in fluidic and microfluidics platforms, such as serving as inlets, outlets, storage units, and trapping components. In addition to channels and wells, SLIPAA can generate other configurations as defined by CAD design. Figure 5.9d illustrates a fluidic chip comprising 1 mm deep channels and wells.

5.4 CONCLUSIONS

A new technique using a nanosecond laser source for processing structures with different geometries in soda-lime glass substrates with dimensions in the millimetre range and vertical sidewalls is proposed. The technique consists of a subaquatic LIPAA process (SLIPAA), where the metallic target and the substrate are separated by a layer of water. This layer helps to confine the plasma generated over the target and to improve the material removal from the glass. The combination of the mechanical shock waves generated by the laser target irradiation, the plasma and the cavitation bubbles are responsible for the glass ablation.

By this method, rectangular shaped channels with a variety of dimensions and excellent quality straight edges can be obtained when a minimum of 10 laser scans are applied. The highest depth mean value has been obtained for 30 laser passes, corresponding to 1385.56 μm, and achieving channels with vertical sidewalls. While the depth was found to decrease with the laser repetition rate, the roughness of the bottom of the channels increases with higher repetition rate. There is no upper limit on the width of the channels, which can be selected by varying the number of parallel laser scans. Regarding minimum achievable width, good-quality channels of 300 μm width and aspect ratio of 4.53 were manufactured. To demonstrate more clearly the potential of the technique, a comparative study between SLIPAA and LIPAA is also shown. In both cases, the depth of the structures increases with the number of laser repetitions, achieving its maximum value for 30 passes. However, a significant difference in mean channel depth is observed with LIPAA, where the highest value achieved is 662.92 μm.

Moreover, EDX analysis on samples fabricated with SLIPAA and LIPAA revealed that transference of impurities from the metallic target to the channels surface is observed, however this transfer is much less significant in the case of SLIPAA. Moreover, SEM examination of the samples exposed less evidence of debris on both the bottom of the samples and the substrate along the edges of the channels when using SLIPAA compared to the manufacture of the

structures with LIPAA. Deeper structures are obtained with multiple laser scans by incorporating a water flow and continuously readjusting the laser beam focus onto the metallic target. The technique presented here is not limited to the manufacturing of channels, allowing to obtain structures with different geometries overcoming the typical depth limitations of laser-fabricated structures on glass. In particular, wells of 4.14 mm deep were fabricated in 5 mm thick soda-lime substrates. Our findings indicate that SLIPAA can become an exceptionally effective method for laser processing applications that require significant material removal.

6. STEREOLITHOGRAPHYAS KEY TECHNOLOGY FOR MANUFACTURING MICROFLUIDIC DEVICES

This chapter is a partial reprint of:

Bastián Carnero[a], Carmen Bao-Varela[a], Ana Isabel Gómez-Varela[a], Ezequiel Álvarez[b,c] and María Teresa Flores-Arias[a,*], *Microfluidic devices manufacturing with a stereolithographic printer for biological applications*, Materials Science and Engineering: *C* (2021), DOI: 10.1016/j.msec.2021.112388

[a]Photonics4Life research group, Departamento de Física Aplicada, Facultade de Física and Facultade de Óptica e Optometría, Universidade de Santiago de Compostela, Campus Vida, Santiago de Compostela, 15782, Spain

[b]Cardiology Group, Health Research Institute of Santiago de Compostela (IDIS), University Hospital of Santiago de Compostela (SERGAS), Trav. Choupana s/n, Santiago de Compostela, 15706 Spain, and Centro de Investigacion Biomedica en Red de Enfermedades Cardiovasculares (CIBERCV), Madrid, Spain

[c]Department of Pharmacology, Pharmacy and Pharmaceutical Technology, Universidade de Santiago de Compostela, Santiago de Compostela, 15782, Spain

and

Bastián Carnero[a,b], Carmen Bao-Varela[a], Ana Isabel Gómez-Varela[a], and María Teresa Flores-Arias[a,*], *Internal microchannel manufacturing using Stereolithographic 3D printing*, Trends and Opportunities of Rapid Prototyping Technologies (2022), DOI: 0.5772/intechopen.102751

[a]Photonics4Life research group, Departamento de Física Aplicada, Facultade de Física and Facultade de Óptica e Optometría, Universidade de Santiago de Compostela, Campus Vida, Santiago de Compostela, 15782, Spain

[b]BFlow S.L., Edificio Emprendia, Campus Vida, Santiago de Compostela, 15782, Spain

6.1 INTRODUCTION

3D printing has evolved to become one of the most revolutionary manufacturing techniques. The capacity to directly and consistently produce highly detailed structures without involving many of the usual steps or equipment of conventional technologies has democratized the access to the manufacturing process to a vast quantity of industries, researchers and individuals (Bull & Groves, 2009; Shallan et al., 2014a). The microfluidics field is no stranger to the impact that 3D printing can have in its microfabrication procedures (Y. Y. Chen et al., 2020; Rupal et al., 2019b), mainly dominated by techniques as photolithography or reactive ion etching (RIE), that usually require the use of very specific facilities, produce a highly polluting chemical waste (R. H. Liu et al., 2000a; Nabesawa et al., 2008) and only allow 2D surface structuring. In this field, one of the main goals is to fabricate complex devices that mimic, for instance, different structures of the human body, kown as organ-on-a-chip (OOC), by combining superficial (inward and outward) and internal channels with several kind of pillars (Carrell et al., 2020a; C. Liu et al., 2012). This is where 3D printing stands out as it makes possible, with a user-friendly equipment and software, the realization of 3D structures in volume with great structural complexity.

As we mentioned in Introduction 2.2.3.5, two 3D printing technologies can be highlighted from the rest: Fused Deposition Modelling (FDM) and Stereolithography (SLA). In this thesis we will focus in SLA printers, which utilize the photopolymerization principle to perform a layer-by-layer cure of a liquid resin deposited in a tank, forming the desired structure. Once the light source (generally a laser) with the smallest possible spot and the appropriate resin have been selected, surface quality and the agreement between the designed dimension and the obtained ones, can be improved by controlling the piece orientation during the fabrication process. There are infinite ways to orient a piece to be printed, so a detailed study of the influence of the slope of the faces in the photopolymerization process is interesting to know the best configurations to fabricate a device. The key idea to understand this influence is that a rotation in the piece will modify the way in which the printer slices the original object (Heidt, Rogosic, Bonni, Passariello-Jansen, Dimech, Lowdon, Arreguin-Campos, Steen Redeker, Eersels, Diliën, van Grinsven, et al., 2020). Therefore, objects with great surface detail can be printed at an angle that favours the precise curing of their constituent layers. The same applies to internal channels, where a suitable angle could help the removal of uncured resin from inside, helping to avoid obstructions.

In addition to the high superficial quality that SLA printers offer, biocompatible materials that can be printed with this equipment have been developed, increasing the number of potential biological applications. In this field, researchers have printed a bioresorbable airway splint (Zopf et al., 2013), a H_2O_2 and glucose detection device (Comina et al., 2014) or 3D scaffolds (Barron et al., 2004) and platforms (Alapan et al., 2015) for cell seeding. All these examples

show the potential of SLA printers for the fabrication of complex microfluidic devices for biological usage, and make them a good choice for researchers focused on 3D printing of accurate, reliable, and biologically solvent microfluidic devices (Au et al., 2014; Murphy & Atala, 2014).

In this thesis we present a study of microfluidic devices that can be fabricated by Low Force Stereolithography (LFS) technology (see Materials and Methods 4.1.5.2) to be used as organ-on-a-chip (OOC) or as master to replicate OOC in other biocompatible material. This technique improves the precision and accuracy of the OOC fabricated, since a more uniformity deposition of laser energy across the built-in platform is obtained.

A complete and detailed analysis of the printer performance is carried out by testing the printing results of seven compatible resins (three of them being biocompatible). Printing time and the light transmittance of each of the resins are determined due to their relevance to the fabrication process. The formation of internal channels is assessed since LFS stands out over photolithography, RIE (allowing the formation of internal cavities of a vast quantity of orientations and geometries) and other SLA printers. The range of dimension of different kind of channels and pillars that can be accurately fabricated is evaluated. Furthermore, the finishing and precision of inward and outward superficial channels and pillars are analysed at the maximum resolution allowed for each resin, according to the supplier instructions. The replicability of all the resins by soft lithography of PDMS is also studied since the printed structures are of great interest for the manufacture of masters (Chan et al., 2015a; Hwang et al., 2015a). For reasons of completeness, the biocompatibility of the selected resins will be analysed in Section 8.1.

6.2 MATERIALS AND METHODS

6.2.1 3D Printing

In this work, a Form 3B SLA was selected to manufacture the structures of study. As we mentioned, this printer offers a new feature over other stereolithographic printers by two aspects: allowing the printing of biocompatible resins and employing the previously introduced technology, LFS.

To analyse the maximum resolution that can be reached for each of the resins, plates of 3x4 cm with a series of channels and pillars on their surface were designed using Fusion 360 software (Figure 6.1a), introduced in Materials and Methods 4.1.7.1. Channels were printed outwards and inwards from the surface with two different profiles: rectangular (from 50 µm to 1000 µm width) and semicircular (from 30 µm to 750 µm radius). Pillars (outward) and wells (inward) were also printed (from 100 µm to 1600 µm height). Each plate was printed with three different orientations (see Figure 6.1b) respect to the base of the printing arm: at 0º (Figure 6.1c), at 45º with channels parallel to the y axis (Figure 6.1d) and at 45º with channels contained

in the XZ plane (Figure 6.1e). We will call these orientations A, B and C, respectively, to facilitate further discussion. To study the influence of the printing angle on the ability to create internal channels, a quarter annulus crossed by seven internal channels oriented at 0º, 15º, 30º, 45º, 60º, 75º and 90º was printed (Figure 6.1f). This study was performed four times for each resin selected, also varying the diameter of the channels from 250 µm to 1500 µm. Last, round discs with 3.5 cm of diameter and 5 mm of height (Figure 6.1g) were printed to perform optical and further biocompatibility studies on the surface of resins. A two-step polishing process was carried out after fabrication to one or both faces of the discs in order to evaluate the difference in the transmission spectra and the improvement of the optical quality, employing a Logitech PM 2A polisher. In the first step, an iron disc plate and an abrasive solution of Al_2O_3 were used to perform the roughing. The second step consisted on optical polishing of the material combining an expanded polyurethane disc with silica solution.

As we mentioned in Materials and Methods 4.1.5.2 chapter, it is necessary to postcure the pieces in a two-step process. First, the piece is washed in isopropanol (IPA) inside the Form Wash tank during the corresponding time recommended by the supplier for each resin. Secondly, the pieces are left to dry and introduced into the UV Form Cure chamber. This chamber is provided with LEDs emitting at 405 nm and allows also to control the temperature. Washing times, and curing temperatures rand times are presented in Table 4.3.

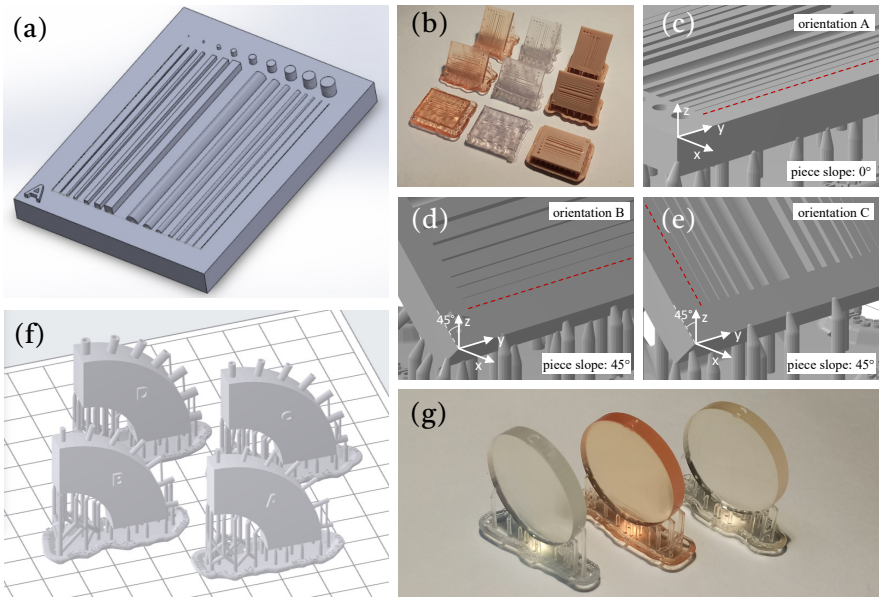

Figure 6.1: 3D pieces printed in this work. a) CAD design of the plates with the outward channels and pillars. b) Picture of three sets of plates with the inward channels and pillars printed in different orientations for three kinds of resins (from left to right: Amber, Flexible and Model, see section 2.2). Images of CAD corresponding to the different printing orientations of the plates: at c) 0º (orientation A), d) at 45º with channels parallel to the y axis (orientation B), and e) at 45º with channels contained in the XZ plane (orientation C). f) Quarter annulus designed to analyse the capacity of the printer to manufacture internal channels. g) Picture of round discs printed for biocompatibility and optical quality studies. Notice the presence of typical scaffolding to support the structures.

Seven stereolithography resins from Formlabs were analysed: Clear V4, Dental LT V1, Tough 2000 V1, BioMed Amber V1, Flexible 80A V1, Elastic 50A V1 and Model V2. One of the most critical parameters when studying the achievable resolution and surface finishing of the prints is the layer height (z-step) that every resin admits. In order to achieve the optimal performance in each case, the pieces were always printed with the maximum resolution (minimum z-step) available for each of the resins. Thereby, the theorical Minimum Thickness of the Layer (MTL) was 25 μm for Clear and Model resins; 50 μm for Tough, Amber and Flexible; and 100 μm for Elastic and Dental.

6.2.2 Soft lithography of PDMS

The PDMS was prepared from Sylgard 184 elastomer (Dow Chemical Company, Midland, Michigan) and selected as the polymer to carry out the replication studies given its optical transparency, permeability to gases, elasticity, and biocompatibility. PDMS is one of the most used polymers to fabricate microfluidic devices (McDonald et al., 2000b; Raj M & Chakraborty, 2020b), allowing the cells to have a suitable environment for experimentation, and was synthesized by mixing the monomer and the curing agent in a ratio 10:1 (according to the supplier specifications). The mixture was then deposited on the printed plates inside a Petri dish, forming a small silicone sheet and introduced in a vacuum chamber 40 min at 400 mbar to remove bubbles produced during the mixing process. Finally, the Petri dish with the degassed PDMS was cured in an oven for 12h at 60ºC.

6.2.3 Data collection

Confocal images of the microchannels manufactured on the plates and superficial roughness measurements were obtained using a 3D optical profilometer S neox. A Nikon MM-400 (Materials and Methods 4.1.6.1) metallurgic microscope was used when the depth of the channel was too large for confocal inspection, as is the case of the manufactured internal channels. In this case, the channels were illuminated in a transmission light configuration that allowed us to measure the lumen of each one. Images were acquired using a LU Plan Fluor objective with a 5× magnification and a CCD camera Nikon DS-FI2. Five measures were performed for each channel, obtaining a geometric mean and a standard deviation. Images of longitudinal sections of the microchannel internal surfaces were obtained with a 3D optical profilometer S neox (Materials and Methods 4.1.6.3.1) working in confocal mode.

To measure the transmission spectra of the transparent resins, a PerkinElmer Lamb25 (Materials and Methods 4.1.6.6) spectrometer was used. This spectrometer performed a measurement of the transmittance of the disk between 190 nm and 1100 nm, in 1 nm intervals. Furthermore, a Field Emission Scanning Electron Microscope was used to make the SEM images presented in the work. The possible transference of material from the master to the replica was evaluated by Energy Dispersive X-Ray (EDX).

6.3 RESULTS AND DISCUSSION

6.3.1 Printing time

To evaluate the feasibility of implementing this technique in a mass production system, the printing time of the different resins was compared, since it can be an important parameter to take into account if this technique wants to be exploited in the industry. The time employed for printing the same set of pieces (consisted of the three orientation study plates (Figure 6.1b) and the four internal channels study annulus (Figure 6.1f)) was measured for each resin, facilitating direct comparison. Even though the pieces were the same, the printer used a different volume for each resin. Each piece was printed with the MTL allowed for the selected resin. Table 6.1: Printing time, volume and MTL of the resins used in this study.

Table 6.1 shows the values described above as well as the ratio between the volume (V) of resin used and the printing time (t).

Priting Resin	Time (min)	Volume (ml)	V/t (µl/min)	MTL
Model	829	37	45	25
Clear	731	42	57	25
Tough	600	42	70	50
Elastic 5	585	42	72	100
Flexible	561	43	77	50
Amber	360	38	106	50
Dental LT	163	37	227	100

Table 6.1: Printing time, volume and MTL of the resins used in this study.

Dental resin proves to be the fastest printing, with a V/t ratio of 227 µl/min, followed by Amber resin, with a ratio of 106 µl/min. It can be observed that the resolution is not decisive in the printing time since resins with a lower MTL can be printed in less time than resins with a higher MTL. This occurs with Flexible and Amber resins, which despite having both a resolution of 50 µm, take less time to print the same piece than in the case of Tough, with a resolution of 100 µm. However, Model and Clear resins, with a resolution of 25 µm, take the longest time to print.

6.3.2 Transmission spectra of the resins

The optical transparency is another important property to consider when selecting a particular resin for the fabrication of microfluidic devices that are going to be used in experiment that need to be inspected by optical techniques. Transparency allows the possibility of using optical images systems for inspection in different applications, for example, bright field or fluorescence images (Urrios et al., 2016).

The discs printed for the transparency studies were inserted in the spectrometer to measure the transmission spectra of the five studied transparent resins: Amber, Clear, Dental, Flexible and Elastic. A polishing treatment was carried out on the transparent resins that allowed it (Clear, Dental and Amber), to analyse its influence on the optical quality. Elastic and Flexible resin discs were proven to be very difficult to polish, as they showed great deformability. The polishing of the discs has a great influence on its surface roughness, that in this work was measured using the arithmetical mean roughness of the surface (S_a), according to ISO 25178. For this purpose, areas of equal size (1 mm^2) were analyzed by confocal microscopy before and after being polished. The results showed that S_a went from 1.977 ± 0.187 µm to 0.239 ± 0.018 µm in the the case of Amber resin; from 1.281 ± 0.306 µm to 0.214 ± 0.013 µm in the case of Clear resin, and from 4.296 ± 1.047 µm to 0.242 ± 0.028 µm in the case of Dental resin.

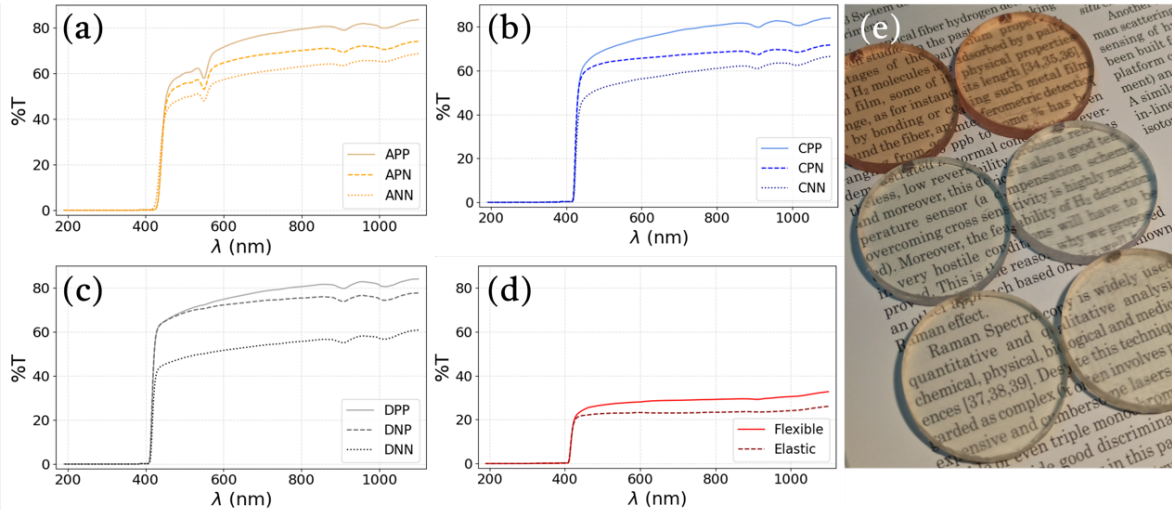

Figure 6.2: Transmittance curves obtained for the resins: a) Amber, b) Clear, c) Dental, d) Flexible and Elastic. e) Visual inspection of the transparency achieved by the discs of the three resins with both (left) and neither (right) face polished. NN: Neither face polished (solid line); NP: a face polished (dashed line); and PP: both faces polished (dotted line).

Figure 6.2a-c show the transmittance curves obtained for discs with different polished faces. All the resins show a total absorption in the ultraviolet wavelength range. The transmittance increases as the wavelength increases from visible to near infrared wavelength range (400-1100 nm). In the case of Amber (Figure 6.2a), a peak of absorption appears at 550 nm. For the Clear (Figure 6.2b) and Dental (Figure 6.2c) resins two absorption peaks appear at 900 nm and 1010 nm. The total transmittance experiments an increase of around 20% when both faces are polished, with the three resins reaching a very similar transmittance for this case. Dental resin shows the greatest transmittance in the visible range (where excitation wavelengths are normally found in fluorescence microscopy), reaching 60% for 430 nm and achieving up to 80% for 750 nm. Otherwise, Amber and Clear resins show a 60% transmittance for wavelengths around 465 nm, but both reach 80% for 750 nm. As a great absorption is not observed near the excitation wavelengths of fluorescence imaging systems, typically located around 480 nm,

these resins are suitable to be used with them. In the near-infrared range, the transmittance is very high and never lower than 80% once both sides are polished.

In the case of Flexible and Elastic resins (Figure 6.2d), the measured transmittance was low, not reaching 40% for the visible spectrum. Moreover, transmittance cannot be improved by an easy polishing process due to their elasticity. This makes their use undesirable as resins for making microfluidics devices that need optical inspection.

6.3.3 Superficial structures

Superficial channels are the basic element in essentially all microfluidics devices. They are responsible for guiding the fluid through the valves, mixers or pumps that make up the system and correct operation will depend on their quality. Thereby, a suitable channel for microfluidics will have a regular and continuous profile, accurate size and must be manufactured in the most suitable material depending on its application. The same occurs for wells, that can be used as repositories, pillars, with application in circulating tumour cell capturing (Nieto et al., 2015b) or act as autoalignment connectors (see Materials and Methods 4.2.1), of great interest when it comes to forming internal cavities in the devices.

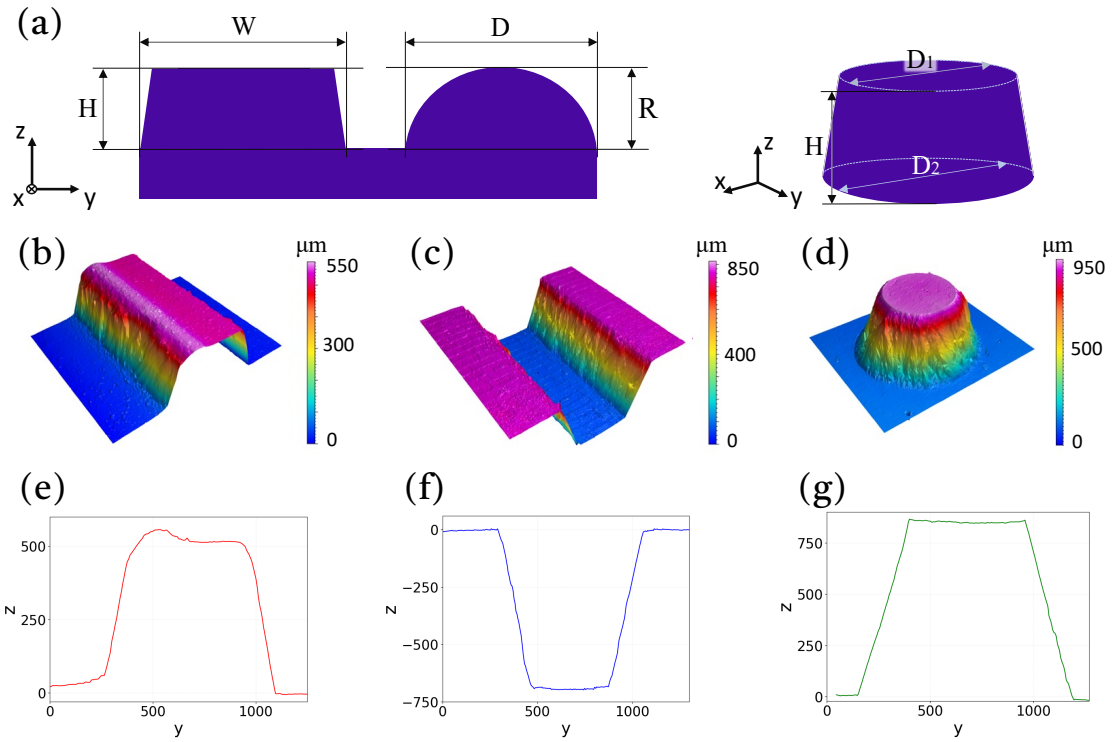

Figure 6.3: Typical parameters of a) superficial channels and pillars. Design of rectangular channels verify H=W, semicircular channels verify R=D/2 and pillars D_1=D_2=H. Confocal images for illustration of b) outward channel fabricated with the Model resin and e) its corresponding profile, c) inward channel fabricated with the Clear resin and f) its corresponding profile, and d) outward pillar fabricated with the Dental resin and g) its corresponding profile. All the pictures were taken with a 10× confocal microscope objective.

A study of the superficial performance of structures was conducted in this work. For this, the topology of the plates shown in Figure 6.1b was used. These plates have rectangular and semicircular channels printed (outwards and inwards) on their surface. The main design parameters for these elements (Figure 6.3a) are: i) height (H) and width (W) for rectangular channels (verifying H=W); ii) radius (R) and diameter (D) for semicircular channels (verifying 2R=D); and iii) top diameter (D_1), bottom diameter (D_2) and height (H) for pillars (verifying D_1=D_2=H).

As can be seen in Figure 6.3, the printed channels show a trapezoidal profile, despite being designed with a CAD rectangular profile. This result is observed both in the outward (Figure 6.3b) and inward (Figure 6.3c) channels and even in the pillars (Figure 6.3d) for all the resins used. To facilitate the interpretation of the data, aspect ratios of the superficial structures printed in Clear resin are plotted in Figure 6.4. The chosen ratios were H/W for rectangular channels, 2R/D for semicircular channels and ($2D_2$-D_1)/H for pillars. All the channels and pillars were designed with an aspect ratio equal to 1. The deviation from 1 is an indicative of the extent that the structures differ from the original design. In Figure 6.4, each subfigure presents the aspect ratios corresponding to the three orientations indicated in Figure 6.1c-e: A (red dot), B (blue star) and C (green square).

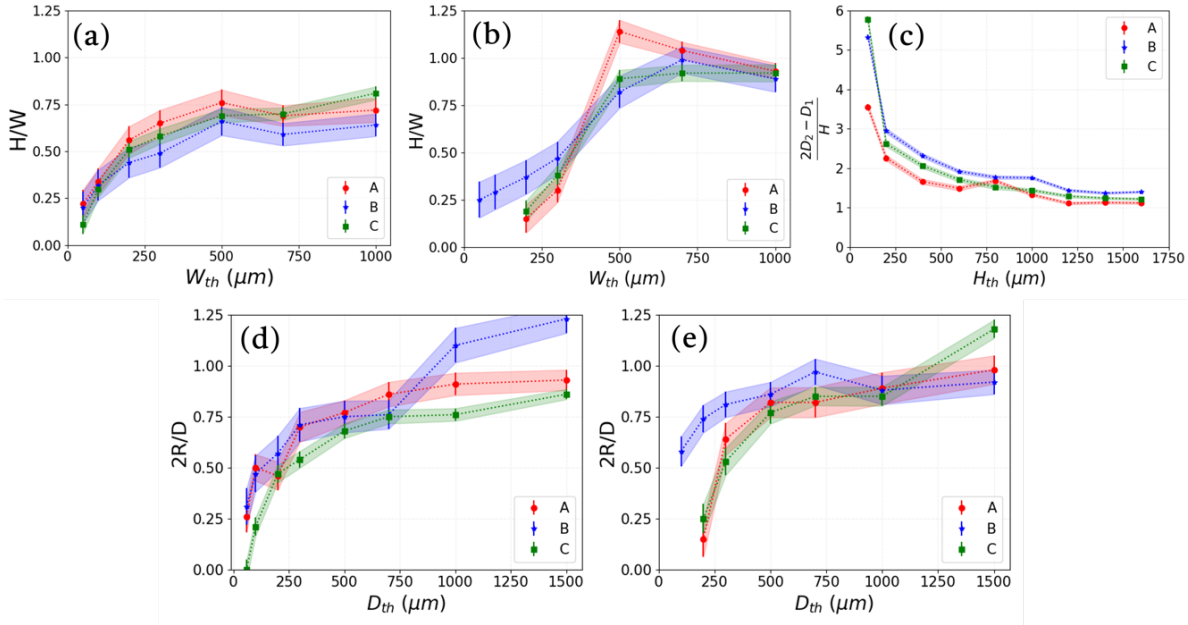

Figure 6.4: Aspect ratios obtained for the surface structures printed in Clear resin corresponding to: (a) outward and (b) inward rectangular channels; (c) outward pillars; (d) outward and (e) inward semicircular channels. Structures were designed on the surface of plates printed at: orientation A (red dot); orientation B (blue star) and orientation C (green square), as shown in Figure 6.1c-e. W_{th}, H_{th} and D_{th} denote the theoretical weight, height, and diameter, respectively.

Two printing regimes were observed for outward rectangular channels (Figure 6.4a). First, small channels (0-500 μm) show an aspect ratio that increases with the theoretical width. For

these cases, the ratio value is low and does not even reach 0.75 until 500 μm, where orientations A and B obtain their best performance. In this case, for orientation A, with an aspect ratio of 0.75, the printing accuracy (defined as the percentage ratio between the printed result and the designed structure size) is 101% in height and 153% in width. Until now, orientation A showed the higher aspect ratio, followed by C and B (0.69 and 0.66 for 500 μm, respectively), but this scenario changes for larger channels (500-1000 μm), where the observed tendency differs: orientation A stabilizes around 0.70 aspect ratio, while C reaches to 0.8. Orientation B gets its best result for 500 μm and shows the lowest aspect ratio (0.63) of the three printing orientations for a theoretical width of 1000 μm. As observed, the rectangular outward channels did not reach an aspect ratio of 1, indicating that no channel as high as wide was printed.

For inward rectangular channels, two regimes can be also identified (Figure 6.4b). For small channels (0-500 μm), the aspect ratio cannot exceed 0.5, although it continues increasing as the theoretical width does. In this regime, orientation B provides a higher ratio (0.47 for 300 μm), followed by C and A (0.37 and 0.30 for 300 μm, respectively), in contrast to the previous case. For larger channels (500-1000 μm), a performance gap is observed, with all aspect ratios being above 0.75 showing a decreasing trend especially pronounced for orientation A. For channels with a theoretical width of 700 μm, the three orientations practically reach a ratio of 1. Orientation B stands out in this case, reaching a 0.99 aspect ratio and a printing accuracy of 95% in height and 96% in width. For this reason, inward channels represent an improvement in the global aspect ratio for rectangular channels, especially in the range between 700 μm and 1000 μm of width, were they all are near to 1.

For outward pillars, a bottom diameter greater than the top diameter is observed in all cases (Figure 6.4c), causing the aspect ratio to be greater than 1 for all the theoretical heights. This phenomenon is more pronounced for small heights (0-500 μm), in which the profile of the pillar is smoothed, reaching a hemisphere shape (in a limit case), with an aspect ratio between 2 and 6. For larger heights (500-1600 μm), all ratios remain between 1 and 2, showing orientation A the best result. A ratio of 1.12 and a printing accuracy of 104% in height, 110% in bottom diameter and 102% in top diameter was observed for this orientation and a theoretical height of 1600 μm, followed by C and B (1.22 and 1.40, respectively). Wells (inward pillars) did not form correctly, so that the correct identification and measurement of their main parameters could not be performed. The concrete details of this phenomenon will be discussed later.

For outward semicircular channels, the observed trend is unique since the aspect ratio grows as the theoretical diameter increases for all studied orientations (Figure 6.4d). Anyway, two different trends can be described depending on whether the aspect ratio deviates more than 0.25 from 1, and therefore defining two regimes. For small diameters (0-500 μm), channels are below an aspect ratio of 0.75, except for the orientation A, which manages to reach 0.76 for 500 μm. For larger diameters (500-1500 μm), channels are formed with an aspect ratio between 0.75 and

1.25. Orientation A stands out for diameters of 1500 µm, reaching a ratio 0.93 and a printing accuracy of 100% in height and 107% in diameter.

Finally, for inward semicircular channels (Figure 6.4e), no orientation exceeds an aspect ratio of 0.75 before 500 µm in diameter, except orientation B for 300 µm. For diameters greater than 500 µm, the ratio tendency changes, going from increasing for all the orientations to stabilizing around to 0.85 for B, increasing slightly for A and stabilizing before growing for C. The closest ratio to 1 is measured for orientation A at 1500 µm in diameter, achieving a value of 0.98 and a printing precision of 95% in height and 98% in diameter.

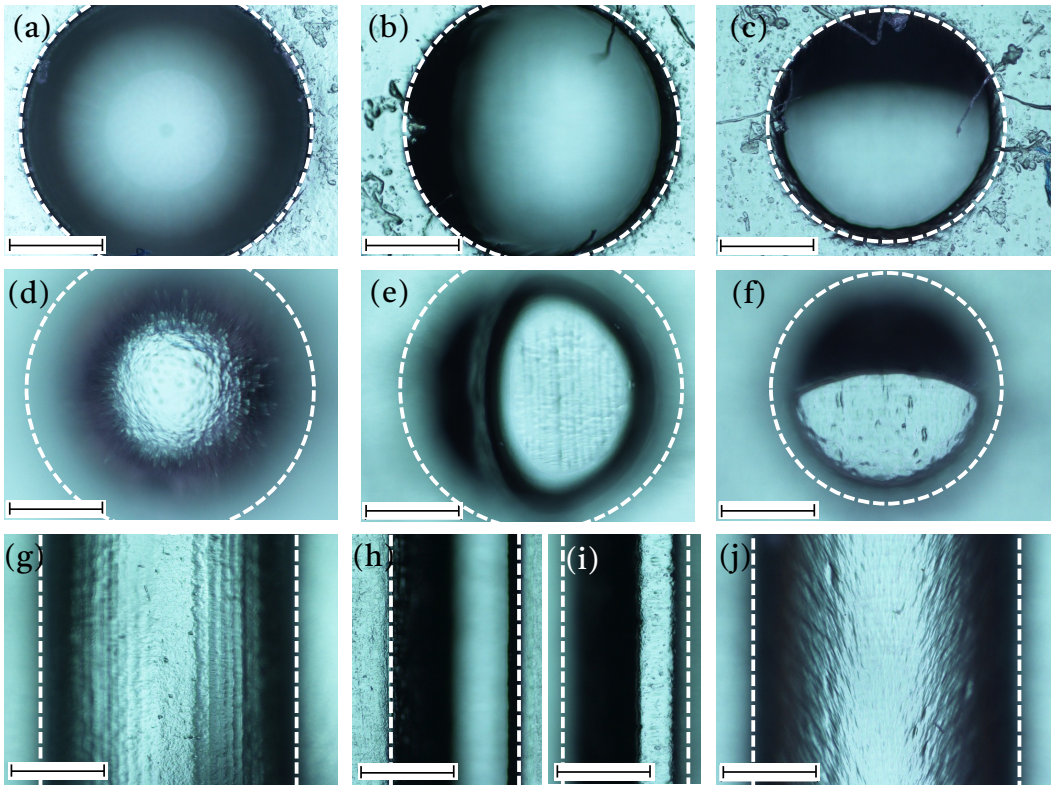

Figure 6.5: Optical microscope images of inward structures printed for Clear resin. Pictures of top and bottom (respectively) surfaces of the wells printed at: a), d) orientation A; b), e) orientation B; and c), f) orientation C. g) Picture of the bottom surface of semicircular channel printed at orientation A. Picture of the h) top and i) bottom surfaces of rectangular channel printed at orientation B. j) Picture of the bottom surface of semicircular channel printed at orientation C. All the pictures were taken with a 5× microscope objective. Scale bar 500 µm.

However, no information about the appearance of the surfaces can be extrapolated from the aspect ratios, since they only offer information about the deviation from the original rectangular, semicircular or cylindrical designed profile. Figure 6.5 shows optical microscope images of the inward channels and wells printed for Clear resin at A (left), B (middle) and C (right) orientations. Although the top diameters of the wells are formed correctly (Figure 6.5a-c), maintaining a constant radius with a regular border for all the orientations, the same does

not applies to their bottom diameter (Figure 6.5d-f). The removal of uncured resin did not occur properly during the printing process, promoting its accumulation inside the wells and causing that the cylindrical profile of the structures could not be measured (as mentioned above). This effect explains that the border of the bottom diameter of the well printed at orientation A cannot be identified (Figure 6.5d), since the uncured resin was homogeneously deposited, curving the walls. This phenomenon is even more noticeable for wells printed with an inclination respect to the base since the resin can be seen accumulated on the side (Figure 6.5e) or top (Figure 6.5f) wall of the wells.

This unwanted accumulation of resin can also be observed for inward channels, although its impact can be minimized by choosing a suitable inclination. In the first place, for pieces printed with orientation A, the accumulation of resin occurs homogeneously in the walls (Figure 6.5g), although its presence does not significantly affect the profile given the original curved shape (for semicircular channels). On the other hand, for channels printed with orientation B, the uncured resin produces a large profile loss from the surface (Figure 6.5h) to the bottom (Figure 6.5i) of rectangular channels, since the resin is deposited all along of one of the walls. This orientation produces the largest deviations from an ideal channel, so it is not recommendable to use it for inward channels, whether rectangular or semicircular. Finally, orientation C stands out as the most advisable orientation, since the accumulation of the resin will only occur at the end of the channel, leaving the intermediate region free of obstructions and maintaining the appropriate profile (Figure 6.5j) to the extent indicated in Figure 6.4b and e.

In summary, the inclination has demonstrated to be a critical parameter for properly form small and inward structures when evacuating the resin, whose viscosity helps it to accumulate in regions where a sudden change in profile takes place. The evacuation is largely determined by gravity, and a correct orientation (with channels perpendicular to the base) will favour resin to accumulate in areas whose profile is not so valuable, such as the end of the channels, in which microfluidic connectors are generally placed.

Figure 6.6 shows FESEM images of selected outward channels printed in different resins at orientation C. Clear resin allows the formation of outward channels with a suitable topology for microfluidic applications: the edges of the channels are well defined (Figure 6.6a and b), the surface is smooth (S_a= 1.281 ± 0.306 μm) (Figure 6.6c), and the working range adequately goes from hundreds of microns to several millimetres (see Figure 6.6a and d). Channels printed on the Model resin also seem suitable for use in microfluidics (Figure 6.6d), although its surface finishing is slightly less smooth (S_a= 1.444 ± 0.247 μm) (Figure 6.6f) than that obtained for Clear resin. (Figure 6.6c), which may not be advisable for certain applications such as cell growth, where surface roughness is decisive (Aymerich et al., 2015). The same occurs if the channel is intended to replicate (main use of outward channels) using a transparent polymer, since this roughness can affect the subsequent optical inspection. Definitely, these two resins offer the best surface finishing and lowest roughness, which can be explained taking into

consideration the fact that they offer the lowest MTL of all studied resins (as indicated inTable 6.1): 25 µm.

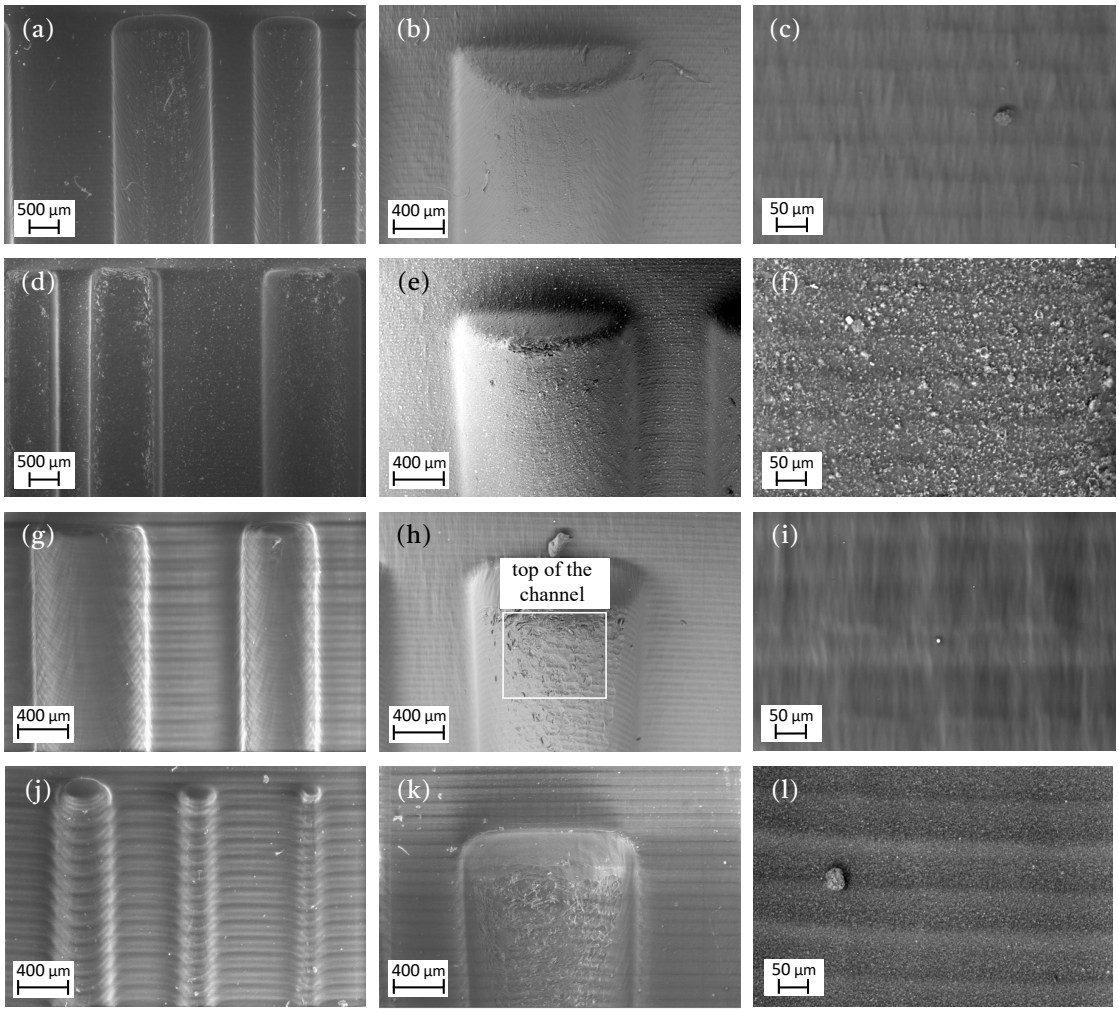

Figure 6.6: FESEM images of the 3D superficial outward channels printed in (a), (b), (c) Clear; (d), (e), (f) Model; (g), (h), (i) Amber and (j), (k), (l) Tough resin. Pictures were taken with the following microscope objectives: a) and d) 50×; b), e), g), h), j) and k) 100×; and c), f), i) and l) 500×.

For resins with a higher MLT, as Amber (S_a= 1.977 ± 0.187 µm) (Figure 6.6g-i) and Tough (S_a= 3.736 ± 0.713 µm) (Figure 6.6j-l) the z-step (50 µm) begins to be noticeable on their surface. This effect may not be very critical for channels that are large enough compared to the step (Figure 6.6g), but it can create wavy borders for channels with a diameter in the same order of magnitude (Figure 6.6j). The Amber resin also shows a high flaking in the top region of the channel, very pronounced at its end (Figure 6.6h). Certain irregularities can also be observed on the top region of channels printed in Tough resin (Figure 6.6k). Flexible resin, despite offering the same z-step of 50 microns and an intermediate roughness (S_a= 2.723 ± 0.239 µm), produces more bent channels than these two resins, producing even not straight channels for orientation A. This is due to its deformability, which makes it very vulnerable to the stresses

produced during printing process and translates into an inability to reach the goal accuracy of this study. Finally, Dental (S_a= 4.296 ± 1.047 μm) and Elastic (S_a= 8.280 ± 1.738 μm) resins, with a 100 μm z-step are limited from start to only form large channels since the step is very noticeable for structures under few hundred microns.

6.3.4 Internal channels

The manufacturing of internal channels with a continuous and unobstructed lumen is one of the main challenges for actual SLA printers, because of their many applications in microfluidics (Heidt, Rogosic, Bonni, Passariello-Jansen, Dimech, Lowdon, Arreguin-Campos, Steen Redeker, Eersels, Diliën, van Grinsven, et al., 2020; Moreno-Rivas et al., 2019b). The fabrication of cavities in a bulk with a proper lumen is a very difficult process, since the photopolymerization of each layer is sustained by the previous one, so the evacuation of the non-polymerised resin can be tedious (Carnero, Bao-Varela, et al., 2022).

In many cases, the goal of obtaining unobstructed channels goes against the need for the printer to introduce scaffolds in the largest cavities, causing that internal channel collapse if some supports are not used during the printing. In addition, the own resolution of the printer can act as a limiter for very small channels, which, a priori, would not pose a structural challenge. In order to properly establish the dimensional limit between small channels and large cavities and to study the dependence of the internal channel performance on the diameter and angle of the printer, quarter annulus crossed by internal channels (Figure 6.1f) were printed for each resin.

From the obtained results, three printing regimes can be defined. In the case of channels with small diameters (250 μm), no channel was fabricated for any resin at any angle, so no data can be presented. It can be concluded that, for these sizes, the formation of internal cavities in this range is not possible due to its small size, which prevents the correct evacuation of the resin. This implies that, the resolution for structures inside the printed piece is lower than the resolution for external ones, as structures of this size could be formed if they were made on the surface.

Next, for 500–1000 μm in diameter (medium diameters), channels begin to be formed (see Figure 6.7a,b) as will be detailed below. The bottom of these channels has been measured using the experimental configuration presented in Figure 6.9a. We defined the accuracy as the ratio between the printed and theoretical designed diameter, in percentage. The tendency observed is an increase of experimental diameters as the printing angle increases, for a theoretical fixed value. For channels of 500 μm in diameter (Figure 6.7b) Amber and Dental resins provide the best results, almost reaching a 100% accuracy for an angle of 90°. In addition, for angles greater than 60°, they are all above 80% accuracy, together with Model resin. For lower values of the angles, the channels are narrower than those designed and are more incomplete (longitudinally) as the angle decreases, so for 15°, only Amber Clear and Model

resins form channels and for 0°, none. Longitudinally, Clear and Dental only form complete channels for 90° while Amber resin enables the formation of complete channels for 60°, 75° and 90°. For other values, the channels are not completely formed, although the unobstructed length of the channel increases as the angle increases (Figure 6.9b).

When channels of 1000 μm in diameter (Figure 6.7b) are fabricated, the printing accuracy suffers a global increase, being always above 70% for every studied angle. As the angle increase, an improvement in the precision is observed, and from 45°, all resins show an accuracy of more than 80% (except for Model, which shows a more irregular trend). The best results are obtained for 90°, where all the resins are above 90%, being the Model resin the exception, reaching an 88%.

In the case of channels with 1500 μm in diameter (wide channels), an 85% on accuracy is achieved for all channels at every studied angle (Figure 6.7c). The length of the channels increases until they form completely (unobstructed) at 45° for Clear resin and at 15° for Amber and Dental resin. For greater angles, complete channels are formed for these resins. For these diameters, results are particularly suitable for angles greater than 60° degrees, where all resins show a printing accuracy greater than 95%, being the exception again the accuracy of Model resin, which is much closer to 90%. Therefore, internal channel with wide diameters allows to fabricate internal cavities for any angle and do not need scaffolding inside. Note that, in the case of the Tough and Model resin, the length of the channels cannot be evaluated by naked eye due to their opacity.

Channels fabricated at 45° and 500 μm in diameter were chosen for inspecting the internal surface of unobstructed channels. In particular, Tough, Clear and Model resins were selected to be analysed because of their different properties (z-step, biocompatibility, transparency…). Figure 6.8 shows confocal images of longitudinal sections of the channels, where it can be observed that semi-circular designed profile is properly translated to the printed pieces. By comparing the confocal images of the Tough (Figure 6.8a) vs. Clear (Figure 6.8b) and Model (Figure 6.8c) resins, a decrease of the surface waviness with the z-step is observed. The smoothest profile was achieved using the Model resin.

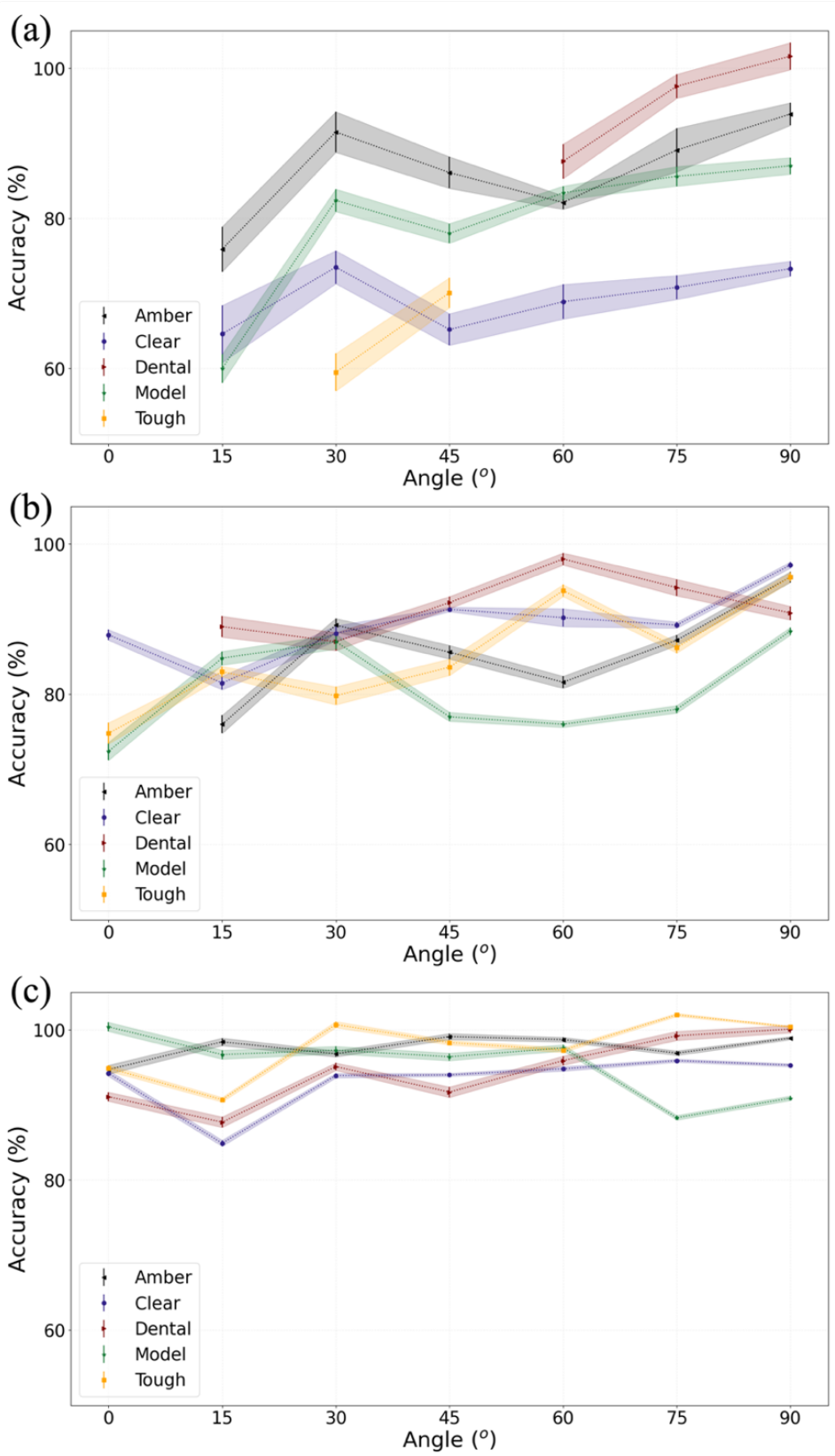

Figure 6.7: Accuracy of the printing for the internal channels with diameters of a) 500 µm, b) 1000 µm and c) 1500 µm in diameter, respectively. The error bars represent the standard deviation of the accuracies, and the area between the errors has been filled to facilitate the interpretation of the graphs.

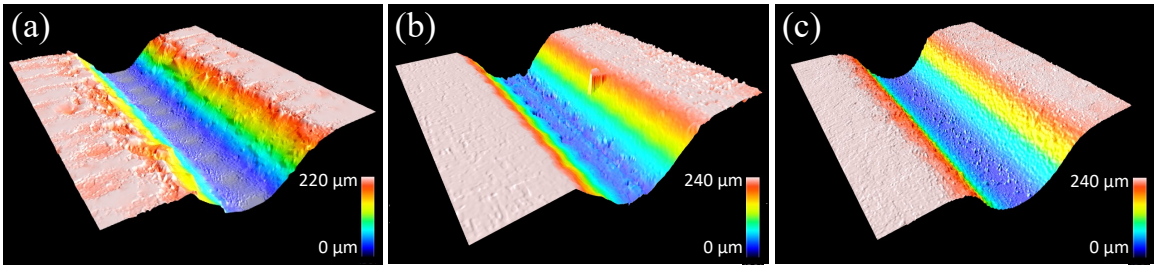

Figure 6.8: Confocal images of sections of channels designed with 500 µm in diameter and printed at 45° using: (a) Tough, (b) Clear and (c) Model resin.

From the previous analysis, and using the configuration presented in Figure 6.9a, we were able to analyse the influence of the angle of impression in preventing (Figure 6.9b) or favouring (Figure 6.9c,d) the formation of internal channels, so a larger angle (closer to 90°) is observed as the most suitable for channels to form properly and to have dimensions closer to those designed. The other key parameter found in this study is the diameter. As we have seen, a larger diameter allows results to be obtained with a higher resolution (Figure 6.9d). The fact that orientation and diameter are so critical in the manufacture of channels is rooted in the way SLA printers operate and is intimately related to the evacuation of uncured resin, which will be more likely to occur the larger the channel and the more perpendicular the channel to the base (so gravity can enhance evacuation).

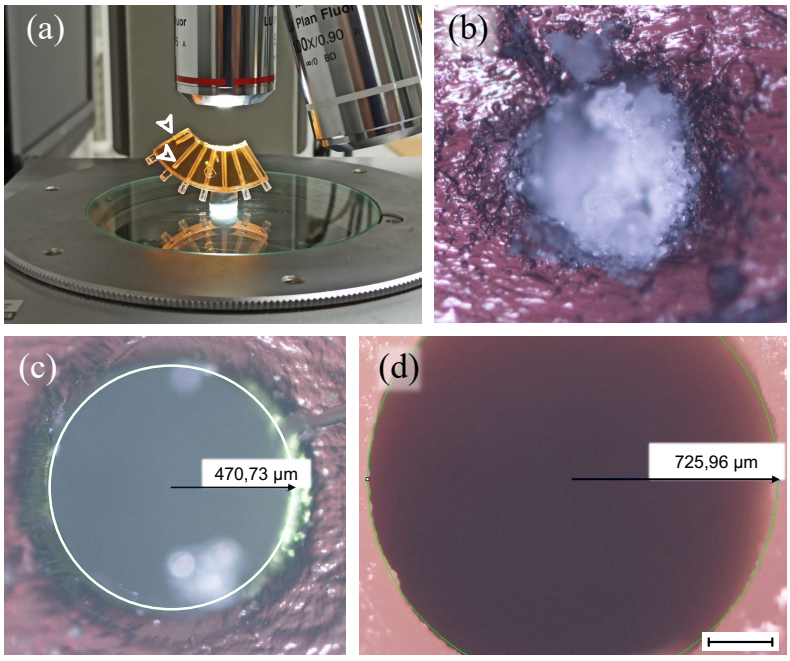

Figure 6.9: a) Experimental configuration used to measure the internal channels of the 3D printed quarter annulus, using a microscope. White arrows point channels not fully formed, printed at 0° and 15° (for the case of Amber resin). Pictures of b) obstructed and c) unobstructed channels, with 500 µm of theoretical diameter, printed with Amber resin at 0° and 75°, respectively. d) Unobstructed channel printed using Model resin, at an angle of 75° and a theoretical diameter of 1000 µm. The images were taken with a 5× microscope objective. Scale bar 250 µm.

6.3.5 Replicability

Sometimes it is important to produce a master for posterior replication. In this section, the possibilities that resins offer as materials to manufacture master elements and the quality of the replications obtained from the printed master are analysed. For this, the outward channels fabricated in Section 6.3.3 were replicated by soft lithography of PDMS, creating cavities in the polymer.

Some resins showed poor performance in replicating PDMS, so not all of them could be used as master. This is the case with Amber (Figure 6.10a-c) and Dental (Figure 6.10d-f) resin. In Figure 6.10b the two most interesting regions for replication analysis are highlighted: the bottom of the channels and the base region. For the bottom, many irregularities and micro-cracks were produced during the soft lithography replication of these resins (Figure 6.10c,f), causing that the original topology of the channels could not be transmitted to the replica. The same occurs for the base regions that despite being originally flat, show a high irregularity and flaking when replicated, especially noticeable in the case of Dental resin (Figure 6.10d-e). For Flexible and Elastic resins, the replication process cannot be studied since the polymer failed to cure properly. The PDMS layer deposited on these resins showed a semi-liquid state that made it impossible to observe the topology of study. These reasons make not convenient the use of the four resins for master manufacturing.

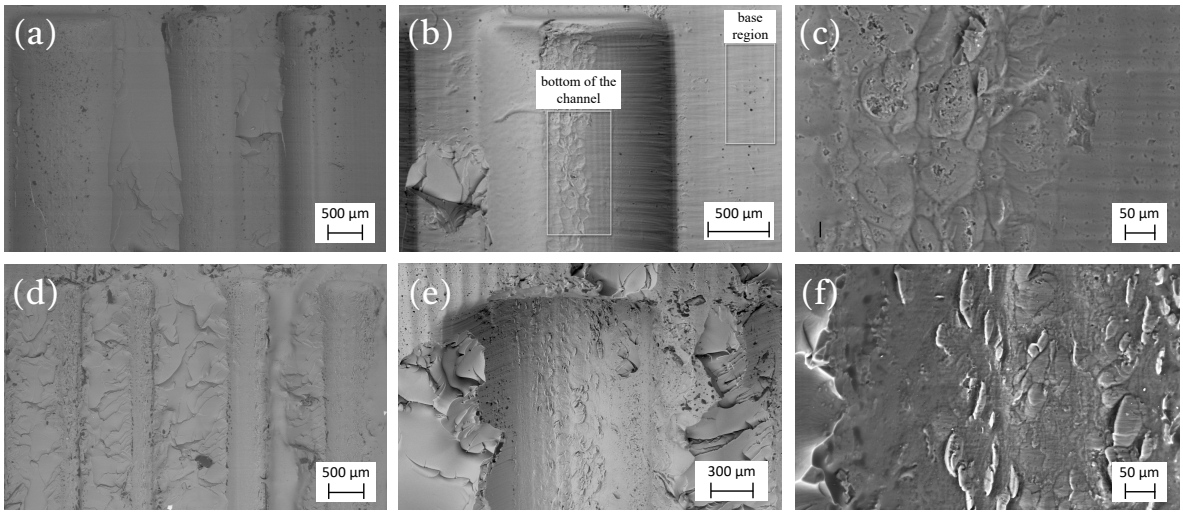

Figure 6.10: FESEM images SEM images of PDMS soft lithography replicas of superficial channels printed in (a), (b), (c) Amber and (d), (e), (f) Dental resin. The PDMS replicated inward channels show a poor replication performance. Pictures were taken with the following microscope objectives: a) and d) 50×; b) and e) 100×; and c) and f) 500×.

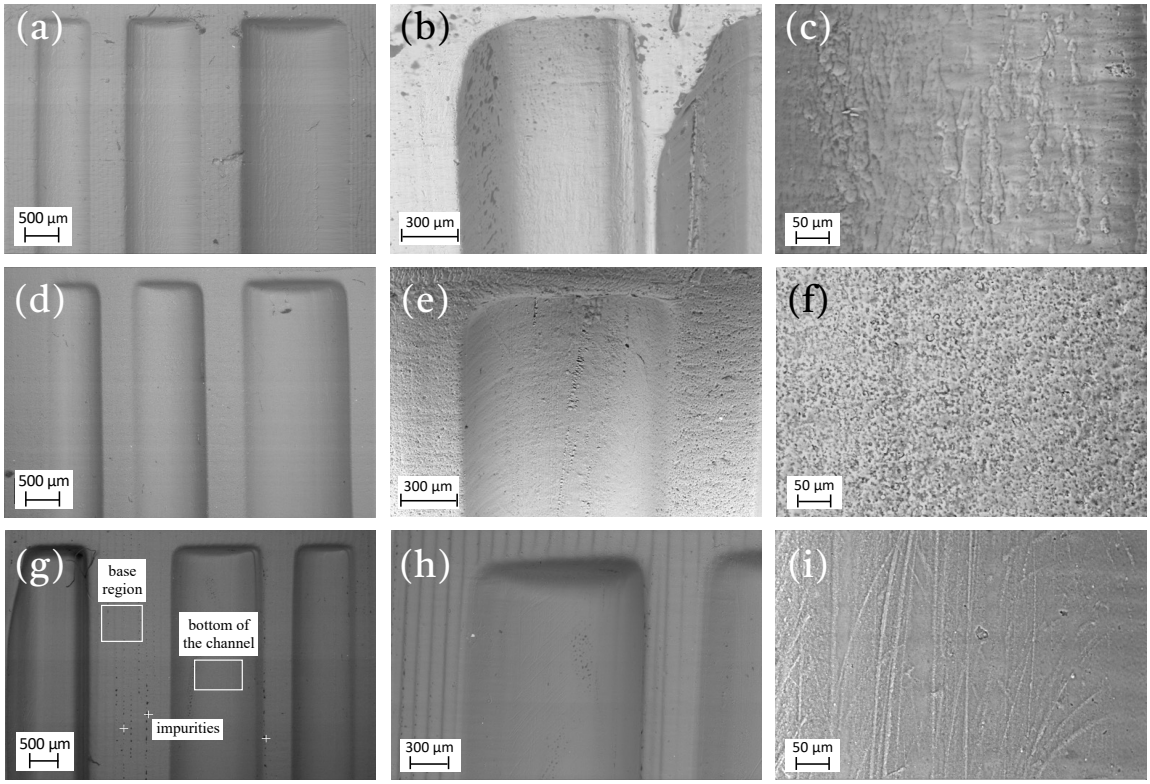

Figure 6.11: FESEM images SEM images of PDMS soft lithography replicas of superficial channels printed in (a), (b), SEM images of PDMS soft lithography replicas of superficial channels printed in (a), (b), (c) Clear; (d), (e), (f) Model and (g), (h), (i) Tough resin. Regions analysed by EDX are also highlighted. The PDMS replicated inward channels show a good replication performance. Pictures were taken with the following microscope objectives: a) and d) 50×; g) 45×; b) and e) 150×; h) 100×; and c), f) and i) 500×.

However, three other studied resins allowed a high-quality PDMS replication from masters made of: Clear, S_a= 1.478 ± 0.355 µm (Figure 6.11a-c); Model, S_a= 1.672 ± 0.633 µm (Figure 6.11d-f); and Tough, S_a= 3.831 ± 0.487 µm (Figure 6.11g-i). For them, the polymer surface managed to reproduce the respective surface pattern and a very similar roughness, so that an almost exact replica was obtained. In this scenario, the quality of the PDMS channel will depend only on the quality of master, so all the previous study and optimization of the printer performance can be transferred to the replicated channel.

An EDX analysis of the surfaces of the replicated channels in PDMS was performed to determine if there are any transference of the resin to the PDMS during the soft lithography. Figure 6.12 shows the EDX spectra obtained for the three regions of the PDMS replica obtained from a Tough resin master: i) base region (Figure 6.12a), ii) bottom of the channel (Figure 6.12b) and iii) visible impurities (Figure 6.12c).

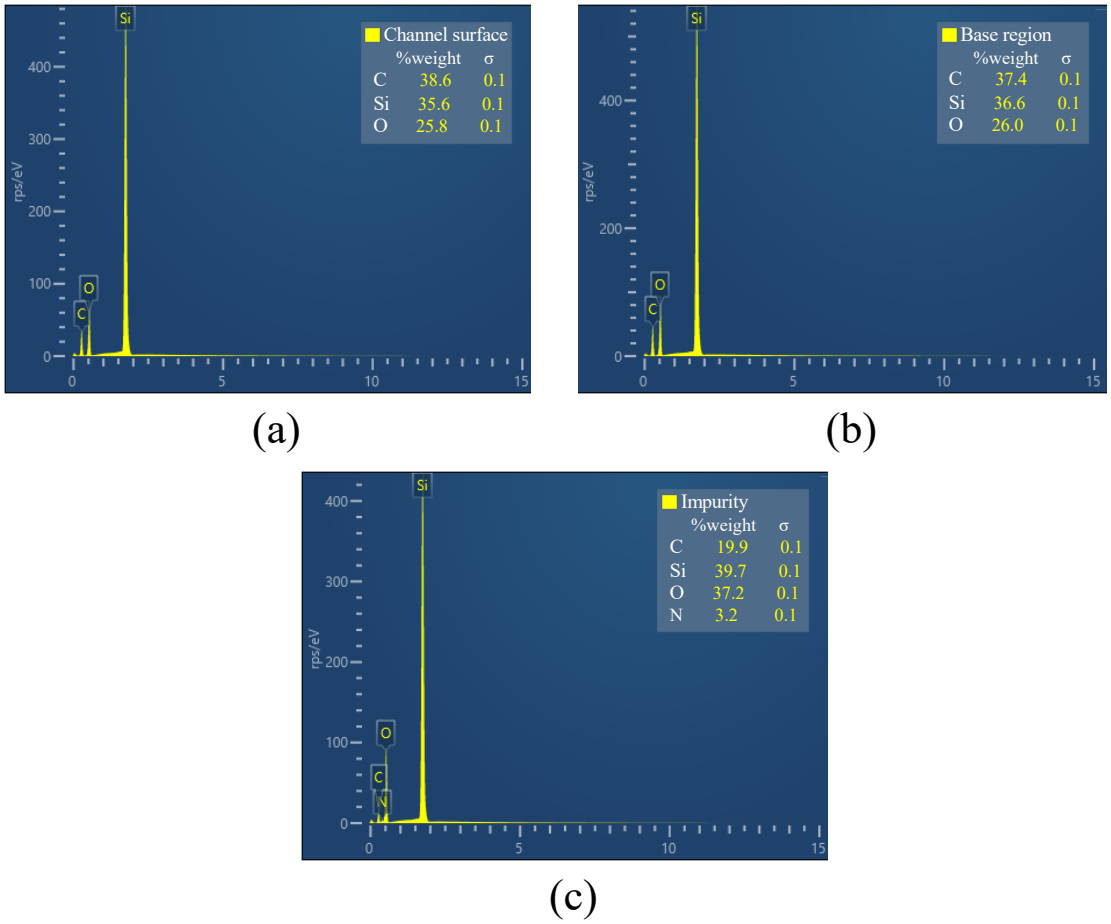

Figure 6.12: FESEM images EDX spectra of the (a) channel surface, (b) base region and (b) impurity observed on the PDMS replica obtained from a Tough resin master.

For the bottom of the channels and base regions of PDMS, the analysis showed approximately the same weight percentage of C (40%), Si (35%) and O (25%). The obtained spectra were quite similar for the rest of the replicas. These results agree with the elements that form the polymer (C_2H_6OSi). The used equipment cannot detect elements lighter than Be, which explains the absence of H in the spectrum. Moreover, the measurement of the various observed impurities on the replicated surfaces yielded a result similar to the previous spectrum except for the presence of N, that varied depending on the master resin, being 1.5% for Amber, 3.2% for Tough and 4.3% for Clear resin. The presence of these contaminants could come from the N originally present in the resins. Thereby, a transfer of impurities from the master to the replica produced during the soft lithography process was detected. The extent to which this contamination may be critical to the proper functioning of a microfluidic device should be assessed in each specific case.

6.4 CONCLUSIONS

Microfluidics is a field that requires multidisciplinary technologies capable of manufacturing highly detailed structures in a repeatable and precise way. 3D printing has a short but promising path in this area, democratizing access to manufacturing techniques through simple procedures and very low waste production. In particular, SLA printers stand out thanks to recent developments in laser technologies, which make them the most extended option capable of achieving greater precision within the current additive manufacturing technologies. In this chapter, the most important functionalities for manufacturing solvent microfluidic devices are tested for the first time using a Low Force Stereolithography (LFS) technique. A set of seven printing resins (Clear, Dental, Tough, Amber, Flexible, Elastic and Model) was studied according to the needs of most of the microfluidic devices used for biological and biomedical research.

A piece containing several structures used in microfluidic devices, such as superficial channels (inward and outward), internal channels and pillars was designed. The most important features: range of dimensions and accuracy, time of printing and transparency of the materials used were studied.

We can conclude that Dental resin required the shortest printing time, followed by Amber and Flexible while Model and Clear resin, printed at the maximum resolution, took the longest one. The transmission spectra of the transparent resins were measured. It was found that polishing increases the transmittance for Amber, Clear and Dental resins, reaching around 80% transmittance for the visible range, where fluorescence microscopy excitation lengths are typically found.

Regarding the formation of internal channels, the accumulation of resin was found to be a determining factor in causing obstructions and malformation of the channels. To avoid this phenomenon, two aspects were crucial: the diameter of the channels and their printing orientation. While for channels with a diameter less than 500 μm obstructed lumen were formed, for greater diameter values, an open lumen was obtained. For angles greater than 60º and diameters greater than 500 μm, resins such as Dental or Amber managed to form channels with a printing accuracy over 80%. For larger diameters (1000 μm), the accuracy was >70% and continued to increase with the angle. For channels of 1500 μm in diameter, all the resins studied achieved an accuracy >90%. The surface performance of the printer was also analysed by studying the topology of a series of channels and pillars printed inwards and outwards. The fabricated structures showed certain deviations compared to the designed ones that were quantified by various aspect ratios. Taking Clear resin as an example, it was observed that the ratios almost reached 1 as the channels increased in size. In general, two printing regimes can be distinguished for channels. Small channels (0-500 μm) deviate significantly from the designs with aspect ratios below 0.75, since the resolution of the printer is not capable of forming such

small structures. For larger channels (500-1500 μm), the ratios obtained were between 0.75 and 1.25. All the analysed resins follow a similar behaviour, and their accuracy is determined by the MTL, where Clear and Model resins stand out. The surface finishing of the structures was also assessed. For the inward ones, it was found that printing orientation is critical and can favour unwanted accumulation of resin on the sides of the channels and wells. Channels manufactured with an orientation perpendicular to the base showed the best uncured resin evacuation.

Manufacturing of structures made up of resins to be used as masters was also analysed. Clear, Model and Tough resin showed a good performance when the material used for soft lithography replication was PDMS. On the contrary, a poor transference of the original topology was observed for Amber and Dental resins. The polymer did not cure on the Flexible and Elastic resins, so we can conclude that these resins are not convenient for master manufacturing.

7. HYBRID TECHNIQUE FOR SUPERFICIAL MICROPATTERNING BY COMBINING PULSED LASER ABLATION AND STEREOLITHOGRAPHIC 3D PRINTING FOR MICROFLUIDICS APPLICATIONS

This chapter is a partial reprint of:

Bastián Carnero[a,b], Yago Radziunas-Salinas[a], Bruno K. Rodiño-Janeiro[b], Sylvana Varela Ballesta[b,c] and M. Teresa Flores-Arias[a], *Versatile hybrid technique for passive straight micromixer manufacturing by combining pulsed laser ablation, stereolithographic 3D printing and computational fluid dynamics*, Lab on a Chip (2024), DOI: 10.1039/D4LC00009A

[a]Photonics4Life research group, Departamento de Física Aplicada, Facultade de Física, iMATUS, Universidade de Santiago de Compostela, Campus Vida, Santiago de Compostela, 15782, Spain

[b]BFlow SL, Edificio Emprendia, Santiago de Compostela, 15706, Spain

[c]Departament d'Enginyeria Mecànica, Universitat Rovira i Virgili, Tarragona, 43007, Spain

---

7.1 INTRODUCTION

As we have seen in previous chapters, micropatterning surfaces has emerged as need in industry and many research fields: physics, engineering, chemistry, biology, and medicine. In this chapter a novel hybrid manufacturing technique that combines Pulsed Laser Ablation (PLA) and Stereolithography (SLA), will be introduced. In this chapter, the validity of the technique will be granted by two different results: the manufacturing of a straight micromixer and an array of microlens.

7.1.1 The role of micromixers in microfluidics

The relevance, potential, and strengths of microfluidics have been introduced in previous chapters and thoroughly discussed in the literature (Whitesides, 2006). In this section, we will delve in the topic of mixing, a complex issue in the field due to the prevalence of low Reynolds numbers (Re)[1] in these systems. At low Reynolds numbers, the inertia of fluid motion is negligible compared to viscous forces, leading to laminar flow profiles. In such laminar flows, the inherent mixing of fluids via diffusion alone is often insufficient to achieve the desired level of homogeneity of the solution or the completeness of the reaction.

To address this limitation, microfluidic researchers have incorporated micromixing strategies inside of microreactors, that play a crucial role in a broad range of applications including synthesis of nanoparticles (Agha et al., 2023; K. Guo et al., 2022), selective polymerization (Bally et al., 2011; Ziegenbalg et al., 2012), chemical analysis (Sato et al., 2003), molecular biology (Burns et al., 1998; Conde et al., 2020) and point-of-care applications (Ganguli et al., 2020). Consequently, micromixers fall into two main categories: active and passive. In one hand, active micromixers use external forces or energy sources, such as electric fields, acoustic waves (Conde et al., 2020), or magnetic fields (Y. Wang et al., 2008) to actively induce mixing in the microfluidic channels. On the other hand, passive micromixers rely on the structural characteristics of the microchannel design to promote mixing without involving external sources. They frequently incorporate microstructures such as ridges (Koo & So, 2022), grooves, or serpentines (R. H. Liu et al., 2000b) capable of disrupting the characteristic laminar flow of microscale fluids. In our case of study, we will focus on channels featuring grooves in the bottom, which are classified as slanted micromixers (Ianovska et al., 2018).

These passive slanted micromixers are of great interest: they consume minimal power, making them ideal for portable applications; they exhibit robustness, not depending on continuous operation of mechanical or electrical components; and they offer cost-efficiency and easy integration into complex microfluidic systems.

[1] $Re = \rho v L/\mu$, where ρ is the density, v the flow speed, L the characteristic length and μ the dynamic viscosity of the fluid.

To this end, optical technologies have been essential to accurately manufacture this wide variety of 2D and 3D microstructures capable of creating turbulent flows and enhancing diffusion (Stroock et al., 2002; Zhendong et al., 2012). Until now, photolithography has been the most used optical technology for fabricating devices with application in the field of microfluidics (Carrell et al., 2020b), characterised by complex and time-consuming protocols to micropattern photoresists in 2D, which also produce highly polluting chemical waste. Thereby, in recent years, the rapid developments in lasers have favoured the appearance of different technologies that can be used to microstructure different substrates in a more user-friendly way. This is the case of Pulsed Laser Ablation (PLA), that allows us to achieve outstanding resolutions when micropatterning 2D surfaces, enabling the creation of micro (Gómez-Varela et al., 2022; Nieto, Delgado, et al., 2014a; Wlodarczyk et al., 2019) and nano (Bai et al., 2018) structures with promising results. The 3D printers based on the selective Stereolithography (SLA) of liquid resins have made easier to manufacture 3D objects with significant structural complexity (ranging in the hundreds of micrometres and millimeters), demonstrating substantial potential in the field of microfluidics (Carnero et al., 2021; Shallan et al., 2014b; Turpin et al., 2022) and, in particular, micromixers (Conde et al., 2020; Corbel et al., 2012; Kuo et al., 2019). Both technologies have the potential to overcome the complexities and limitations associated with traditional photolithographic manufacturing methods, in terms of time consumption, scalability, cost and pollution.

Micromixers such as the ones that will be presented in this thesis have been used to perform chemical reactions in the literature. For instance, Koo et al. (Koo & So, 2022) proposed the fabrication of a microreactor using a fuse deposition modelling 3D printer. In this chapter various printing angles were considered to form structures that will be replicated by soft lithography of PDMS creating a groove pattern on the replicas. These authors utilized channels with structures in a similar dimensional range to the one that will be presented in our study (800µm diameter channels with grooves ranging from 200 to 300 µm), improving the mixing performance of several iodide-iodate reactions (Villermaux-Dushman method (Fournier et al., 1996)), as the angle and flowrate increased.

Other works have highlighted the advantages of the slanted groove micromixer positioned on the bottom side of the channel in diverse applications. For instance, Xu et al. (C. Xu et al., 2006) demonstrated the synthesis of a statistical-copolymer-brush composition gradient of two monomers following the manufacturing protocol of Cabral et al. (Cabral et al., 2004) This technique based on frontal photopolymerization of a photoresist sandwiched between two glass slides allows to obtain outward grooves of 190 and 340 µm on the bottom of a 600 µm channel, which is close to the results presented in this thesis.

In another case, Abonnenc et al. (Abonnenc et al., 2008) fabricated a microreactor through UV-photoablation of a micromachined channel (of 100 µm of width and 35 µm of depth) on a polyethyleneterephthalate (PET) sheet, obtaining 45° oriented inward grooves of 35 µm in

depth. This device was used to conduct a tagging reaction to enable protein tagging for applications in liquid chromatography-mass spectrometry workflows.

Beyond direct chemical reactions, Moon et al. developed a slanted groove micromixer, obtained by photolithography, and replicated in PDMS, featuring grooves of 50µm width and 10 µm of diameter (Moon et al., 2010). This reactor was applied in their next work to create an enzymatic microreactor for continuous glucose level monitoring via subcutaneous microdialysis in rats (Moon et al., 2013).

In light of the interest garnered by these devices and their applications, this thesis presents for the first time to our knowledge, a novel hybrid technique that combines PLA and SLA to simply manufacture and test straight micromixers featuring different patterns.

7.1.2 The role of microlens in microfluidics

Refractive microlens have emerged as a crucial element in optics and photonics (Yuan et al., 2018). Since 1980, researchers and companies have developed numerous manufacturing techniques (Fujita et al., 1981; Eisenberg et al., 1989; Yang et al., 1999) capable of satisfy different requirements as: optical quality, cost-effectiveness, scalability, or endurance. Microlens made of glass have historically been the most studied and developed, and many technologies can be highlighted in this field: reactive ion etching, laser irradiation or ion exchange. However, eventually, new materials as optical plastics as Poly(methyl methacrylate (PMMA), Polycarbonate (PC) or Polystyrene (PS) started to be used instead of glass (Pantelis & McCartney, 1994), with very interesting properties to facilitate the manufacturing. In this field, techniques as photoresist reflow, laser beam shaping, photopolymerization, laser ablation or e-beam writing can be highlighted.

Regarding its applications, microlens-based devices have been very useful, for example, in optical communications systems (Ko et al., 2004), where fibre coupling is performed with microlens arrays. Recent holography approximations also involve the use of microlens for augmented reality glasses. Furthermore, microfluidic systems begin to involve the use of microlens for high-speed imaging of single cells in flow environments (Holzner et al., 2018) or selective photopolymerization of photocurable solutions (Paruli et al., 2021).

The numerous applications of microlens, especially in the growing field of microfluidics, make necessary for new technologies to emerge to solve certain limitations such as the high cost and complexity of most manufacturing processes. As with micromixers, the optical technologies of PLA and Stereolithography SLA present new opportunities for manufacturing. The proposed hybrid technique enables the rapid fabrication of millimeter-scale substrates, which can subsequently be micropatterned as desired using a laser, obtaining a resin master that can be replicated using PDMS soft lithography.

7.2 MATERIALS AND METHODS

7.2.1 Manufacturing

The proposed manufacturing process of micromixers and microlens consists of two steps, in which each technique, PLA (Introduction 2.2.3.3) and SLA (Introduction 2.2.3.5) is used in its most suitable dimensional range (millimetres and micrometres, respectively).

7.2.1.1 Stereolithographic 3D Printing

A Form 3B SLA 3D (Materials and Methods 4.1.5.2) printer was used to produce the micromixer masters and the microlenses substrates. Commercial Model V2 (Materials and Methods 4.1.3) resin from Formlas was selected as printing resin given the resolution it offers (25 µm in Z), its performance when replicating polymers (Carnero et al., 2021) and the good response to the laser ablation in the infrared (IR) regime (Figure 7.1a). In the post curing process, the piece was washed in 2-propanol and cured into a UV chamber for 60 minutes at 60°C.

In the case of micromixers, printed substrates featured inward and outward square section (0.55×0.55 mm^2) channels on its surface (Figure 7.1b). These channels, 25 mm long, incorporate a bifurcation at the beginning, intended to introduce two samples to be mixed. Thereby, Y-shaped micromixers (Shi et al., 2012) were designed using the Computer Aided Design (CAD) software Fusion 360 (Materials and Methods 4.1.7.1) and then managed with the printer software Preform. In the microlens case, a flat resin plate was printed.

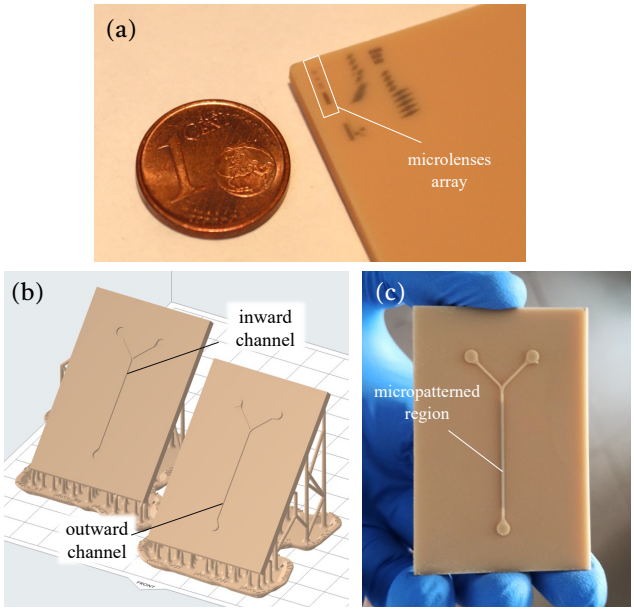

Figure 7.1: a) Photograph of the flat resin surface where microlens arrays were manufactured by PLA. A euro cent is placed nearby as a reference. b) CAD image of the printed plates featuring the Y-Shaped microchannels (inward and outward) on its surface. c) Photography of a plate with an outward channel on its surface after PLA micropatterning.

7.2.1.2 Pulsed laser ablation

PLA micropatterning of the bottom (top) area of the inward (outward) microchannel was performed (Figure 7.1c), in the micromixer case. For the manufacturing of the microlens, the flat surface of substrate (Figure 7.1a) was also ablated using a femtosecond laser, in particular the Santiago TErawatt Laser (STELA) of the Laser Laboratory for Acceleration and Applications (L2A2) facility at Santiago de Compostela (Materials and Methods 4.1.5.1.2).

The design of the ablation patterns was made using the Fusion 360 CAD software. The target was maintained always at the focal length of the microscope thanks to a co-lineal laser feedback with a resolution of 0.4 μm. During irradiation of the target the focal position is automatically readjusted.

7.2.1.3 Soft lithography of PDMS

In the micromixer case, outward channels were employed as the master structures, creating inward channels by replication with soft lithography of Polydimethylsiloxane (PDMS). For its part, the ablated holes of the flat plate were also replicated to obtain outward microlens arrays. PDMS is one of the most used polymers to fabricate microfluidic devices given its optical transparency, permeability to gases, elasticity, and biocompatibility (Hwang et al., 2015b),(Chan et al., 2015b). PDMS was prepared from Sylgard 184 elastomer. The replication process consisted of the following steps: the uncured (1:10 ratio) polymer was deposited on the master fabricated by SLA and micropatterned by PLA and introduced in a vacuum chamber 40 min at 400 mbar to remove bubbles produced during the mixing process. Finally, the master with the degassed PDMS was cured in an oven for 12h at 60°C and easily peeled off. After that, PDMS replicas were easily demoulded from the resin master.

7.2.1.4 Polishing

A water-assisted polishing process was performed using three different grit sizes of water proof abrasive paper (15, 400 and 1000), starting with the lowest grit value and progressing to the highest. Each polishing step was conducted for 10 minutes under a constant flow of water. This protocol grants a gradual removal of the superficial material.

7.2.2 Sealing of the channels

Two different approaches were used to seal the micromixer channels to introduce flow through them. These two techniques depend on whether the channel is 3D printed (made of resin) or replicated (made of PDMS). 3D printed channels were sealed using transparent PET/acrylic adhesive films. The stickers are easy to apply, ensure reliable containment of fluids, prevent contamination, and show optical transparency.

Replicated PDMS channels were punched (to create the fluid entries) and plasma bonded to a microscope glass slide. For this, a Zepto Plasma Cleaner (Materials and Methods 4.1.4.2) was

employed, exposing the surfaces to an oxygen plasma. The power was fixed at 20W, and the pieces were exposed during 20s. Bonded devices were then thermally treated during 30 mins at 90°C.

7.2.3 Micromixer validation

Understanding the flow behaviour and mixing efficiency within micromixers is crucial for optimizing their performance and application in various fields. In this section, we delve into the investigation of micromixer flows through two different approaches: peristaltic pump fluid perfusion and CFD simulation.

7.2.3.1 Flow essays

For testing the real performance of the micromixers, a peristaltic pump and dyes were used. Four channels Minipuls 3 Peristaltic Pump (Materials and Methods 4.1.4.3) pump was employed, allowing us to precisely control the flow rate and ensure consistent flow conditions for accurate measurements and observations. To assess the mixing capabilities of the micromixers, different colour dyes (blue and yellow) were introduced simultaneously into the system. The selection of multiple dyes offers the advantage of visualizing and quantifying the mixing process, as a distinct colour pattern emerges because of efficient or inefficient mixing. The flow was stablished through a 3-stop Pump Platinum-cured silicone Tubing (Inner Diameter (ID) 1mm and Outer Diameter (OD) 3 mm) (Darwin, Paris, France), connected with stopper connectors and silicon tubing (ID 1mm and OD 3 mm). Straight connectors were used to introduce flow in the micromixer. The used flowrate was Q=1 ml/min, which corresponds to Re=30.16.

7.2.3.2 Computer Fluid Dynamics Simulation

Computational Fluid Dynamics (CFD) allows the analysis of various flow characteristics, such as fluid velocity (Maionchi et al., 2022), pressure distribution, and mixing patterns (Florez et al., 2022) employing numerical modelling and simulation of the incompressible Navier-Stokes equations. Its use has been reported in medical disciplines (Casas-Arozamena et al., 2021) and, in particular, with micromixers (Aubin et al., 2005). In this chapter, CFD simulations were used to test the geometries and corresponding performance of manufactured micromixers, employing ANSYS Fluent software (Materials and Methods 4.1.7.2). Numerical simulations were developed considering incompressible fluids, no friction, double precision, laminar flow, transient, pressure based solver, implicit volume of fluid, implicit body force, dispersed interface modelling, and two-phase volume of fluid model with a disperse interphase modelling. For the primary phase we considered H_20 (ρ_1= 998.2 kg/m^3, μ_1= 0.001003 kg/ms) and for the secondary phase we selected a hypothetical fluid with ρ_2= 997.2 kg/m^3, μ_2= 0.001002 Kg/ms (physical properties differ 0.1% from the H20 properties) without surface tension coefficient between two phases. Another sample was considered to test the adaptability of the micromixers,

in that case, an aqueous solution of water with glycerine at 20% was chosen as the first phase (ρ_3=1047 kg/m^3 and μ_3=0.00184 kg/ms), and a hypothetical fluid differing by 0.1 % from the first one (ρ_4=1046 kg/m^3 and μ_4=0.00183 kg/ms) was selected as the second phase.

The inlet 1 and 2 were set at Q=1 mil/min and the outlet was set at atmospheric pressure (101,325 Pa). The other surfaces were set as wall with no slip condition. A tetrahedral mesh refined near the walls was employed to enhance accuracy in regions characterized by high gradients of velocity. Mixtures were considered isothermal and isobaric.

Three meshes of varying grid density and size were considered, comprising 99,668 elements for Grid 1, 358,813 elements for Grid 2, and 509,873 elements for Grid 3. The simulation for a micromixer featuring 20° oriented grooves was conducted on all three grids. When comparing the maximum velocity values to the theoretical value (v=0.2204 m/s), Grid 2 exhibited a deviation of approximately 5% (Grid 1 offers a deviation of 10%), providing good accuracy while requiring less computational effort compared to Grid 3. Consequently, all simulation cases were conducted using grids with a number of elements of the order of Grid 2 and Q=0.5, 1, 2 ml/min, which corresponds to Re=15, 30, 60.

Simulations were run until critical convergence of residuals of 10^{-6} under a SIMPLE solution method with 200 steps of 0.01 seconds and the maximum interaction/time steps of 20. The spatial discretization includes a least square cell-based gradient, PRESTO! discretization for pressures, second order Upwind momentum, first order Upwind volume fraction and first order implicit transient formulation.

7.2.4 Data collection

Confocal images of the microstructures manufactured on the plates were taken using a 3D optical profilometer S Neox (Materials and Methods 4.1.6.3.1). This profilometer allowed us to measure the dimensions (measurements were taken 10 times, obtaining a mean value and its corresponding standard deviation) and to analyse the morphology of the channels. A Nikon MM-400 metallurgic microscope (Materials and Methods 4.1.6.1) was used to acquire the optical images, using a LU Plan Fluor objective with a 5× magnification and a CCD camera Nikon DS-FI2. Additionally, a SkyScan 1272 X-ray microCT (Materials and Methods 4.1.6.7) was used to analyse the manufactured microlenses arrays.

7.2.5 Microlens focal measuring

For characterizing the manufactured microlens arrays, the optical setup introduced in Materials and Methods 4.2.1 was displayed to analyse the focus of the lenses.

7.3 RESULTS AND DISCUSSION

7.3.1 Micromixer manufacturing

7.3.1.1 Laser parameters for manufacturing

The first step in the experimental section consisted of a comprehensive study focused on the optimization of laser ablation parameters. Specifically, we conducted experiments involving the micropatterning of grooves by PLA on a flat resin surface. During these experiments, we systematically varied the laser Power (P) and the Number of passes (N), to find the optimal channel results, analysing thermal damage, homogeneity, regular profile, and dimensions by confocal/optical images (Figure 7.2). Velocity of 2D platforms (where the resin plate is placed) was fixed at 1 mm/s.

First, geometric data was collected using the confocal microscope, which allowed us to measure the width (Figure 7.2a) and depth (Figure 7.2b) of the fabricated channels. Since these average measurements are not sufficient to describe the real aspect of the channels, the results were cross-checked with confocal images (Figure 7.2c-j).

In terms of channel width (W), a clear correlation is observed between this width and the power of the pulses (Figure 7.2a): the channels, for a specific power, are wider than those obtained for lower powers. This is verified for 1, 2 and 3 passes of the laser. However, for each one of the powers studied, the number of passes does not always imply an increase in the width of the channel. This behaviour is observed in the results for higher powers (110, 130 and 150 mW) and lower ones (10 mW), and occurs for different reasons: in the case of higher powers, for example 150 mW (Figure 7.2c), the deeper channel is obtained for 1 pass, while an inhomogeneous result is observed for 2 and 3 passes. This phenomenon has its origin in the immediate arrival of the very energetic second and third pulses, that prevent the ejection and adequate evacuation of material, that is instantly recasted in the borders of the channels, reducing its width.

For lower powers, for example 10 mW (Figure 7.2i), manufactured microchannels present a regular structure for only 1 laser pass. When the number of passes is increased, this low energy value of the pulses is unable to ablate the previously ablated areas in a constant manner, creating small irregular grooves along the channel. In this scenario, the concept of average width does not adequately describe the result, since, as it varies locally (the same applies for depths, as can be seen in Figure 7.2j). For intermediate powers, for example 90 (Figure 7.2e) and 50 mW (Figure 7.2g), in general terms, a greater number of passes increases the width of the channel, since the energy is enough to allow vaporization and proper elimination of the material after the first laser pass and no recasting is observed.

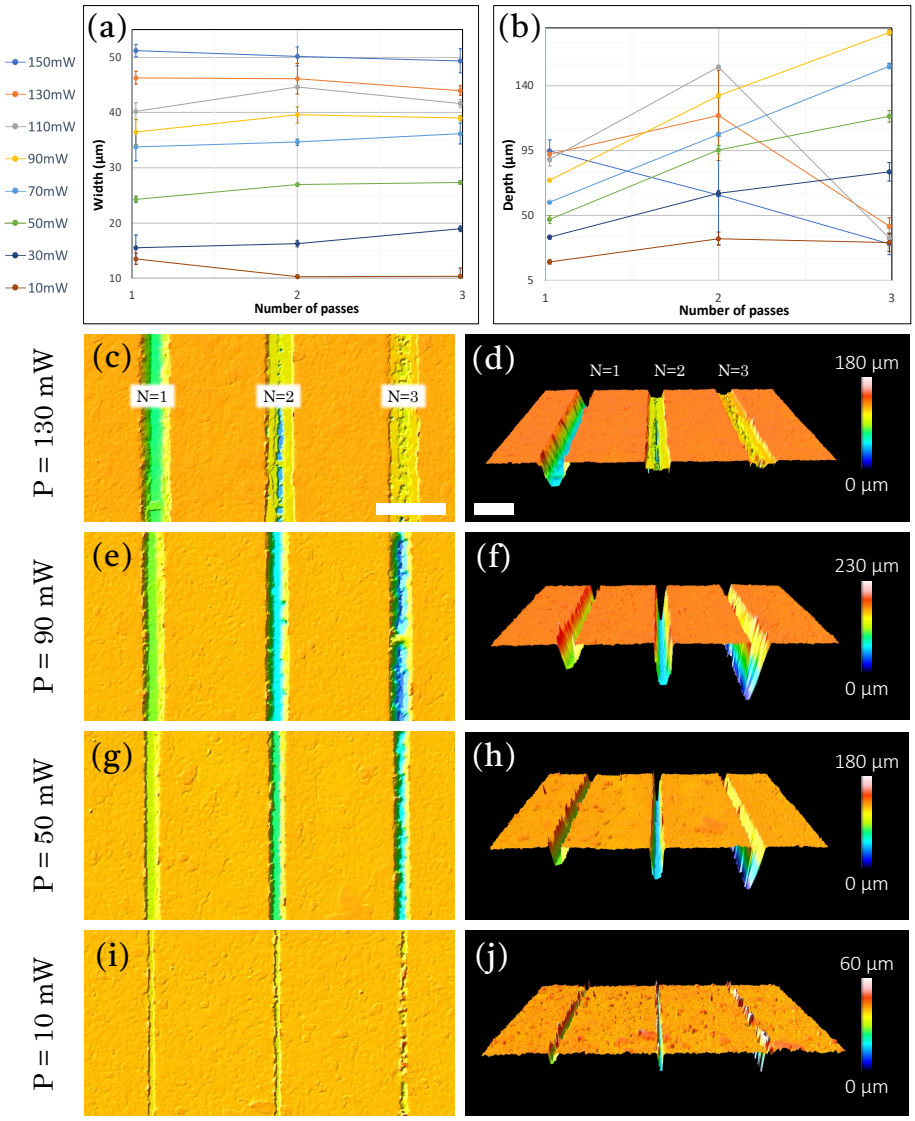

Figure 7.2: Average a) width and b) depth of the microchannels ablated by PLA on the surface of the resin for different powers (10-130 mW) and laser passes (1-3). Top (left) and 3D (right) confocal images of microchannels obtained for c), d) 130, e), f) 90, g), h) 50 and i), j) 10 mW, respectively. Scale bars: 100 µm.

Regarding the Depth (D) of the channels (Figure 7.2b), we observe two regimes with very different behaviours. For high powers (150, 130 and 110 mW), as mentioned before, the arrival of the second and third pulse favour the collapse of the walls and the accumulation of the material in the remaining space, that is immediately recasted and deposited again inside the channel (Figure 7.2d). This favours that for these three powers, when three passes are performed, depths fall to approximately 20 µm. For two passes, some material can escape so, for 130 and 110 mW we reach microchannels with a depth around 100 µm. For lower powers (10-90 mW), we obtain a more effective result, pulses do not block the removal of material and the depth increases with the number of passes. In this regime, the higher the power, the deeper the channels will be (comparing the same number of passes). The uniformity of channel depths

is verified, as evidenced by 3D confocal images for P=90, 50 mW (Figure 7.2f,h) and two passes.

After an extended analysis of the results obtained for different values of power for the ablation, the selected one was 90 mW, combined with 2 passes, with which we can obtain channels with a width of W=39.6 ± 1.9 µm and diameter D=129.1 ± 2.3 µm. This energy and passes were selected because they are at the intermediate point between high and low powers, producing optimal ablation results (Figure 7.2e) and allowing the patterning of regular, homogeneous, and reproducible superficial channels.

To this point, obtained channels are within the dimensional range of some reported in the literature (Kee & Gavriilidis, 2008; Williams et al., 2008), suggesting that the fluid penetration into these channels is expected to be sufficient. However, concerning the demolding of PDMS from the master (see Chapter 6.3.5), it is necessary to slightly increase the channel width to prevent any polymer retention within the master. To reach this goal wider channels are needed, which lead to the following approach: obtaining a wide channel through the ablation of two or more contiguous lines on a flat resin surface. The ablation results of several contiguous lines cannot be directly extrapolated from the results obtained for a single line, so a new study and optimization of parameters was carried out evaluating the ablation results for 2 and 3 contiguous lines depending on the separation distance between them (d) and maintaining the previous ablation parameters: 90 mW, 2 passes and 1mm/s.

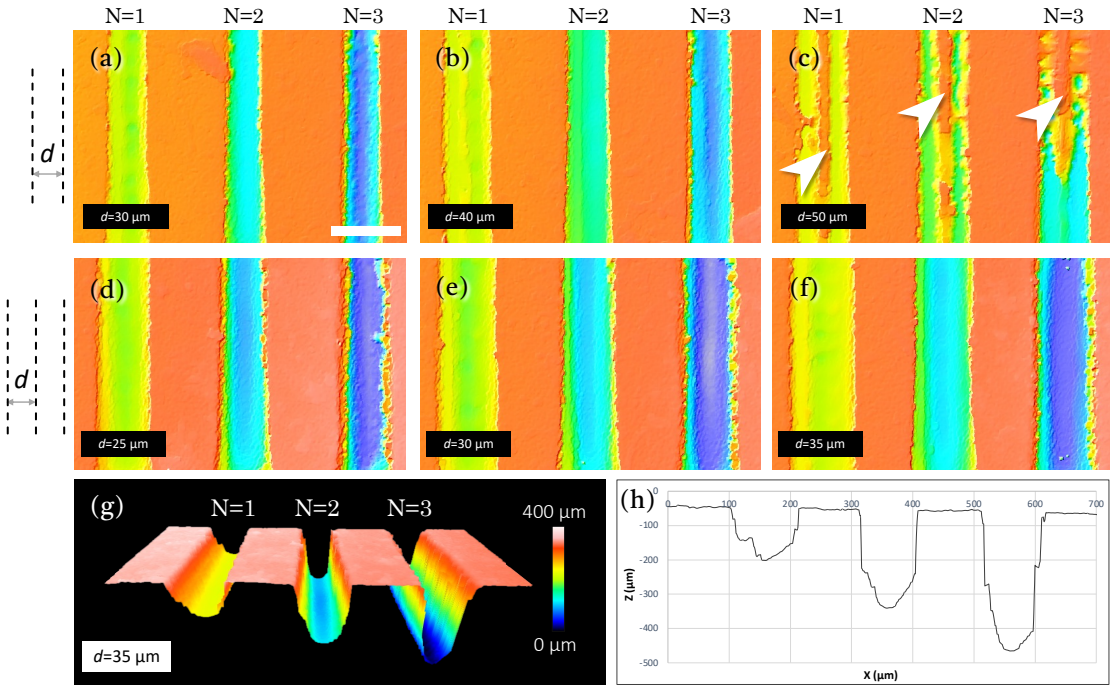

Figure 7.3: Confocal images of the obtained laser ablated microchannels on the surface of the resin. Upper row shows the results when 2 lines were ablated contiguously at different separations: a) 30, b) 40 and c) 50 µm. Middle row shows results when 3 lines were contiguously ablated with d) 25, e) 30 and f) 35 µm of separation, respectively. g) 3D confocal profile and h) cross section of microchannels obtained in f).

The results of this study are shown in Figure 7.3. In this figure, several confocal images are presented, in the top row, those corresponding to the study of two contiguous lines and in the middle row, those corresponding to three lines. For 2 lines, the energy is very spatially confined, and a big quantity of material is removed, promoting the creation of the deepest channels (D=330.0 ± 4.2 μm, W=67.2 ± 3.2 μm) for d=20 μm and N=3. These dimensions are significantly greater than those obtained for the study performed for a single line. This is expected since widening the channel allows the material to be be eliminated in a larger amount. In this case, the structures have a W/D ratio that has to be to be increased in order to promote liquid insertion and non-trapping of PDMS during replication, as we mentioned before. For greater separation distances, the energy fails to adequately remove the material in the intermediate region, being especially noticeable in Figure 7.3c, where a raised, not ablated region (highlighted with arrows) is observed between the two contiguous lines.

More adequate results are obtained when using three contiguous lines, since the intermediate line grants a proper ablation of the intermediate region, thus obtaining a wider channel with a regular bottom. For the lowest separation studied, 25 μm (Figure 7.3d), the energy density per area is very high, so that the edges are irregular, and some breaks can be observed, especially for N=3. These results will not grant a proper sealing of the channels when using adhesive film or plasma bonding, and some leakages of fluids can occur. Similar scenario is observed for d=30 μm. Regarding d = 35 μm (Figure 7.3f), we consider that the results obtained for N = 2 are the most appropriate since they allow obtaining a channel with the appropriate size (D = 230.9 ± 4.7 μm, W = 95.5 ± 5.2 μm) for the sample to enter, featuring a homogeneous channel bottom and a regular edge that will favour sealing without leakage. A 3D confocal image of these results can be seen in Figure 7.3g, in addition to a cross section profile (Figure 7.3h), where the regular vertical walls of the channels can be observed.

7.3.1.2 Micropatterning results and characterization

Two different protocols were used in the manufacturing process. In Protocol 1, PLA was used to micropattern the bottom of inward channels, which were sealed directly using an adhesive film for immediate use. In Protocol 2, we employed PLA to micropattern the top of outward channels, with the intention of later replicating them through PDMS soft lithography to obtain the final micromixers. It is worth mentioning that in this case walls were added to the masters in order fill them with PDMS. This protocol makes possible the production of multiple replicas of the micromixers, feature of great interest for scaling up the production process. In both cases, the following PLA parameters were used: an average power of 90 mW, 3 contiguous lines separated 35 μm, 2 passes per line, repetition rate of 1kHz and 1mm/s of platform velocity.

7.3.1.2.1 Inward channels

Various images illustrating the results of Protocol 1 are displayed in Figure 7.4. One channel was intentionally left unpatterned as a control.

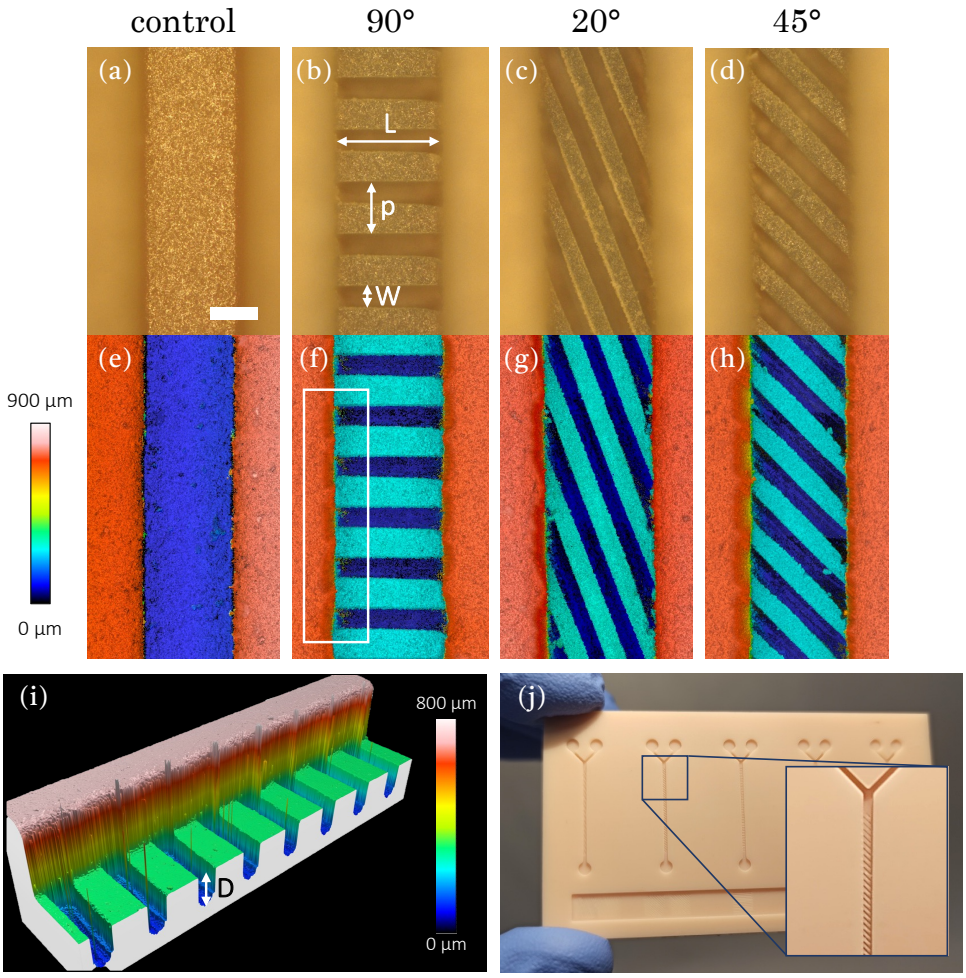

Figure 7.4: Optical (top) and confocal (bottom) microscope images of the micropatterned structures on the bottom of 3D printed microchannel, featuring: a), e) None, b), f) 90°, c), g) 20°, and d, h) 45° oriented grooves, respectively. Scale bar: 300 µm. Magnification: 5×. i) Confocal image of the highlighted area in picture f). j) Picture of the 3D printed resin plate where all structures were micropatterned. Enlarged view of the inner part of one micromixer is shown. Measured groove parameters (W, L, D, p) are also denoted in the image.

In Figure 7.4a,e, the printing quality is notorious, as evidenced by the consistent edge regularity and channel straightness. The characteristic roughness of the surfaces printed by SLA was studied in detail Chapter 6, in which a value of $S_a = 1.444 \pm 0.247$ µm vas measured for the employed resin. Subsequently, following the application of PLA with the specified parameters on the bottom of the channel, we can observe the formation of oriented grooves. In these grooves, a set of distinctive parameters (Width (W), Length (L), Depth (D), and Period (p)) can

be identified and measured using profiles derived from the confocal images. The values obtained are presented in Table 7.1.

Angle (°)	Width (µm)	Lenght (µm)	Depth (µm)	Period (µm)
90	94.3 ± 8.3	488.3 ± 8.1	243.5 ± 15.5	235.3 ± 3.3
20	86.6 ± 4.0	1429.3 ± 14.8	253.3 ± 11.1	167.0 ± 4.0
45	89.3 ± 2.5	631.8 ± 14.4	248.3 ± 9.8	189.7 ± 4.0

Table 7.1: Measured parameters of the ablated structures at the bottom of the channel.

In the case of 90° oriented structures, optical image (Figure 7.4b) exhibits no thermal damage and consistent results in terms of structures formation at the bottom of the channel. When assessing their dimensions, we note that the width of these grooves (94.3 ± 8.3 µm) match what was obtained in the parameter study (95.5 ± 5.2 µm). In terms of groove length, it is somewhat shorter than anticipated (designed channels had 550×550 μm^2 section). This discrepancy arises from the manner in which the printer constructs square-section structures, resulting in a shape closer to a trapezoid(Carnero et al., 2021), with a narrower base width compared to the top. Given that ablation takes place in this specific region, the grooves end up measuring less in length. Additionally, a minor accumulation of residue is visible along the sides of the channel. This accumulation can be seen in the confocal image (Figure 7.4f) and can be attributed to the challenge of effectively removing volatilized debris. The highlighted area in this image is presented in a 3D view in Figure 7.4i, helping us to better understand the ablation results and the achieved depths for this orientation (243.5 ± 15.5 µm), which agree with the previously obtained results on a flat surface (230.9 ± 4.7 µm). The difference between the width and the period allows us to determine the width of the ridges, which are structures formed by the resin that is not subjected to ablation. These structures, measuring 140 µm in width, are slightly wider than the grooves and exhibit a squarer section.

Regarding the 20° oriented structures, Figure 7.4c displays well-defined grooves that are slightly narrower (86.6 ± 4.0 µm) than those achieved at 90°. This difference is due to the overlapping of the three contiguous lines used in PLA when ablation is performed at a certain angle. Notably, the accumulation of residues in these inward channels is the most significant among all the observed, as evident in the confocal image (Figure 7.4g). This can be attributed to the greater length of these structures (1429.3 ± 14.8 µm) in comparison to the others, which favours that a larger amount of material is volatilized and carried towards the edges of the channel during PLA. The period allows us to estimate a closer dimensional similarity between the grooves and ridges, which are approximately 80 µm in width in this case. Finally, these channels show the greatest of the depths obtained (253.3 ± 11.1 µm), due to the greater overlapping of the lines above mentioned.

For channels with 45° oriented structures (Figure 7.4d), the width of the ridges (89.3 ± 2.5 μm) is an intermediate point between 0° and 20°, just as happens for the orientation angle. The same applies for the depth of the ridges (248.3 ± 9.8 μm). Confocal image (Figure 7.4h) shows a subtle accumulation of debris in certain areas, somewhat distant from the edges of the channel. However, no thermal damage is observed in any case and results agree with the ones obtained in Section 7.3.1.1. Period indicates a proper match between the grooves and ridges, of approximately 90 μm in width.

The versatility of the proposed manufacturing technique has also enabled the creation of three micropatterned channels (and two controls) effortlessly and reproducibly on a single multichannel resin plate (Figure 7.4j), where five unpatterned channels were printed at first. The total manufacturing time for the three structures has not exceed fifteen minutes. The integration of these microstructures within the same platform allows for convenient experimentation and direct comparison of their performance. These devices can be used directly by sealing them using an adhesive film.

7.3.1.2.2 Outward channels

The outcomes of Protocol 2 (corresponding to outward channels) are showed in Figure 7.5 and Figure 7.6, while Table 7.2 presents the values of the parameters of the structures. Just as in previous section, we deliberately left the first channel without patterning, as shown in the confocal images (Figure 7.5a), that is properly translated to the PDMS replica (Figure 7.5e). Previously mentioned surface roughness of the employed resin is evident in the replica. This underscores the remarkable level of detail that PDMS can faithfully replicate, extending down to the micrometer scale.

Regarding the channels with 90° oriented structures, the first step consisted of micropatterning the top of outward channels by PLA. Ablation and soft lithography results are shown in Figure 7.5b,f and allow us to observe the correct formation of the grooves, featuring W= 98.3 ± 6.3 μm in the master of resin and and W= 123.0 ± 3.8 μm in the replica. It is worth mentioning that this difference in size is since it is a replication process, the ridges in master are the structures that form the grooves in the replicas and vice versa. A very simple verification of these outcomes is that the sum of both widths must be equal to the period, which virtually happens within the standard deviations. Furthermore, the periods coincide for both the master and the replica, demonstrating the precision of the soft lithography technique used in this process. Regarding the length, the measured value for outward channels is greater than that of the inward ones. This is because during SLA printing the outward channels release a larger amount of uncured resin, allowing them to achieve a less trapezoidal shape, closer to a square. The most significant difference compared to the previous case lies in the depth measurement (301.3 ± 9.9 μm), which is 70 μm greater than what was obtained during the parameter study on a flat surface. This increase originates from the ablation being carried out on a structure that

is raised above its surroundings (Figure 7.6a). As a result, the resin can be volatilized and eliminated without restrictions when surrounded by air. Finally, a more comprehensive 3D confocal view of the proper replication of the master structure into PDMS replica can be observed in Figure 7.6a,d.

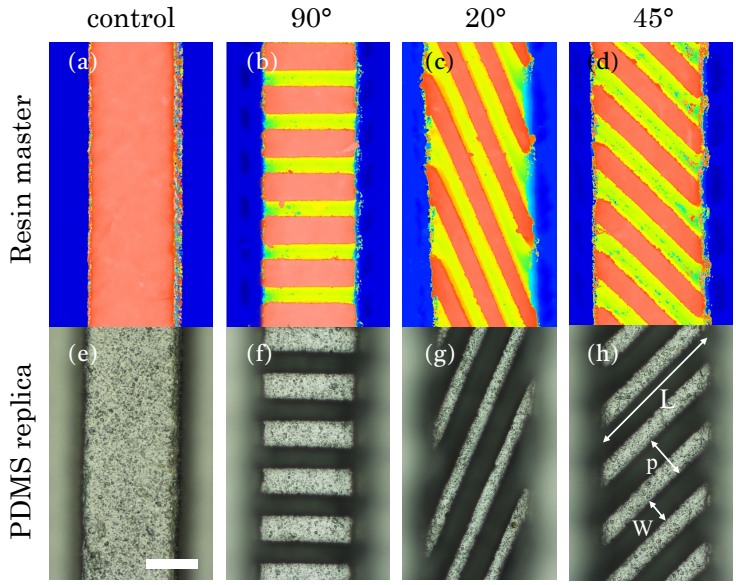

Figure 7.5: Confocal (top) and optical (bottom) microscope images of the micropatterned structures on the top of printed microchannel (top) (a-d) and its corresponding PDMS replicas (bottom) (e-h), featuring: a), e) None, b), f) 90°, c), g) 20°, and d, h) 45° oriented grooves. Measured groove parameters (W, L, p) are also shown in the image. Scale bar: 300 µm. Magnification: 5×.

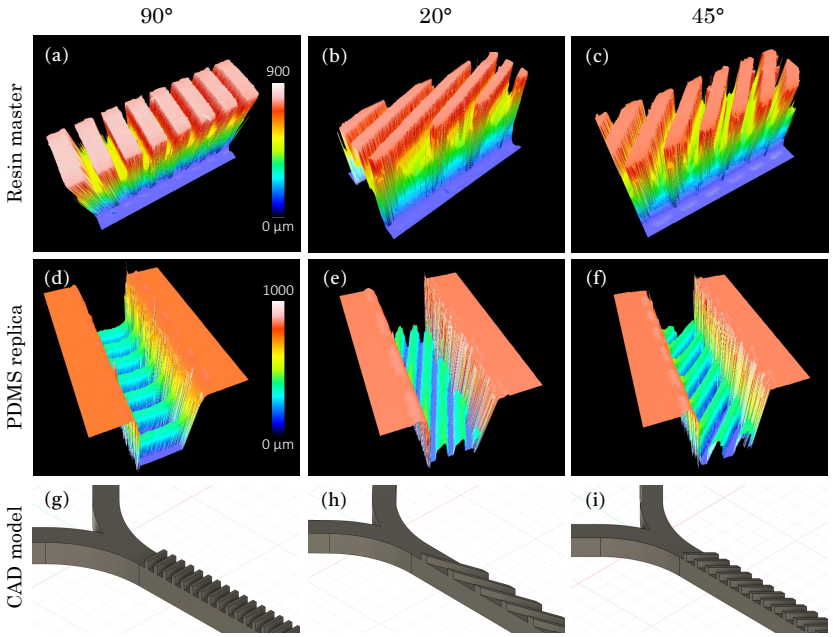

Figure 7.6: 3D Confocal view of the micropatterned structures on the top of printed microchannel (top)(a-c), their corresponding PDMS (mid)(d-f) and CAD (bottom)(g-i) replicas featuring: a), d), g) 90°; b), e), h) 20°, and c), f), i) 45° oriented grooves.

	Angle (°)	Width (µm)	Lenght (µm)	Depth (µm)	Period (µm)
Resin master	90	98.3 ± 6.3	502.8 ± 9.5	301.3 ± 9.9	234.0 ± 7.0
	20	87.7 ± 2.1	1438.5 ± 30.7	299.3 ± 17.2	179.0 ± 3.0
	45	88.8 ± 5.6	648.3 ± 14.4	306.5 ± 12.9	182.3 ± 6.6
PDMS replica	90	123.0 ± 4.8	495.0 ± 4.8	293.3 ± 12.4	227.3 ± 4.6
	20	98.0 ± 4.6	1318.5 ± 36.1	299.0 ± 25.0	177.7 ± 16.5
	45	99.8 ± 5.1	690.8 ± 20.8	306.3 ± 39.5	188.3 ± 9.2

Table 7.2: Measured dimensions of the ablated structures at the top of the channel and corresponding dimensions of the PDMS replicas.

For channels featuring structures oriented at 20°, the master grooves exhibit similar dimensions (W = 87.7 ± 2.1 µm and L = 1438.5 ± 30.7 µm) as the PDMS replicas (W=98.0 ± 4.6 µm and L=1318.5 ± 36.1 µm) and both are consistent with the study of parameters. Meanwhile, the depth follows the same trend as the obtained for 45°, being significantly greater than that achieved on a flat surface due to increased debris release, so deeper structures are obtained (Figure 7.6b) and translated to replica (Figure 7.6e). A very illustrative result of the replication process explored in this section is the production of specular images of the original pattern, so that if the master structure is oriented at 20° (Figure 7.5c), with reference to the vertical axis in the photo, the replica will be oriented at -20° (Figure 7.5g). After the structures were fabricated and characterized through confocal microscopy, they were recreated using CAD software (Figure 7.6g,h,i) to conduct further simulations.

7.3.1.3 Flow essays

To demonstrate the efficiency of the micromixer fabricated, flow experiments were carried out using a peristaltic pump to assess their mixing performance (Figure 7.7). Two different dyes (yellow and blue) were simultaneously introduced into the micromixers, representing distinct fluid streams (Figure 7.7a). By observing the resulting colour patterns, the efficiency and effectiveness of the mixing process within, in terms of the homogeneity of the green colour obtained at the outlet). PDMS replicated micromixers were utilized due to their complete transparency. Resin micromixers are expected to yield similar results, but their opaqueness makes it challenging to capture images by optical microscopy.

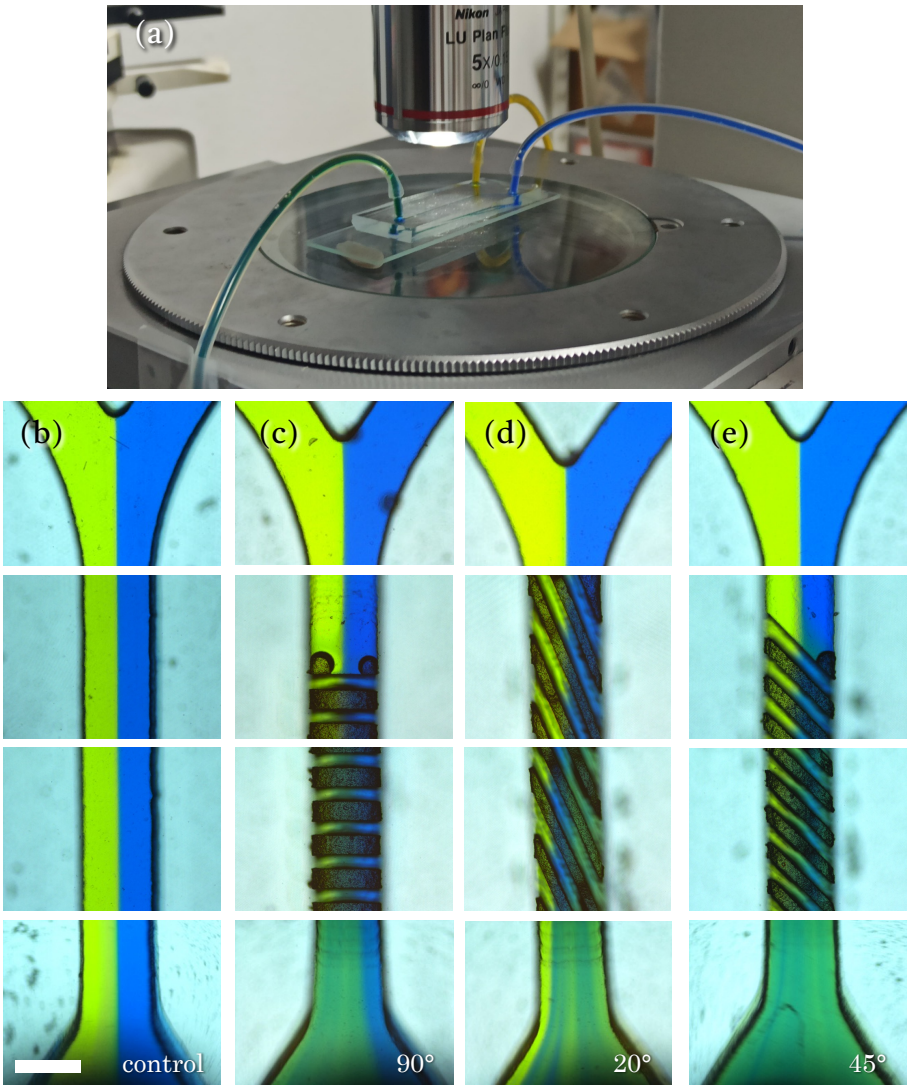

Figure 7.7: a) Experimental setup used in the flow essays were two dyes (blue and yellow) were mixed in the micromixers under an optical microscope. Optical microscope images (5×) of mixing test inside manufactured micromixers featuring b) none, c) 90°, d) 20°, and e) 45° oriented grooves. Scale bar: 500 μm.

In the first column (Figure 7.7b), it is evident that the blue and yellow dyes remain segregated and do not mix effectively within the 25 mm microchannel. This is mainly due to laminar flow, characterized by flow streams moving in parallel layers with minimal interaction, caused by the absence of microstructures designed to induce turbulent mixing. Moving to the second case with structures oriented at 90°, as depicted in Figure 7.7c, notable differences from the first image become apparent.

Initially, bubble trapping is observed when the fluid interacts with the first set of structures. However, this issue seems to be localized, and, overall, colours significantly mix at the device's outlet. This suggests that the 90° oriented structures do enhance the efficiency of dye mixing compared to the previous configuration without microstructures. Nevertheless, it is worth

noting that the presence of blue colour dominance on the right side could be attributed to specific flow patterns or uneven distribution of structures within the device. In next column, corresponding to structures oriented at 20° (Figure 7.7d), effective mixing is also observed at the device's outlet. Nevertheless, visible streams of yellow colour, reminiscent of the blue streams in the previous micromixer, indicate that there are still areas where mixing is not entirely uniform. Finally, the micromixer featuring 45° oriented grooves, as illustrated in Figure 7.7e, demonstrates the most promising results, with an extremely homogeneous mixture at the outlet. In this case, green colour at the output exhibits the greatest uniformity observed, surpassing all other flow configurations.

In summary, 45° configuration appears to overcome the limitations observed in the previous images, offering a high degree of mixture homogeneity. This makes it a promising choice for fluid mixing applications in micromixers. However, it's important to note that these experimental results are largely qualitative, making it challenging to draw definitive conclusions. As such, quantitative methods are needed to give us a better understanding of the system behaviour.

7.3.1.4 Numerical simulations

7.3.1.4.1 Simulation of manufactured micromixers.

To quantitatively assess the effectiveness of the micromixers, simulations were conducted on the manufactured micromixers (Figure 7.8). and mixing histograms were obtained. Water volume fraction is represented in the x-axis for two cross sections located at two distances, starting from the junction: x_1=-5.1 mm (red histogram) and x_2=-9.5 mm (blue histogram), arbitrarily chosen. On the other hand, y-axis illustrates the percentage of counts recorded at these two sections. For the sections, their colour scalebar represents the volume fraction of water in each pixel, that can be interpreted as the degree of mixing. Volume fractions close to green coloured pixels indicate a balanced coexistence of both liquids, while reddish or bluish pixels represent the solely presence of one phase.

For quantitatively assess the degree of mixing in each histogram, we define the Efficient Mixing Index (EMI) as

$$EMI = \frac{number\ of\ counts\ with\ water\ volume\ fraction\ between\ 0.4-0.6}{total\ number\ of\ counts}$$

Henceforth, the EMI will be calculated at x_2 cross section, as a higher degree of mixture is expected given the higher distance from the fluids meeting point.

Figure 7.8a shows a transversal section of the micromixer without structural elements at the bottom (acting as control). The cross sections reveal poor liquid mixing performance, that agrees with the absence of green pixels. The histogram shows nearly identical lateral

distributions for both cross sections across the microchannel, separated with a gap corresponding to the range of 0.4-0.5 water volume fraction. An EMI = 0.100 was obtained, implying that complete mixing is not achieved.

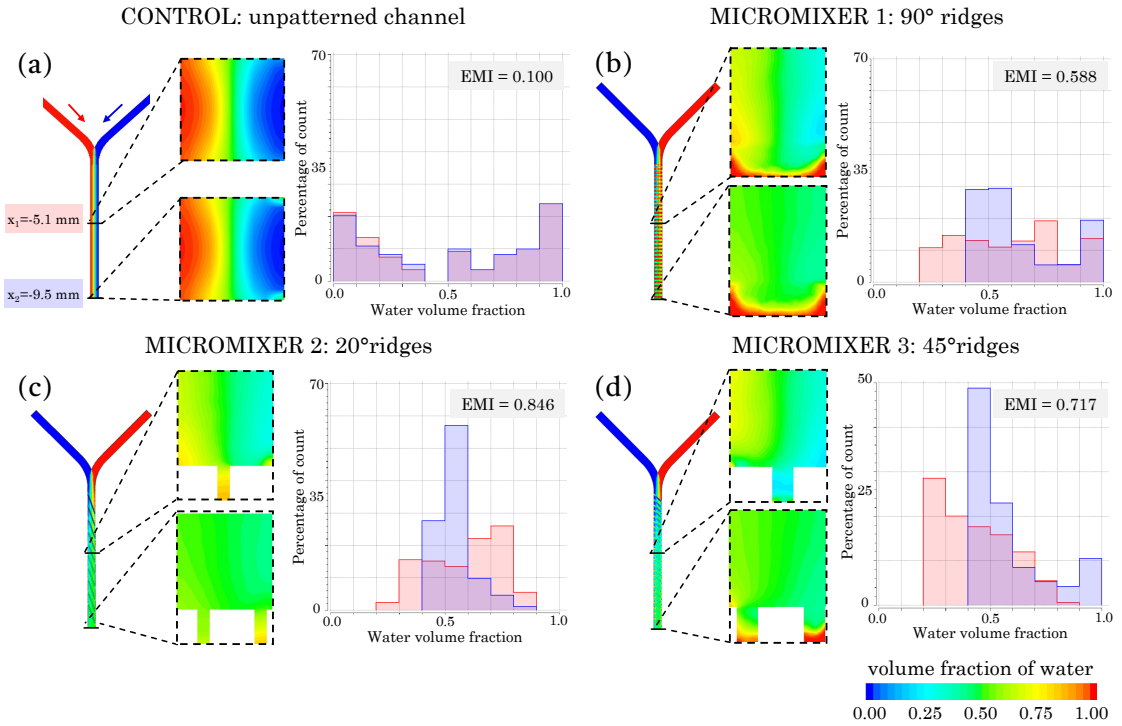

Figure 7.8: Top view, transversal section, and histograms of the volume fraction (from 0 to 1) of two flow samples inside an a) unpatterned microchannel and manufactured micromixers featuring b) 90°, c) 20° and d) 45° micropatterned grooves. Histograms correspond to two different points of the micromixer, x1= -5.1 mm (red) and x2= -9.5 mm (blue). Corresponding Efficient Mixing Index (EMI) is presented for each histogram.

Figure 7.8b illustrates the initial proposed micromixer featuring angled structures at a 90° orientation (Figure 7.8b), designed to enhance the mixing process. In this configuration, the histograms display a more centralized pattern, signifying that a notorious portion of the sample is in a state of mixing. At position x_1, the majority of data points fall within the range of 0.2 to 0.8 of water volume fraction, while at position x_2, de degree of mixture increases reaching an EMI=0.588. It's worth noting that the histograms show a substantial portion of the sample composed of pure water (between 0.9 and 1), accounting for 15% at x_1 and almost 20% at x2. This phenomenon is particularly noticeable in the cross-section, where it becomes evident that in the lower region of the mixer, corresponding to the grooves, water becomes trapped. This can be explained by the higher density of the water used in the simulations (ρ_1= 998.2 kg/m3) compared to the other fluid (ρ_2= 997.2 kg/m3), causing the fluid dynamics to promote downward flow and preventing effective interaction between the samples. Nevertheless, if we disregard the region containing the grooves, the mixture is highly favourable at position x_2, as indicated by the green colour in the top region, corresponding to 0.5 water volume fraction. In

the case of the micromixer featuring 20° angled structures (Figure 7.8c), a significant improvement in mixing performance was observed compared to the previous cases discussed. At position x_1, the histogram distribution shows wide profile, and the largest bar of the histogram (27%) corresponds to points clustering around 0.6 and 0.8 of water volume fraction.

However, the micromixer demonstrates its most promising outcomes, showcasing an EMI=0.846 at position x_2, which is closest to achieving complete mixing. This substantial improvement is visually evident in the cross-sectional views, where colour variations persist at x_1 but disappear at x_2, presenting a fully homogeneous distribution. Nevertheless, a phenomenon like the previous case is observed, with the lower structures tending to trap water. However, if we exclude this lower region, and we only compare the upper section with the control section (Figure 7.8a), the results are of total mixture.

Finally, results corresponding to micromixer with 45° angled structures (Figure 7.8d) position corresponds to an intermediate configuration between the results obtained for the 90° and 20° counterparts. Specifically, when examining position x_1, a significant portion of data points falls within the range of 0.2 to 0.4 for the water volume fraction. This performance ameliorates at position x_2, where EMI=0.717 was obtained, indicating a high mixing performance. However, like previous cases, unmixed water (accounting for 10%) becomes apparent in x2, primarily located in the lower region, and confined within the microstructures.

These findings emphasize the pivotal role of structural micromixer design in the mixing process. A closer examination reveals that structures performed at a 20° angle consistently deliver the most favourable outcomes over their counterparts at 90° and 45°, facilitating more thorough and uniform fluid blending. However, these simulations slightly diverge from experimental findings that favour the 45° angle. This can be attributed to not only simulations assuming highly ideal conditions but also experiments involving inherent variability. In terms of simulation, several simplified conditions were employed for computational efficiency, such as no sliding wall (not applicable to PDMS, an elastic material), isothermal and isobaric conditions (whereas temperature and pressure were not controlled during experiments), use of pure water and a similar sample (compared to dyed water used experimentally), short simulation time, neglect of gravity, and mesh size considerations. Experimentally, deviations arise from roughness resulting from the PDMS soft lithography process. This process transfers both resin and laser generated roughness, leading to less-than-ideal groove edges, a factor neglected in simulations.

Nevertheless, in both cases (simulation and experiments), it is clear that the incorporation of microstructures at the bottom of the mixer significantly enhances mixing compared to a flat channel (EMI=0.846 in Figure 7.8c compared to EMI=0.100 in Figure 7.8a). Among the various angle possibilities, mixing improves as the angle decreases from 90° (perpendicular to the channel).

7.3.1.5 Simulation of other micromixer configurations.

To optimize the micromixer design in terms of mixing efficiency, various configurations were evaluated using CFD simulations. Doubling the groove height resulted in a performance decrease, reaching an EMI of 0.231. In contrast, doubling the groove width significantly improved efficiency, achieving an EMI of 0.907. Doubling the height of slanted grooves at 20° and 45° also enhanced mixing performance. The most favourable results were observed for double width at 20° and 45° with EMIs of 0.982 and 0.997, respectively. Additionally, varying flow rates and fluid properties were analysed, yielding satisfactory results, such as an EMI of 0.863 at 20° for both Q=0.5 ml/min and a glycerine-water mixture (separated studies). These findings confirm the versatility of the micromixer designs.

7.3.1.6 Final devices

The versatility of this technique has been proved, enabling the straightforward, cost-effective, rapid, and user-friendly production of six distinct slanted micromixers for microfluidic applications. These micromixers feature micropattern at 20°, 45°, and 90° and were fabricated in resin or PDMS (Figure 7.9). Protocol 1 (depicted in Figure 7.9a,b) enables the manufacturing of microrreactors within a timeframe of less than 2 hours (1:30 h for substrate printing and 30 minutes for ablation). For its part, Protocol 2 (Figure 7.9c,d,e) requires a longer duration, due to PDMS curing process, which spans approximately 12 hours after printing and PLA. However, it is noteworthy that this replication step is very common in microfluidics workflows and can be seamlessly integrated into researcher routine by allowing the components remain in the oven overnight. Furthermore, some authors use a shorter curing time (Kaigala et al., 2007). After that, the final step consists in bonding the PDMS replicas to glass, which takes less than half an hour. Given the diverse nature of research projects, each user must focus in selecting the most suitable protocol in terms of time and resources to achieve optimal results.

In essence, the proposed process in this thesis represents a significant reduction in manufacturing time compared to photolithography, the predominant technology in microfluidics manufacturing, which can require days to complete. Another advantage of this technique is its capability to easily modify micropatterning designs simply by employing the laser software, virtually in real-time. This enhances the prototyping and testing processes for the devices. Moreover, our method is not contaminant and generates minimal waste as the 3D printer used to fabricate the masters reuses liquid resin that remains unphotopolymerized during the process. In the ablation process, only a negligible amount of dust (vaporized resin) is produced, which is promptly removed by the laser cleaning system.

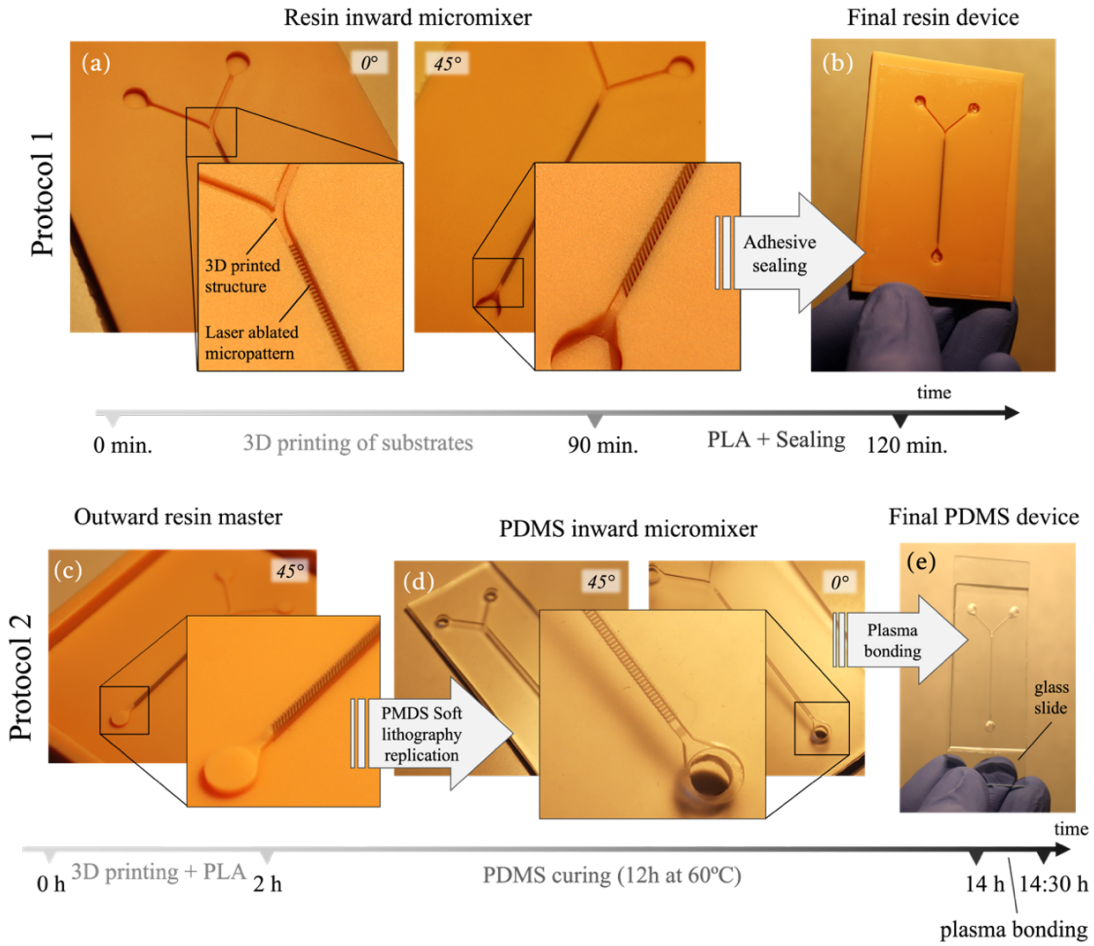

Figure 7.9: The two proposed protocols for manufacturing microreactors (micromixers in this case). In Protocol 1, the sequence begins with the 3D printing of a resin substrate, followed by PLA of inward channels at a) various orientations (e.g., 0°, 45°). These channels can then be b) sealed using an adhesive stick, and the entire process is completed in just 2 hours. Protocol 2 initiates with the c) 3D printing of masters (with added walls to retain replication polymer) and PLA of outward channels, followed by the d) soft lithography replication of the structures using PDMS. Subsequently, the replicas can be peeled off and e) plasma bonded to a glass slide. This protocol has an approximate duration of 14 h.

7.3.2 Microlens manufacturing.

7.3.2.1 Laser parameters for manufacturing.

The goal of this section is to determine the optimal laser ablation parameters for Model resin. For this, the study will focus on the formation holes instead of ridges and grooves, as previously. For this purpose, a series of marks were made by focusing the laser with different powers and number of passes on normally printed (S_a=1.5782 ± 0.2901 µm) and polished (S_a=0.6609 ± 0.1253 µm) resin surface. This consisted in the study of the effect of 1, 2 and 3 beam passes combined with the following ranges of power parameters: 10-130 mW range for unpolished resin and 20-180 mW for polished resin. The results of this analysis are summarized in Figure

7.10, which allows us to evaluate the ablation outcomes, ranging from minimal impact on the material to the point where undesired effects occur.

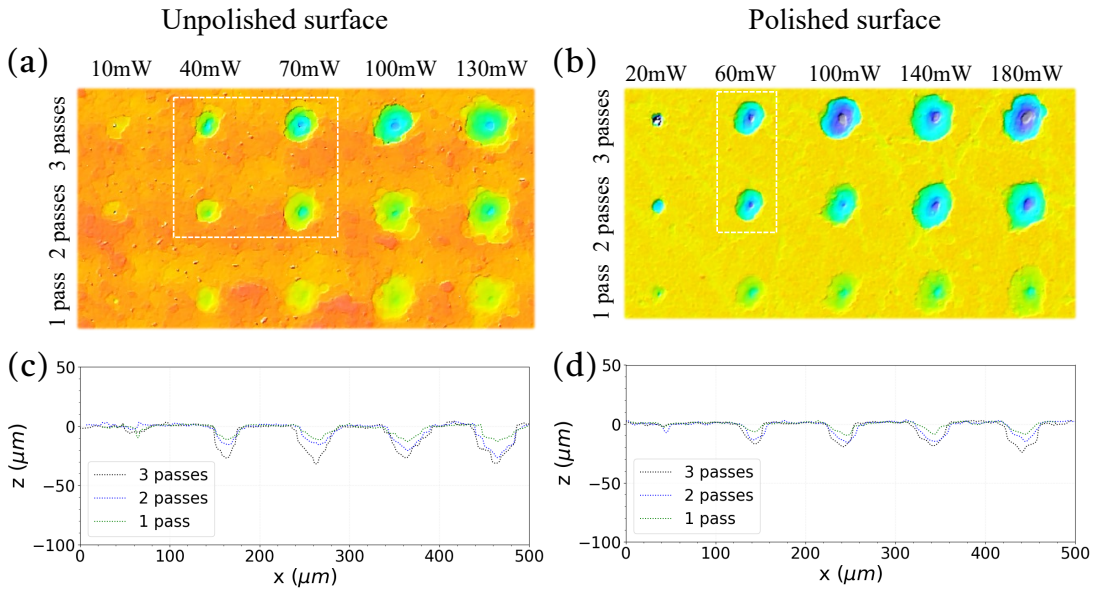

Figure 7.10: Confocal images of the ablation test performed for (a) unpolished and (b) polished surface of the resin with different beam passes (1-3) and powers (10-180 mW). Transversal section of the holes manufactured in the (c) unpolished and (d) polished surfaces.

First, for the case of unpolished resin, we observed how the ablation produces a series of marks for all parameters of study (Figure 7.10a). These marks range from small 15 µm diameter spots for 1 pass and 10 mW to larger 50 µm holes for 3 passes and 130 mW. Figure 7.10c shows the different cross-sectional profiles of the holes overlapped, revealing that higher passes and power resulted in greater diameters and depths of the holes. Furthermore, to obtain values for the diameter and depth of each hole, measurements were conducted 10 times for each, utilizing cross-sections at various angles. These results are presented in Figure 7.11.

Concerning diameters (Figure 7.11a), we observe a consistent increase across different passes, starting at around 20 µm for 10 mW and reaching 45 µm approximately for 130 mW in all cases. However, concerning depths (Figure 7.11b), the differences between the number of passes become more evident. With just one pass, the removal of material is very low, increasing depth by only 10 µm despite the power increase from 10 mW to 130 mW. It is with multiple passes that the effect begins to accumulate, increasing by about 20 µm in depth for two passes (from 7 to 27 µm) and even 26 µm (from 8 to 34 µm) for the three passes within the studied power range. Therefore, no information about the finishing of the created structures can be extrapolated. For this reason, when selecting appropriate ablation parameters, we should crosscheck with confocal images (Figure 7.10) to identify those holes with more circular symmetry, as this is the most common profile for microlens. As can be seen, once the powers exceed 100 mW, excessive energy is transferred to the material and the ablation result is not

adequate, as the edges are very irregular and produce non-circular holes. That is why, for unpolished resin, the selected range of parameters for the ablation of the structures was chosen between 2 and 3 passes and 40 and 70 mW (marked area in Figure 7.10a).

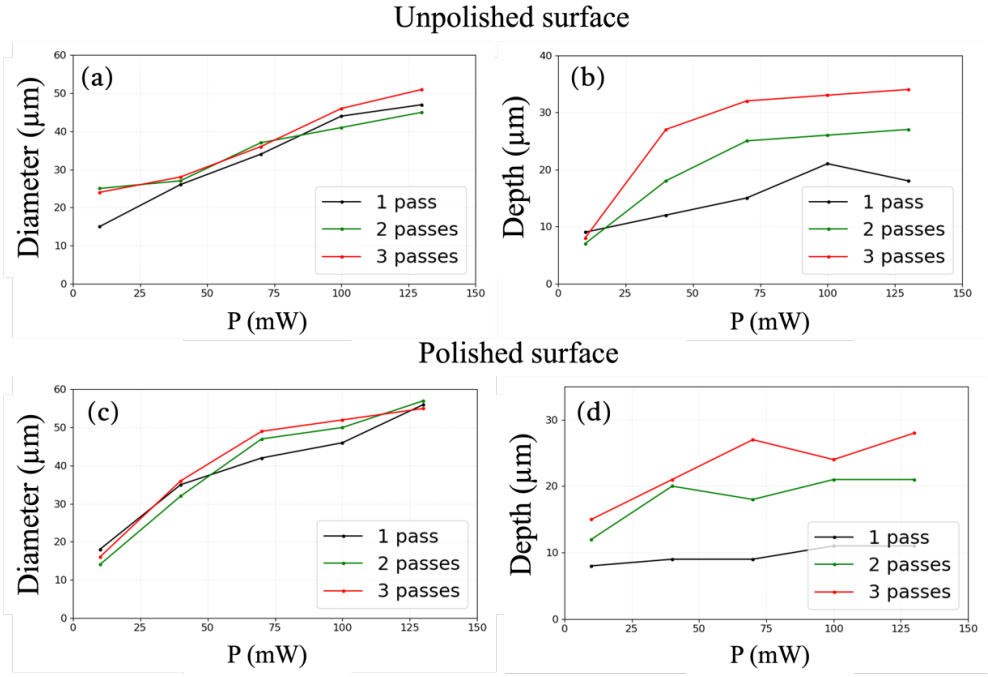

Figure 7.11: Evolution of the a), c) diameter and b), d) depth of the ablated holes with the studied parameters for unpolished (top) and polished (bottom) surfaces.

Regarding the polished resin, once again all the selected parameters are capable of removing material to a greater or lesser extent (Figure 7.10b), resulting in an array of holes from which the profiles can be taken for performing measurements (Figure 7.10d). The results for the diameters in this case are quite similar to those obtained for the unpolished resin, showing an upward trend with power (Figure 7.11c). However, it is noticeable that to obtain similar results, in the case of polished resin, a higher power was required. This difference may be attributed to the fact that polishing removes the most superficial layer of the resin, which is more susceptible to radiation, exposing the interior of the piece, which is significantly more opaque and less responsive to PLA. Therefore, the holes start with diameters close to 10 µm for 20 mW and increase with power until reach approximately 55 µm (a subtly higher value than in the previous case). The results for 3 and 1 passes initially appear similar but diverge at 40 mW, with 2 passes yielding higher results than 1 pass. Regarding depths (Figure 7.11d), the attenuation effect of removing the surface layer with polishing is very notorious for one pass, with which the material removal is minimal, achieving only a 3 µm increase (from 8 to 11 µm) in depth during the 20-180 mW range. With additional passes, material removal increases, although it is still lower than in the unpolished case: the maximum achievable depth with 2 passes is 21 µm (compared to 26 µm previously), and with 3 passes, it reaches 28 µm (compared to 34 µm previously). Regarding the selected interval for the manufacturing, as can be seen in Figure 7.10b, the edges

of the holes become irregular from 100 mW onwards, deviating from the circular profile. Therefore, for polished resin, the selected range of parameters for the ablation of the structures was selected between 2 and 3 passes and 50 and 60 mW (marked area in Figure 7.10b).

7.3.2.2 Manufactured microlens arrays

7.3.2.2.1 Unpolished surface

The subsequent stage of the research involved the fabrication of various arrays (20 × 20 microlens and 100 µm of period) of inward microlens utilizing identical parameters on the unpolished surface of the resin via PLA. Figure 7.12 illustrates the outcomes for the unpolished resin, presenting confocal images of the surfaces. The initial observation underscores the reproducibility of our methodology, as evidenced by the consistent formation of microlens in a regular pattern. However, certain defects are discernible, notably in Figure 7.12a, corresponding to 40 mW and 2 passes, where irregular borders of the highlighted (in the red circle) microlens are apparent. These defects can be attributed to the pronounced superficial roughness of unpatterned surfaces, which can foster non-uniform laser ablation. Additionally, Figure 7.12a depicts outcomes for the lower energy levels, that may be insufficient to adequately remove the material. Increasing the number of passes enhances the outcomes, as evidenced by Figure 7.12c, corresponding to 40 mW and 3 passes, where the borders of the holes are more clearly defined. This trend persists with increasing power, as depicted in Figure 7.12b and d, corresponding to 50 mW and 2 and 3 passes, respectively.

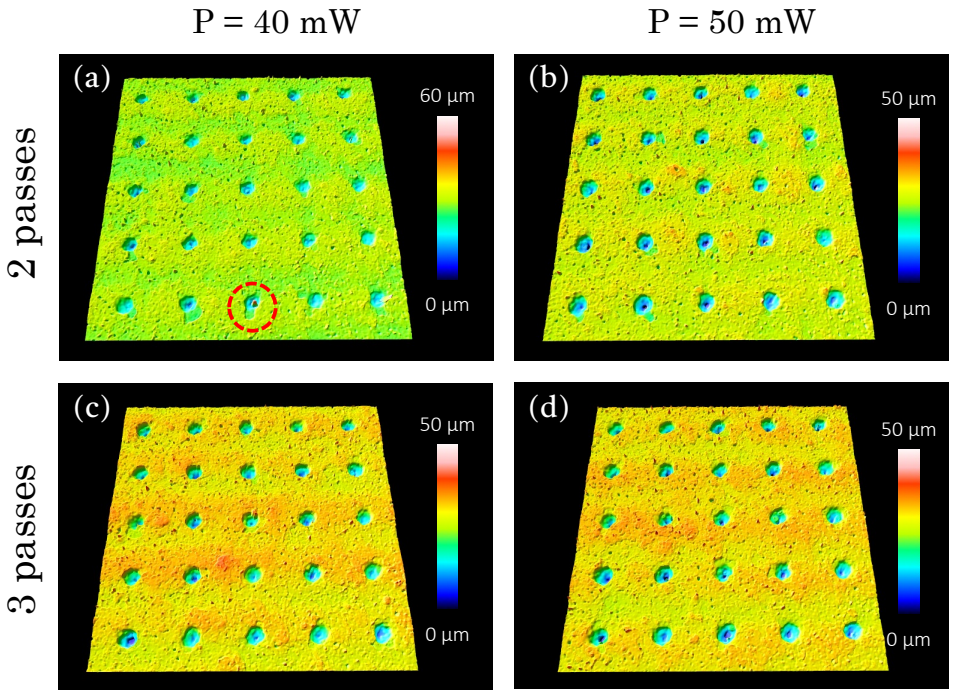

Figure 7.12: Confocal images of microlens arrays manufactured on unpolished resin surface employing a) 40 mW and 2 passes (red circle marks a highly irregular border), b) 50 mW and 2 pases, c) 40 mW and 3 passes and d) 50 mW and 3 passes.

Geometric data of these structures were extracted from the confocal images, and the results are tabulated in Table 7.3. The data reveals that both diameter and depth increase with laser power and passes, consistent with the findings in Figure 7.11. All diameters and depths hover around 25 µm, with slight variations corresponding to the laser parameters. This results highlight the similarity in magnitudes between the depth and diameter for each lens. To properly analyse this aspect, a ratio between diameter and depth was calculated. This ratio serves as a determinant of the degree to which our lenses conform to a spherical shape, aligning with our objectives. The closer the ratio is to 2, the more spherical the lens is expected to be. However, for the unpolished resin, this ratio remains relatively low, averaging around 1, indicating a more ellipsoidal shape rather than a spherical one. The underlying cause of this outcome can once again be attributed to the non-uniform surface of the unpolished material, which may concentrate the energy of the beam in a localized area rather than distributing it evenly. The most favourable outcomes in terms of sphericity are achieved for lenses manufactured at 40 mW and 2 passes, yielding a ratio of 1.23. Nevertheless, this ratio remains too low to consider the lens truly spherical, rendering this scenario less desirable.

	a	**b**	**c**	**d**
Laser Power (mW)	40	50	40	50
Laser passes	2	2	3	3
Diameter (µm)	22.8 ± 3.5	24.4 ± 5.8	26.0 ± 4.8	29.7 ± 4.5
Depth (µm)	18.5 ± 4.8	22.0 ± 5.4	25.4 ± 12.3	29.2 ± 12.3
Diameter/Depth	1.23	1.11	1.02	1.02

Table 7.3: PLA parameters, measured dimensions, and diameter/depth ratios of the microlens arrays manufactured on the unpolished resin surface.

7.3.2.2.2 Polished surface

20×20 and 100 µm of period arrays of inward microlens were also micropatterned onto the polished surface of the resin using PLA. The results obtained from various confocal images are depicted in Figure 7.13. A notable observation, in addition to the previously noted reproducibility, is the reduction in surface roughness, resulting in a surface more homogeneous. Another significant improvement is observed in the regularity of the lens borders. As previously mentioned, the surface polishing removes superficial layers, resulting in a more uniform ablation process. However, the least satisfactory results are evident in Figure 7.13a, corresponding to the use of 50 mW power and 2 passes, obtaining microlens with irregular border (specially the one highlighted in the red circle)In this instance, the deviation from ideality of the lens borders is most pronounced due to the lower power employed and incomplete material removal.

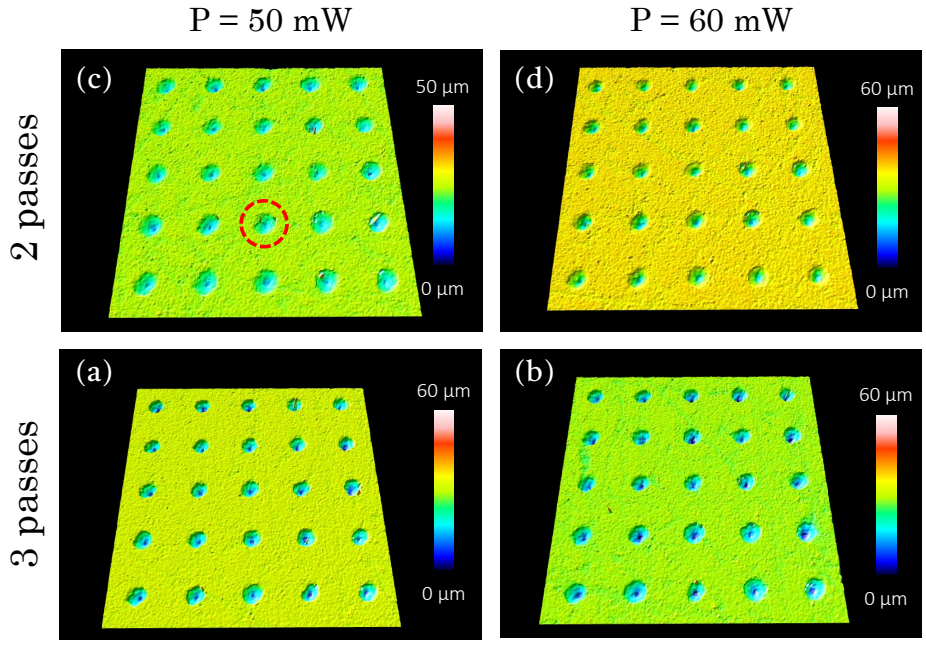

Figure 7.13: Confocal images of microlens arrays manufactured on polished resin surface employing a) 50 mW and 2 passes, b) 60 mW and 2 pases, c) 50 mW and 3 passes and d) 60 mW and 3 passes.

Corresponding measured data for the manufactured lenses are presented in Table 7.4. Like the previous case, both the diameter and depth increase with laser power and passes, as illustrated in Figure 7.13. In this scenario, all diameters are approximately 40 µm, with depths averaging around 20 µm. Notably, the improvement in PLA outcomes is evident, as the diameters are now double the depth, closely resembling a spherical shape. This outcome aligns more closely with our objectives and can be verified using the diameter/depth ratio. The most spherical lenses are obtained employing 50 mW and 2 passes, offering a ratio of 1.89, followed by a ratio of 2.15 for 60 mW and 2 passes.

	a	**b**	**c**	**d**
Laser Power (mW)	50	60	50	60
Laser passes	2	2	3	3
Diameter (µm)	36 ± 4.2	43 ± 5.4	39 ± 3.7	45 ± 7.0
Depth (µm)	19 ± 2.1	20 ± 3.5	23 ± 5.8	26 ± 4.2
Diameter/Depth	1.89	2.15	1.69	1.73

Table 7.4: PLA parameters, measured dimensions, and diameter/depth ratios of the microlens arrays manufactured on the polished resin surface.

7.3.2.3 Replication of the structures by PDMS soft lithography

Once the ablation parameters were analyzed and optimized, manufactured inward arrays were replicated employing PDMS soft lithography, for further analysis using microcomputed

tomography (Figure 7.14a). This replication was performed for polished and unpolished resin masters. Three of these arrays can be observed in a 7×2×0.5 mm^3 volume (Figure 7.14b) extracted from the PDMS replica introduced in the MicroCT scanner. Within this section, three distinct arrays are observable, each delineated by surrounding walls formed through the ablation of square perimeters in the resin. Each of these arrays were fabricated with laser parameters presed in Table 7.4, with the aim of assessing the quality of the replicas.

The replicas obtained were of good quality since the vast majority of the microlens have formed correctly, detaching completely from the master. In Figure 7.14c, the replicate is correct except for the absence of a lens in the upper right region (Figure 7.14c). In Figure 7.14d, corresponding to 50 mW and 3 passes, a complete replicate of the lenses is observed. Finally, in Figure 7.14e, a region can be observed on the left in which the profile of the lenses has been disturbed, in some cases not forming at all.

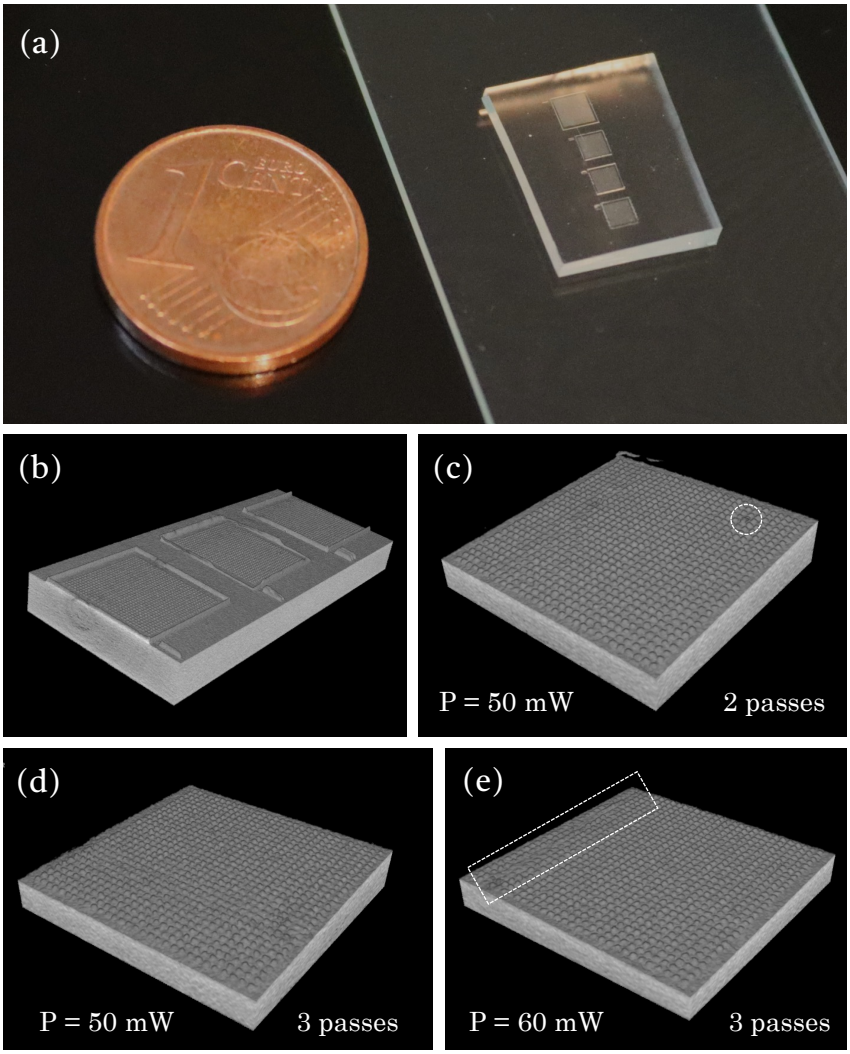

Figure 7.14: a) Picture of 4 arrays of microlens made of PDMS (placed on a glass slide). A euro cent is placed nearby as a reference. MicroCT images of b) a section of three arrays, and detailed look of 3 different arrays, corresponding to c) 50 mW, 2 passes; d) 50 mW, 3 passes; and e) 60 mW, 3 passes.

It is important to note that the demoulding step of PDMS soft lithography represents one of the most critical steps in the overall process. Once a defect occurs during demoulding, it becomes exceedingly challenging to rectify it in subsequent replicates. This is primarily because if a PDMS lens breaks during demoulding and becomes lodged within the hole created by PLA, subsequent replication processes will fail to fill this structure, resulting in the cessation of lens formation in successive iterations of the process. Nevertheless, PDMS typically demonstrates adequate replication of structures on the micron scale.

7.3.2.4 Focus characterization

7.3.2.4.1 Unpolished surface

Utilizing the optical setup detailed in Materials and Methods 4.2.1, an analysis of the focal length of the fabricated microlens manufactured on unpolished substrate was conducted. This involved capturing and measuring the focal properties of the lenses using two distinct sensors: a beam profiler and an optical camera.

The examination commenced with the acquisition of a flat field image, as depicted in Figure 7.15a, where the sensor was positioned with free space between it and the laser source. Upon the introduction of the microlens into the setup, a noticeable transformation in the acquired profile was observed. The microlens exhibited their ability to reconfigure the energy distribution of the incoming light, effectively concentrating it into regular patterns that closely mimicked the original square pattern of the arrays. This redistribution of energy is clearly observed in Figure 7.15b-e. A striking observation from the images is the uniformity and consistency of the pattern formed by the microlens, with the energy distribution appearing most regular in the case where 50 mW and 3 passes of power were utilized.

Furthermore, Figure Figure 7.15f-i presents optical images capturing the focus of the microlens. These images provide additional insights into the behaviour of the lenses and further corroborate the findings obtained from the beam profiler and sensor data.

Subsequently, experimental focal distance and theoretically derived focal length (calculated using the thin lens equation[2] based on experimental radius) were crosschecked. These comparative results are tabulated in Table 7.5, alongside a relative error quantifying the disparity between experimental and theoretical focal lengths.

The findings revealed significant deviations attributable to irregularities encountered during the fabrication process of microlenses on an unpolished substrate. Notably, the relative errors surpassed 25% for half of the cases, with a discernible trend of increasing error corresponding to decreasing focal length. This discrepancy originates from the previously mentioned

[2] $\frac{1}{f} = (n-1)\left[\frac{1}{R_1} - \frac{1}{R_2}\right]$

observation that the lenses we produced exhibit more of an elliptical structure rather than the spherical shape assumed in the thin lens equation.

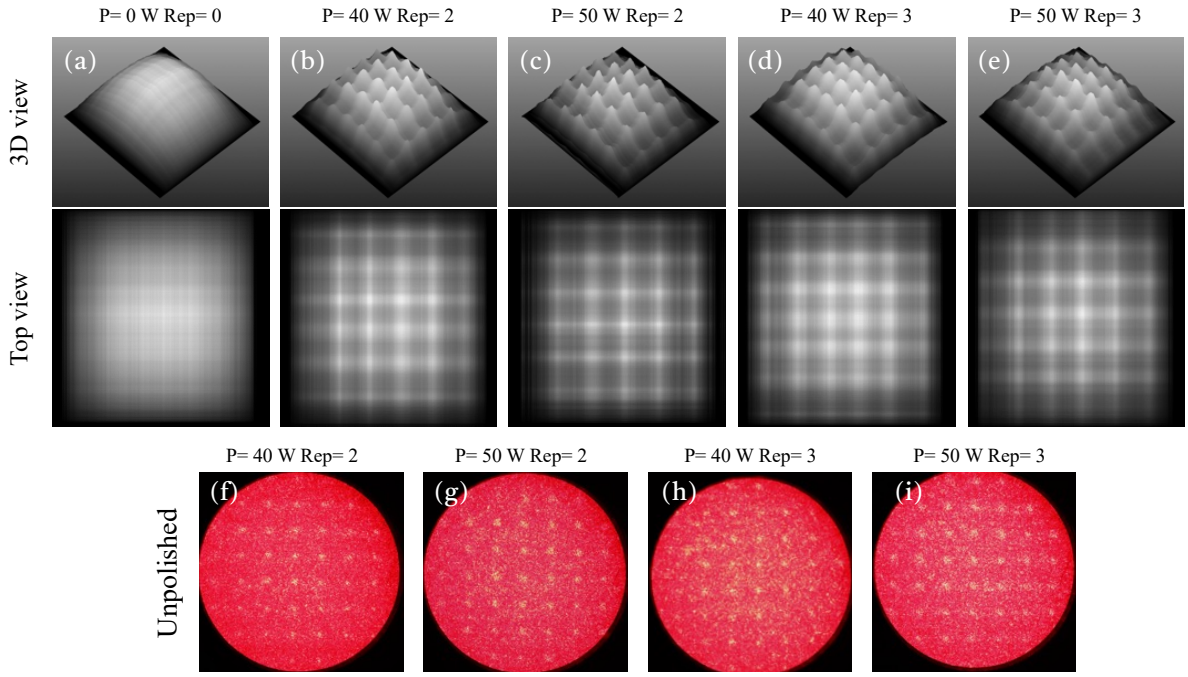

Figure 7.15: Images at the focal plane of microlens obtained using a beam profiler (top) and an optical camera (bottom), manufactured on an unpolished substrate by PLA. Different laser parameters were used in the manufacturing process: a) 0 mW, 0 repetitions; b), f) 40 mW, 2 repetitions; c), g) 50 mW, 2 repetitions; d), h) 40 mW, 3 repetitions; and e), i) 50 mW, 3 repetitions. Repetition rate: 1kHz. Platform velocity 1mm/s.

Moreover, the substantial standard deviation observed in the experimental focal length measurements underscores the unreliability of this method. Additionally, Figure 7.15 illustrates pronounced light noise resulting from uneven light distribution caused by surface roughness, leading to light scattering into inter-lens regions. Polishing the surfaces previous to PLA can reduce this drawbacks.

	a	**b**	**c**	**d**
Theoretical f (µm)	45	55	62.5	72.5
Experimental f (µm)	31.8 ± 9.8	40.1 ± 12.3	48.6 ± 8.9	59.0 ± 12.2
Relative error[3] (%)	29	27	22	19

Table 7.5: Theoretical focal length obtained employing the measured diameter of lenses for the unpolished resin. Experimental focal length measured employing the optical setup. Relative error between two magnitudes.

[3]Relative error = |(Experimental f - Theoretical f)/Theoretical f| · 100

7.3.2.4.2 Polished surface

In this case, analysis of the focal length of the fabricated microlens manufactured on polished substrate was conducted, employing the same setup as before. Results are presented in Figure 7.16. Once more, inserting the microlens arrays into the path of the laser beam results in the refraction of light, which subsequently conforms to the pattern corresponding to the arrangement of the original lenses. The main difference between this and the previous case is the fact that now the peaks observed in the 3D view of the beam profiler are more sharpen (Figure 7.16b-e), since the roughness reduction also reduces the noise (unwanted scattered light). This phenomenon can also be observed in the photographs taken of the focal plane (Figure 7.16f-i). These images reveal reduced scattering between the focal points, particularly evident in cases presented in Figure 7.16f,g. However, undesired scattered light still persists. Several strategies can be employed to enhance this outcome: further compacting the arrays by reducing the spacing between microlenses and applying chemical treatments to the resin to eliminate residual roughness on both the surface and the ablated microlenses. These approaches will be explored in future research.

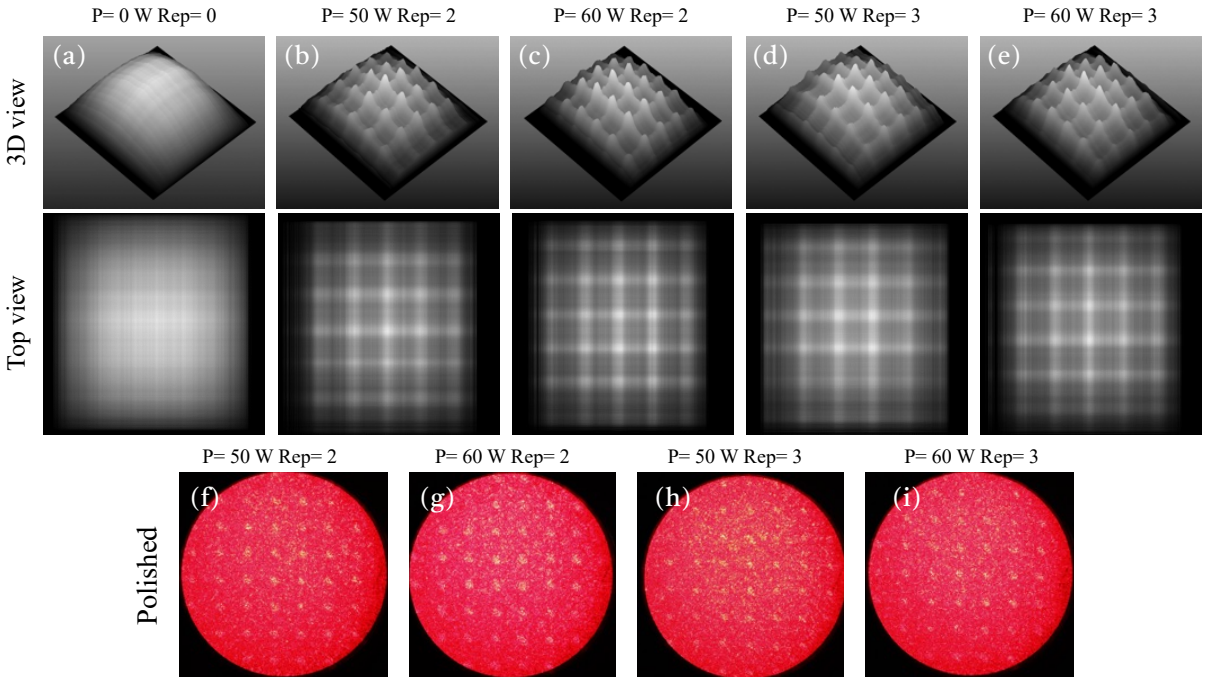

Figure 7.16: Images at the focal plane of microlens obtained using a beam profiler (top) and a optical camera (bottom), manufactured on a polished substrate by PLA. Different laser parameters were used in the manufacturing process: a) 0 mW, 0 repetitions; b), f) 50 mW, 2 repetitions; c), g) 60 mW, 2 repetitions; d), h) 50 mW, 3 repetitions; and e), i) 60 mW, 3 repetitions. Repetition rate: 1kHz. Platform velocity 1mm/s.

Similarly to before, the focal distances of the lenses were measured and compared with their theoretical values. In this case, the results (presented in Table 7.6 are much closer, with errors of only 10% (and even lower in some cases). This improvement is attributed to a better ablation achieved through surface polishing, which brings the holes created by ablation, and

consequently, the replicated lenses, closer to a semi-spherical geometry. The focal lengths are around 50 μm. The best result is obtained for 60 mW and 2 repetitions, with a relative focal error of 6%. This array provides one of the focal planes with the sharpest focal points and less scattered light (Figure 7.16f,g).

	a	**b**	**c**	**d**
Theoretical f (μm)	47,5	50	57,5	65
Experimental f (μm)	42.5 ± 6.1	52.9 ± 7.3	52.3 ± 5.6	57.6 ± 5.7
Relative error (%)	10	6	9	11

Table 7.6: PLA parameters and measured dimensions of the microlens arrays manufactured on polished resin surface.

7.4 CONCLUSIONS

7.4.1 Micromixer

In this chapter a novel hybrid technique combining PLA and SLA is proposed for manufacturing and testing passive micromixers, of great interest in the field of microfluidics. For this, an optimization of laser ablation power for microchannel fabrication was carried out. The width and depth of channels were measured, finding that power is correlated with channel width, and more passes generally widened the channels. However, high power pulses may cause irregularities. Optimal parameters for regular, homogeneous channels were identified as 90 mW, repetition rate of 1kHz, 1mm/s of platform velocity and 2 passes, resulting in channels with a width of 39.6 ± 1.9 μm and a depth of 129.1 ± 2.3 μm. To enhance fluid flow and proper PDMS removal, wider channels were desired, achieved by ablating two or more contiguous lines with varying separations. The results showed that ablating three contiguous lines with a 35 μm separation provided the most suitable channels, with a width of 95.5 ± 5.2 μm and a depth of 230.9 ± 4.7 μm.

Using these parameters, two manufacturing protocols were developed, with the goal of manufacture various groove patterns with different orientations in the channels (that will enhance mixing). Protocol 1 is focused on micropatterning the bottom of inward channels using PLA, to be sealed directly with adhesive film for immediate use. In the case of 90° oriented structures, optical images revealed consistent groove formation, featuring a width of 94.3 ± 8.3 μm and depth of 243.5 ± 15.5 μm. For 20° structures, narrower grooves (86.6 ± 4.0 μm) were observed due to the overlap of the lines achieving a greater depth (253.3 ± 11.1 μm). For 45° structures, an intermediate scenario was obtained. Protocol 2 starts with the creation of grooves on the top of outward channels using PLA for subsequent replication through PDMS soft lithography, facilitating scalable production. For 90° orientation, proper groove formation (W=123.0 ± 4.8 μm) is achieved. In this protocol, grooves in the master become ridges in the

replicas and vice versa. The depth of master grooves is notably greater (301.3 ± 9.9 μm) than the obtained in Protocol 1, since ablation on an elevated structure increases to debris release. Figures show a 3D confocal view of successful master-to-replica transfer and show similar surface roughness, demonstrating high the replication capability of PDMS.

Flow experiments were conducted in micromixers with different orientations (90°, 20°, and 45°) using a peristaltic pump and coloured dyes. The 45° orientation presents the most homogeneous mixing, offering promise for fluid mixing applications, but quantitative methods were required for more definitive insights. For this, CFD simulations were used, revealing the following behaviours: in a control micromixer without structures, mixing was ineffective; a micromixer with 90° structures improves mixing, with some trapped water in the grooves; the 20° angled structures demonstrated significant improvement, with more homogeneous mixing capabilities than the others. Finally, the 45° angled structures provided intermediate results. Different scenarios involving new geometries, flowrates and physical properties were introduced, yielding the following conclusions: first, doubling groove width significantly enhances mixing efficiency, resulting in a nearly perfect mixture. Second, the micromixers demonstrate high versatility when considering various fluid properties (density and viscosity), producing outcomes closely resembling the original conditions. In brief, simulation results favoured 20° structures, while experiments preferred 45°, but both showed that microstructures enhance mixing compared to flat channels, with lower angles contributing to better mixing.

In summary, a significant advancement for the fabrication of passive micromixers is presented, by a versatile hybrid technique that combines SLA and PLA in their most suitable dimensional range.

7.4.2 Microlens

This chapter presents a comprehensive investigation aimed to the manufacturing of microlens arrays by combining SLA and PLA. Unlike the previous study, focused primarily on microchannel formation, this research delves into the process of hole manufacturing, crucial for the creation of precise microlenses. For this, a meticulous study was carried out to determine optimal ablation parameters for Model resin. The study encompassed various laser powers and passes, evaluating their impact on both unpolished and polished resin surfaces. Confocal images and measured dimensions synthesized the outcomes, aiding in identifying suitable parameters that strike a balance between material removal and desired hole morphology. For unpolished resin, confocal images revealed deviations from ideal circular symmetry, indicating a more ellipsoidal shape. The optimal parameters for unpolished resin were determined to be 2 to 3 passes and 40 to 70 mW, obtaining inward microlenses of around 25 μm in diameter and depth. On polished resin surfaces, microlens arrays exhibited improved regularity and reduced surface roughness, resulting in more uniform ablation outcomes. The diameters and depths of the microlens increased with power and passes, with a more spherical shape observed. The selected

range for polished resin ablation was 2 to 3 passes and 50 to 60 mW, achieving inward microlenses of around 40 μm in diameter and 20 μm in depth.

Replication of microlens arrays using PDMS soft lithography yielded satisfactory results, demonstrating good replication fidelity. However, careful demoulding is crucial to avoid defects that can compromise subsequent replicates. Focus measurements conducted on both unpolished and polished substrates provided valuable insights into the optical characteristics of the fabricated microlenses. These measurements revealed significant discrepancies between the experimental and theoretical focal lengths, particularly pronounced in the case of unpolished substrates. The observed deviations were attributed to irregularities in microlens shape and surface roughness, which led to increased light scattering and inaccuracies in focal length determination. In contrast, polished substrates exhibited superior performance, with errors reduced to 10% or less, owing to improved ablation quality and reduced surface roughness.

Additionally, it's worth noting that the use of flexible microlenses offers several advantages beyond their optical properties. Their inherent flexibility makes them inherently less fragile, and allows them to conform to different surfaces, offering high adaptability for integration into flexible devices and systems, especially those requiring conformal optics or optical components on curved surfaces. Furthermore, to address the challenge of surface roughness, a chemical etching process could be considered. Chemical etching has the potential to reduce surface roughness, thereby improving the focusing properties of the microlens and potentially reducing the relative errors observed in focal length measurements. This approach could further enhance the performance and reliability of microlens arrays, making them more suitable for various applications in optics and imaging.

8. BIOLOGICAL APPLICATIONS

This chapter is a partial reprint of:

Carlos Casas-Arozamena[a], Alberto Otero-Cacho[b], Bastian Carnero[c] , Cristina Almenglo[d,e], Maria Aymerich[c], Lorena Alonso-Alconada[a] , Alba Ferreiros[a] , Alicia Abalo[a] , Carmen Bao-Varela[c] , Maria Teresa Flores-Arias[c], Ezequiel Alvarez[d,e,f], Alberto P. Muñuzuri[b] and Miguel Abal[a,g]*, *Haemodynamic-dependent arrest of circulating tumour cells at large blood vessel bifurcations as new model for metastasis,* Scientific Reports (2021), DOI: 10.1038/s41598-021-02482-x

[a]Translational Medical Oncology Group (Oncomet), Health Research Institute of Santiago de Compostela (IDIS), University Hospital of Santiago de Compostela (SERGAS), Trav. Choupana s/n, 15706 Santiago de Compostela, Spain.

[b]Institute CRETUS, Group of Nonlinear Physics, Department of Physics, University of Santiago de Compostela, 15782 Santiago de Compostela, Spain.

[c]Photonics4Life Research Group, Applied Physics Department, Faculty of Physics, University of Santiago de Compostela, 15782 Santiago de Compostela, Spain.

[d]Cardiology Group, Health Research Institute of Santiago de Compostela (IDIS), University Hospital of Santiago de Compostela (SERGAS), Trav. Choupana s/n, 15706 Santiago de Compostela, Spain.

[e]Centro de Investigacion Biomedica en Red de Enfermedades Cardiovasculares (CIBERCV), Madrid, Spain.

[f]Department of Pharmacology, Pharmacy and Pharmaceutical Technology, University of Santiago de Compostela, 15782 Santiago de Compostela, Spain.

[g]Centro de Investigacion Biomedica en Red de Cancer (CIBERONC), Monforte de Lemos 3-5, 28029 Madrid, Spain.

*email: miguel.abal.posada@sergas.es

and:

Ana I. Gómez-Varela[a,*], Antonio Viña[b], Carmen Bao-Varela[a], María Teresa Flores-Arias[a], Bastián Carnero[a], Mercedes González-Peteiro[c], José Ramón González-Juanatey[d], and Ezequiel Álvarez, *Biocompatibility Testing of UV-Curable Polydimethylsiloxane for Human Umbilical Vein Endothelial Cell Culture on-a-Chip,* ACS Omega (2024), DOI: https://doi.org/10.1021/acsomega.4c01148

[a]Photonics4Life Research Group, Departamento de Física Aplicada, Facultade de Física and Facultade de Óptica e Optometría, Instituto de Materiais (iMATUS), Universidade de Santiago de Compostela, Santiago de Compostela E15782, Spain

[b]Departamento de Farmacología, Farmacia y Tecnología Farmacéutica, Universidade de Santiago de Compostela, Santiago de Compostela 15782 A Coruña, Spain

[c]Departamento de Enfermería, Santiago de Compostela, A Coruña 15782, Spain

[d]Instituto de Investigación Sanitaria de Santiago de Compostela (IDIS), Complexo Hospitalario Universitario de Santiago de Compostela (CHUS), Santiago de Compostela, A Coruña 15706, Spain; Departamento de Medicina, Universidad de Santiago de Compostela, Santiago de Compostela 15706 A Coruña, Spain; Servicio de Cardiología y Unidad de Hemodinámica, Complexo Hospitalario Universitario de Santiago de Compostela (CHUS), SERGAS, Santiago de Compostela 15706 A Coruña, Spain

[e]Departamento de Farmacología, Farmacia y Tecnología Farmacéutica, Universidade de Santiago de Compostela, Santiago de Compostela 15782 A Coruña, Spain; Departamento de Medicina, Universidad de Santiago de Compostela, Santiago de Compostela 15706 A Coruña, Spain; Servicio de Cardiología y Unidad de Hemodinámica, Complexo Hospitalario Universitario de Santiago de Compostela (CHUS), SERGAS, Santiago de Compostela 15706 A Coruña, Spain; CIBERCV, 28029 Madrid, Spain

*email: anaisabel.gomez@usc.es

This chapter presents some biological applications of the microfluidic platforms manufactured using the techniques presented in the previous chapters. We begin with a detailed biocompatibility study of the materials used, employing Human Umbilical Vein Endothelial Cells (HUVEC). A microfluidic platform designed to elucidate the homing mechanisms of Circulating Tumour Cells (CTC) within metastatic processes is introduced, employing bifurcated Y-shaped microchannels. Furthermore, the development of a sensorized microfluidic Ussing chamber, a widely utilized analytical device in biomedicine for studying biological barriers, is described.

8.1 BIOCOMPATIBILITY OF THE MANUFACTURED DEVICES

8.1.1 Introduction

Once all the aspects related to the manufacture of channels to obtain the most precise and physiologically mimetic results are analysed, it is necessary to focus on the study of a critical aspect for printed microfluidic devices in biological and biomedical applications: biocompatibility (Gharib et al., 2022; Zommiti et al., 2022).

Biocompatibility is defined as the material harmlessness in biological systems. In other words, a biocompatible material should not cause toxicity, inflammation, or rejection by the body and must be safe for use in medical or biological applications. Talking about biocompatibility in general terms can be misleading since is essential to conduct a detailed study for the specific cell line intended to be used (Aymerich et al., 2016). A material considered biocompatible for one type of cell line may exhibit completely different interactions and potentially harmful effects with another cell line, being especially relevant in the case of comparing cancerous cell lines and primary cultures. This variability necessitates a meticulous and cell type-specific approach to biocompatibility testing

In this chapter, the biocompatibility of several specific materials will be evaluated including: transparent 3D printing **resins**; standard PDMS, the main polymer used during in microfluidics for soft lithography (McDonald & Whitesides, 2002) and UV curable PDMS (UV-PDMS) (Jiang et al., 2022), a new type of PDMS that can be cured through UV irradiation and can simplify manufacturing protocols.

8.1.2 Materials and methods

8.1.2.1 3D printing resins

Round discs with a diameter of 3.5 cm and a height of 5 mm were printed to conduct biocompatibility studies on the surface of 3D printing resins (Materials and Methods 4.1.3), specifically by evaluating cell proliferation under static conditions. The biocompatibility of PDMS and various printing resins, along with the respective disinfection or sterilization

protocols, according with the suppliers, are detailed in Table 8.1. To grant the manufacturing of useful and versatile microfluidic platforms, only transparent (see Chapter 6.3.2) and replicable (see Chapter 6.3.5) 3D printing resins (Amber, Clear, and Dental) were selected for the biocompatibility studies.

A two-step polishing process was carried out after fabrication to one or both faces of the discs in order to evaluate the difference in the transmission spectra and the improvement of the optical quality, employing a Logitech PM 2A polisher. In the first step, an iron disc plate and an abrasive solution of Al_2O_3 were used to perform the roughing. The second step consisted on optical polishing of the material combining an expanded polyurethane disc with silica solution.

Priting Resin	**Biocompatible**	**Sterilizable**	**Disinfectable**	**Transparency**	**Method of sterilization/ disinfection**
Clear V4	✓	✓	✓	✓	Autoclavation
BioMed Amber V1	✓	✓	✓	✓	Autoclavation
Dental LT V1*	✓	×	✓	✓	70% IPA for 5 minutes
Elastic 50A V1	×	✓	✓	✓	Autoclavation
Tough 2000 V1	×	×	×	×	-
Model V2	×	×	×	×	-
Flexible 80A V1	×	×	×	✓	-
PDMS	✓	×	×	✓	Autoclavation

Table 8.1: Manufacturer properties of the different resins used in our study and for PDMS. The autoclavable pieces underwent 5 cycles of pre-vacuum steam sterilization at 132°C with a 4-minute sterilization phase and 30 minutes dry phase. Pieces were allowed to cool 30 minutes between cycles. *In this work, Dental resin was autoclaved once without showing deterioration.

HUVEC adhesion was analysed with a Leica DMIL inverted phase contrast microscope with a digital camera EC3. Fluorescence images of the cell cultures were acquired using an inverted fluorescence microscope Zeiss Axio Vert A1.

8.1.2.2 PDMS and UV-PDMS

Two types of PDMS were studied: thermally cured PDMS and UV-PDMS. The UV-PDMS presents some advantages with respect to prototyping efficiency, as it cures in a matter of minutes compared to the hours required for thermally cured PDMS. However, it is significantly more expensive.

8.1.2.2.1 Preparation

For the thermally cured PDMS **(**Materials and Methods 4.1.2.1), the commercial Sylgard 184 elastomer (Dow Chemical Company) was utilized, which consists of a prepolymer base, and a cross-linking agent mixed in a 10:1 weight ratio, then degassed and cured with a temperature ramp from room temperature to 60 °C over 30 minutes, followed by 12 hours at 60 °C.

For UV-PDMS **(**Materials and Methods 4.1.2.2), KER-4690 A/B (Shin-Etsu Europe BV) was used, mixed in a 50:50 ratio, degassed, and cured with a 405 nm LED flood at 5.34 mW/cm² for 10 minutes at 50 °C. Both PDMS types were cast in Petri dishes and cured as described for biocompatibility assays.

8.1.2.2.2 Manufacturing method of the microfluidic device

For *in vitro* studies, microfluidic Y-shaped devices featuring a complete channel with circular internal sections of 2 mm (UV-PDMS) and 1 mm (PDMS) in diameter were manufactured as the junction of two semichannels. So, for each device, two different masters were fabricated by stereolithography (SLA) in Clear resin, featuring the autoalignment connectors introduced in Materials and Methods 4.2.1 (Figure 8.1a). These connectors grant the precise matching and bonding of the two parts (Figure 8.1b), enabling the formation of a fully circular channel on the inside (Figure 8.1c) in an efficient, fast and reproducible manner. The masters were filled with two types of PDMS, the conventional and the UV-PDMS. Both were degassed, cured, demolded, and bonded using oxygen plasma treatment, followed by a 30-minute thermal treatment at 90 °C to enhance optical quality and sealing of the device parts.

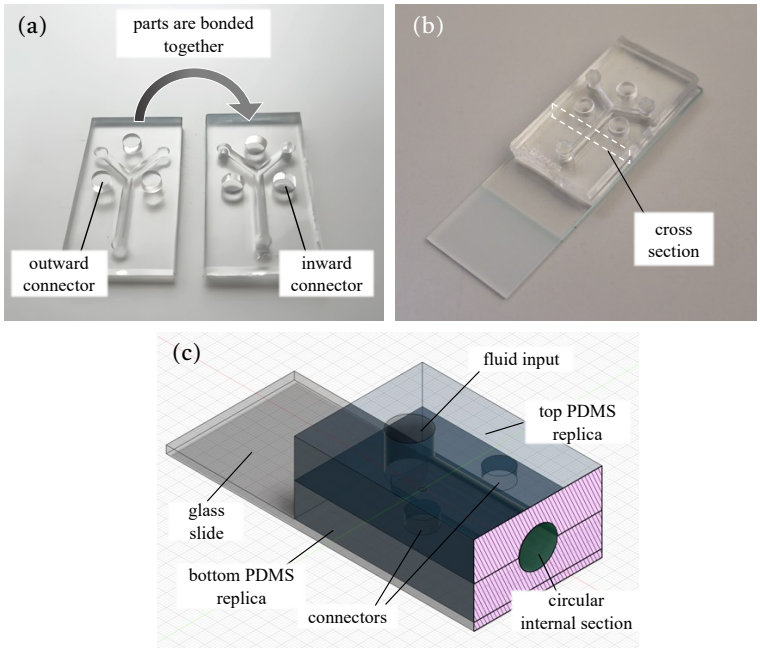

Figure 8.1: Images of the two components that constitute the device a) prior to and b) following the bonding process. c) CAD cross section of the microfluidic device featuring a Y-shaped channel of 2 mm with circular internal section.

8.1.2.2.3 HUVEC culture in PDMS and UV-PDMS substrates

The endothelium, which lines the interior surface of blood vessels, serves as an ideal model for evaluating flow conditions in biocompatibility studies. In this context, Human Umbilical Vein Endothelial Cells (HUVEC) have been utilized in biocompatibility assays as primary cell cultures. Isolated HUVEC were isolated from freshly obtained human umbilical cords donated under informed consent and following previously described protocols (Paradela-Dobarro et al., 2016). HUVEC were cultured on 0.2% gelatin-precoated flasks or dishes and grown in complete Endothelial Growth Medium (EGM)-2 media supplemented with 2% fetal bovine serum in a humidified atmosphere with 5% CO_2 at 37 °C. To ensure endothelial phenotype, cells used in experiments were between the second and seventh passages.

For cell adhesion and growth experiments, 40 mm-glass Petri dishes filled with PDMS or UV-PDMS, were sterilized by autoclaving and precoated with 0.2% gelatin in PBS. Standard six-well polystyrene plates were precoated similarly for comparison. Confluent HUVEC cultures were detached with trypsin and seeded in the Petri dishes or plates at 10,000 cells/cm².

For seeding HUVEC in Y-shaped channels, these were precoated with fibronectin and gelatin solution, followed by seeding HUVEC at 10^6 cells/ml in two rounds, ensuring a confluent monolayer on the inner surface of the channel after overnight incubation.

8.1.2.2.4 Observation and staining of HUVEC

Cell adhesion to PDMS or UV-PDMS surfaces was evaluated 3 hours after HUVEC seeding and analysed by phase contrast microscopy at 100× and 200× magnification, and images were processed with CellSens software (Olympus). Cell growth was measured after 24 hours of culture by phase contrast or fluorescent microscopy. For fluorescent microscopy, cells were stained with calcein AM, a cell viability probe, incubated at 2 µg/ml for 5 minutes at 37 °C. The calcein solution was then replaced with complete EGM-2 medium, and cells were observed under a fluorescence microscope. Cell growth progression was monitored at 48-96 hours by phase contrast imaging.

8.1.2.2.5 Flow experiments in PDMS and UV-PDMS devices

A closed circuit was set up for applying flow in PDMS and UV-PDMS channels using a peristaltic pump (REGLO digital model, Ismatec), as presented in Figure 8.2. Sterilized silicone tubes were connected to the inlets and outlets of Y-shaped microfluidic devices. The outlet tubes were collected in a glass reservoir with a rubber septum filled with 6 ml of EGM-2 medium, recirculating by the peristaltic pump through the microfluidic device. The circuit was placed in a cell culture incubator at 37 °C at 5% CO_2.

Flow experiments are established 12-16 hour after cell seeding. Flow started at 0.5 ml/min, increasing progressively every hour until the desired flow rate was reached (flow rates of 1.5,

2.5, 4, and 6 ml/min for 6 hours). After each experiment, the flow was stopped, and cells were fixed with 4% paraformaldehyde. After two washes with PBS, nuclei were stained using Hoechst 33342 and analysed using a fluorescence microscope to observe the distribution of HUVEC at the main branch, bifurcation, and two branches of the channel.

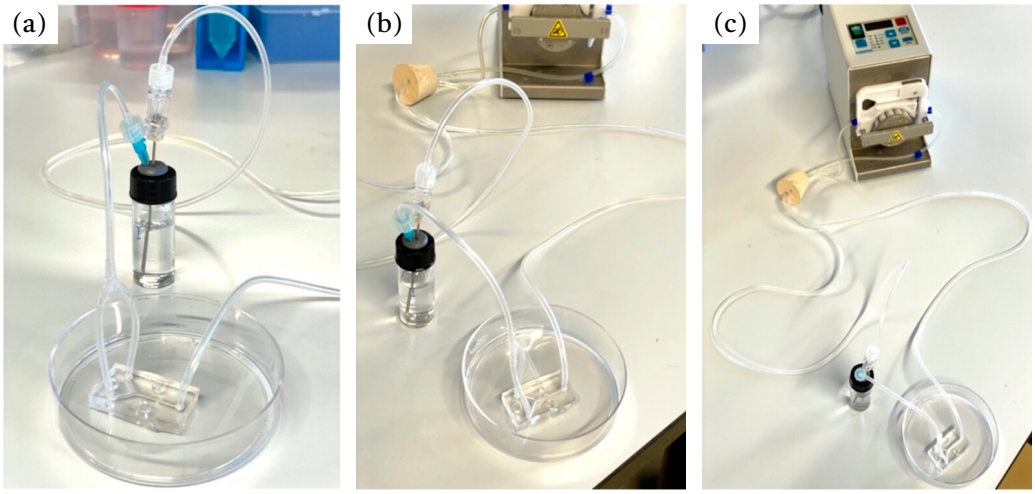

Figure 8.2: Setup of a circuit assembly for flow application on a microfluidic device. a) Close-up view of the device and its connection to the medium reservoir bottle. b) View of the recirculation through the device. c) Panoramic view of the whole system (peristaltic pump, device and reservoir).

8.1.3 Results and discussion

Biocompatibility can be tested at different levels attending to the category of body contact (from transient-contacting to implant devices) and to the evaluation process (physicochemical or biological analysis). In the case of microfluidic devices manufactured for biological or biomedical investigation, the possibility of inclusion of mammalian cells is of particular importance. Therefore, the materials and the finishing should guarantee cell adhesion and viability. As we mentioned, a study on the cell viability of HUVEC was carried out, given its great potential in microfluidic applications (Yeon et al., 2012), in particular in the field of cardiovascular diseases (S. Chen et al., 2017; Aymerich et al., 2017b).

8.1.3.1 Biocompatibility on 3D printing resins

In the first place, several studies were performed on the surface of the 3D printing resins employed in this thesis. HUVEC were cultured (10,000 cells/cm^2) on plastic (Figure 8.3a) and on the three polished resins: Amber (Figure 8.3b,e), Dental (Figure 8.3c,f) and Clear (Figure 8.3d,g). The cells were also seeded on the unpolished surfaces of the same resins (e-g), but the surface roughness avoided a correct observation. After 4h of seeding, cells were inspected on an optical microscope to test their adhesion. This time was enough for HUVEC to adhere to the surface of culture and to spread through it, as normally observed under standard conditions on plastic material. Amber, Dental, and Clear resins showed similar behaviour to HUVEC adhesion.

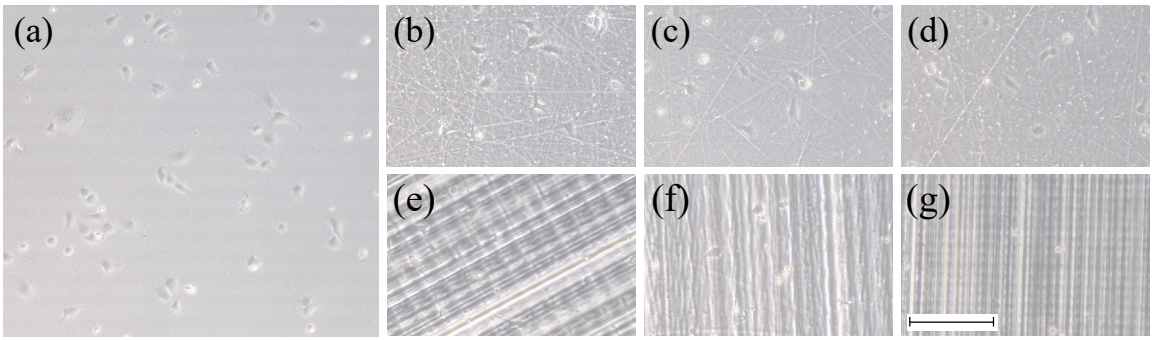

Figure 8.3: Optical microscope images of HUVEC cultures on a) plastic control dishes and on the polished (top) and unpolished (bottom) surface of b), e) Amber; c), f) Dental and d), g) Clear resin. The images were acquired 4h after cell seeding. All the pictures were taken with a 100× magnification. Scale bar 100 μm.

After adhesion, HUVEC in an appropriate cell growth medium start to divide, forming colonies of cells than in these conditions will expand over the surface of culture until form a confluent monolayer with cells in a hexagonal or cuboidal form with large nuclei. If culture is maintained, cells will adopt a cobblestone-shaped layer, simulating the morphology of the endothelium *in vivo* (Medina-Leyte et al., 2020).

Cell viability over the different surfaces was tested with a fluorescent dye for living cells (Figure 8.4). Calcein AM is a cell-permeant molecule that is converted in a fluorescent dye by the intracellular sterases in living cells. Thereby, HUVEC were stained after several hours of culture and their evolution was followed until 24h after seeding. Despite a similar adhesion was observed in the Amber, Clear and Dental resins, the evolution of the cultures was different. On Dental (Figure 8.4c) and Clear (Figure 8.4d) resins, HUVEC did not increase their cellular surface and there was no significant cell growth after 24h post-seeding (Table 8.2). HUVEC maintained constricted their proportions and colonies of cells seemed not to evolve. On the other hand, a different behaviour was observed in the Amber resin (Figure 8.4b). In this case, after 24h of culture (Figure 8.4f), HUVEC maintained their spread as observed in the control experiments over plastic surface (Figure 8.4a) and the mean cell surface was even larger, indicating a good adaptation to the surface. Colonies of cells also grew, and the culture progressed to confluence in a similar extent than the control experiment over conventional plastic materials. Note that although the growth is lower in number of cells, the cell area increases (Table 8.2).

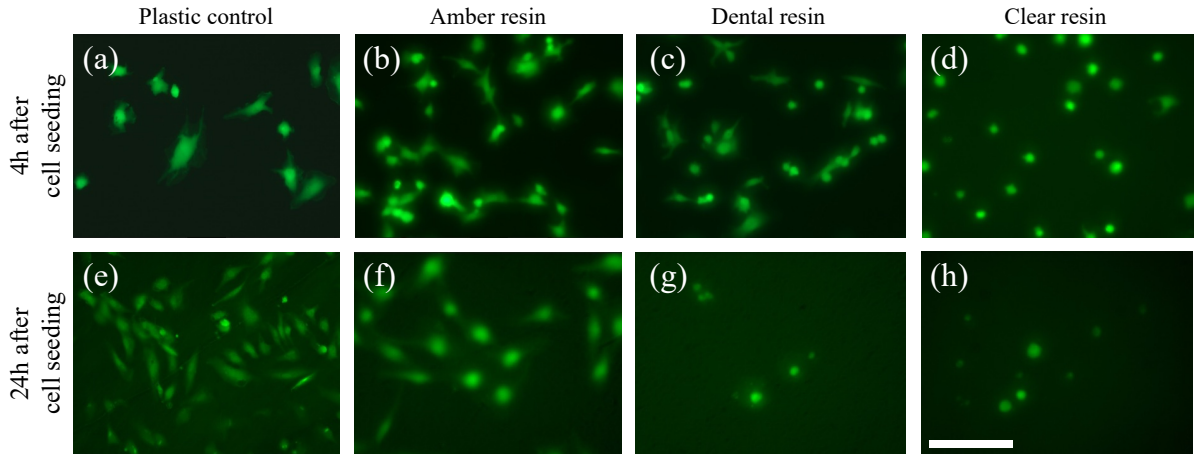

Figure 8.4: Fluorescence microscope images of HUVEC cultures with life-staining calcein AM on the polished surface of a) standard plastic, b) Amber, c) Dental and d) Clear resins. The images were acquired 4h (top) and 24h (bottom) after cell seeding. All the pictures were taken with a 100X magnification. Scale bar 200 μm.

Priting Resin	**Culture growth at 24h (%)**	**Cell area (μm^2)**
Control (polyestyrene)	479.7 ± 49.3	499.9 ± 86.2
Amber	165.2 ± 45.1*	940.8 ± 5.9*
Clear	-39.2 ± 2.1*	629.3 ± 20.0
Dental	39.1 ± 27.6*	690.4 ± 3.3

Table 8.2: Cell growt after 24h of culture measured as percentage of cells numbers and area of the cells. *p<0.005 with respect to control, using t-Student's test.

In conclusion, although the resins Clear and Dental showed biocompatibility to HUVEC in terms of cell adhesion, it seems that only Amber resin gathers the characteristics needed to guarantee HUVEC adhesion to the surface and the progression and maintenance of the HUVEC culture over the time. These results partially agree with a previous work (Kreß et al., 2020b) in which bad biocompatibility of Clear resin with human adipose-derived mesenchymal stem cells, but a relatively acceptable compatibility for Dental LT resin was observed. However, biocompatibility depends not only on the material used, but also on the type of cells employed for the assay. On this regard, Hart et al. observed better compatibility for Clear resin than for Dental LT, using HL-1 cells (Hart et al., 2020b). These cells are derived from rat atrial cardiac myocytes. Altogether suggests that the confirmation of biocompatibility should be done for each type of cells and in the optimal conditions of culture.

8.1.3.2 Biocompatibility on PDMS and UV-PDMS

The behavior of the HUVEC culture over surfaces of PDMS or UV-PDMS was first compared. HUVEC were seeded in surfaces made from these materials, and their morphology

and viability were checked after 24 (Figure 8.5a,c,e) and 48 h (Figure 8.5b,d,f) in comparison with conventional polystyrene culture plates. HUVEC were able to adhere to both, PDMS (Figure 8.5c,d) and UV-PDMS (Figure 8.5e,f) materials and create a viable culture after 48 h. Cells seem not to spread and grow at the same velocity as in conventional plastic material. However, the experiment confirmed two issues: both PDMS materials were biocompatible with HUVEC culture, and the optical quality of UV-PDMS for microscopy was really good, surpassing that of PDMS. This is evident considering the transmission spectra of the samples. In this graph, that can be consulted in Materials and Methods 4.1.2, both PDMS materials are highly transparent from the UVA to the NIR spectral region, with very flat behaviour in the visual region. A higher transmittance spectrum on the UV-PDMS substrate in the visible and NIR light domain is attained with an increase of approximately 5% compared to thermally cured PDMS.

Additionally, we studied the combination of different ratios of A and B components to prepare UV-PDMS, to test which proportion showed better biocompatibility. HUVEC were cultured for 24 h in UV-PDMS surfaces prepared from a range of proportions of A and B components of 40–60%. After 24 h, the best ratio for HUVEC adhesion and growth was observed for the mix of 50:50 weight ratio. This was estimated by counting the number or adhered-living cells after 24 h of culture and/or the number of clusters of cells formed. As a result, 50:50 was the ratio used in the rest of the experiments with UV-PDMS.

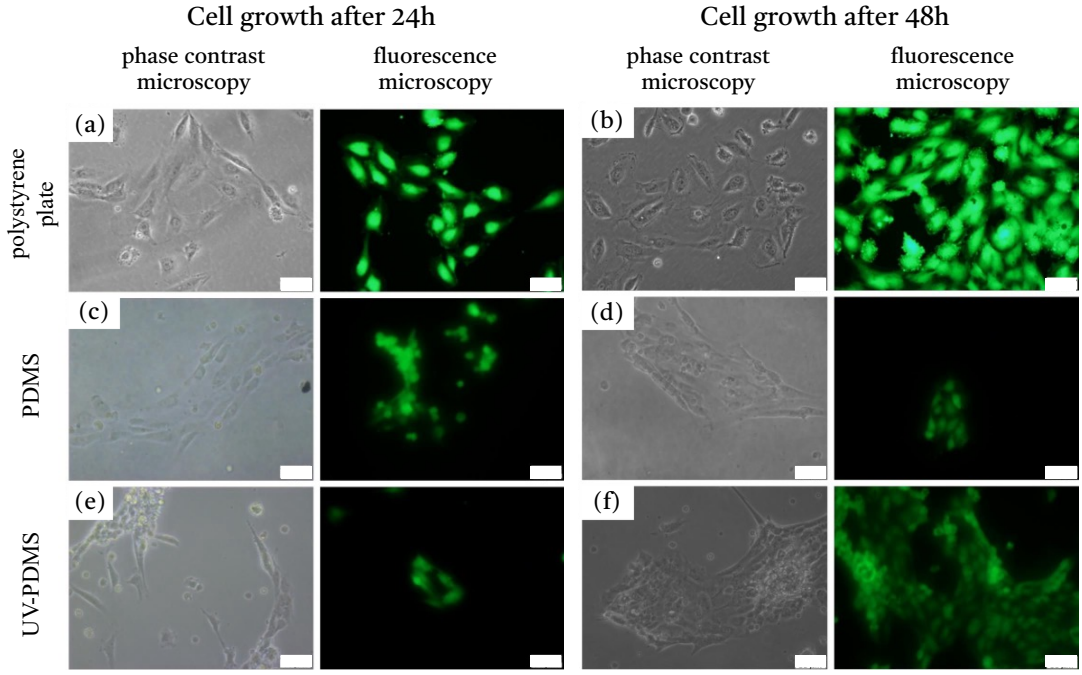

Figure 8.5: Representative images after a,c,e) 24h and b,d,f) 48 h of seeding HUVEC in different surfaces of culture: a,b) conventional polystyrene for cell culture, c,d) PDMS, and e,f) UV-PDMS. For each culture time, left column corresponds to images acquired under contrast phases microscopy. Right column corresponds to images acquired under fluorescence microscopy from cells stained with calcein-AM. Scale bar: 50 µm

8.1.3.3 Cell adhesion on UV-PDMS and PDMS devices under flow conditions

Cell adhesion and viability of HUVEC in channels of UV-PDMS were first tested. Channels based on the conditions of fabrication used showed good properties for HUVEC adhesion, and after 7 h of culture in static conditions, cells formed a confluent monolayer in all the locations of the channel (Figure 8.6). They were also in a good state of viability, as demonstrated by calcein-AM staining (Figure 8.7).

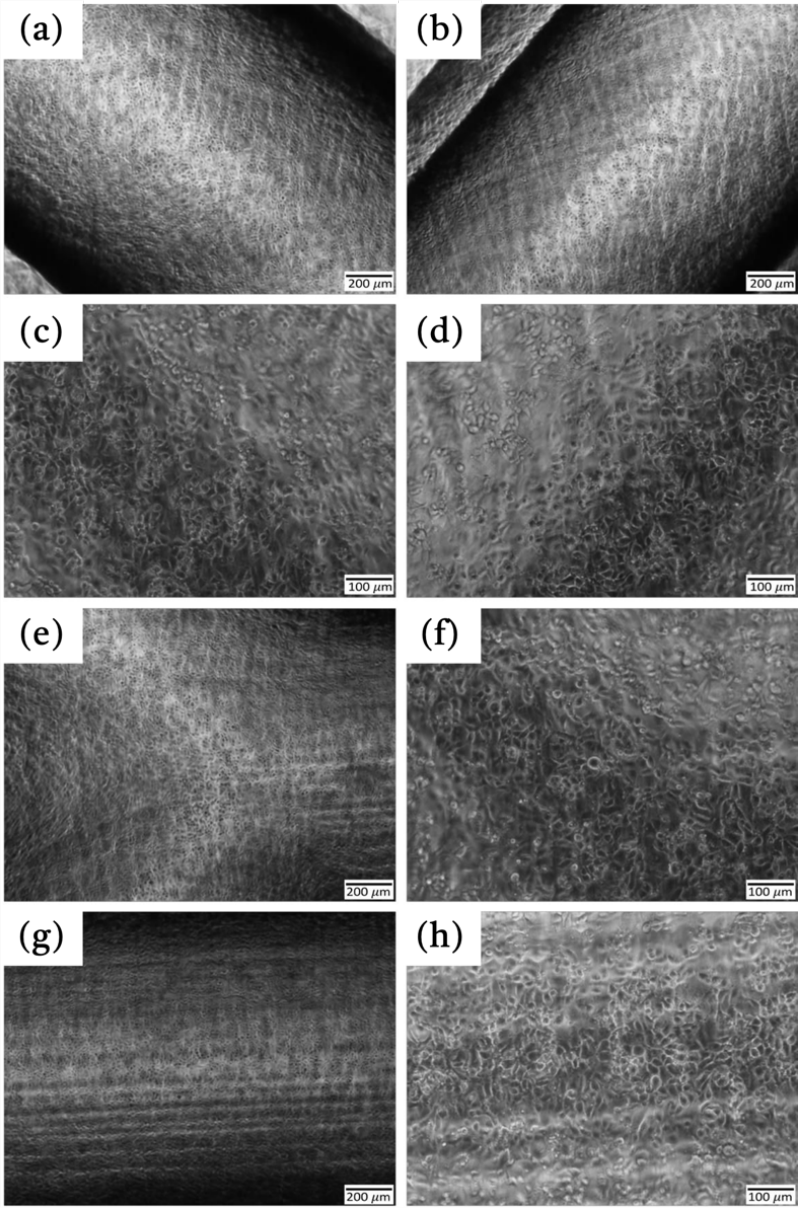

Figure 8.6 Representative images after 7 h of seeding HUVEC in a channel of UV-PDMS acquired by phase contrast microscopy. Images from different locations of the channel, acquired with different magnifications. a) and c) right branch of the channel. b) and d) left branch. e) and f) bifurcation. g) and h) major branch.

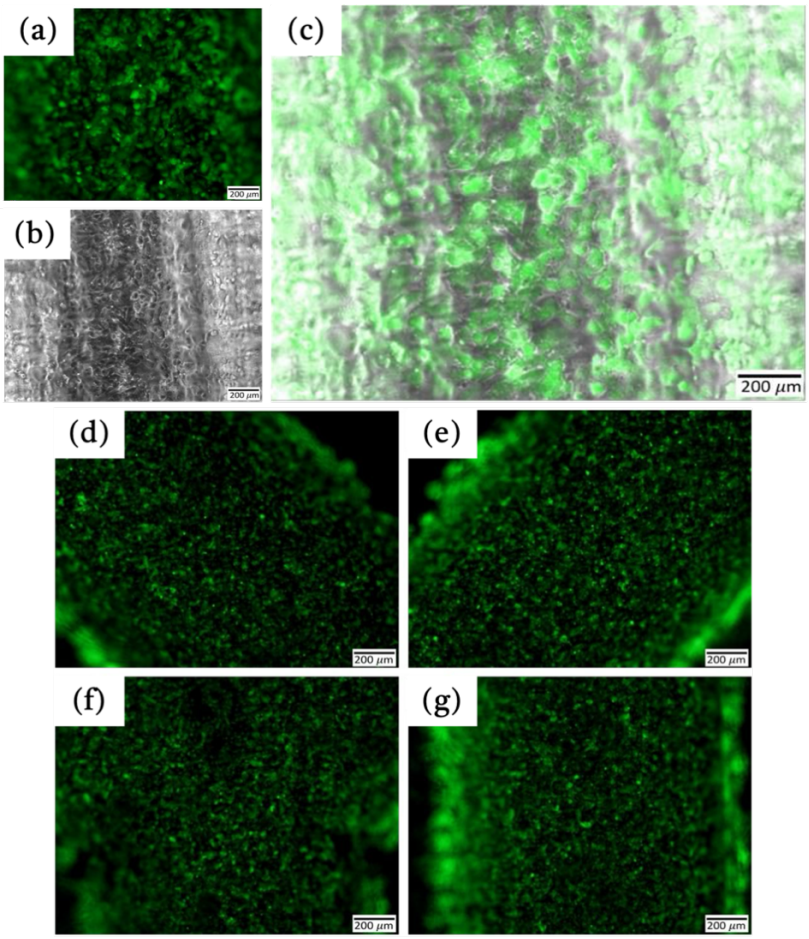

Figure 8.7: HUVEC viability in channels of UV-PDMS. Cells were stained with calcein-AM, a fluorescent viability probe. a) main branch under fluorescence, b) main branch under phase contrast microscopy, and c) merged images of a) and b). d-g) are images of fluorescence (viable cells) from the right d) and left e) branches, bifurcation f) and g) major branch.

In the flow experiments, UV-PDMS devices were used to seed HUVEC and analyze their behavior under different flow conditions in a range of 1.5-6 ml/min (Figure 8.8a-d). After reaching the maximum flow rate, this was maintained in all cases for 6-7 h. Quantification of the HUVEC that still adhered to the walls of the channel after exposure to the flow was done by staining the nuclei of the cells with Hoechst 33342.

It was confirmed that from the lowest flow rate of 1.5 ml/min (Figure 8.8a) to the maximum flow rate of 6 ml/min (Figure 8.8d) applied, cell occupancy after flow exposure was maintained in all the observed portions of the channel (main channel, bifurcation point, and side branches of the channel). Counts of HUVEC nuclei per surface unit were indistinguishable from one condition to another, featuring a cell occupation always over 90% of the wall surface.

A similar result was observed for the channels fabricated in PDMS, as illustrated in Figure 8.9. In the left section, viable HUVEC are stained green with calcein acetoxymethyl (AM) ester, indicating cell viability. In the right panel, nuclei are stained blue with Hoechst 33342. The

variation in the predominant green or blue fluorescence is due to the focal plane: the non-planar nature of the device causes different planes to highlight either the cytoplasm and cell surface or the nuclei. This distinction can be observed with confocal microscopy, which provides clarity between planes, but can also occur with epifluorescence microscopy. This confirms that the channel is entirely covered with live HUVEC.

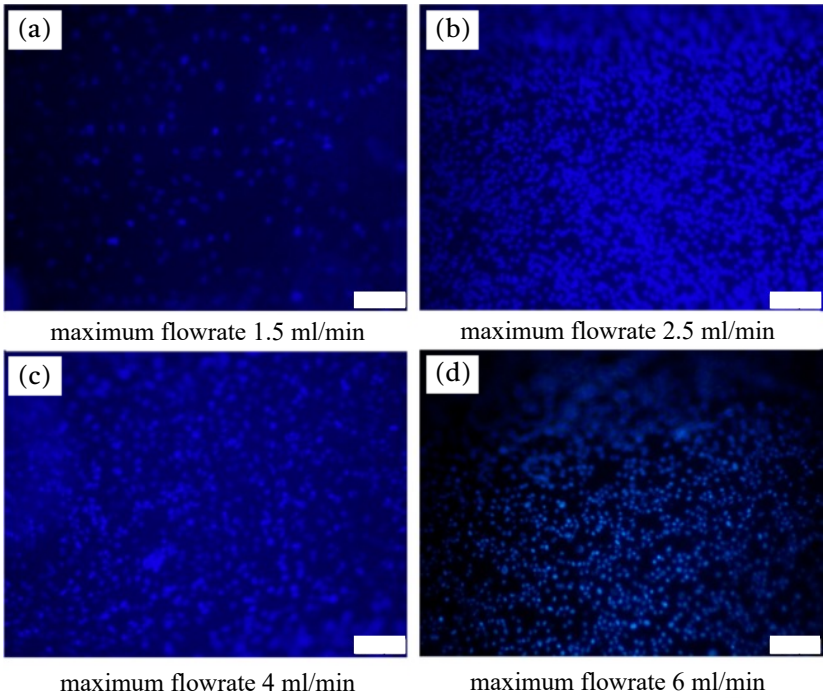

Figure 8.8: Fluorescence images of cell culture under different maximum flowrates: a) 1.5 ml/min, a) 2.5 ml/min, a) 4 ml/min, a) 6 ml/min. HUVEC nuclei stained with Hoechst 33342 in the main branch of the Y-shape channels, observed after exposure to the indicated flow rates for 6–7 h. Scale bar: 100 µm.

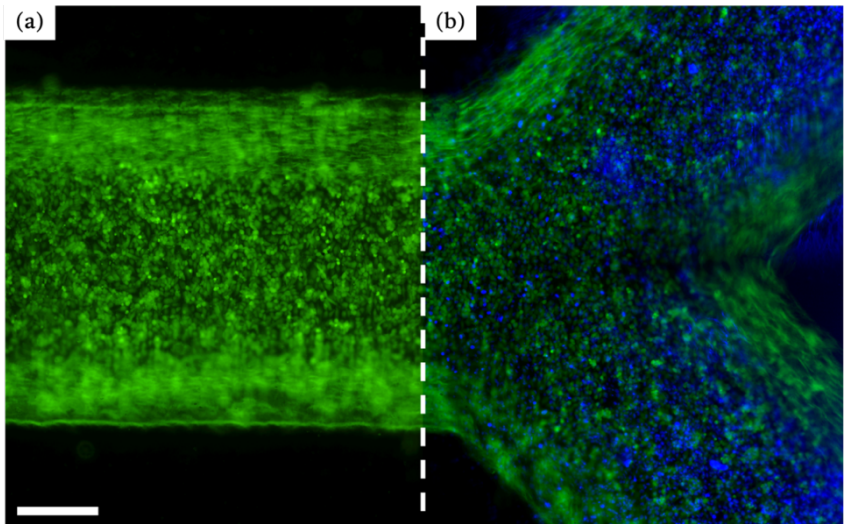

Figure 8.9: HUVEC viability in channels of PDMS. Cells were stained green with calcein-AM and blue with Hoechst 33342, fluorescent viability probes. a) Main branch and b) secondary branches under fluorescence microscopy. Scale bar: 250 µm.

These studies demonstrates that UV-PDMS is biocompatible for HUVEC culture, similar to the widely used thermally cured PDMS. UV-PDMS offers significant advantages, including superior optical clarity, enhanced handling, and processing characteristics due to shorter curing times and a simplified UV curing process, although its high cost compared to PDMS makes it not very suitable for the small scale production that we handle in the academic environment, especially in the prototyping phases. Flow experiments showed that PDMS and UV-PDMS surfaces effectively supported HUVEC without detachment, highlighting its suitability for microfluidic device applications. In summary, both polymers show great potential for developing microfluidic devices for cell-based assays and other biological applications.

8.2 BLOOD VESSEL BIFURCATION AS MODEL FOR STUDYING PHYSICAL CAUSES OF TUMORAL CELLS ARRESTING

8.2.1 Introduction

Metastasis, the primary cause of cancer-related deaths (Lambert et al., 2017), marks a critical juncture in a patient evolution, often necessitating a shift in treatment strategies towards chemotherapy or targeted therapies. Central to this process is the homing of Circulating Tumour Cells (CTC) to distant metastatic niches, a pivotal step in metastatic colonization (Dasgupta et al., 2017; Klein, 2020). CTC may become trapped in small capillaries before adapting to their new environment and colonizing the site (Follain et al., 2020). Alternatively, they can interact with endothelial cells through ligand-receptor contacts, facilitating their adhesion, crawling, and transmigration (Rejniak, 2016). Pre-metastatic niches can also enhance CTC homing efficiency by remodelling the microenvironment (Peinado et al., 2017).

Understanding the mechanical and geometrical factors of the vascular system and associated hemodynamic flows is crucial (Brodland & Veldhuis, 2012; Font-Clos et al., 2020), especially in early metastasis steps. Factors like low shear forces and signalling between tumour and endothelial cells contribute to CTC entrapment and extravasation in the microvasculature (Kienast et al., 2010). Hemodynamic factors such as shear rates, stress gradients, and recirculation may also influence tumour cell adhesion (Fu, 2018). Flexibility of metastatic cells enables interaction with endothelial cells under shear stress, leading to adhesion at microvessels (Pepona et al., 2020). Moreover, vorticity at microvessel branches can increase tumour cell adhesion (P. Guo et al., 2014).

Considering this, our study aims to evaluate specific regions within veins or arteries that may facilitate the arrest of tumour cells due to localized reductions in flow velocities. This study seeks to elucidate the systematic impact of these regions, which could potentially be modulated through clinical interventions by adjusting blood flow parameters. To achieve this, bifurcated Y-shaped microchannels were manufactured employing laser ablation stereolithography and

soft lithography of PDMS. These microchannels, characterized by a semicircular cross-section, serve as platforms for endothelial cell culture under physiological flow conditions.

8.2.2 Materials and methods

8.2.2.1 Manufacturing method of the microfluidic device

Vascular bifurcation represents a complex and interesting geometry within human blood vessels, characterized by a combination of laminar flow regions, areas of reduced flow velocity, and zones of flow recirculation. To experimentally evaluate the behaviour of the CTC in this context, we fabricated microfluidic device featuring a Y-shaped channel (Figure 8.10a) with semicircular internal section of 2 mm. For this, masters were manufactured by SLA and laser ablation following the protocol described in Materials and Methods 4.2.1. The master was replicated by soft-lithography in PDMS, employing a 10:1 ratio of monomer and curing agent, respectively. To remove all the bubbles in the PDMS, this was introduced in a vacuum chamber 40 min at 400 mbar and cured at a furnace for 2 h at 40 °C. After curing, The PDMS replica was then peeled of the master. This final device was bonded by the oxygen plasma activation (see Materials and Methods 4.1.4.2) to a microscope glass slide (Figure 8.10b). This biocompatibility resulting from the moisturized surface of the channels was further enhanced with the collagen biocoating, both for CTC arrest as well as for endothelial monolayer formation.

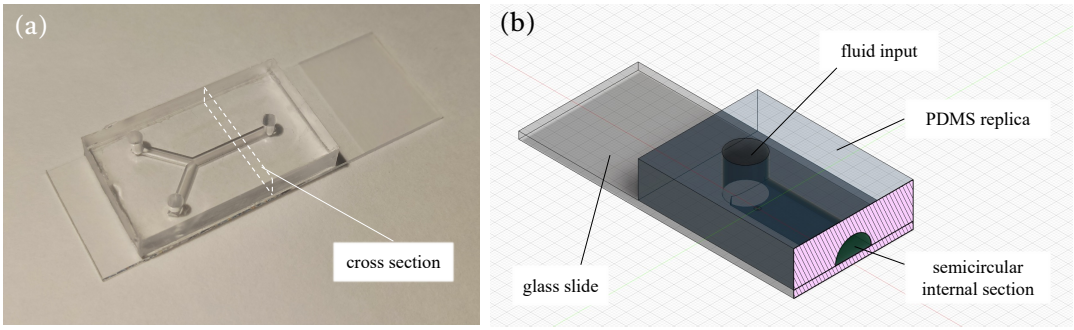

Figure 8.10: a) Image and b) CAD cross section of the microfluidic device featuring a Y-shaped channel of 2 mm with semicircular internal section.

Preliminar *in vitro* studies were performed using PDMS replicas of masters manufactured by indirect laser writing technique (LIPAA) in a soda-lime glass substrate. In this protocol, the glass masters features of a semicircular hollow that is replicated with liquid silicone. After solidifying, silicone structure is removed and introduced in the bottom of a Petri dish which is finally covered by uncured PDMS. The laser used was a Nd:YAG laser (Materials and Methods 4.1.5.1) working at a wavelength of 1064 nm with a pulse duration of 20 ns. The parameters used of the laser were: 667 mJ energy per pulse, repetition rate of 12 kHz and a scan speed of 1000 mm/s. The hatching was 25 μm.

8.2.2.2 Computational simulations

A numerical approach has been done to simulate and characterize the behaviour of CTC by considering a mathematical model to describe representative and physiological large blood vessel bifurcations (Otero-Cacho et al., 2018). Vessels of two millimetres in diameter and semicircular cross section were also considered, with an inlet fluid flow of 3 ml/min and zero pressure outlet conditions; guaranteeing Reynolds numbers lower than 100 and, thus, laminar flow. CTC-like particles (n=20,000) were modelled as rigid spheres with a diameter of 14 μm (Awe et al., 2017) and a density of 1.05 g/ml (Bryan et al., 2014).

It is worth noting that the *in silico* results presented in this section were developed by other members of the multidisciplinary group. However, the main results will be included here for the sake of completeness.

8.2.2.3 MDA-MB-231 and HUVEC cell culture

The MDA-MB-231, green fluorescent protein (GFP)-labelled MDA-MB-231 and MDA-MB-231 shTIMP1 cells (Abreu et al., 2020) were maintained using Dulbecco's Modified Eagle Medium (DMEM) (Lonza, Walkersville, MD, USA) supplemented with 10% FBS (Gibco, Grand Island, NY, USA) and 1% penicillin–streptomycin (Gibco, Grand Island, NY, USA) in a humidified atmosphere at 37 °C and 5% CO_2. Cells lines were subcultured twice a week when an 80% confluency was reached. Briefly, the culture medium was aspirated, and the dish (Corning, New York, NY, USA) was washed with Dulbecco's Phosphate Buffered Saline (DPBS) (Sigma-Aldrich, St. Louis, MO, USA) then cells were detached using Trypsin–Ethylenediaminetetraacetic acid (EDTA) (Lonza, Walkersville, MD, USA).

HUVEC were isolated from freshly obtained human umbilical cords donated under written informed consent from mothers, and following the method previously described (Paradela-Dobarro et al., 2016). All the procedures were approved by the Ethics Committee for Clinical Research at Galicia, according to the World Medical Association Declaration of Helsinki. Briefly, HUVEC were cultured on 0.2% (w/v) gelatine (Sigma-Aldrich; Merck Life Science S.L.U., Madrid, Spain) pre-coated flasks or dishes (Corning, New York, NY, USA) and grown in complete EGM-2 media (Endothelial Growth Medium-2, Lonza, Basel, Switzerland), containing 2% FBS between other components, in a humidity-saturated atmosphere with 5% CO_2 at 37 °C. Cells for the experiments were used between the second and seventh passages.

8.2.2.4 *In vitro* CTC perfusion assay

In all experiments the microfluidic chambers were coated with Type I collagen from rat tail (Sigma-Aldrich, St. Louis, MO, USA) at 100 μg/ml for 20 min at room temperature. Washed once with Dublecco's PBS (DPBS) and cells were recirculated at a physiological 3 ml/min velocity for up to 2 h. Afterwards, the microfluidic chambers were washed with DPBS for 5 min to remove any remaining CTC in circulation. The adhered cells were fixed using

paraformaldehyde (PFA) 4% (Ted Pella, INC., Redding, CA, USA) for 10 min and then washed with PBS. Microfluidic chambers were analysed using a LEICA DMi8 fluorescence microscope (Leica Microsystems, Wetzlar, Germany). The integrated intensity measured by ImageJ (Bethesda, Maryland, USA) analysis was used to quantify the number of CTC arrested at the bifurcation. Mann Whitney test was used to determine the statistical relationship between the different conditions. A p-value ≤ 0.05 was set as the level of significance.

8.2.2.5 Adhesion assay

The MDA-MB-231 shTIMP1 cells were labelled using the Vybrant DiD cell-labelling solution (Life Technologies, Eugene, OR, USA) as previously described. Red tagged TIMP1 silenced MDA-MB-231 cells and GFP-labelled MDA-MB-231 cells were perfused at a 1:1 ratio as previously described.

8.2.2.6 Endothelial assay

For the experiments, HUVEC at confluence were detached with trypsin (0.25% in Hank's balanced salt solution with 1 mM EDTA; Gibco, Thermo Fisher Scientific, Waltham, MA, USA) and seeded in fibronectin (5 µg/ml in 0.02% gelatine; Gibco) pre-coated PDMS channels at a concentration of 1.5×10^6 cells/ml. HUVEC were labelled with calcein-AM (Invitrogen, Thermo Fisher Scientific, Waltham, MA, USA) at a 1 µM concentration for 20 min. Then, cells were rinsed twice to remove unlabelled calcein-AM. MDA-MB-231 cells were labelled using the Vybrant DiD cell-labelling solution (Life Technologies, Eugene, OR, USA) as previously mentioned. Perfusion started at 0.5 ml/min to avoid damage to the monolayer, velocity was doubled every 15 min until reaching 1.5 ml/min for 2 h.

8.2.2.7 Viscosity assay

GFP-labelled MDA-MB-231 cells were resuspended in 20 ml of either non-conditioned medium, 0.5% hydroxypropyl methylcellulose (Sigma-Aldrich, St. Louis, MO, USA) supplemented medium, or 100% FBS. To minimize the impact of any eventual deposition of matrix components from the FBS on the channels, a preconditioning with FBS circulating in the microfluidic chambers for 1 h was performed previous to the perfusion of the CTC in all conditions as previously described.

8.2.2.8 *In vivo* CTC perfusion assay

For intracardiac perfusion, 8-week-old female SCID-beige mice (n = 3) (Janvier Labs, Le Genest Saint-Isle, France) were housed under specific-pathogen-free conditions and underwent procedures approved by the Use Committee for Animal Care from the Universidad de Santiago de Compostela. Anesthesia was administered using 2% isoflurane, and sterile surgery was performed after preparing the area. A midline incision was made to access the heart, where an

inlet needle was inserted into the left ventricle and the right atrium punctured. After washing with DPBS, 10^6 GFP-labelled MDA-MB-231 cells were perfused through the vascular system at 1 ml/min for 5 min to simulate cellular events and confirm CTC arrest at blood vessel bifurcations. Blood vessels were then labeled with Vybrant DiI, and lungs were removed, fixed, and sectioned for microscopy using a LEICA DMi8. Compliance with ARRIVE guidelines was ensured. This study aimed for qualitative confirmation of CTC arrest, and no control group, randomization, or statistical analysis was used. All animals tested positive for GFP-MDA-MB-231, so none were excluded.

It is worth noting that the *in vivo* results presented in this section were developed by other members of the multidisciplinary group. However, the main results will be included here for the sake of completeness.

8.2.1 Results and discussion

8.2.1.1 Arresting of circulating tumour cells in blood vessel bifurcation

Numerical simulations at the bifurcation (Figure 8.11a) show that most CTC follow the fastest streamlines in the center of the main vessel (green lines in Figure 8.11b), while a small fraction (about 0.1%) deviates due to inertia, reaching low-velocity areas near the vessel wall at the bifurcation vertex (carina), represented by blue lines in Figure 8.11b. In these low-velocity areas, the prolonged residence time of CTC may allow interaction with the endothelial walls, potentially leading to adhesion.

Subsequently, manufactured microfluidic devices were utilized (Figure 8.11c) employing rates comparable to those in computational studies, considering the concentration of spheres and cells per ml, the flow rate and the perfusion time. Furthermore, these CTC perfusion rates hold clinical relevance, given the mean detection of 1–10 CTC per 7.5 ml in metastatic breast cancer patients and a median survival rate of 3 years, and adapting and scaling the probability of CTC events in a precise position of the vasculature during the clinical history of these patients to a laboratory assay. As observed in the representative images capturing the GFP-fluorescent trajectories of the perfused CTC, behaving in concordance with the theorical prediction, the vast majority flowed into the secondary channels following the mainstream flow lines (see representative trajectories by GFP-fluorescent wakes left by flowing CTC in Figure 8.11d) and did not present any arrest or homing at this level of the vasculature, further circulating towards hypothetic capillaries and microvessels. Also as predicted by the numerical simulations, a marginal component of the CTC in the principal channel continued flowing straight towards the carina, and reached the area characterized by a reduced flow velocity (Figure 8.11e).

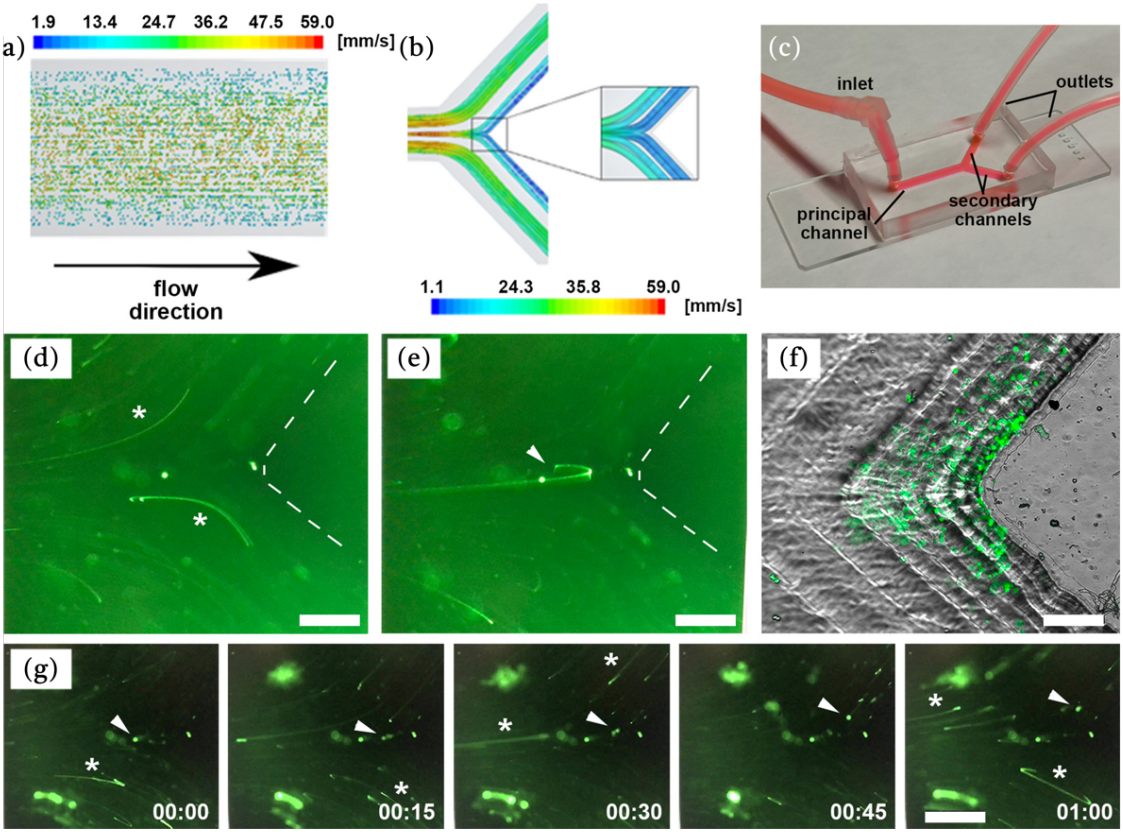

Figure 8.11: a) Schematic representation of the distribution of particles and color-coded velocities in the direction of the flow. b) Graphical description of the flow-lines distribution at the bifurcation of a representative blood vessel based on the numerical simulations of the mathematical model. The streamlines are color-coded following the value of the velocity in mm/s. c) Image of the microfluidic Y-shaped microchannel connected to the perfusion pump for the *in vitro* fluidic experiments mimicking a vessel bifurcation. d,e) Representative fluorescence images of the trajectories of GFP-tagged CTC in the microfluidic devices following the high-velocity streamlines from the principal towards the secondary channel (asterisks in panel d), and the minoritarian component following the inertial trajectories towards the low-velocity area at the carina (white arrow in panel e). Vertex of the bifurcation has been delineated by dashed lines. f) Arrest of GFP-tagged CTC at the low-velocity area of the bifurcation resulting from the inertial trajectories upon CTC recirculation. g) Representative sequence of a GFP-tagged CTC illustrating the residence time at the carina (white arrow), in comparison with the trails resulting from the majoritarian CTC following the high-velocity streamlines (asterisks); the entire sequence lasts one second, as numerically indicated. Scale bar: 200 µm.

The carina was manufactured to mimic the physiological geometry. Several experiments were conducted with the devices manufactured by laser, but achieving a carina with a smooth profile proved challenging with this fabrication technology. To address this, Stereolithography (SLA) was explored as an alternative fabrication method. Various configurations were tested to produce a carina that precisely resembled the anatomical structure observed in real scenarios. A design with a more rounded corner was achieved, ensuring that the response of the CTCs upon impact was as realistic as possible.

Upon recirculation, the microchannels were further perfused with phosphate buffer solution (PBS) for 5 min to remove any floating CTC remaining in circulation, and cells adhered to the collagen coating were fixed with paraformaldehyde (PFA, 4%). Notably, the accumulative effects of the CTC at the carina led to a systematic arrest of tumour cells at the area in front of the carina (Figure 8.11f). The quantification of CTC arrested at the carina of the bifurcations resulted in a mean 85 ± 10 (mean ± SD) cells; considering the number of cells per ml, the flow rate and the duration of the perfusion, around a 0,0005% of the recirculated CTC arrested at this specific area of the simulated large blood vessels. This indicates that a small percentage of tumour cells approaching the bifurcation are eventually arrested, suggesting that the time of residence at this area of low velocity is critical for the CTC to interact with the surface of the channels. The representative sequence of an individual CTC inertially flowed towards the vertex of the bifurcation, illustrates its residence at this area of low velocities for a relevant duration (white arrow in Figure 8.11g), in comparison with the majoritarian mainstream lines.

8.2.1.2 Influence of angle of bifurcation

The causality of this observation was further confirmed by altering the bifurcation angle. Numerical simulations proved that the area near the vertex of the bifurcation, characterized by reduced flow velocity, is directly influenced by the surface area of the carina exposed to the inertial flow lines. This exposure should affect the number of CTC reaching this area and their residence time. Concordantly, the experimental *in vitro* microfluidic model comprising the perfused MDA-MB-231 metastatic cells recirculating into the PDMS channels fabricated with bifurcations angles of 30°, 45° and 90° resulted in an increased arrest of the CTC as the angle increases (Figure 8.12a). The quantification of the CTC arrest confirmed the increment of this event as the angle of the bifurcations and, consequently, the area of low flow, rate increases (Figure 8.12b). All this supports the specificity of the low-velocity area event in the proximity of large vessel bifurcations impacting on CTC fate, and excludes an artefactual observation related to the numerical and experimental conditions. It must be considered that biomechanics constrains within the microcirculation can tune the metastatic potential of the CTC in terms of morphological features and gene expression that may affect their fate and aggressiveness (Cognart et al., 2020). The magnitude of the low-velocity area at the bifurcation is also dependent on the blood flow, affecting the Reynolds number, with very low flow rates associated with large areas of reduced velocity that may result in a prolonged residence of the CTC and an increased homing.

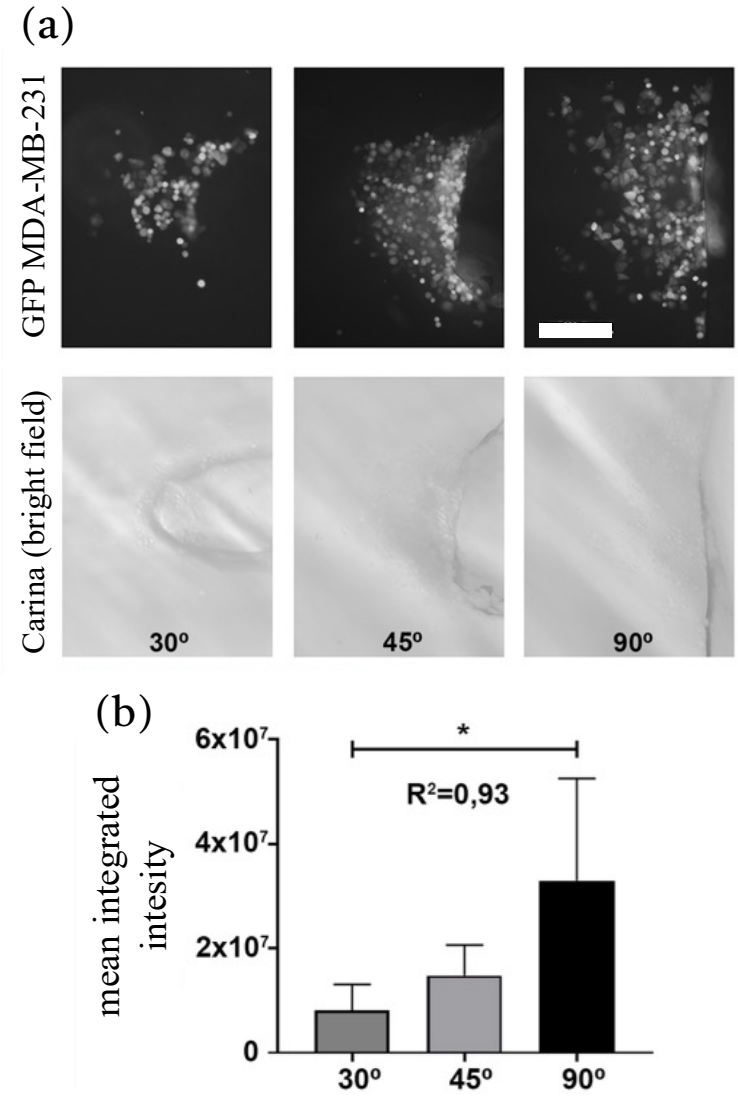

Figure 8.12: a) Representative fluorescence GFP-tagged CTC images (upper row), illustrating the concordant CTC arrest at the carina as the angle of the bifurcation increases as represented in the bright field panels (lower row); the size bar is valid for all the images. b) Quantification of CTC arrest calculated by integrated intensity, is graphically described (*t*-test $p > 0.05$; $R^2 = 0.93$). Scale bar: 200 μm.

8.2.1.3 *In vitro* and *in vivo* validation

Once we described the CTC arrest singularity at the carina of the blood vessel bifurcations resulting from these marginal but relevant inertial trajectories and the adhesive capabilities of metastatic tumour cells at the reduced velocity flow areas, we explored whether these events are compatible with more complex *in vitro* and *in vivo* preclinical models. For this, we first reproduced *in vitro* an endothelial monolayer covering the surface of the microfluidic devices by seeding 1.5×10^6 primary HUVEC onto the channels pre-treated with collagen and fibronectin for 24 h (Figure 8.13).

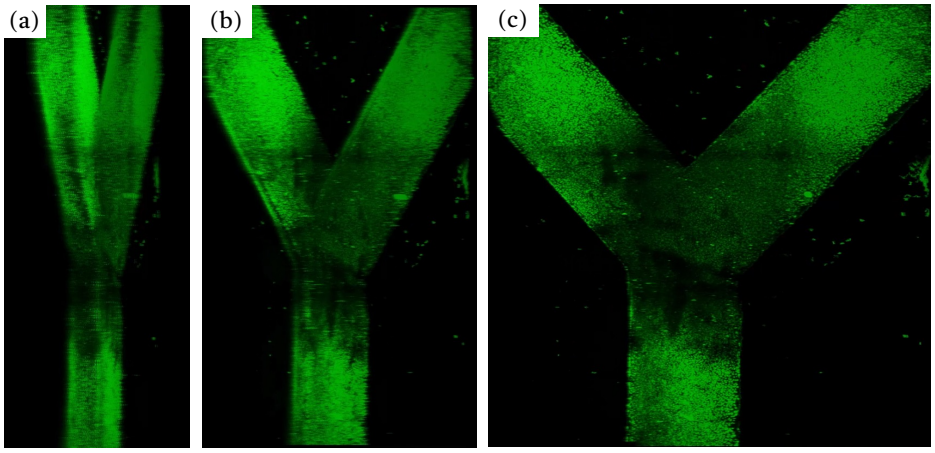

Figure 8.13: Reconstruction of the whole microchannel coated with calcein-labelled HUVEC cells. The sequence represents a 60° rotation.

Endothelial cells were labelled with calcein before recirculation of DiD-fluorescence labelled MDA-MB-231 cells for 2 h at 1.5 ml/min, to avoid the fragmentation of the endothelial layer. As shown in Figure 8.14a, CTC arrest at the carina covered by the endothelial monolayer was evidenced, suggesting the formation of cell–cell contacts with the endothelial cells during the lapse time of CTC stay at the low velocity area generated at the carina of the large blood vessel bifurcations. High-resolution imaging in zebrafish embryos already demonstrated not only the relevance of blood flow in the arrest, adhesion and extravasation of tumor cells (Follain et al., 2018), but also in the remodelling of the endothelium for further extravasation (Follain et al., 2021). These results are also indicative of the reproducibility of the CTC close-to-the-border trajectories and homing event in a more clinically relevant scenario.

Experiments were validated by *in vivo* circulation of CTCs by perfusing GFP-labelled MDA-MB-231 cells into the left ventricle of a mice and right atrium of mice. After perfusion with 10×10^6 CTCs at 1 ml/min for 5 minutes, blood vessels were labelled with DiI. The lungs, the target organ for CTC arrest, were then removed, fixed, and sectioned for microscopy. This allowed us to confirm CTC arrest at large blood vessel bifurcations and in alveolae via fluorescent microscopy (Figure 8.14b). These findings align with preclinical models and suggest that inertial trajectories at bifurcation vertices contribute to metastasis formation. Simulations and autopsy data indicate that up to 40% of metastasis distribution may be influenced by mechanical and geometrical effects in blood circulation (Font-Clos et al., 2020).

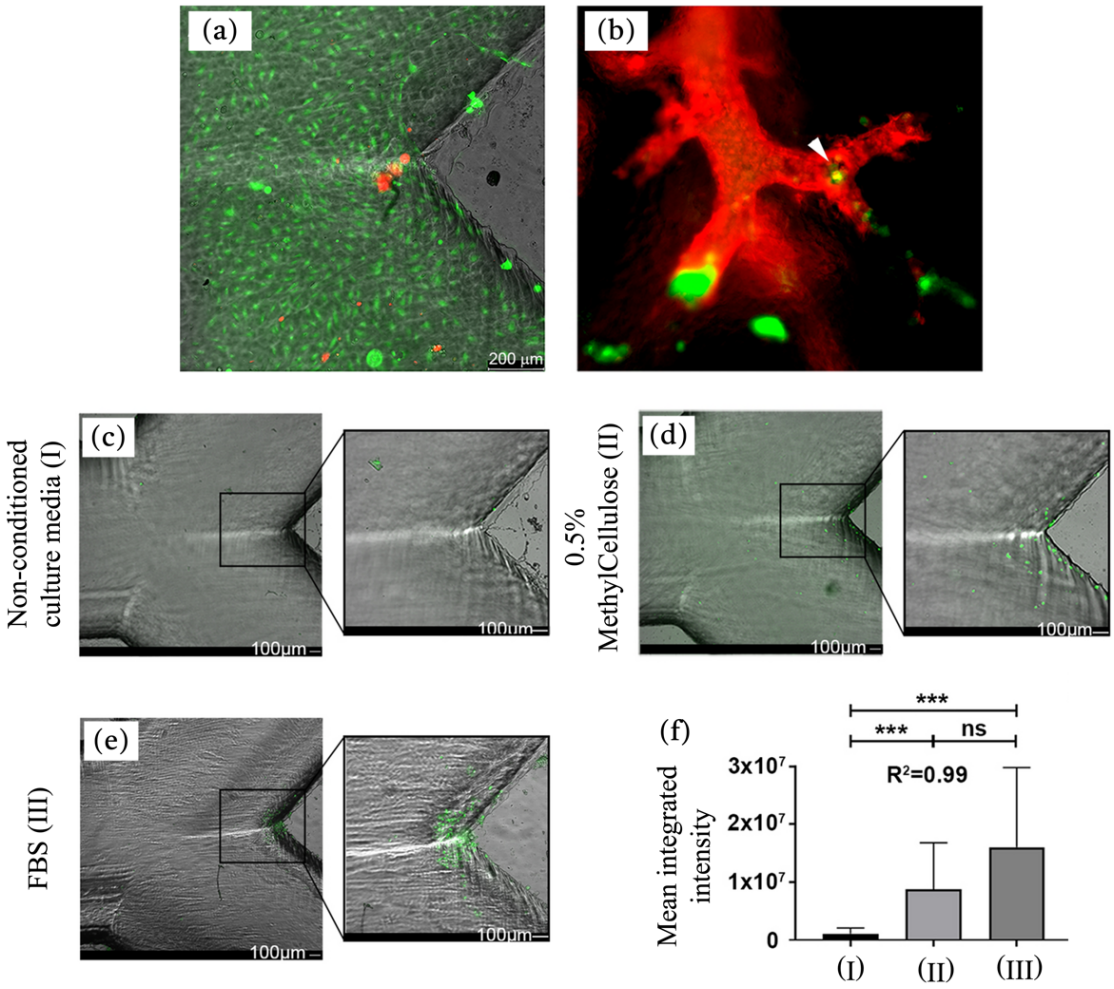

Figure 8.14: a) DiD-labelled MDA-MB-231 cell (red CTC) arrest at the bifurcation of the Y-microchannel covered with calcein-labelled primary HUVEC cells (green endothelial monolayer). b) Representative image of GFP-labelled MDA-MB-231 cells (green CTC) perfused in mice before direct labelling of the vasculature of the lung with DiI dye (red blood vessels), illustrating the CTC arrest at the carina of vessel bifurcations (arrowhead) in an *in vivo* preclinical model. The size bar in panel A is valid also for panel B. GFP-labelled MDA-MB-231 cells embedded in three different types of fluids: c) non-conditioned basal culture media (upper panels), d) 0.5% Methylcellulose (middle panels), and e) FBS (foetal bovine serum), showing improved CTC arrest at the low-velocity areas of the carina as the viscosity of the medium is increased. f) Quantification of CTC arrest calculated by integrated intensity, is graphically described. Statistical differences were found between the groups, seeing higher levels of CTC arrest with higher viscosity levels (t-test, ***$p < 0.001$; $R^2 = 0.99$).

8.2.1.4 Influence of the viscosity of the fluid

We finally investigated whether the modulation of those components that participate in the definition and behaviour of the blood flow could minimize the contribution of the inertial homing of CTC at the bifurcations that may be in part underlying the generation of distant metastasis. For this, we modified the viscosity of the fluid as the main variable defining the Reynolds number that determines the fate of tumour cells in circulation, and compared the

homing of recirculating GFP-labelled MDA-MB-231 cells in: (I) basal culture medium without foetal bovine serum (FBS) as the basic medium condition (Figure 8.14c) with the lowest viscosity (1.46 mPa·s); (II) FBS as the medium condition (Figure 8.14d) with the highest viscosity (1.935 mPa·s); and (III) basal culture medium complemented (Figure 8.14e) with 0.5% methylcellulose as a non-biological component adding viscosity to the medium (2.29 mPa·s), in a similar range as the FBS. The microchannels in all conditions were pre-treated with FBS before recirculation of the CTC, to avoid any contribution of the protein and matrix components of the FBS. As shown, CTC perfused in non-conditioned culture media with the smallest viscosity were found to arrest less efficiently at the carina of the microchannels (Figure 8.14c), compared to those perfused in culture media supplemented with 0.5% of Methylcellulose (Figure 8.14d), or to the CTC recirculating in FBS (Figure 8.14e).

Intriguingly, and as shown by fluorescence quantification of the CTC at the bifurcation of the channels under the three different conditions (Figure 8.14f), although no statistical significance was achieved CTC arrest was found to be more efficient in FBS condition compared to 0.5% Methylcellulose, with similar but lower viscosity value, suggesting that in addition to the physical components of the fluid and the adhesive capabilities of the CTC, other biological factors may be affecting CTC homing at large blood vessel bifurcations, like CTC aggregation or clustering upon adhesion (Bidard et al., 2008).

These findings confirm that flow dynamics significantly influence the arrest of circulating CTC in low-velocity areas, such as those found at major blood vessel bifurcations. They also suggest clinical opportunities to inhibit these events, given that blood viscosity is primarily influenced by haematocrit and coagulation homeostasis. Variations in haematocrit can modulate CTC adhesion to vessel walls, their velocity in blood flow, and red blood cell aggregation (Xiao et al., 2017). Similarly, factors in the coagulation cascade, like factor V, play a role in CTC interaction with vascular endothelium and metastasis efficiency (Deng et al., 2020). From a therapeutic perspective, anticoagulant drugs such as low molecular weight heparin and warfarin, which reduce blood viscosity, have demonstrated anti-tumour and anti-metastatic activity (Ejaz et al., 2021; C.-H. Lee et al., 2019). These drugs may also modulate growth factors, inhibit selectin-mediated interactions between tumour cells, leukocytes, platelets, and endothelial cells mediating the hematogenous metastasis (Läubli & Borsig, 2009). Clinical studies have shown improved survival with effective inhibition of the metastatic cascade, rather than affecting primary tumours (Bobek & Kovařík, 2004). Additionally, aspirin has shown promise as an adjuvant cancer therapy by influencing blood flow, viscosity, and microenvironment-cantered mechanisms that reduce metastasis (Lucotti et al., 2019).

8.3 MICROFLUIDIC USSING CHAMBER

8.3.1 Introduction

The study of biological barriers, which are essential to ensure the proper organism function, has become one of the growing fields in microfluidics (Xavier et al., 2023; Y. I. Wang et al., 2017). In particular, the epithelial barrier of the gut controls the absorption of nutrients, water, and limits the invasion of bacteria (Nicolas et al., 2021). There are several platforms to study the intestinal barrier, but one of the most relevant is the Ussing chamber (Sjöberg et al., 2013; Thomson et al., 2019), a device used to study ion transport across epithelial tissues both from cell cultures and *ex vivo* intestinal mucosa. Named after the Danish physiologist Hans Ussing who pioneered their use in the 1950s, Ussing chambers have become indispensable tools in physiological and pharmacological research, particularly in fields such as gastroenterology, nephrology, and drug delivery. This device is composed of two fluid compartments separated by a permeable membrane cultured with epithelial cells or *ex vivo* intestinal mucosa (Figure 8.15a). By applying an electric potential across the tissue and monitoring the resulting current, researchers can investigate barrier functions, since cells can stablish a tight barrier controlling both transcellular and paracellular transport of molecules. The original design of the Ussing chamber system is rather intricate and not particularly user-friendly (Figure 8.15b,c), utilizing a high volume of sample and lacking compatibility with the widely used multiwell plate format and the orientation of the epithelial barrier difficult microscopic analysis.

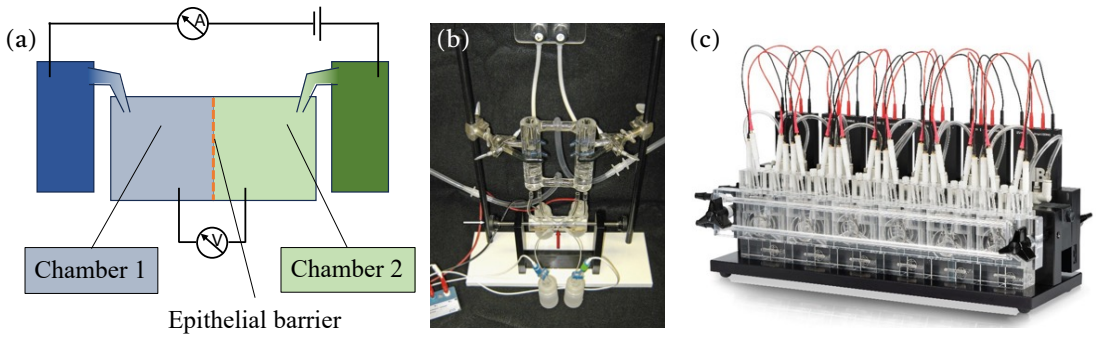

Figure 8.15: a) Scheme of a Ussing Chamber. b), c) Current Ussing chambers are complex systems.

The aim of this section is to develop a sensorised, microfluidic Ussing chamber, making it easier to use, reducing the required volume of reagents (Carius et al., 2021), and offering compatibility with microscopy, perfusion and parallelisation. The manufactured platform will be validated through Trans-Epithelial Electrical Resistance (TEER) measurements through microporous epithelial Caco-2 cell monolayer.

8.3.1.1 The relation of tight junctions with TEER

Tight junctions are multiprotein complexes that maintain cellular barriers and regulate paracellular permeability, controlling the passage of solutes and water. The integrity and

functionality of tight junctions is regulated by intracellular calcium (Ca^{2+}) concentrations, being essential for the assembly and stability of these junctions. The absence of Ca^{2+} disrupts tight junction integrity and as result, ions can freely pass between cells, leading to a decrease in electrical resistance (R). Cellular maturation and growth involve the development and formation of tight junctions, which generally increases electrical resistance over time with epithelial barrier maturation. Common Ca^{2+} ion chelating agents, such as EDTA, EGTA, and citrate, can be used to disrupt the epithelial barrier. Although each has distinct calcium-binding dynamics, they all essentially trap Ca^{2+}, preventing the formation of tight junctions and initially reducing R. However, when Ca^{2+} becomes available again (i.e. the chelating capacity of these agents is exceeded), the function of tight junctions is restored, leading to a subsequent increase in resistance. In this section, manufactured Ussing chamber will be employed to monitor real-time variations in R (which impact TEER) of the epithelial Caco-2 cell monolayer in presence of chelants.

8.3.2 Materials and methods

8.3.2.1 Manufacturing method of the microfluidic device

Microfluidic devices were fabricated according to the protocol detailed in Materials and Methods 4.2.1. Initially, 3D printed masters were produced and subsequently replicated using soft lithography of PDMS. In this case, 23G needles (0.6 mm in diameter) were utilized to form internal channels within the PDMS by embedding them in the uncured PDMS. The PDMS was then cured by placing the filled masters in a furnace at 60 °C for 12 hours. These internal channels act as guides for Ag/AgCl electrodes. Finally, the two halves of the Ussing chamber were bonded through O_2 plasma activation (Materials and Methods 4.1.4.2).

8.3.2.2 Caco-2 cell culture

Caco-2 cells were grown in MEM supplemented with 20% FBS, 1 mM Na-pyruvate, 100 $U \cdot ml^{-1}$ penicillin and 100 $\mu g \cdot ml^{-1}$ streptomycin (1% Pen/Strep),) in a cell culture incubator at 37ºC and 5% CO_2. To form an intestinal epithelium, cells were seeded at 10^5 cells/cm^2 and grown in 12-well semi-permeable inserts (transwell), featuring PET membranes of 1 µm pore size. Cells were maintained in the transwell during 21 days to ensure full differentiation, allowing the formation of a tight barrier. Differentiation was monitored by TEER weekly. The membranes were cut using an 8 mm punch and sandwiched between the two chambers, leaving an exposed area of 1.12 cm^2.

8.3.2.3 TEER measurement

TEER ($\Omega \cdot cm^2$) was quantified utilizing the 4-point probe method (Srinivasan et al., 2015). The setup involved voltage-sensing Ag/AgCl electrodes (manufactured following procedure introduced in Materials and Methods 4.2.3) connected to a epithelial Volt-Ohm Meter (EVOM^2)

by Millicell. This device delivers an AC square-wave current of 10 µA at 12.5 Hz to measure electrical resistance (R). Baseline resistance values (R_m) from blank porous membranes were also recorded and subtracted from each measurement. TEER values were then normalized to the endothelial culture area (A) using the formula:

$$TEER = (R - R_m) \cdot A$$

A comparative analysis of resistance measurements was conducted between the Ussing chamber electrode system outcomes and conventional "chopstick" electrodes within a transwell setup.

8.3.3 Results and discussion

8.3.3.1 Development of a sensorised microfluidic Ussing chamber.

As mentioned in the introduction, conventional Ussing chambers are cumbersome and difficult to integrate with multiplexing and microscopy. Therefore, we propose a rotated design, with the epithelial membrane positioned horizontally instead of vertically (see Figure 8.15a). This approach simplifies the creation of an array of microfluidic chambers within the commonly used 6 well plate (P6) format in biology (Figure 8.16a). Additionally, this design facilitates seamless integration with a reflection or transmission microscope for capturing images of the top or bottom chambers, respectively, while maintaining culture under flow conditions.

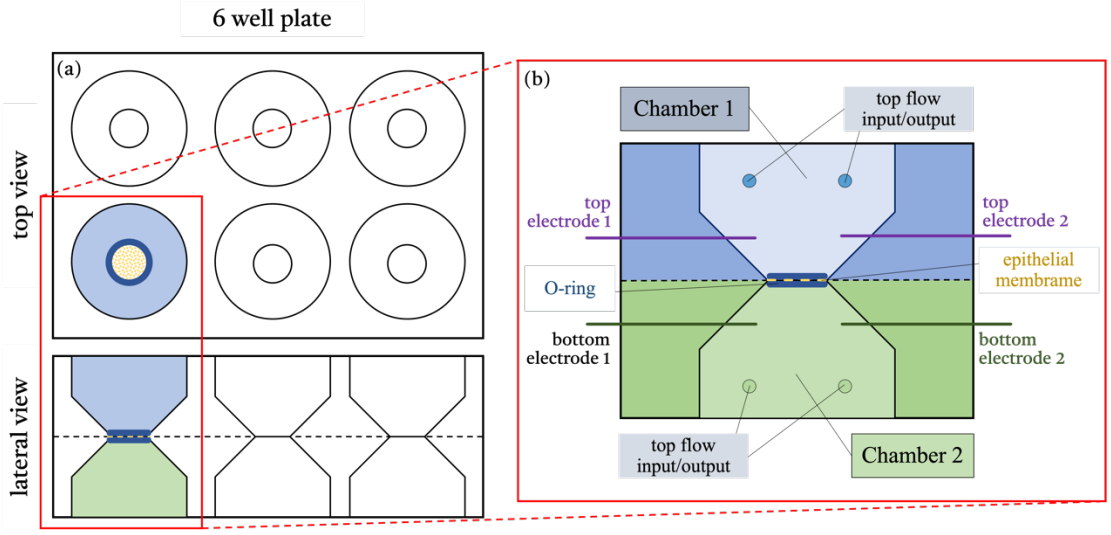

Figure 8.16: Conceptualization of the sensorised microfluidic Ussing Chamber. a) Top and lateral view of 6 multiplexed Ussing Chambers in the format of a standard 6-well plate. b) Detailed look to one of the microfluidic Ussing Chamber, featuring two chambers, four electrodes, the O-ring, the epithelial membrane and four flow inputs/outputs.

To simplify the prototyping phase, efforts were concentrated on the fabrication of a single well, with dimensions aimed to correspond to one-sixth of a standard P6 plate. The design of

this device posed a challenge due to the requirement of a conical internal cavity that cannot be demoulded with the traditional soft lithography structures (i.e., if the master structure that forms the cavity is attached to the base). The obvious solution would be to print the conical structure upright, but this would make it impossible to form the autoalignment connectors, necessary to match both halves (see Materials and Methods 4.2.1), on the air exposed face. The proposed solution involved printing a conical pillar that could be attached to the master. This pillar featured a position guide at its base to ensure the reproducible alignment of the ports, allowing insertion in only one specific configuration (Figure 8.17a). Internal channels were also printed on the lateral of the resin master to introduce needles to form both flow and electrode ports (Figure 8.17b) when the uncured PDMS is deposited inside (Figure 8.17c). With this approach, PDMS replica could be removed with the pillar inside and the connectors could be printed on the base (Figure 8.17d).

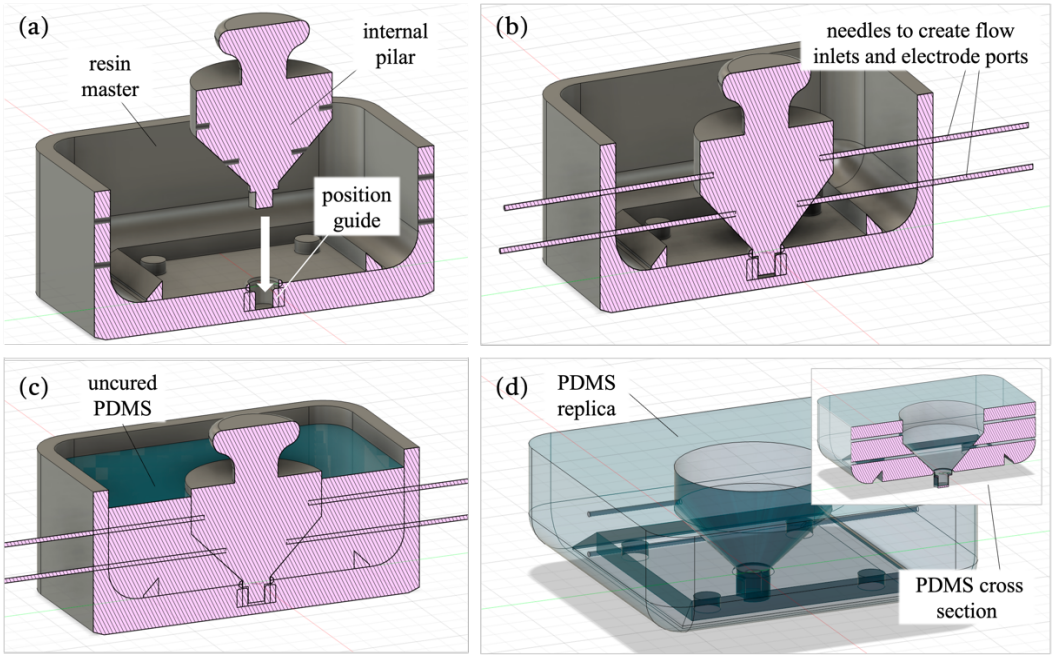

Figure 8.17: Conceptualization of Ussing chamber. First, a) an attachable conic pilar was designed to match the master. Next, b) needles are inserted in the lateral holes and c) the master is filled with uncured PDMS. After curing, the pillar and needles are removed forming d) the chamber and the ports, respectively. A cross section of the PDMS replica is also presented.

The manufacturing process started with the printing of both master and pillar (Figure 8.18a), which were designed to interlock seamlessly. Subsequently, needles were carefully inserted into the lateral holes of the master (Figure 8.18b), followed by pouring of uncured PDMS. Once cured, the needles (Figure 8.18c), the replica (Figure 8.18d), and the pillar (Figure 8.18e) were extracted, resulting in the formation of a chamber and the fluid/electrode ports (Figure 8.18f). Two identical PDMS slabs were bonded together resulting in a top and bottom chamber, which are separated by a microporous membrane. Bonding was achieved by plasma activation and an

O-ring was used to hold the porous membrane in place and avoid leakage (Figure 8.18g). The two fluid/electrode ports on either side allow each one for the introduction of liquid flow, and electrodes, used to measure TEER. After the prototyping process, a new Ussing chamber was manufactured, with reduced dimensions, which finally correspond to the P6 broadly used in biological and medical studies (Figure 8.18h,i).

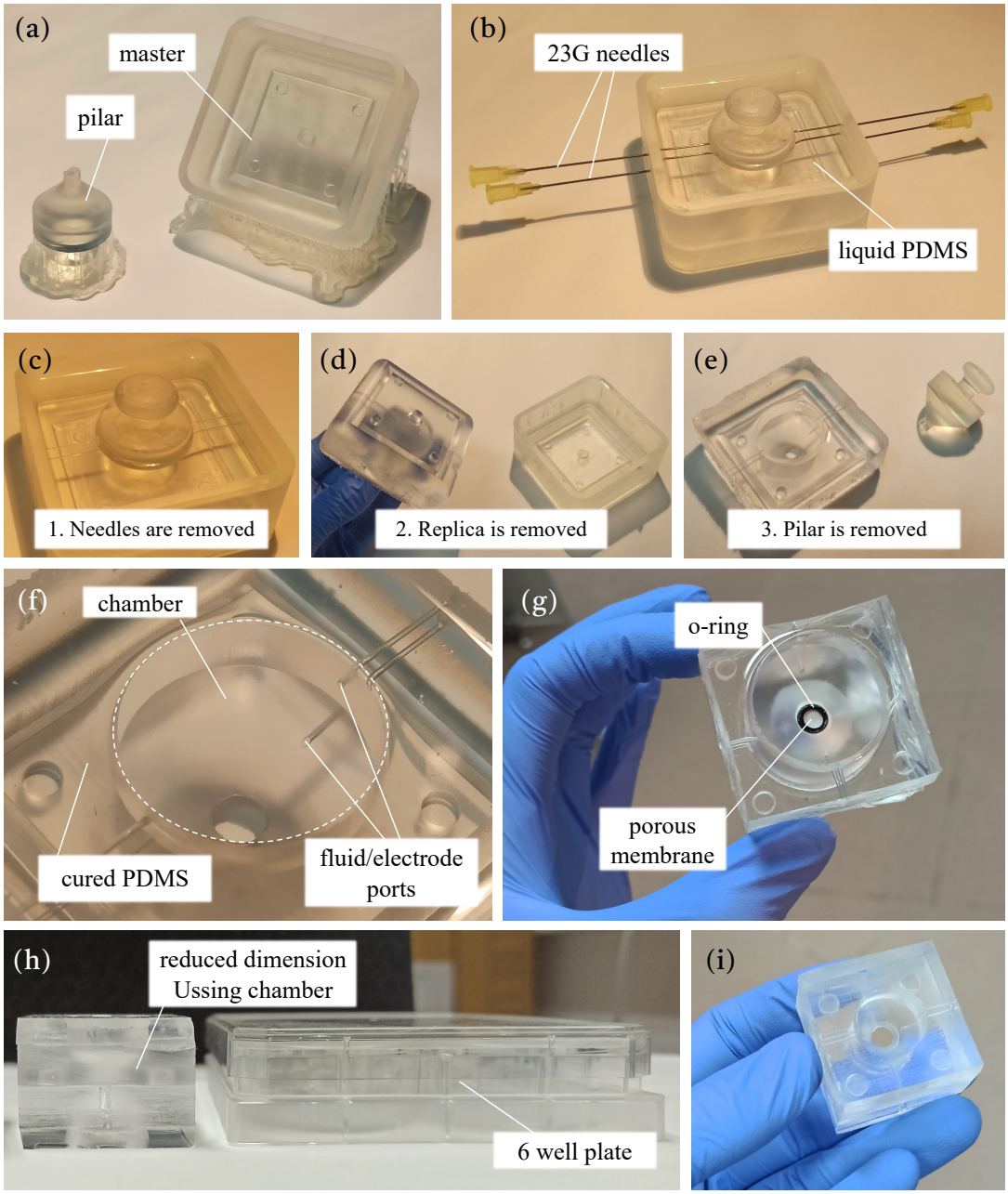

Figure 8.18: Manufacturing process of Ussing Chamber. First, a) the master and the pillar, which can be coupled, are printed. Next, b) 23G needles are inserted and the master is filled with uncured 10:1 PDMS. After curing: c) needles, d) PDMS replica and e) pilar are removed forming f) the chamber with the fluid/electrode ports. Finally, g) both halves are bonded, featuring an O-ring to fix the porous membrane in between. h) A reduced sized prototype was developed to fit the dimensions of P6, i) making it more handily.

8.3.3.2 Assessment of Caco-2 monolayer integrity in a sensorised microfluidic Ussing Chamber

The integrity of the Caco-2 monolayer (Figure 8.19a) was assessed by introducing the electrodes through the device ports (Figure 8.19b) and measuring TEER by connecting to a Epithelial Volt Ohm Meter (EVOM^2) from Millicell (Figure 8.19c). The TEER was calculated by subtracting the readings of cell-free inserts from the cell cultured inserts and multiplying by the surface area of the membrane (all measurements were done in duplicate). Simultaneously, measurements were made inside the transwell to compare the dynamics with the values obtained in the Ussing chamber (Figure 8.19d).

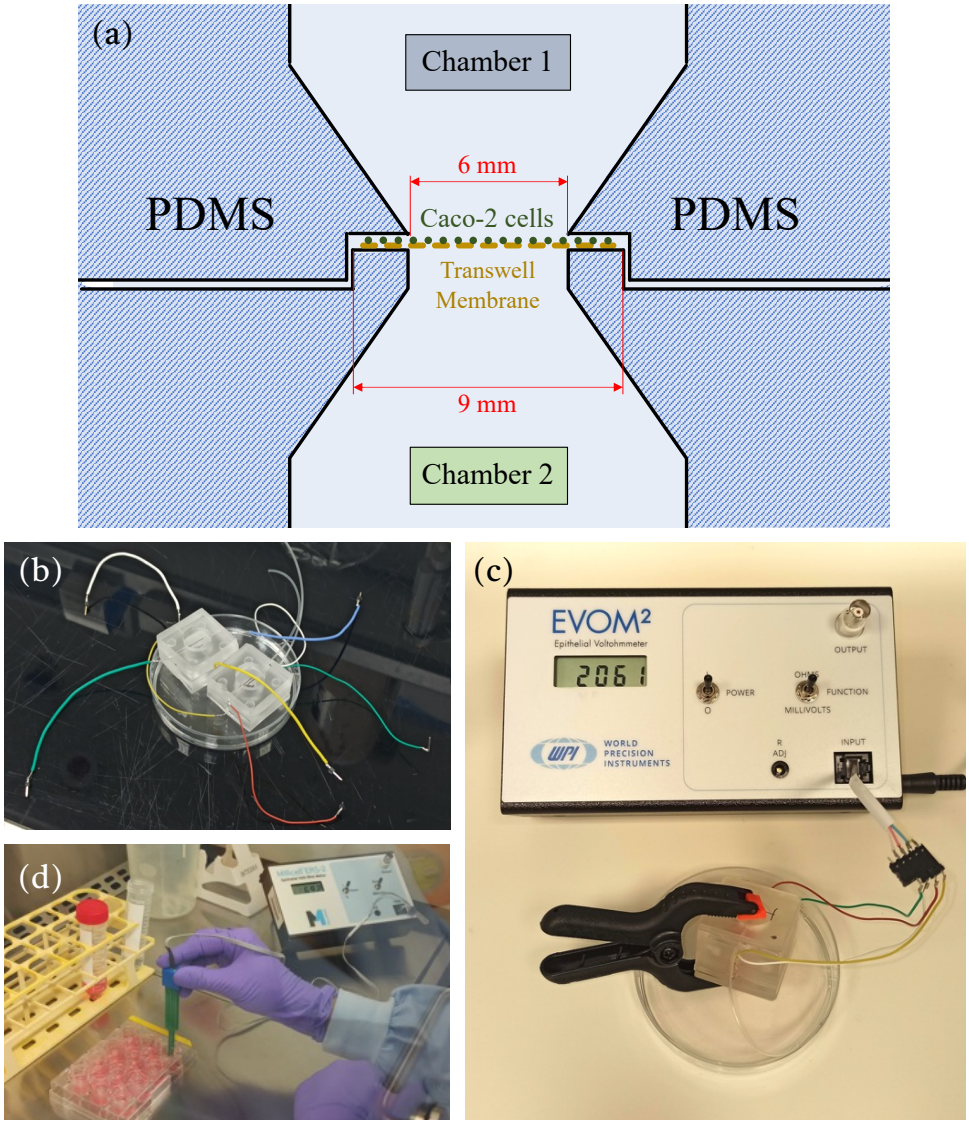

Figure 8.19: a) Schematic representation of the Caco-2 monolayer introduced inside the Ussing chamber, over the transwell membrane. b) Two manufactured Ussing chambers with the electrodes and wires coupled, allowing the connection to an c) epithelial volt ohm meter. A clamp was employed to secure the components, ensuring a tight fit and preventing leakage. d) Measurement was crosschecked with chopstick measurements inside the transwell.

The experiment for test our device had the following in consideration: cells with calcium cisterns form tight junctions, crucial for cell adhesion. As we mentioned in the introduction, calcium plays a central role in the regulation of tight junctions, and its chelation leads to increasing ion permeability and decreasing resistance. As cells differentiate, tight junctions strengthen, reducing the pass of ions through the barrier and, in consequence, increasing TEER. Chelating agents like EDTA will allow to show the role of tight junctions on intestinal barrier on a dynamic TEER measurement. Figure 8.20a shows the evolution of the TEER over time inside the manufactured chamber. Basal conditions were performed with live cells in HBSS with Ca^{2+} and Mg^{2+} ions. Then, HBSS without Ca^{2+} and Mg^{2+} and with 2mM EDTA was introduced during 15 mins at a flowrate of 1 mil/min to induce a temporary barrier dysfunction. Subsequently, HBSS with Ca^{2+} and Mg^{2+} was reintroduced to simulate a recovery step. The Ussing chambers showed a 48% decrease in TEER for the first 17 mins (Region I), followed by a rapid recovery (Region II), related with the re-introduction of Ca^{2+} and Mg^{2+} ions, during 15 mins. During the following 4 hours in the presence of the ions, TEER value showed a slow long term recovery (Region III).

The experimental TEER values were normalized relative to those measured in the transwell, in order to compare with data obtained from the microfluidic Ussing chamber. Despite obtained elevated TEER values in the Ussing chamber, probably attributable to membrane damage during the punching process (or the distance between the electrodes in the using chamber, which significantly exceeds that of the chopsticks.) the temporal dynamics observed in both datasets were notably congruent.

In Figure 8.20b, it can be observed that both sets of data (Ussing chamber and transwell) exhibited similar temporal trends. This observation signifies that both methodologies facilitated real-time monitoring of the presence of the chelating agent EDTA and the delineated Regions (I, II, III): an initial TEER decrease following EDTA introduction, prompt recovery upon reintroduction of Ca^{2+} and Mg^{2+}, and subsequent gradual long-term TEER increase. These results validate the capacity of the proposed sensorised microfluidic Ussing chamber to make time-resolved TEER measurements. Such methodologies are pivotal for studies exploring the permeability and integrity of epithelial barriers across diverse physiological and pathological contexts.

The manufactured Ussing Chamber allows the observation of this behaviour, with a notorious decrease in TEER during the first 17 mins and an increase after that, corresponding to the presence of Ca^{2+} and Mg^{2+} ions again.

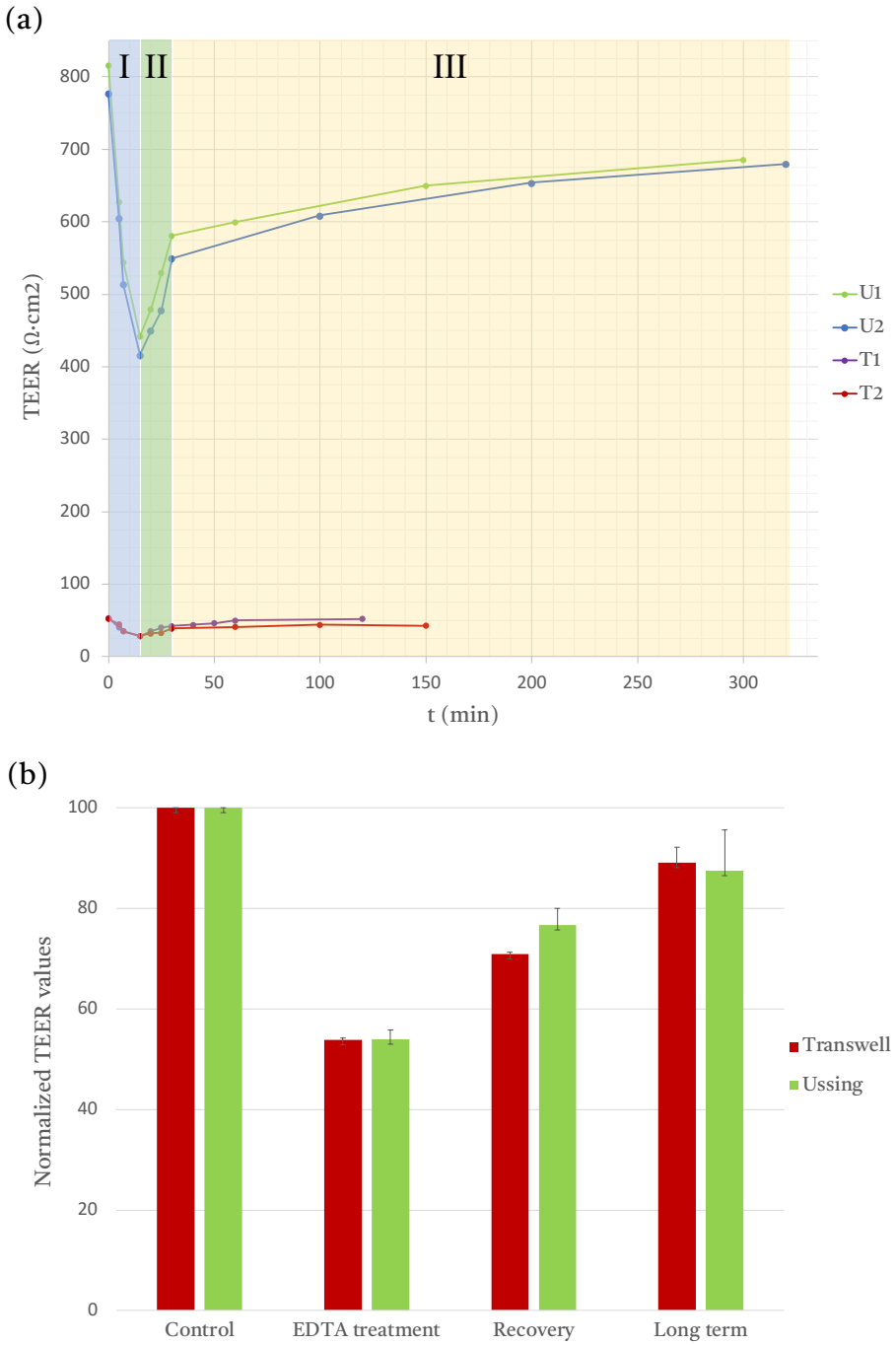

Figure 8.20: a) TEER behaviour over time in presence of EDTA (U: Ussing, T: Transwell). b) Normalized TEER values of Ussing measurement in comparison to transwell.

8.4 CONCLUSIONS

8.4.1 Biocompatibility assay

Biocompatibility study with HUVEC in 3D printing resins revealed different behaviour for each one. Whereas the three resins, Amber, Dental and Clear allowed the adhesion of HUVEC to their polished surfaces to a similar extent, cell growth after 24 h was not observed in all the

resins. HUVEC were not able to grow over Dental and Clear resins and after 24 h the culture did not progress. On the contrary, HUVEC grew over Amber resin to a similar extent that cultures made over conventional plastic material. Therefore, Amber showed an adequate biocompatibility, in terms of cell adhesion and cell growth for HUVEC.

Regarding the biocompatibility of PDMS materials, comparable outcomes were observed between thermally cured PDMS and UV-cured PDMS in HUVECs culture. Additionally, UV-PDMS demonstrated notable advantages over traditional PDMS, including superior optical clarity, shorter curing times, and simplified process enabled by UV light utilization. However, the cost of UV-cured PDMS is notably higher than that of standard PDMS, making it less advisable for use in low-volume production and prototyping. Flow experiments revealed that both PDMS variants supported HUVECs without detachment under flow conditions, highlighting its suitability for microfluidic platform applications.

8.4.2 Blood vessel bifurcation

This chapter introduces a microfluidic platform designed to investigate the mechanisms underlying the arrest of CTC at the vertex of blood vessel bifurcations.

In the first place, mathematical models and numerical simulations were used to study the behaviour of CTC at blood vessel bifurcations. The models demonstrate that while the majority of CTC follow high-velocity streamlines in the main vessel and move into secondary channels, a small, but significant fraction, deviates from these paths due to inertial effects. This deviation leads to these cells being trapped in low-velocity regions, particularly at the carina, the vertex of the bifurcation, where they exhibit prolonged residence time. This phenomenon is crucial because it increases the likelihood of CTC interacting with and adhering to the endothelial walls, a key step in the metastatic process.

Next, experimental validation using Y-shaped microfluidic devices, manufactured by laser ablation and soft lithography of PDMS of a 3D printer resin master, confirms the theoretical predictions. The GFP-tagged CTC predominantly follow high-velocity streamlines into secondary channels, while a minor fraction is observed to accumulate at the carina in low-velocity regions. This experimental observation aligns with the simulations and underscores the role of inertial forces in the selective arrest of CTC at these critical junctions.

The study also highlights the influence of bifurcation angle on CTC arrest. Numerical simulations and experimental results show that larger bifurcation angles lead to a more extensive low-velocity zone at the carina, resulting in greater CTC accumulation. This finding emphasizes the importance of vessel geometry in modulating CTC behaviour and their potential for metastasis. Additionally, variations in fluid viscosity significantly impact CTC behaviour. Higher viscosity enhances CTC arrest at bifurcations, which correlates with changes in the Reynolds number and affects flow dynamics. This suggests that both the physical properties of

the fluid and biological factors such as CTC aggregation play significant roles in CTC arrest and potential for metastasis. These results were further validated in in vitro and in vivo models. In vitro experiments with endothelial monolayers and in vivo studies with mice confirm that CTCs indeed arrest at bifurcations, interact with endothelial cells, and contribute to metastasis. Drugs that affect blood viscosity or coagulation, such as low molecular weight heparin, warfarin, and aspirin, might provide therapeutic avenues for mitigating metastasis by modulating the physical and biological factors influencing CTC behaviour.

Overall, these findings provide valuable insights into the mechanical and geometrical factors affecting CTC behaviour and highlight potential strategies for clinical intervention to reduce metastatic spread.

8.4.3 Microfluidic Ussing chamber

A new horizontally-rotated sensorised microfluidic Ussing chamber design has been proposed and developed. This concept overcomes the limitations of traditional chambers by enabling seamless integration with multiplexing and microscopy. It is compatible with a P6 format and allows for easy imaging of both the top and bottom chambers under flow conditions. Prototyping focused on a single well, scaled to one-sixth of a P6 plate. The chamber was manufactured by soft lithography of PDMS of 3D printed masters that featured a conical pillar to create the internal cavity and autoalignment connectors for proper match. Internal channels were formed to introduce flow and electrode ports, leading to the desired chamber structure. The final assembly involved bonding two PDMS slabs, separated by a microporous epithelial membrane secured by an O-ring to prevent leakage.

The integrity of the Caco-2 monolayer was evaluated using the manufactured Ussing chamber. TEER measurements were conducted by inserting electrodes and connecting them to an EVOM^2. TEER values were calculated by subtracting cell-free insert readings from cell-cultured insert readings and multiplying by the membrane surface area. Parallel measurements in the transwell provided comparative dynamics. Both the Ussing chamber and transwell showed similar temporal TEER trends, despite higher TEER values in the Ussing chamber due to membrane damage during punching. The study demonstrated a TEER decrease after EDTA introduction, followed by recovery with Ca^{2+} and Mg^{2+} reintroduction, and a gradual long-term TEER increase. These results confirm the Ussing chamber capability for real-time monitoring epithelial barrier integrity and permeability, highlighting its potential for advanced research.

9. CONCLUSIONS

This section will outline the main findings and insights obtained from the research conducted during this thesis. While each chapter contains its own detailed conclusions, a concise and unified summary of all findings is presented. Additionally, the planned future research will be briefly discussed in this section, highlighting potential areas for further investigation.

- A new technique called Subaquatic indirect Laser-Induced Plasma-Assisted Ablation (SLIPAA) has been developed, which overcomes the limitations encountered when fabricating deeper channels with straight walls using conventional indirect laser ablation protocols. This technique uses a nanosecond laser source (since is one of the most used in the industry) to process various geometries in soda-lime glass substrates, employing a water layer to confine plasma and enhance material removal.
  - SLIPAA produces high-quality rectangular channels with vertical sidewalls and excellent edge precision. Channels of various widths and depths, up to 1400 μm (the figures are rounded for clarity) with a minimum width of 300 μm, are achieved with a power (P) of 4.92 W mW, a repetition rate (ν) of 10 kHz, 30 passes (N) and a velocity (v) of 200 mm/s
  - SLIPAA outperforms LIPAA, with deeper structures (up to 1400 μm vs. 660 μm) and less impurity transfer and debris on channel surfaces. The technique also provides better surface quality and fewer contaminants.
  - SLIPAA is not limited to channel fabrication but also can create structures with diverse geometries, including wells up to 4 mm deep in 5 mm thick substrates, making it highly effective for extensive material removal.
- 3D printing, particularly stereolithography (SLA), has been studied in deep as manufacturing technology for microfluidics, as it offers a promising and precise approach for fabricating final devices and masters. This technology provides high accuracy, reduced production times, and minimal waste production.
  - Seven commercial resins (Clear, Dental, Tough, Amber, Flexible, Elastic, Model) were evaluated for microfluidic applications. Dental resin had the shortest printing time, while Model and Clear resins achieved the highest resolution but required more time. It

was found that polishing increases the transmittance for Amber, Clear and Dental resins, reaching around 80% transmittance for the visible range, of interest in fluorescence microscopy.

- The surface performance of the printer was analysed by examining the topology of printed channels and pillars, revealing deviations from the designs, with aspect ratios for small channels (0-500 μm) below 0.75 and larger channels (500-1500 μm) between 0.75 and 1.25. Clear and Model resins showed the best accuracy.
- The surface finishing of the structures indicated that printing orientation is crucial, as perpendicular orientation to the base facilitated the best uncured resin evacuation, preventing unwanted resin accumulation on the sides of channels and wells.
- Regarding internal channels, the accumulation of resin was identified as a key factor leading to obstructions and malformations in internal channels. Channels with diameters greater than 500 μm and printing orientations over 60º achieved high printing accuracy, with resins like Dental and Amber exceeding 80% accuracy. Larger channels (1000-1500 μm) further improved accuracy, reaching over 90% for all resins studied.
- Clear, Model, and Tough resins performed are the best option for creating masters for soft lithography of PDMS, whereas Amber and Dental resins showed poor topology transfer. Flexible and Elastic resins were unsuitable for master manufacturing due to curing issues.

❖ A novel hybrid technique combining PLA and SLA for manufacturing microfluidic structures (micromixers and microlens) has been developed. This technique involves performing surface structuring of SLA 3D printed substrates using PLA, employing each technology in its most suitable dimensional range (millimeters and microns, respectively).

- For surface patterning, optimal laser parameters were found: P=90 mW, ν=1kHz, N=2 and a v=1 mm/s, resulting in channels with a width of 40 μm and a diameter of 130 μm. Wider channels, desired for better fluid flow and PDMS removal during replication, were achieved by ablating multiple contiguous lines, with three lines separated 35 μm producing the best results.
- Regarding micromixers, two manufacturing protocols were developed: Protocol 1 focused on inward channel micropatterning using PLA and adhesive film for sealing, while Protocol 2 created grooves on outward channels using PLA to serve as masters for PDMS soft lithography.
- Flow experiments and CFD simulations showed that micromixers with structured channels significantly improved mixing efficiency compared to flat channels, with 20° and 45° orientations offering the best results.

- Concerning microlens arrays, the proposed hybrid technique shows promising results. An optimal range for ablation parameters was established for both unpolished and polished resin surfaces. For unpolished surfaces, the optimal parameters were: P= 40-50 mW, ν=1kHz, N=2-3 and v=1 mm/s. This resulted in inward microlens with diameters and depths of approximately 25 μm featuring focal distances around 50 μm. For polished resin surfaces, the optimal parameters were: P=50-60 mW, ν=1kHz, N=2-3 and v=1 mm/s. This configuration produced inward microlenses with diameters of about 40 μm and depths of 20 μm, featuring focal distances around 50 μm.
- Polished resin yielded more regular and spherical microlenses with improved optical performance, whereas unpolished resin showed deviations in shape and surface roughness, which affected the accuracy of the focal length and resulted in increased light scattering.
- Replication of microlens arrays using PDMS soft lithography was effective but required careful handling to avoid defects. Flexible microlenses demonstrated advantages in adaptability for various applications.

❖ A biocompatibility study with HUVEC using various 3D printing resins and PDMS was developed under static and flow conditions.

- Amber, Dental, and Clear resins permitted similar levels of HUVEC adhesion to their polished surfaces. However, cell growth after 24 hours was not observed across all resins. HUVEC were unable to proliferate on Dental and Clear resins, with cultures stagnating after 24 hours. In contrast, HUVEC grew on Amber resin to a degree comparable to growth on conventional plastic materials, indicating that Amber resin has adequate biocompatibility in terms of cell adhesion and proliferation.
- Regarding PDMS materials, both thermally cured and UV-curable PDMS (UV-PDMS) demonstrated comparable biocompatibility with HUVECs. UV-PDMS offered notable advantages over traditional PDMS, such as superior optical clarity, shorter curing times, and a simplified process due to UV light curing. Nevertheless, UV-PDMS is significantly more expensive than standard PDMS, making it less ideal for low-volume production and prototyping.
- Flow experiments showed that both PDMS types supported HUVEC without detachment under flow conditions, underscoring their suitability for microfluidic platform applications.

❖ A study to investigate the mechanisms underlying the arrest of CTC at the vertex of blood vessel bifurcations was performed.

- Symulations reveal that while most CTC follow high-velocity streamlines in the principal vessel, a small but significant fraction deviates due to inertial effects. This

deviation causes these cells to accumulate in low-velocity regions at the vertex of blood vessel bifurcations, particularly at the carina. This prolonged residence time enhances the likelihood of CTC interacting with and adhering to endothelial walls, a critical step in the metastatic process.

- The experimental validation using Y-shaped microfluidic devices, manufactured by combining SLA and soft lithography of PDMS, confirms the theoretical predictions made by the simulations. GFP-tagged CTC predominantly follow high-velocity paths into secondary channels, while a minor fraction accumulates at the low-velocity carina. These observations reinforce the role of inertial forces in the selective arrest of CTC at critical junctions, aligning with the numerical simulations.
- A study on the impact of bifurcation angle was performed, demonstrating that larger bifurcation angles increase the extent of the low-velocity zone at the carina, leading to greater CTC accumulation. This highlights the importance of vessel geometry in influencing CTC behaviour. Additionally, variations in fluid viscosity affect CTC arrest. Higher viscosity enhances CTC accumulation at bifurcations due to changes in Reynolds number and flow dynamics.
- The findings are corroborated by *in vitro* experiments with endothelial monolayers and *in vivo* studies in mice, which confirm CTC arrest at bifurcations and their interaction with endothelial cells. These results suggest that modulating blood viscosity or coagulation with drugs such as low molecular weight heparin, warfarin, or aspirin may offer therapeutic strategies to reduce metastasis. By altering the physical and biological factors influencing CTC behaviour, these interventions could help mitigate metastatic spread and improve clinical outcomes.

❖ A novel horizontally-rotated sensorized microfluidic Ussing chamber is proposed. This approach overcomes traditional limitations by integrating multiplexing and microscopy seamlessly. This design allows for effective imaging of both the top and bottom chambers under flow conditions and is compatible with a P6 format.

- The manufacturing of the chamber, which combines SLA and soft lithography of PDMS, represents a significant advancement in the features of this platform. Ag/AgCl electrodes were manufactured and effectively integrated into the interior of the chambers allowing the connection to a volt-ohm meter.
- The manufactured Ussing chamber effectively evaluated the integrity of the Caco-2 monolayer through TEER measurements, with results consistent with those obtained from parallel transwell assays. The observed TEER trends, including the decrease following EDTA treatment and subsequent recovery, confirm the chamber capability to monitor epithelial barrier integrity and permeability in real-time. This validates the

chamber performance and its suitability for advanced research in barrier dynamics and permeability.

FUTURE WORK

If one compares the initial objectives outlined at the beginning of the thesis with the conclusions, some differences are revealed. This discrepancy is, however, an inherent aspect of the scientific method and essential to the advance of knowledge. While some questions remain unanswered, a significant number of answers have been discovered in the process.

Therefore, the focus must now shift to the future. Regarding the continuation of this work and this particular line of research, it is clear that there is still a long way to go. One of the areas I consider most important to expand is the study of the Ussing chamber, which came right at the end of this thesis and whose potential has not yet been exploited. The next logical step would be to fabricate an array of six Ussing chambers and integrate them with microscopy systems, monitoring the results automatically. Additionally, investigating other chelant agents or treatments and new epithelial barriers would be valuable. Furthermore, investigating other membrane parameters, such as the apparent permeability coefficient, could provide valuable insights and be readily facilitated using our device.

On the other hand, the fabrication of physiologically mimetic structures using 3D printed masters for PDMS replication offers limitless possibilities. This technique can replicate a vast array of organs, vessels, nerves, and tissues *in vitro*. The potential is further enhanced if we integrate the developed hybrid technique, which uses surface microstructuring with PLA to recreate diverse physiological topologies within the larger channel structure. Consequently, the next step would be to conduct a study on the most promising physiological models as benchmarks. Additionally, exploring new polymers and printing resins, particularly softer ones, could lead to significant advancements. Mimicking the delicate, flexible outer walls of vessels remains a challenge, and developing a 3D coffin (similar as occurs in embossing) could be an innovative approach. This method would allow the creation of internal channels surrounded by a thin layer of PDMS rather than within a solid block, potentially enabling the study of diseases such as carotid stenosis or aneurysms.

Finally, on a personal note, I am particularly interested in the potential that microfluidics offers for cooling structures. This relatively unexplored field stems from the observation of how living organisms cool themselves through a network of vessels that transport water across the skin surface to dissipate heat, leveraging the high specific heat capacity of water. This mechanism could be of immense value for cooling machinery or computers. Cooling issues incur millions of euros in annual losses due to unwanted energy dissipation.

10. LIST OF PUBLICATIONS

10.1 JOURNAL PUBLICATIONS

The work conducted in this thesis has resulted in the following publications in international journals and books. The author contributions and copyright permissions for the articles that have been reproduced in whole or in part in within this thesis are detailed.

1. Bastián Carnero, Carmen Bao-Varela, Ana Isabel Gómez-Varela and M. Teresa Flores-Arias, *Internal Microchannel Manufacturing Using Stereolithographic 3D Printing*, Trends and Opportunities of Rapid Prototyping Technologies (2022), DOI: 10.5772/intechopen.102751, ISBN: 978-1-80355-727-4

Author contribution: conceptualization, investigation, validation, writing - original draft and review.

2. Ana I. Gómez-Varela, Raúl Sanchez, Bastián Carnero, Luis Diaz-Gomez, M. Teresa Flores-Arias, and Carmen Bao-Varela, *Subaquatic indirect laser ablation technique for glass processing*, Optics Express (2022), DOI: https://doi.org/10.1364/OE.463803

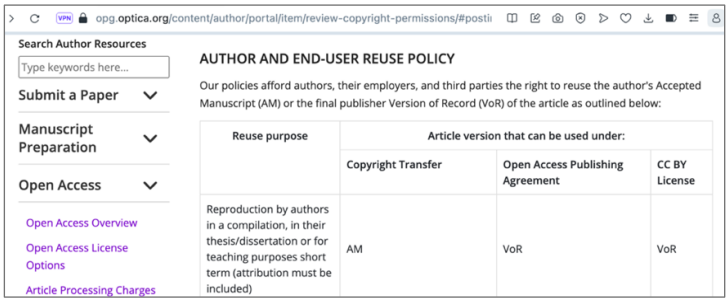

Author contribution: investigation, review.

3. Bastián Carnero, Carmen Bao-Varela, Ana Isabel Gómez-Varela, Ezequiel Álvarez and María Teresa Flores-Arias, *Microfluidic devices manufacturing with a stereolithographic printer for biological applications*, Materials Science and Engineering: C (2021), DOI: 10.1016/j.msec.2021.112388

Author contribution: conceptualization, investigation, validation, writing - original draft and review.

4. Bastián Carnero, Yago Radziunas-Salinas, Bruno K. Rodiño-Janeiro, Sylvana Varela Ballesta and M. Teresa Flores-Arias, *Versatile hybrid technique for passive straight micromixer manufacturing by combining pulsed laser ablation, stereolithographic 3D printing and computational fluid dynamics*, Lab on a Chip (2024), DOI: 10.1039/D4LC00009A

Author contribution: conceptualization, methodology, validation, investigation, writing - original draft and review.

5. Ana I. Gómez-Varela, Antonio Viña, Carmen Bao-Varela, María Teresa Flores-Arias, Bastián Carnero, Mercedes González-Peteiro, José Ramón González-Juanatey, and Ezequiel Álvarez, *Biocompatibility Testing of UV-Curable Polydimethylsiloxane for Human Umbilical Vein Endothelial Cell Culture on-a-Chip*, ACS Omega (2024), DOI: https://doi.org/10.1021/acsomega.4c01148

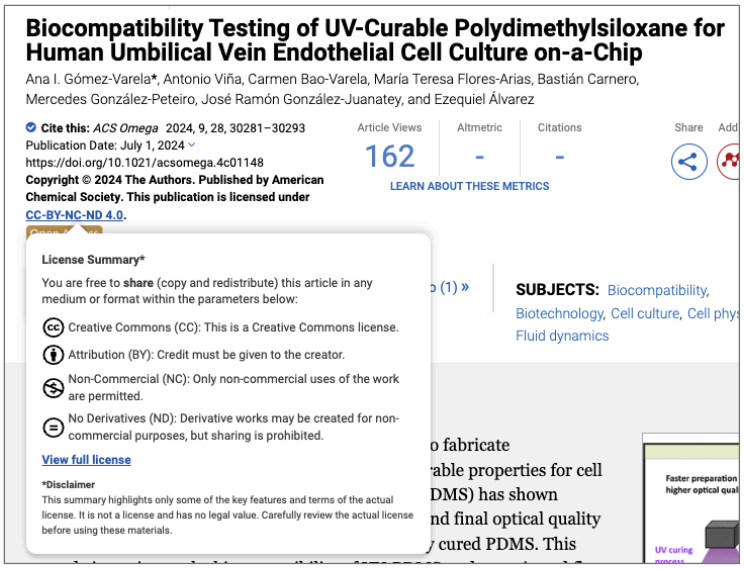

Author contribution: design and fabrication of devices, investigation, review.

6. Carlos Casas-Arozamena, Alberto Otero-Cacho, Bastián Carnero, Cristina Almenglo, María Aymerich, Lorena Alonso-Alconada, Alba Ferreiros, Alicia Abalo, Carmen Bao-Varela, Maria Teresa Flores-Arias, Ezequiel Alvarez, Alberto P. Muñuzuri and Miguel Abal, *Haemodynamic-dependent arrest of circulating tumour cells at large blood vessel bifurcations as new model for metastasis*, Scientific Reports (2021), DOI: 10.1038/s41598-021-02482-x

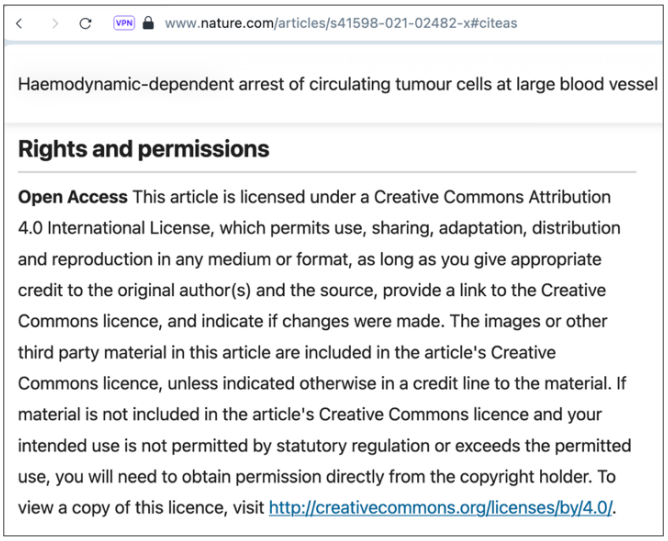

Author contribution: design and fabrication of devices, investigation, analytical tools and data acquisition, review.

7. Chloé Turpin, Marie Laurine Apalama, Bastián Carnero, Alberto Otero-Cacho, Alberto P. Munuzuri, Maria Teresa Flores-Arias, Erick Véliaf, Olivier Meilhac , Emmanuel Bourdon, Ezequiel Álvarez, and Philippe Rondeau, *Impact of Enhanced Phagocytosis of Glycated Erythrocytes on Human Endothelial Cell Functions,* Cells (2022), DOI: 10.3390/cells11142200

Author contribution: Design and fabrication of devices, investigation.

10.1.1 Journal metrics

- *Trends and Opportunities of Rapid Prototyping Technologies* is a book published by IntechOpen.
- *Optics Express* is a journal published by the Optica Publishing Group. It is classified within the second quartile (Q2) for the category of **Optics**, with an Impact Factor of 3.8 in 2022.
- *Materials Science and Engeneering: C* is a journal published by Elsevier Ltd.. It is classified within the first quartile (Q1) for the category of **Materials Science, Biomaterials**, with an Impact Factor of 8.457 in 2021.
- *Lab on a Chip* is a journal published by Elsevier Ltd.. It is classified within the first quartile (Q1) for the category of **Biochemical Research Methods** and **Chemistry, Analytical**, with an Impact Factor of 6.1 in 2023.
- *Scientific Reports* is a journal published by the Nature Publishing Group. It is classified within the second quartile (Q2) for the category of **Multidisciplinary Sciences**, with an Impact Factor of 4.997 in 2021.
- *ACS Omega* is a journal published by American Chemical Society. It is classified within the second quartile (Q2) for the category of **Chemistry, Multidisciplinary**, with an Impact Factor of 3.7 in 2023.
- *Cells* is a journal published by Multidisciplinary Digital Publishing Institute. It is classified within the second quartile (Q2) for the category of **Cell Biology**, with an Impact Factor of 6.0 in 2022.

10.2 PATENTS

From the work carried out in Chapter 5 also stemmed a manufacturing patent registered under number ES2912039 A1 (24.05.2022). The invention refers to a process for glass processing using a laser source. More particularly, this process includes the realization of structures with different geometries and depths in glass substrates, using an underwater indirect laser ablation method.

- Application number: P202230206 (11.03.2022)
- Applicant: Universidade de Santiago de Compostela (100.0%) (ES)
- Inventor/s: Bao Varela, Maria Del Carmen (ES); Gómez Varela, Ana Isabel (ES); Sánchez Cruz, Raul (ES); Carnero Groba, Bastián (ES); Flores Arias, Maria Teresa (ES)

REFERENCES

Abonnenc, M., Dayon, L., Perruche, B., Lion, N., & Girault, H. H. (2008). Electrospray Micromixer Chip for On-Line Derivatization and Kinetic Studies. *Analytical Chemistry*, *80*(9), 3372–3378. https://doi.org/10.1021/ac800058h

Abreu, M., Cabezas-Sainz, P., Pereira-Veiga, T., Falo, C., Abalo, A., Morilla, I., Curiel, T., Cueva, J., Rodríguez, C., Varela-Pose, V., Lago-Lestón, R., Mondelo, P., Palacios, P., Moreno-Bueno, G., Cano, A., García-Caballero, T., Pujana, M. Á., Sánchez-Piñón, L., Costa, C., … Muinelo-Romay, L. (2020). Looking for a Better Characterization of Triple-Negative Breast Cancer by Means of Circulating Tumor Cells. *Journal of Clinical Medicine*, *9*(2), 353. https://doi.org/10.3390/jcm9020353

Agha, A., Waheed, W., Stiharu, I., Nerguizian, V., Destgeer, G., Abu-Nada, E., & Alazzam, A. (2023). A review on microfluidic-assisted nanoparticle synthesis, and their applications using multiscale simulation methods. *Discover Nano*, *18*(1), 18. https://doi.org/10.1186/s11671-023-03792-x

Alapan, Y., Hasan, M. N., Shen, R., & Gurkan, U. A. (2015). Three-Dimensional Printing Based Hybrid Manufacturing of Microfluidic Devices. *Journal of Nanotechnology in Engineering and Medicine*, *6*(2), 1–9. https://doi.org/10.1115/1.4031231

An, R., Li, Y., Dou, Y., Yang, H., & Gong, Q. (2005). Simultaneous multi-microhole drilling of soda-lime glass by water-assisted ablation with femtosecond laser pulses. *Optics Express*, *13*(6), 1855. https://doi.org/10.1364/OPEX.13.001855

Anna, S. L., Bontoux, N., & Stone, H. A. (2003). Formation of dispersions using "flow focusing" in microchannels. *Applied Physics Letters*, *82*(3), 364–366. https://doi.org/10.1063/1.1537519

Au, A. K., Lee, W., & Folch, A. (2014). Mail-order microfluidics: Evaluation of stereolithography for the production of microfluidic devices. *Lab Chip*, *14*(7), 1294–1301. https://doi.org/10.1039/C3LC51360B

Aubin, J., Fletcher, D. F., & Xuereb, C. (2005). Design of micromixers using CFD modelling. *Chemical Engineering Science*, *60*(8–9), 2503–2516. https://doi.org/10.1016/j.ces.2004.11.043

Awe, J. A., Saranchuk, J., Drachenberg, D., & Mai, S. (2017). Filtration-based enrichment of circulating tumor cells from all prostate cancer risk groups. *Urologic Oncology: Seminars and Original Investigations*, *35*(5), 300–309. https://doi.org/10.1016/j.urolonc.2016.12.008

Aymerich López, M. de la I. (2019). *Microstructuring of materials with laser technologies for biomedical applications* [Universidade de Santiago de Compostela]. http://hdl.handle.net/10347/19464

Aymerich, M., Álvarez, E., Bao-Varela, C., Moscoso, I., González-Juanatey, J. R., & Flores-Arias, M. T. (2017a). Laser technique for the fabrication of blood vessels-like models for

preclinical studies of pathologies under flow conditions. *Biofabrication*, *9*(2), 025033. https://doi.org/10.1088/1758-5090/aa6c3d

Aymerich, M., Álvarez, E., Bao-Varela, C., Moscoso, I., González-Juanatey, J. R., & Flores-Arias, M. T. (2017b). Laser technique for the fabrication of blood vessels-like models for preclinical studies of pathologies under flow conditions. *Biofabrication*, *9*(2), 025033. https://doi.org/10.1088/1758-5090/aa6c3d

Aymerich, M., Gómez-Varela, A., Álvarez, E., & Flores-Arias, M. (2016). Study of Different Sol-Gel Coatings to Enhance the Lifetime of PDMS Devices: Evaluation of Their Biocompatibility. *Materials*, *9*(9), 728. https://doi.org/10.3390/ma9090728

Aymerich, M., Nieto, D., & Flores-Arias, M. T. (2015). Laser-based surface multistructuring using optical elements and the Talbot effect. *Optics Express*, *23*(19), 24369. https://doi.org/10.1364/OE.23.024369

Azadgoli, B., & Baker, R. Y. (2016). Laser applications in surgery. *Annals of Translational Medicine*, *4*(23), 452–452. https://doi.org/10.21037/atm.2016.11.51

Bai, S., Serien, D., Hu, A., & Sugioka, K. (2018). 3D Microfluidic Surface-Enhanced Raman Spectroscopy (SERS) Chips Fabricated by All-Femtosecond-Laser-Processing for Real-Time Sensing of Toxic Substances. *Advanced Functional Materials*, *28*(23), 1706262. https://doi.org/10.1002/adfm.201706262

Bally, F., Serra, C. A., Hessel, V., & Hadziioannou, G. (2011). Micromixer-assisted polymerization processes. *Chemical Engineering Science*, *66*(7), 1449–1462. https://doi.org/10.1016/j.ces.2010.07.026

Barron, J. A., Wu, P., Ladouceur, H. D., & Ringeisen, B. R. (2004). Biological Laser Printing: A Novel Technique for Creating Heterogeneous 3-dimensional Cell Patterns. *Biomedical Microdevices*, *6*(2), 139–147. https://doi.org/10.1023/B:BMMD.0000031751.67267.9f

Battat, S., Weitz, D. A., & Whitesides, G. M. (2022). An outlook on microfluidics: The promise and the challenge. *Lab on a Chip*, *22*(3), 530–536. https://doi.org/10.1039/D1LC00731A

Behera, R. R., & Sankar, M. R. (2015). State of the Art on Under Liquid Laser Beam Machining. *Materials Today: Proceedings*, *2*(4–5), 1731–1740. https://doi.org/10.1016/j.matpr.2015.07.007

Beloso Aragón, Á. L. (2019). *Fabricación mediante láser de un estimulador eléctrico para aplicaciones biomédicas: Fabricación, caracterización y simulación* [Universidade de Santiago de Compostela]. http://hdl.handle.net/10347/20639

Bennett, J. (2017). Measuring UV curing parameters of commercial photopolymers used in additive manufacturing. *Additive Manufacturing*, *18*, 203–212. https://doi.org/10.1016/j.addma.2017.10.009

Berry, S. M., Maccoux, L. J., & Beebe, D. J. (2012). Streamlining Immunoassays with Immiscible Filtrations Assisted by Surface Tension. *Analytical Chemistry*, *84*(13), 5518–5523. https://doi.org/10.1021/ac300085m

Bhattacharjee, N., Urrios, A., Kang, S., & Folch, A. (2016). The upcoming 3D-printing revolution in microfluidics. *Lab on a Chip*, *16*(10), 1720–1742. https://doi.org/10.1039/C6LC00163G

Bidard, F.-C., Pierga, J.-Y., Vincent-Salomon, A., & Poupon, M.-F. (2008). A "class action" against the microenvironment: Do cancer cells cooperate in metastasis? *Cancer and Metastasis Reviews*, *27*(1), 5–10. https://doi.org/10.1007/s10555-007-9103-x

Bloembergen, N. (1982). Nonlinear optics and spectroscopy. *Reviews of Modern Physics*, *54*(3), 685–695. https://doi.org/10.1103/RevModPhys.54.685

Bobek, V., & Kovařík, J. (2004). Antitumor and antimetastatic effect of warfarin and heparins. *Biomedicine & Pharmacotherapy*, *58*(4), 213–219. https://doi.org/10.1016/j.biopha.2003.11.007

Böhme, R., & Zimmer, K. (2004). Low roughness laser etching of fused silica using an adsorbed layer. *Applied Surface Science*, *239*(1), 109–116. https://doi.org/10.1016/j.apsusc.2004.05.095

Bohr, N. (1913). On the constitution of atoms and molecules. *The London, Edinburgh, and Dublin Philosophical Magazine and Journal of Science*, *26*(151), 1–25. https://doi.org/10.1080/14786441308634955

Born, M., Wolf, E., Bhatia, A. B., Clemmow, P. C., Gabor, D., Stokes, A. R., Taylor, A. M., Wayman, P. A., & Wilcock, W. L. (1999). *Principles of Optics: Electromagnetic Theory of Propagation, Interference and Diffraction of Light* (7th ed.). Cambridge University Press. https://doi.org/10.1017/CBO9781139644181

Bourkoula, A., Constantoudis, V., Kontziampasis, D., Petrou, P. S., Kakabakos, S. E., Tserepi, A., & Gogolides, E. (2016). Roughness threshold for cell attachment and proliferation on plasma micro-nanotextured polymeric surfaces: The case of primary human skin fibroblasts and mouse immortalized 3T3 fibroblasts. *Journal of Physics D: Applied Physics*, *49*(30), 304002. https://doi.org/10.1088/0022-3727/49/30/304002

Bozkurt, Y., & Karayel, E. (2021). 3D printing technology; methods, biomedical applications, future opportunities and trends. *Journal of Materials Research and Technology*, *14*, 1430–1450. https://doi.org/10.1016/j.jmrt.2021.07.050

Brambley, D., Martin, B., & Prewett, P. D. (1994). Microlithography: An overview. *Advanced Materials for Optics and Electronics*, *4*(2), 55–74. https://doi.org/10.1002/amo.860040203

Brodland, G. W., & Veldhuis, J. H. (2012). The Mechanics of Metastasis: Insights from a Computational Model. *PLoS ONE*, *7*(9), e44281. https://doi.org/10.1371/journal.pone.0044281

Broquin, J.-E., & Honkanen, S. (2021). Integrated Photonics on Glass: A Review of the Ion-Exchange Technology Achievements. *Applied Sciences*, *11*(10), 4472. https://doi.org/10.3390/app11104472

Bryan, A. K., Hecht, V. C., Shen, W., Payer, K., Grover, W. H., & Manalis, S. R. (2014). Measuring single cell mass, volume, and density with dual suspended microchannel resonators. *Lab Chip*, *14*(3), 569–576. https://doi.org/10.1039/C3LC51022K

Bulgakova, N. M., & Bulgakov, A. V. (2001). Pulsed laser ablation of solids: Transition from normal vaporization to phase explosion: *Applied Physics A Materials Science & Processing*, *73*(2), 199–208. https://doi.org/10.1007/s003390000686

Bull, G., & Groves, J. (2009). The Democratization of Production. *Learning & Leading with Technology*, *37*(3), 36–37.

Burns, M. A., Johnson, B. N., Brahmasandra, S. N., Handique, K., Webster, J. R., Krishnan, M., Sammarco, T. S., Man, P. M., Jones, D., Heldsinger, D., Mastrangelo, C. H., & Burke, D. T. (1998). An Integrated Nanoliter DNA Analysis Device. *Science*, *282*(5388), 484–487. https://doi.org/10.1126/science.282.5388.484

Bzik, V. A., & Brayden, D. J. (2016). An Assessment of the Permeation Enhancer, 1-phenyl-piperazine (PPZ), on Paracellular Flux Across Rat Intestinal Mucosae in Ussing Chambers. *Pharmaceutical Research*, *33*(10), 2506–2516. https://doi.org/10.1007/s11095-016-1975-4

Cabral, J. T., Hudson, S. D., Harrison, C., & Douglas, J. F. (2004). Frontal Photopolymerization for Microfluidic Applications. *Langmuir*, *20*(23), 10020–10029. https://doi.org/10.1021/la049501e

Cailleaux, S., Sanchez-Ballester, N. M., Gueche, Y. A., Bataille, B., & Soulairol, I. (2021). Fused Deposition Modeling (FDM), the new asset for the production of tailored medicines. *Journal of Controlled Release*, *330*, 821–841. https://doi.org/10.1016/j.jconrel.2020.10.056

Carius, P., Dubois, A., Ajdarirad, M., Artzy-Schnirman, A., Sznitman, J., Schneider-Daum, N., & Lehr, C.-M. (2021). PerfuPul—A Versatile Perfusable Platform to Assess Permeability and Barrier Function of Air Exposed Pulmonary Epithelia. *Frontiers in Bioengineering and Biotechnology*, *9*, 743236. https://doi.org/10.3389/fbioe.2021.743236

Carnero, B., Bao-Varela, C., Gómez-Varela, A. I., Álvarez, E., & Flores-Arias, M. T. (2021). Microfluidic devices manufacturing with a stereolithographic printer for biological applications. *Materials Science and Engineering: C*, *129*, 112388. https://doi.org/10.1016/j.msec.2021.112388

Carnero, B., Bao-Varela, C., Gómez-Varela, A. I., & Flores-Arias, M. T. (2022). Internal Microchannel Manufacturing Using Stereolithographic 3D Printing. In *Trends and Opportunities of Rapid Prototyping Technologies*. IntechOpen. https://doi.org/10.5772/intechopen.102751

Carnero, B., De Las Heras, A., Doval, A., Martín-Rodríguez, Á., Muñoz-Ramos, A., García-Cabrera, A., Rodríguez-Fernández, C. D., Insua-Costa, D., Romo-Díez, I., Rodríguez-Pérez, I., Prada-Rodrigo, J., Varela-Carballo, J., Sánchez-Hernández, M., Martínez-Morillo, M. J.,

Guerras-Rodríguez, M., Pérez, M., Fernández-Rodicio, S., Villa-Ortega, V., Segundo-Staels, V. W., & Flores-Arias, M. T. (2022). Celebrating a face-to-face congress of young researchers in Optics after the pandemic years: The I NW MYRO. *EPJ Web of Conferences*, *266*, 13004. https://doi.org/10.1051/epjconf/202226613004

Carnero, B., Radziunas-Salinas, Y., Rodiño-Janeiro, B. K., Ballesta, S. V., & Flores-Arias, M. T. (2024). Versatile hybrid technique for passive straight micromixer manufacturing by combining pulsed laser ablation, stereolithographic 3D printing and computational fluid dynamics. *Lab on a Chip*, *24*(10), 2669–2682. https://doi.org/10.1039/D4LC00009A

Carrell, C. S., McCord, C. P., Wydallis, R. M., & Henry, C. S. (2020a). Sealing 3D-printed parts to poly(dimethylsiloxane) for simple fabrication of Microfluidic devices. *Analytica Chimica Acta*, *1124*, 78–84. https://doi.org/10.1016/j.aca.2020.05.014

Carrell, C. S., McCord, C. P., Wydallis, R. M., & Henry, C. S. (2020b). Sealing 3D-printed parts to poly(dimethylsiloxane) for simple fabrication of Microfluidic devices. *Analytica Chimica Acta*, *1124*, 78–84. https://doi.org/10.1016/j.aca.2020.05.014

Casas-Arozamena, C., Otero-Cacho, A., Carnero, B., Almenglo, C., Aymerich, M., Alonso-Alconada, L., Ferreiros, A., Abalo, A., Bao-Varela, C., Flores-Arias, M. T., Alvarez, E., Munuzuri, A. P., & Abal, M. (2021). Haemodynamic-dependent arrest of circulating tumour cells at large blood vessel bifurcations as new model for metastasis. *Scientific Reports*, *11*(1), 23231. https://doi.org/10.1038/s41598-021-02482-x

Chan, H. N., Chen, Y., Shu, Y., Chen, Y., Tian, Q., & Wu, H. (2015a). Direct, one-step molding of 3D-printed structures for convenient fabrication of truly 3D PDMS microfluidic chips. *Microfluidics and Nanofluidics*, *19*(1), 9–18. https://doi.org/10.1007/s10404-014-1542-4

Chan, H. N., Chen, Y., Shu, Y., Chen, Y., Tian, Q., & Wu, H. (2015b). Direct, one-step molding of 3D-printed structures for convenient fabrication of truly 3D PDMS microfluidic chips. *Microfluidics and Nanofluidics*, *19*(1), 9–18. https://doi.org/10.1007/s10404-014-1542-4

Charee, W., & Tangwarodomnukun, V. (2018). Dynamic features of bubble induced by a nanosecond pulse laser in still and flowing water. *Optics & Laser Technology*, *100*, 230–243. https://doi.org/10.1016/j.optlastec.2017.10.019

Charee, W., Tangwarodomnukun, V., & Dumkum, C. (2015). Laser ablation of silicon in water under different flow rates. *The International Journal of Advanced Manufacturing Technology*, *78*(1–4), 19–29. https://doi.org/10.1007/s00170-014-6625-6

Chen, J. K., Tzou, D. Y., & Beraun, J. E. (2006). A semiclassical two-temperature model for ultrafast laser heating. *International Journal of Heat and Mass Transfer*, *49*(1–2), 307–316. https://doi.org/10.1016/j.ijheatmasstransfer.2005.06.022

Chen, S., Sun, Y., Neoh, K. H., Chen, A., Li, W., Yang, X., & Han, R. P. S. (2017). Microfluidic assay of circulating endothelial cells in coronary artery disease patients with angina pectoris. *PLOS ONE*, *12*(7), e0181249. https://doi.org/10.1371/journal.pone.0181249

Chen, Y. Y., Kingston, B. R., & Chan, W. C. W. (2020). Transcribing In Vivo Blood Vessel Networks into In Vitro Perfusable Microfluidic Devices. *Advanced Materials Technologies*, *5*(6), 2000103. https://doi.org/10.1002/admt.202000103

Chichkov, B. N., Momma, C., Nolte, S., Alvensleben, F., & Tünnermann, A. (1996). Femtosecond, picosecond and nanosecond laser ablation of solids. *Applied Physics A Materials Science & Processing*, *63*(2), 109–115. https://doi.org/10.1007/BF01567637

Cognart, H. A., Viovy, J.-L., & Villard, C. (2020). Fluid shear stress coupled with narrow constrictions induce cell type-dependent morphological and molecular changes in SK-BR-3 and MDA-MB-231 cells. *Scientific Reports*, *10*(1), 6386. https://doi.org/10.1038/s41598-020-63316-w

Comina, G., Suska, A., & Filippini, D. (2014). Low cost lab-on-a-chip prototyping with a consumer grade 3D printer. *Lab Chip*, *14*(16), 2978–2982. https://doi.org/10.1039/C4LC00394B

Conde, A. J., Keraite, I., Ongaro, A. E., & Kersaudy-Kerhoas, M. (2020). Versatile hybrid acoustic micromixer with demonstration of circulating cell-free DNA extraction from sub-ml plasma samples. *Lab on a Chip*, *20*(4), 741–748. https://doi.org/10.1039/C9LC01130G

Corbel, S., Charles, G., Becheikh, N., Roques-Carmes, T., & Zahraa, O. (2012). Modelling and design of microchannel reactor for photocatalysis. *Virtual and Physical Prototyping*, *7*(3), 203–209. https://doi.org/10.1080/17452759.2012.708837

Culshaw, B., & Kersey, A. (2008). Fiber-Optic Sensing: A Historical Perspective. *Journal of Lightwave Technology*, *26*(9), 1064–1078. https://doi.org/10.1109/JLT.0082.921915

Dasgupta, A., Lim, A. R., & Ghajar, C. M. (2017). Circulating and disseminated tumor cells: Harbingers or initiators of metastasis? *Molecular Oncology*, *11*(1), 40–61. https://doi.org/10.1002/1878-0261.12022

Delgado, T., Nieto, D., & Flores-Arias, M. T. (2016). Soda-lime glass microlens arrays fabricated by laser: Comparison between a nanosecond and a femtosecond IR pulsed laser. *Optics and Lasers in Engineering*, *86*, 29–37. https://doi.org/10.1016/j.optlaseng.2016.05.001

Deng, X., Feng, Z., Zhu, L., Chen, N., Deng, Y., Li, Y., Li, R., Wang, L., Luo, M., & Wu, J. (2020). Platelet-Derived Factor V Is an Important Determinant of the Metastatic Potential of Circulating Tumor Cells. *Frontiers in Oncology*, *10*, 558306. https://doi.org/10.3389/fonc.2020.558306

Donaldson, K. E., Braga-Mele, R., Cabot, F., Davidson, R., Dhaliwal, D. K., Hamilton, R., Jackson, M., Patterson, L., Stonecipher, K., & Yoo, S. H. (2013). Femtosecond laser–assisted cataract surgery. *Journal of Cataract and Refractive Surgery*, *39*(11), 1753–1763. https://doi.org/10.1016/j.jcrs.2013.09.002

Dudutis, J., Zubauskas, L., Daknys, E., Markauskas, E., Gvozdaitė, R., Račiukaitis, G., & Gečys, P. (2022). Quality and flexural strength of laser-cut glass: Classical top-down ablation versus water-assisted and bottom-up machining. *Optics Express*, *30*(3), 4564. https://doi.org/10.1364/OE.447143

Einstein, A. (1917). Quantum Theory of Radiation. *Physikalische Zeitschrift*, *18*, 121–128.

Eisenberg, N. P., Karsenty, A., Broder, J., Abitbol, M., & Yossef, N. B. (1989). A New Process For Manufacturing Arrays Of Microlenses. *6th Mtg in Israel on Optical Engineering*, *1038*, 388–399. https://doi.org/10.1117/12.951075

Ejaz, U., Akhtar, F., Xue, J., Wan, X., Zhang, T., & He, S. (2021). Review: Inhibitory potential of low molecular weight Heparin in cell adhesion; emphasis on tumor metastasis. *European Journal of Pharmacology*, *892*, 173778. https://doi.org/10.1016/j.ejphar.2020.173778

Estevez, M. C., Alvarez, M., & Lechuga, L. M. (2012). Integrated optical devices for lab-on-a-chip biosensing applications. *Laser & Photonics Reviews*, *6*(4), 463–487. https://doi.org/10.1002/lpor.201100025

Feynman, R. P. (1959). There's plenty of room at the bottom [data storage]. *Journal of Microelectromechanical Systems*, *1*(1), 60–66. https://doi.org/10.1109/84.128057

Florez, S. L., Campaña, A. L., Noguera, M. J., Quezada, V., Fuentes, O. P., Cruz, J. C., & Osma, J. F. (2022). CFD Analysis and Life Cycle Assessment of Continuous Synthesis of Magnetite Nanoparticles Using 2D and 3D Micromixers. *Micromachines*, *13*(6), 970. https://doi.org/10.3390/mi13060970

Follain, G., Herrmann, D., Harlepp, S., Hyenne, V., Osmani, N., Warren, S. C., Timpson, P., & Goetz, J. G. (2020). Fluids and their mechanics in tumour transit: Shaping metastasis. *Nature Reviews Cancer*, *20*(2), 107–124. https://doi.org/10.1038/s41568-019-0221-x

Follain, G., Osmani, N., Azevedo, A. S., Allio, G., Mercier, L., Karreman, M. A., Solecki, G., Garcia Leòn, M. J., Lefebvre, O., Fekonja, N., Hille, C., Chabannes, V., Dollé, G., Metivet, T., Hovsepian, F. D., Prudhomme, C., Pichot, A., Paul, N., Carapito, R., … Goetz, J. G. (2018). Hemodynamic Forces Tune the Arrest, Adhesion, and Extravasation of Circulating Tumor Cells. *Developmental Cell*, *45*(1), 33-52.e12. https://doi.org/10.1016/j.devcel.2018.02.015

Follain, G., Osmani, N., Gensbittel, V., Asokan, N., Larnicol, A., Mercier, L., Garcia-Leon, M. J., Busnelli, I., Pichot, A., Paul, N., Carapito, R., Bahram, S., Lefebvre, O., & Goetz, J. G. (2021). Impairing flow-mediated endothelial remodeling reduces extravasation of tumor cells. *Scientific Reports*, *11*(1), 13144. https://doi.org/10.1038/s41598-021-92515-2

Font-Clos, F., Zapperi, S., & La Porta, C. A. M. (2020). Blood Flow Contributions to Cancer Metastasis. *iScience*, *23*(5), 101073. https://doi.org/10.1016/j.isci.2020.101073

Fournier, M.-C., Falk, L., & Villermaux, J. (1996). A new parallel competing reaction system for assessing micromixing efficiency—Experimental approach. *Chemical Engineering Science*, *51*(22), 5053–5064. https://doi.org/10.1016/0009-2509(96)00270-9

Fujii, T. (2002). PDMS-based microfluidic devices for biomedical applications. *Microelectronic Engineering*, *61–62*, 907–914. https://doi.org/10.1016/S0167-9317(02)00494-X

Fujita, T., Nishihara, H., & Koyama, J. (1981). Fabrication of micro lenses using electron-beam lithography. *Optics Letters*, *6*(12), 613. https://doi.org/10.1364/OL.6.000613

Ganguli, A., Mostafa, A., Berger, J., Aydin, M. Y., Sun, F., Ramirez, S. A. S. D., Valera, E., Cunningham, B. T., King, W. P., & Bashir, R. (2020). Rapid isothermal amplification and portable detection system for SARS-CoV-2. *Proceedings of the National Academy of Sciences*, *117*(37), 22727–22735. https://doi.org/10.1073/pnas.2014739117

Gečys, P. (2015). Nanosecond Laser Processing of Soda-Lime Glass. *Journal of Laser Micro/Nanoengineering*, *10*(3), 254–258. https://doi.org/10.2961/jlmn.2015.03.0003

Gharib, G., Bütün, İ., Muganlı, Z., Kozalak, G., Namlı, İ., Sarraf, S. S., Ahmadi, V. E., Toyran, E., Van Wijnen, A. J., & Koşar, A. (2022). Biomedical Applications of Microfluidic Devices: A Review. *Biosensors*, *12*(11), 1023. https://doi.org/10.3390/bios12111023

Gómez-Varela, A. I., Sanchez, R., Carnero, B., Diaz-Gomez, L., Flores-Arias, M. T., & Bao-Varela, C. (2022). Subaquatic indirect laser ablation technique for glass processing. *Optics Express*, *30*(21), 37536. https://doi.org/10.1364/OE.463803

Gong, H., Bickham, B. P., Woolley, A. T., & Nordin, G. P. (2017). Custom 3D printer and resin for 18 μm × 20 μm microfluidic flow channels. *Lab on a Chip*, *17*(17), 2899–2909. https://doi.org/10.1039/C7LC00644F

Gross, A. J., & Herrmann, T. R. W. (2007). History of lasers. *World Journal of Urology*, *25*(3), 217–220. https://doi.org/10.1007/s00345-007-0173-8

Guo, K., Chen, Y., Zhou, Z., Zhu, S., Ni, Z., & Xiang, N. (2022). A novel 3D Tesla valve micromixer for efficient mixing and chitosan nanoparticle production. *ELECTROPHORESIS*, *43*(21–22), 2184–2194. https://doi.org/10.1002/elps.202200077

Guo, P., Cai, B., Lei, M., Liu, Y., & Fu, B. M. (2014). Differential arrest and adhesion of tumor cells and microbeads in the microvasculature. *Biomechanics and Modeling in Mechanobiology*, *13*(3), 537–550. https://doi.org/10.1007/s10237-013-0515-y

Hamad, A. H. (2016). Effects of Different Laser Pulse Regimes (Nanosecond, Picosecond and Femtosecond) on the Ablation of Materials for Production of Nanoparticles in Liquid Solution. In R. Viskup (Ed.), *High Energy and Short Pulse Lasers*. InTech. https://doi.org/10.5772/63892

Hanada, Y., Sugioka, K., Miyamoto, I., & Midorikawa, K. (2005). Double-pulse irradiation by laser-induced plasma-assisted ablation (LIPAA) and mechanisms study. *Applied Surface Science*, *248*(1–4), 276–280. https://doi.org/10.1016/j.apsusc.2005.03.050

Hanada, Y., Sugioka, K., Miyamoto, I., & Midorikawa, K. (2007). Colour marking of transparent materials by laser-induced plasma-assisted ablation (LIPAA). *Journal of Physics: Conference Series*, *59*, 687–690. https://doi.org/10.1088/1742-6596/59/1/145

Hanada, Y., Sugioka, K., Obata, K., Garnov, S. V., Miyamoto, I., & Midorikawa, K. (2006). Transient electron excitation in laser-induced plasma-assisted ablation of transparent materials. *Journal of Applied Physics*, *99*(4), 043301. https://doi.org/10.1063/1.2171769

Hart, C., Didier, C. M., Sommerhage, F., & Rajaraman, S. (2020a). Biocompatibility of Blank, Post-Processed and Coated 3D Printed Resin Structures with Electrogenic Cells. *Biosensors*, *10*(11), 152. https://doi.org/10.3390/bios10110152

Hart, C., Didier, C. M., Sommerhage, F., & Rajaraman, S. (2020b). Biocompatibility of Blank, Post-Processed and Coated 3D Printed Resin Structures with Electrogenic Cells. *Biosensors*, *10*(11), 152. https://doi.org/10.3390/bios10110152

Heidt, B., Rogosic, R., Bonni, S., Passariello-Jansen, J., Dimech, D., Lowdon, J. W., Arreguin-Campos, R., Steen Redeker, E., Eersels, K., Diliën, H., Van Grinsven, B., & Cleij, T. J. (2020). The Liberalization of Microfluidics: Form 2 Benchtop 3D Printing as an Affordable Alternative to Established Manufacturing Methods. *Physica Status Solidi (a)*, *217*(13), 1900935. https://doi.org/10.1002/pssa.201900935

Heidt, B., Rogosic, R., Bonni, S., Passariello-Jansen, J., Dimech, D., Lowdon, J. W., Arreguin-Campos, R., Steen Redeker, E., Eersels, K., Diliën, H., van Grinsven, B., & Cleij, T. J. (2020). The Liberalization of Microfluidics: Form 2 Benchtop 3D Printing as an Affordable Alternative to Established Manufacturing Methods. *Physica Status Solidi (a)*, 1900935. https://doi.org/10.1002/pssa.201900935

Hof, L., & Abou Ziki, J. (2017). Micro-Hole Drilling on Glass Substrates—A Review. *Micromachines*, *8*(2), 53. https://doi.org/10.3390/mi8020053

Holzner, G., Du, Y., Cao, X., Choo, J., Demello, A. J., & Stavrakis, S. (2018). An optofluidic system with integrated microlens arrays for parallel imaging flow cytometry. *Lab on a Chip*, *18*(23), 3631–3637. https://doi.org/10.1039/c8lc00593a

Hong, K.-M., & Shin, Y. C. (2017). Prospects of laser welding technology in the automotive industry: A review. *Journal of Materials Processing Technology*, *245*, 46–69. https://doi.org/10.1016/j.jmatprotec.2017.02.008

Hopp, B., Vass, C., Smausz, T., & Bor, Z. (2006). Production of submicrometre fused silica gratings using laser-induced backside dry etching technique. *Journal of Physics D: Applied Physics*, *39*(22), 4843–4847. https://doi.org/10.1088/0022-3727/39/22/015

Hwang, Y., Paydar, O. H., & Candler, R. N. (2015a). 3D printed molds for non-planar PDMS microfluidic channels. *Sensors and Actuators A: Physical*, *226*, 137–142. https://doi.org/10.1016/j.sna.2015.02.028

Hwang, Y., Paydar, O. H., & Candler, R. N. (2015b). 3D printed molds for non-planar PDMS microfluidic channels. *Sensors and Actuators A: Physical*, *226*, 137–142. https://doi.org/10.1016/j.sna.2015.02.028

Ianovska, M. A., Mulder, P., & Verpoorte, E. (2018). *Novel micromixers based on chaotic advection and their application—A review*. https://www.semanticscholar.org/paper/Novel-micromixers-based-on-chaotic-advection-and-%E2%80%94a-Ianovska-Mulder/31a5a5833b26b653259f87eecac3630684f1ce54

Itina, T. E. (2005). Nonlinear fluence dependencies in femtosecond laser ablation of metals and dielectric materials. *Optical Engineering*, *44*(5), 051109. https://doi.org/10.1117/1.1904591

Jacobs, Paul Francis. (1992). Fundamentals of Stereolithography. In *Rapid prototyping & manufacturing: Fundamentals of stereolithography* (pp. 196–211).

Jiang, B., Shi, X., Zhang, T., & Huang, Y. (2022). Recent advances in UV/thermal curing silicone polymers. *Chemical Engineering Journal*, *435*, 134843. https://doi.org/10.1016/j.cej.2022.134843

Jo, B.-H., Van Lerberghe, L. M., Motsegood, K. M., & Beebe, D. J. (2000). Three-dimensional micro-channel fabrication in polydimethylsiloxane (PDMS) elastomer. *Journal of Microelectromechanical Systems*, *9*(1), 76–81. https://doi.org/10.1109/84.825780

Jones, N. (2012). Science in three dimensions: The print revolution. *Nature*, *487*(7405), 22–23. https://doi.org/10.1038/487022a

Kaigala, G. V., Ho, S., Penterman, R., & Backhouse, C. J. (2007). Rapid prototyping of microfluidic devices with a wax printer. *Lab on a Chip*, *7*(3), 384. https://doi.org/10.1039/b617764f

Kee, S. P., & Gavriilidis, A. (2008). Design and characterisation of the staggered herringbone mixer. *Chemical Engineering Journal*, *142*(1), 109–121. https://doi.org/10.1016/j.cej.2008.02.001

Kienast, Y., Von Baumgarten, L., Fuhrmann, M., Klinkert, W. E. F., Goldbrunner, R., Herms, J., & Winkler, F. (2010). Real-time imaging reveals the single steps of brain metastasis formation. *Nature Medicine*, *16*(1), 116–122. https://doi.org/10.1038/nm.2072

Kim, K. H., Kim, K. S., Ji, Y. J., Kang, J. E., & Yeom, G. Y. (2021). Silicon nitride deposited by laser assisted plasma enhanced chemical vapor deposition for next generation organic electronic devices. *Applied Surface Science*, *541*, 148313. https://doi.org/10.1016/j.apsusc.2020.148313

Klein, C. A. (2020). Cancer progression and the invisible phase of metastatic colonization. *Nature Reviews Cancer*, *20*(11), 681–694. https://doi.org/10.1038/s41568-020-00300-6

Knowlton, S., Yu, C. H., Ersoy, F., Emadi, S., Khademhosseini, A., & Tasoglu, S. (2016). 3D-printed microfluidic chips with patterned, cell-laden hydrogel constructs. *Biofabrication*, *8*(2), 025019. https://doi.org/10.1088/1758-5090/8/2/025019

Ko, C.-H., Lin, C.-H., Tsai, B.-C., Shih, H.-H., Wu, C.-T., Chao, Y.-L., Chou, Y.-K., Chu, C.-H., Chiou, Y.-T., & Chen, R. (2004). Development of microlens arrays for high-speed optical communication. *Micro-Optics: Fabrication, Packaging, and Integration*, *5454*, 121–128. https://doi.org/10.1117/12.545371

Koechner, W. (1976). *Solid-State Laser Engineering* (Vol. 1). Springer New York. https://doi.org/10.1007/978-1-4757-8519-7

Kogelnik, H., & Li, T. (1966). Laser beams and resonators. *Proceedings of the IEEE*, *54*(10), 1312–1329. https://doi.org/10.1109/PROC.1966.5119

Koo, D., & So, H. (2022). Facile microfabrication of three dimensional-patterned micromixers using additive manufacturing technology. *Scientific Reports*, *12*(1), 6346. https://doi.org/10.1038/s41598-022-10356-z

Kreß, S., Schaller-Ammann, R., Feiel, J., Priedl, J., Kasper, C., & Egger, D. (2020a). 3D Printing of Cell Culture Devices: Assessment and Prevention of the Cytotoxicity of Photopolymers for Stereolithography. *Materials*, *13*(13), 3011. https://doi.org/10.3390/ma13133011

Kreß, S., Schaller-Ammann, R., Feiel, J., Priedl, J., Kasper, C., & Egger, D. (2020b). 3D Printing of Cell Culture Devices: Assessment and Prevention of the Cytotoxicity of Photopolymers for Stereolithography. *Materials*, *13*(13), 3011. https://doi.org/10.3390/ma13133011

Krstulović, N., Shannon, S., Stefanuik, R., & Fanara, C. (2013). Underwater-laser drilling of aluminum. *The International Journal of Advanced Manufacturing Technology*, *69*(5–8), 1765–1773. https://doi.org/10.1007/s00170-013-5141-4

Kruusing, A. (2004). Underwater and water-assisted laser processing: Part 1—general features, steam cleaning and shock processing. *Optics and Lasers in Engineering*, *41*(2), 307–327. https://doi.org/10.1016/S0143-8166(02)00142-2

Kuo, A. P., Bhattacharjee, N., Lee, Y., Castro, K., Kim, Y. T., & Folch, A. (2019). High-Precision Stereolithography of Biomicrofluidic Devices. *Advanced Materials Technologies*, *4*(6), 1800395. https://doi.org/10.1002/admt.201800395

Lambert, A. W., Pattabiraman, D. R., & Weinberg, R. A. (2017). Emerging Biological Principles of Metastasis. *Cell*, *168*(4), 670–691. https://doi.org/10.1016/j.cell.2016.11.037

Läubli, H., & Borsig, L. (2009). Heparins Attenuate Cancer Metastasis: Are Selectins the Link? *Cancer Investigation*, *27*(5), 474–481. https://doi.org/10.1080/07357900802647136

Lee, C.-H., Jung, K.-H., Cho, D. J., & Jeong, S.-K. (2019). Effect of warfarin versus aspirin on blood viscosity in cardioembolic stroke with atrial fibrillation: A prospective clinical trial. *BMC Neurology*, *19*(1), 82. https://doi.org/10.1186/s12883-019-1315-5

Lee, J. H., Prud'homme, R. K., & Aksay, I. A. (2001). Cure depth in photopolymerization: Experiments and theory. *Journal of Materials Research*, *16*(12), 3536–3544. https://doi.org/10.1557/JMR.2001.0485

Lee, S. H., Heinz, A. J., Shin, S., Jung, Y.-G., Choi, S.-E., Park, W., Roe, J.-H., & Kwon, S. (2010). Capillary Based Patterning of Cellular Communities in Laterally Open Channels. *Analytical Chemistry*, *82*(7), 2900–2906. https://doi.org/10.1021/ac902903q

Lenzner, M. (1999). Femtosecond laser-induced damage of dielectrics. *International Journal of Modern Physics B*, *13*(13), 1559–1578. https://doi.org/10.1142/S0217979299001570

Lenzner, M., Krüger, J., Sartania, S., Cheng, Z., Spielmann, Ch., Mourou, G., Kautek, W., & Krausz, F. (1998). Femtosecond Optical Breakdown in Dielectrics. *Physical Review Letters*, *80*(18), 4076–4079. https://doi.org/10.1103/PhysRevLett.80.4076

Li, Q., Zhou, X., Wang, Q., Liu, W., & Chen, C. (2023). Microfluidics for COVID-19: From Current Work to Future Perspective. *Biosensors*, *13*(2), 163. https://doi.org/10.3390/bios13020163

Liu, C., Liao, Y., He, F., Shen, Y., Chen, D., Cheng, Y., Xu, Z., Sugioka, K., & Midorikawa, K. (2012). Fabrication of three-dimensional microfluidic channels inside glass using nanosecond laser direct writing. *Optics Express*, *20*(4), 4291. https://doi.org/10.1364/OE.20.004291

Liu, R. H., Stremler, M. A., Sharp, K. V., Olsen, M. G., Santiago, J. G., Adrian, R. J., Aref, H., & Beebe, D. J. (2000a). Passive mixing in a three-dimensional serpentine microchannel. *Journal of Microelectromechanical Systems*, *9*(2), 190–197. https://doi.org/10.1109/84.846699

Liu, R. H., Stremler, M. A., Sharp, K. V., Olsen, M. G., Santiago, J. G., Adrian, R. J., Aref, H., & Beebe, D. J. (2000b). Passive mixing in a three-dimensional serpentine microchannel. *Journal of Microelectromechanical Systems*, *9*(2), 190–197. https://doi.org/10.1109/84.846699

Lu, J., Xu, R. Q., Chen, X., Shen, Z. H., Ni, X. W., Zhang, S. Y., & Gao, C. M. (2004). Mechanisms of laser drilling of metal plates underwater. *Journal of Applied Physics*, *95*(8), 3890–3894. https://doi.org/10.1063/1.1667273

Lucotti, S., Cerutti, C., Soyer, M., Gil-Bernabé, A. M., Gomes, A. L., Allen, P. D., Smart, S., Markelc, B., Watson, K., Armstrong, P. C., Mitchell, J. A., Warner, T. D., Ridley, A. J., & Muschel, R. J. (2019). Aspirin blocks formation of metastatic intravascular niches by inhibiting platelet-derived COX-1/thromboxane A2. *Journal of Clinical Investigation*, *129*(5), 1845–1862. https://doi.org/10.1172/JCI121985

Maiman, T. H. (1960). Stimulated Optical Radiation in Ruby. *Nature*, *187*(4736), 493–494. https://doi.org/10.1038/187493a0

Maionchi, D. D. O., Ainstein, L., Dos Santos, F. P., & De Souza Júnior, M. B. (2022). Computational fluid dynamics and machine learning as tools for optimization of micromixers geometry. *International Journal of Heat and Mass Transfer*, *194*, 123110. https://doi.org/10.1016/j.ijheatmasstransfer.2022.123110

Mak, G. Y., Lam, E. Y., & Choi, H. W. (2011). Liquid-immersion laser micromachining of GaN grown on sapphire. *Applied Physics A*, *102*(2), 441–447. https://doi.org/10.1007/s00339-010-6169-z

Manenkov, A. A. (2014). Fundamental mechanisms of laser-induced damage in optical materials: Today's state of understanding and problems. *Optical Engineering*, *53*(1), 010901. https://doi.org/10.1117/1.OE.53.1.010901

Manz, A., Harrison, D. J., Verpoorte, E. M. J., Fettinger, James. C., Paulus, A., Lüdi, H., & Widmer, H. M. (1992). Planar chips technology for miniaturization and integration of

separation techniques into monitoring systems. *Journal of Chromatography A*, *593*(1–2), 253–258. https://doi.org/10.1016/0021-9673(92)80293-4

Markauskas, E., & Gečys, P. (2018). Thin water film assisted glass ablation with a picosecond laser. *Procedia CIRP*, *74*, 328–332. https://doi.org/10.1016/j.procir.2018.08.126

McDonald, J. C., Duffy, D. C., Anderson, J. R., Chiu, D. T., Wu, H., Schueller, O. J. A., & Whitesides, G. M. (2000a). Fabrication of microfluidic systems in poly(dimethylsiloxane). *Electrophoresis*, *21*(1), 27–40. https://doi.org/10.1002/(SICI)1522-2683(20000101)21:1<27::AID-ELPS27>3.0.CO;2-C

McDonald, J. C., Duffy, D. C., Anderson, J. R., Chiu, D. T., Wu, H., Schueller, O. J. A., & Whitesides, G. M. (2000b). Fabrication of microfluidic systems in poly(dimethylsiloxane). *Electrophoresis*, *21*(1), 27–40. https://doi.org/10.1002/(sici)1522-2683(20000101)21:1<27::aid-elps27>3.3.co;2-3

McDonald, J. C., & Whitesides, G. M. (2002). Poly(dimethylsiloxane) as a Material for Fabricating Microfluidic Devices. *Accounts of Chemical Research*, *35*(7), 491–499. https://doi.org/10.1021/ar010110q

Medina-Leyte, D. J., Domínguez-Pérez, M., Mercado, I., Villarreal-Molina, M. T., & Jacobo-Albavera, L. (2020). Use of Human Umbilical Vein Endothelial Cells (HUVEC) as a Model to Study Cardiovascular Disease: A Review. *Applied Sciences*, *10*(3), 938. https://doi.org/10.3390/app10030938

Miller, J. C. (Ed.). (1994). *Laser Ablation: Principles and Applications* (Vol. 28). Springer Berlin Heidelberg. https://doi.org/10.1007/978-3-642-78720-1

Moon, B.-U., De Vries, M. G., Cordeiro, C. A., Westerink, B. H. C., & Verpoorte, E. (2013). Microdialysis-Coupled Enzymatic Microreactor for in Vivo Glucose Monitoring in Rats. *Analytical Chemistry*, *85*(22), 10949–10955. https://doi.org/10.1021/ac402414m

Moon, B.-U., Koster, S., Wientjes, K. J. C., Kwapiszewski, R. M., Schoonen, A. J. M., Westerink, B. H. C., & Verpoorte, E. (2010). An Enzymatic Microreactor Based on Chaotic Micromixing for Enhanced Amperometric Detection in a Continuous Glucose Monitoring Application. *Analytical Chemistry*, *82*(16), 6756–6763. https://doi.org/10.1021/ac1000509

Moreno-Rivas, O., Hernández-Velázquez, D., Piazza, V., & Marquez, S. (2019a). Rapid prototyping of microfluidic devices by SL 3D printing and their biocompatibility study for cell culturing. *Materials Today: Proceedings*, *13*, 436–445. https://doi.org/10.1016/j.matpr.2019.03.189

Moreno-Rivas, O., Hernández-Velázquez, D., Piazza, V., & Marquez, S. (2019b). Rapid prototyping of microfluidic devices by SL 3D printing and their biocompatibility study for cell culturing. *Materials Today: Proceedings*, *13*, 436–445. https://doi.org/10.1016/j.matpr.2019.03.189

Murphy, S. V., & Atala, A. (2014). 3D bioprinting of tissues and organs. *Nature Biotechnology*, *32*(8), 773–785. https://doi.org/10.1038/nbt.2958

Nabesawa, H., Hitobo, T., Wakabayashi, S., Aasji, T., Abe, T., & Seki, M. (2008). Polymer surface morphology control by reactive ion etching for microfluidic devices. *Sensors and Actuators B: Chemical*, *132*(2), 637–643. https://doi.org/10.1016/j.snb.2008.01.050

National Research Council (U.S.), National Research Council (U.S.), & National Research Council (U.S.) (Eds.). (2013). *Optics and photonics: Essential technologies for our nation*. National Academies Press.

Nicolas, A., Schavemaker, F., Kosim, K., Kurek, D., Haarmans, M., Bulst, M., Lee, K., Wegner, S., Hankemeier, T., Joore, J., Domansky, K., Lanz, H. L., Vulto, P., & Trietsch, S. J. (2021). High throughput transepithelial electrical resistance (TEER) measurements on perfused membrane-free epithelia. *Lab on a Chip*, *21*(9), 1676–1685. https://doi.org/10.1039/D0LC00770F

Nieto, D., Arines, J., & Flores-Arias, M. T. (2014). Fluence ablation threshold dependence on tin impurities in commercial soda-lime glass. *Applied Optics*, *53*(24), 5416. https://doi.org/10.1364/AO.53.005416

Nieto, D., Couceiro, R., Aymerich, M., Lopez-Lopez, R., Abal, M., & Flores-Arias, M. T. (2015a). A laser-based technology for fabricating a soda-lime glass based microfluidic device for circulating tumour cell capture. *Colloids and Surfaces B: Biointerfaces*, *134*, 363–369. https://doi.org/10.1016/j.colsurfb.2015.07.007

Nieto, D., Couceiro, R., Aymerich, M., Lopez-Lopez, R., Abal, M., & Flores-Arias, M. T. (2015b). A laser-based technology for fabricating a soda-lime glass based microfluidic device for circulating tumour cell capture. *Colloids and Surfaces B: Biointerfaces*, *134*, 363–369. https://doi.org/10.1016/j.colsurfb.2015.07.007

Nieto, D., Delgado, T., & Flores-Arias, M. T. (2014a). Fabrication of microchannels on soda-lime glass substrates with a Nd:YVO4 laser. *Optics and Lasers in Engineering*, *63*, 11–18. https://doi.org/10.1016/j.optlaseng.2014.06.005

Nieto, D., Delgado, T., & Flores-Arias, M. T. (2014b). Fabrication of microchannels on soda-lime glass substrates with a Nd:YVO4 laser. *Optics and Lasers in Engineering*, *63*, 11–18. https://doi.org/10.1016/j.optlaseng.2014.06.005

Nieto, D., Delgado, T., & Flores-Arias, M. T. (2014c). Fabrication of microchannels on soda-lime glass substrates with a Nd:YVO4 laser. *Optics and Lasers in Engineering*, *63*, 11–18. https://doi.org/10.1016/j.optlaseng.2014.06.005

Niino, H., Kawaguchi, Y., Sato, T., Narazaki, A., & Kurosaki, R. (2008). *Surface microstructures of silica glass by laser-induced backside wet etching* (A. S. Holmes, M. Meunier, C. B. Arnold, H. Niino, D. B. Geohegan, F. Träger, & J. J. Dubowski, Eds.; p. 68790C). https://doi.org/10.1117/12.762240

Nikumb, S., Chen, Q., Li, C., Reshef, H., Zheng, H. Y., Qiu, H., & Low, D. (2005). Precision glass machining, drilling and profile cutting by short pulse lasers. *Thin Solid Films*, *477*(1–2), 216–221. https://doi.org/10.1016/j.tsf.2004.08.136

Nobel Prize organisation. (n.d.). *All Nobel Prizes*. https://www.nobelprize.org/prizes/lists/all-nobel-prizes/

Nolte, S., Momma, C., Jacobs, H., Tünnermann, A., Chichkov, B. N., Wellegehausen, B., & Welling, H. (1997). Ablation of metals by ultrashort laser pulses. *Journal of the Optical Society of America B*, *14*(10), 2716. https://doi.org/10.1364/JOSAB.14.002716

O'Briant, S. A., Gupta, S. B., & Vasu, S. S. (2016). Review: Laser ignition for aerospace propulsion. *Propulsion and Power Research*, *5*(1), 1–21. https://doi.org/10.1016/j.jppr.2016.01.004

Otero-Cacho, A., Aymerich, M., Flores-Arias, M. T., Abal, M., Álvarez, E., Pérez-Muñuzuri, V., & Muñuzuri, A. P. (2018). Determination of hemodynamic risk for vascular disease in planar artery bifurcations. *Scientific Reports*, *8*(1), 2795. https://doi.org/10.1038/s41598-018-21126-1

Palmara, G., Frascella, F., Roppolo, I., Chiappone, A., & Chiadò, A. (2021). Functional 3D printing: Approaches and bioapplications. *Biosensors and Bioelectronics*, *175*, 112849. https://doi.org/10.1016/j.bios.2020.112849

Pan, C., Chen, K., Liu, B., Ren, L., Wang, J., Hu, Q., Liang, L., Zhou, J., & Jiang, L. (2017). Fabrication of micro-texture channel on glass by laser-induced plasma-assisted ablation and chemical corrosion for microfluidic devices. *Journal of Materials Processing Technology*, *240*, 314–323. https://doi.org/10.1016/j.jmatprotec.2016.10.011

Pantelis, P., & McCartney, D. J. (1994). Polymer microlens arrays. *Pure and Applied Optics: Journal of the European Optical Society Part A*, *3*(2), 103. https://doi.org/10.1088/0963-9659/3/2/002

Paradela-Dobarro, B., Rodiño-Janeiro, B. K., Alonso, J., Raposeiras-Roubín, S., González-Peteiro, M., González-Juanatey, J. R., & Álvarez, E. (2016). Key structural and functional differences between early and advanced glycation products. *Journal of Molecular Endocrinology*, *56*(1), 23–37. https://doi.org/10.1530/JME-15-0031

Paruli, E., Soppera, O., Haupt, K., & Gonzato, C. (2021). Photopolymerization and Photostructuring of Molecularly Imprinted Polymers. *ACS Applied Polymer Materials*, *3*(10), 4769–4790. https://doi.org/10.1021/acsapm.1c00661

Peinado, H., Zhang, H., Matei, I. R., Costa-Silva, B., Hoshino, A., Rodrigues, G., Psaila, B., Kaplan, R. N., Bromberg, J. F., Kang, Y., Bissell, M. J., Cox, T. R., Giaccia, A. J., Erler, J. T., Hiratsuka, S., Ghajar, C. M., & Lyden, D. (2017). Pre-metastatic niches: Organ-specific homes for metastases. *Nature Reviews Cancer*, *17*(5), 302–317. https://doi.org/10.1038/nrc.2017.6

Pepona, M., Balogh, P., Puleri, D. F., Hynes, W. F., Robertson, C., Dubbin, K., Alvarado, J., Moya, M. L., & Randles, A. (2020). Investigating the Interaction Between Circulating Tumor Cells and Local Hydrodynamics via Experiment and Simulations. *Cellular and Molecular Bioengineering*, *13*(5), 527–540. https://doi.org/10.1007/s12195-020-00656-7

Pravinraj, T., & Patrikar, R. (2018). Modeling and characterization of surface roughness effect on fluid flow in a polydimethylsiloxane microchannel using a fractal based lattice Boltzmann method. *AIP Advances*, *8*(6), 065112. https://doi.org/10.1063/1.5036797

Radier, C., Chalus, O., Charbonneau, M., Thambirajah, S., Deschamps, G., David, S., Barbe, J., Etter, E., Matras, G., Ricaud, S., Leroux, V., Richard, C., Lureau, F., Baleanu, A., Banici, R., Gradinariu, A., Caldararu, C., Capiteanu, C., Naziru, A., … Zamfir, N. V. (2022). 10 PW peak power femtosecond laser pulses at ELI-NP. *High Power Laser Science and Engineering*, *10*, e21. https://doi.org/10.1017/hpl.2022.11

Raj M, K., & Chakraborty, S. (2020a). PDMS microfluidics: A mini review. *Journal of Applied Polymer Science*, *137*(27), 48958. https://doi.org/10.1002/app.48958

Raj M, K., & Chakraborty, S. (2020b). PDMS microfluidics: A mini review. *Journal of Applied Polymer Science*, *137*(27), 1–14. https://doi.org/10.1002/app.48958

Ramsey, J. M. (1999). The burgeoning power of the shrinking laboratory. *Nature Biotechnology*, *17*(11), 1061–1062. https://doi.org/10.1038/15044

Reinstein, D. Z., Archer, T. J., & Gobbe, M. (2012). The History of LASIK. *Journal of Refractive Surgery*, *28*(4), 291–298. https://doi.org/10.3928/1081597X-20120229-01

Rejniak, K. A. (2016). Circulating Tumor Cells: When a Solid Tumor Meets a Fluid Microenvironment. In K. A. Rejniak (Ed.), *Systems Biology of Tumor Microenvironment* (Vol. 936, pp. 93–106). Springer International Publishing. https://doi.org/10.1007/978-3-319-42023-3_5

Roberts, M. A., Rossier, J. S., Bercier, P., & Girault, H. (1997). UV Laser Machined Polymer Substrates for the Development of Microdiagnostic Systems. *Analytical Chemistry*, *69*(11), 2035–2042. https://doi.org/10.1021/ac961038q

Romanov, V., Samuel, R., Chaharlang, M., Jafek, A. R., Frost, A., & Gale, B. K. (2018). FDM 3D Printing of High-Pressure, Heat-Resistant, Transparent Microfluidic Devices. *Analytical Chemistry*, *90*(17), 10450–10456. https://doi.org/10.1021/acs.analchem.8b02356

Ropers, C., Solli, D. R., Schulz, C. P., Lienau, C., & Elsaesser, T. (2007). Localized Multiphoton Emission of Femtosecond Electron Pulses from Metal Nanotips. *Physical Review Letters*, *98*(4), 043907. https://doi.org/10.1103/PhysRevLett.98.043907

Ross, A. M., Jiang, Z., Bastmeyer, M., & Lahann, J. (2012). Physical Aspects of Cell Culture Substrates: Topography, Roughness, and Elasticity. *Small*, *8*(3), 336–355. https://doi.org/10.1002/smll.201100934

Rupal, B. S., Garcia, E. A., Ayranci, C., & Qureshi, A. J. (2019a). 3D Printed 3D-Microfluidics: Recent Developments and Design Challenges. *Journal of Integrated Design and Process Science*, *22*(1), 5–20. https://doi.org/10.3233/jid-2018-0001

Rupal, B. S., Garcia, E. A., Ayranci, C., & Qureshi, A. J. (2019b). 3D Printed 3D-Microfluidics: Recent Developments and Design Challenges. *Journal of Integrated Design and Process Science*, *22*(1), 5–20. https://doi.org/10.3233/jid-2018-0001

Sackmann, E. K., Fulton, A. L., & Beebe, D. J. (2014). The present and future role of microfluidics in biomedical research. *Nature*, *507*(7491), 181–189. https://doi.org/10.1038/nature13118

Sandeep, B., Kannan, T. T. M., Chandradass, J., Ganesan, M., & John Rajan, A. (2021). Scope of 3D printing in manufacturing industries-A review. *Materials Today: Proceedings*, *45*, 6941–6945. https://doi.org/10.1016/j.matpr.2021.01.394

Sato, K., Hibara, A., Tokeshi, M., Hisamoto, H., & Kitamori, T. (2003). Microchip-based chemical and biochemical analysis systems. *Advanced Drug Delivery Reviews*, *55*(3), 379–391. https://doi.org/10.1016/S0169-409X(02)00225-9

Schwartz, G. C., & Schaible, P. M. (1979). Reactive ion etching of silicon. *Journal of Vacuum Science and Technology*, *16*(2), 410–413. https://doi.org/10.1116/1.569962

Schwarz, S., Rung, S., Esen, C., & Hellmann, R. (2021). Ultrashort pulsed laser backside ablation of fused silica. *Optics Express*, *29*(15), 23477. https://doi.org/10.1364/OE.430516

Shallan, A. I., Smejkal, P., Corban, M., Guijt, R. M., & Breadmore, M. C. (2014a). Cost-Effective Three-Dimensional Printing of Visibly Transparent Microchips within Minutes. *Analytical Chemistry*, *86*(6), 3124–3130. https://doi.org/10.1021/ac4041857

Shallan, A. I., Smejkal, P., Corban, M., Guijt, R. M., & Breadmore, M. C. (2014b). Cost-Effective Three-Dimensional Printing of Visibly Transparent Microchips within Minutes. *Analytical Chemistry*, *86*(6), 3124–3130. https://doi.org/10.1021/ac4041857

Shi, X., Xiang, Y., Wen, L.-X., & Chen, J.-F. (2012). CFD Analysis of Flow Patterns and Micromixing Efficiency in a Y-Type Microchannel Reactor. *Industrial & Engineering Chemistry Research*, *51*(43), 13944–13952. https://doi.org/10.1021/ie300985q

Siegman, A. E. (1986). *Lasers*. University Science Books.

Sima, F., Sugioka, K., Vázquez, R. M., Osellame, R., Kelemen, L., & Ormos, P. (2018). Three-dimensional femtosecond laser processing for lab-on-a-chip applications. *Nanophotonics*, *7*(3), 613–634. https://doi.org/10.1515/nanoph-2017-0097

Sjöberg, Å., Lutz, M., Tannergren, C., Wingolf, C., Borde, A., & Ungell, A.-L. (2013). Comprehensive study on regional human intestinal permeability and prediction of fraction absorbed of drugs using the Ussing chamber technique. *European Journal of Pharmaceutical Sciences*, *48*(1–2), 166–180. https://doi.org/10.1016/j.ejps.2012.10.007

Song, X., Wu, X. Q., Xiao, K. L., Li, C., Wang, H. Y., & Jiang, M. Q. (2020). Nanosecond laser ablation of a metallic glass in water: A high time-resolved imaging study. *Philosophical Magazine*, *100*(21), 2708–2720. https://doi.org/10.1080/14786435.2020.1791369

Srinivasan, B., Kolli, A. R., Esch, M. B., Abaci, H. E., Shuler, M. L., & Hickman, J. J. (2015). TEER Measurement Techniques for In Vitro Barrier Model Systems. *SLAS Technology*, *20*(2), 107–126. https://doi.org/10.1177/2211068214561025

Stroock, A. D., Dertinger, S. K. W., Ajdari, A., Mezić, I., Stone, H. A., & Whitesides, G. M. (2002). Chaotic Mixer for Microchannels. *Science*, *295*(5555), 647–651. https://doi.org/10.1126/science.1066238

Sugioka, K., Midorikawa, K., Yamaoka, H., Gomi, Y., Otsuki, M., Hong, M. H., Wu, D. J., Wong, L. L., & Chong, T. C. (2004). *Glass microprocessing by laser-induced plasma-assisted ablation: Fundamental to industrial applications* (M. N. Libenson, Ed.; pp. 1–10). https://doi.org/10.1117/12.580222

Svelto, O. (2010). *Principles of Lasers*. Springer US. https://doi.org/10.1007/978-1-4419-1302-9

Takeshima, N., Narita, Y., Tanaka, S., Kuroiwa, Y., & Hirao, K. (2005). Fabrication of high-efficiency diffraction gratings in glass. *Optics Letters*, *30*(4), 352. https://doi.org/10.1364/OL.30.000352

Tan, D., Wang, Z., Xu, B., & Qiu, J. (2021). Photonic circuits written by femtosecond laser in glass: Improved fabrication and recent progress in photonic devices. *Advanced Photonics*, *3*(02). https://doi.org/10.1117/1.AP.3.2.024002

Thomson, A., Smart, K., Somerville, M. S., Lauder, S. N., Appanna, G., Horwood, J., Sunder Raj, L., Srivastava, B., Durai, D., Scurr, M. J., Keita, Å. V., Gallimore, A. M., & Godkin, A. (2019). The Ussing chamber system for measuring intestinal permeability in health and disease. *BMC Gastroenterology*, *19*(1), 98. https://doi.org/10.1186/s12876-019-1002-4

Träger, F. (Ed.). (2007). *Springer handbook of lasers and optics*. Springer.

Turpin, C., Apalama, M. L., Carnero, B., Otero-Cacho, A., Munuzuri, A. P., Flores-Arias, M. T., Vélia, E., Meilhac, O., Bourdon, E., Álvarez, E., & Rondeau, P. (2022). Impact of Enhanced Phagocytosis of Glycated Erythrocytes on Human Endothelial Cell Functions. *Cells*, *11*(14), 2200. https://doi.org/10.3390/cells11142200

Urrios, A., Parra-Cabrera, C., Bhattacharjee, N., Gonzalez-Suarez, A. M., Rigat-Brugarolas, L. G., Nallapatti, U., Samitier, J., Deforest, C. A., Posas, F., Garcia-Cordero, J. L., & Folch, A. (2016). 3D-printing of transparent bio-microfluidic devices in PEG-DA. *Lab on a Chip*, *16*(12), 2287–2294. https://doi.org/10.1039/c6lc00153j

Verpoorte, E., & De Rooij, N. F. (2003). Microfluidics meets MEMS. *Proceedings of the IEEE*, *91*(6), 930–953. https://doi.org/10.1109/JPROC.2003.813570

Walker, G. M., & Beebe, D. J. (2002). A passive pumping method for microfluidic devices. *Lab on a Chip*, *2*(3), 131. https://doi.org/10.1039/b204381e

Wang, J., Niino, H., & Yabe, A. (1999). One-step microfabrication of fused silica by laser ablation of an organic solution. *Applied Physics A: Materials Science & Processing*, *68*(1), 111–113. https://doi.org/10.1007/s003390050863

Wang, Y. I., Abaci, H. E., & Shuler, M. L. (2017). Microfluidic blood–brain barrier model provides in vivo-like barrier properties for drug permeability screening. *Biotechnology and Bioengineering*, *114*(1), 184–194. https://doi.org/10.1002/bit.26045

Wang, Y., Zhe, J., Chung, B. T. F., & Dutta, P. (2008). A rapid magnetic particle driven micromixer. *Microfluidics and Nanofluidics*, *4*(5), 375–389. https://doi.org/10.1007/s10404-007-0188-x

Whitesides, G. M. (2006). The origins and the future of microfluidics. *Nature*, *442*(7101), 368–373. https://doi.org/10.1038/nature05058

Whitesides, G. M., Ostuni, E., Takayama, S., Jiang, X., & Ingber, D. E. (2001). Soft Lithography in Biology and Biochemistry. *Annual Review of Biomedical Engineering*, *3*(1), 335–373. https://doi.org/10.1146/annurev.bioeng.3.1.335

Williams, M. S., Longmuir, K. J., & Yager, P. (2008). A practical guide to the staggered herringbone mixer. *Lab on a Chip*, *8*(7), 1121. https://doi.org/10.1039/b802562b

Wineland, D. J., & Itano, W. M. (1987). Laser Cooling. *Physics Today*, *40*(6), 34–40. https://doi.org/10.1063/1.881076

Wlodarczyk, K. L., Hand, D. P., & Maroto-Valer, M. M. (2019). Maskless, rapid manufacturing of glass microfluidic devices using a picosecond pulsed laser. *Scientific Reports*, *9*(1), 20215. https://doi.org/10.1038/s41598-019-56711-5

Xavier, M., Rodrigues, P. M., Neto, M. D., Guedes, M. I., Calero, V., Pastrana, L., & Gonçalves, C. (2023). From mouth to gut: Microfluidic *in vitro* simulation of human gastro-intestinal digestion and intestinal permeability. *The Analyst*, *148*(14), 3193–3203. https://doi.org/10.1039/D2AN02088B

Xia, Y., & Whitesides, G. M. (1998). Soft Lithography. *Angewandte Chemie International Edition*, *37*(5), 550–575. https://doi.org/10.1002/(SICI)1521-3773(19980316)37:5<550::AID-ANIE550>3.0.CO;2-G

Xiao, L. L., Liu, Y., Chen, S., & Fu, B. M. (2017). Effects of flowing RBCs on adhesion of a circulating tumor cell in microvessels. *Biomechanics and Modeling in Mechanobiology*, *16*(2), 597–610. https://doi.org/10.1007/s10237-016-0839-5

Xu, B.-B., Zhang, Y.-L., Xia, H., Dong, W.-F., Ding, H., & Sun, H.-B. (2013). Fabrication and multifunction integration of microfluidic chips by femtosecond laser direct writing. *Lab on a Chip*, *13*(9), 1677. https://doi.org/10.1039/c3lc50160d

Xu, C., Barnes, S. E., Wu, T., Fischer, D. A., DeLongchamp, D. M., Batteas, J. D., & Beers, K. L. (2006). Solution and Surface Composition Gradients via Microfluidic Confinement: Fabrication of a Statistical-Copolymer-Brush Composition Gradient. *Advanced Materials*, *18*(11), 1427–1430. https://doi.org/10.1002/adma.200502341

Xu, J., Wu, D., Ip, J. Y., Midorikawa, K., & Sugioka, K. (2015). Vertical sidewall electrodes monolithically integrated into 3D glass microfluidic chips using water-assisted femtosecond-laser fabrication for in situ control of electrotaxis. *RSC Advances*, *5*(31), 24072–24080. https://doi.org/10.1039/C5RA00256G

Xu, X., Goyanes, A., Trenfield, S. J., Diaz-Gomez, L., Alvarez-Lorenzo, C., Gaisford, S., & Basit, A. W. (2021). Stereolithography (SLA) 3D printing of a bladder device for intravesical

drug delivery. *Materials Science and Engineering: C*, *120*, 111773. https://doi.org/10.1016/j.msec.2020.111773

Yang, H., Chou, M.-C., Yang, A., Mu, C.-K., & Shyu, R. F. (1999). Realization of fabricating microlens array in mass production. *Optical Fabrication and Testing*, *3739*, 178–185. https://doi.org/10.1117/12.360143

Yeon, J. H., Ryu, H. R., Chung, M., Hu, Q. P., & Jeon, N. L. (2012). In vitro formation and characterization of a perfusable three-dimensional tubular capillary network in microfluidic devices. *Lab on a Chip*, *12*(16), 2815. https://doi.org/10.1039/c2lc40131b

Yuan, W., Li, L.-H., Lee, W.-B., & Chan, C.-Y. (2018). Fabrication of Microlens Array and Its Application: A Review. *Chinese Journal of Mechanical Engineering*, *31*(1), 16. https://doi.org/10.1186/s10033-018-0204-y

Zhang, J., Sugioka, K., & Midorikawa, K. (1998a). Direct fabrication of microgratings in fused quartz by laser-induced plasma-assisted ablation with a KrF excimer laser. *Optics Letters*, *23*(18), 1486. https://doi.org/10.1364/OL.23.001486

Zhang, J., Sugioka, K., & Midorikawa, K. (1998b). High-speed machining of glass materials by laser-induced plasma-assisted ablation using a 532-nm laser. *Applied Physics A: Materials Science & Processing*, *67*(4), 499–501. https://doi.org/10.1007/s003390050810

Zhang, J., Sugioka, K., & Midorikawa, K. (1998c). Laser-induced plasma-assisted ablation of fused quartz using the fourth harmonic of a Nd + :YAG laser. *Applied Physics A: Materials Science & Processing*, *67*(5), 545–549. https://doi.org/10.1007/s003390050819

Zhang, J., Sugioka, K., & Midorikawa, K. (1999). High-quality and high-efficiency machining of glass materials by laser-induced plasma-assisted ablation using conventional nanosecond UV, visible, and infrared lasers. *Applied Physics A: Materials Science & Processing*, *69*(7), S879–S882. https://doi.org/10.1007/s003390051551

Zhendong, L., Yangcheng, L., Jiawei, W., & Guangsheng, L. (2012). Mixing characterization and scaling-up analysis of asymmetrical T-shaped micromixer: Experiment and CFD simulation. *Chemical Engineering Journal*, *181–182*, 597–606. https://doi.org/10.1016/j.cej.2011.11.105

Zhu, F., Macdonald, N. P., Cooper, J. M., & Wlodkowic, D. (2013). *Additive manufacturing of lab-on-a-chip devices: Promises and challenges* (J. Friend & H. H. Tan, Eds.; p. 892344). https://doi.org/10.1117/12.2033400

Ziegenbalg, D., Kompter, C., Schönfeld, F., & Kralisch, D. (2012). Evaluation of different micromixers by CFD simulations for the anionic polymerisation of styrene. *Green Processing and Synthesis*, *1*(2). https://doi.org/10.1515/gps-2012-0004

Zimmer, K., Böhme, R., Ehrhardt, M., & Rauschenbach, B. (2010). Mechanism of backside etching of transparent materials with nanosecond UV-lasers. *Applied Physics A*, *101*(2), 405–410. https://doi.org/10.1007/s00339-010-5878-7

Zommiti, M., Connil, N., Tahrioui, A., Groboillot, A., Barbey, C., Konto-Ghiorghi, Y., Lesouhaitier, O., Chevalier, S., & Feuilloley, M. G. J. (2022). Organs-on-Chips Platforms Are Everywhere: A Zoom on Biomedical Investigation. *Bioengineering*, *9*(11), 646. https://doi.org/10.3390/bioengineering9110646

Zopf, D. A., Hollister, S. J., Nelson, M. E., Ohye, R. G., & Green, G. E. (2013). Bioresorbable Airway Splint Created with a Three-Dimensional Printer. *New England Journal of Medicine*, *368*(21), 2043–2045. https://doi.org/10.1056/NEJMc1206319

This thesis focuses on the development of microfluidic platforms employing advanced optical technologies for in vitro studies, aimed at improving personalized therapies. It addresses the discrepancy between standard static in vitro experiments and clinical outcomes by creating more physiological environments for cellular studies. To achieve this, various laser-based technologies will be studied in depth, including pulsed laser ablation, subaquatic indirect laser ablation, and stereolithographic 3D printing, emphasizing the advantages they offer over conventional methodologies in the manufacturing processes. Several microfluidic platforms will be developed using laser technologies, which will be tested and applied in the biomedical field, highlighting the great potential of merging both worlds.